INFORMATION TO USERS

This manuscript has been reproduced from the microfilm master. UMI films the text directly from the original or copy submitted. Thus, some thesis and dissertation copies are in typewriter face, while others may be from any type of computer printer.

The quality of this reproduction is dependent upon the quality of the copy submitted. Broken or indistinct print, colored or poor quality illustrations and photographs, print bleedthrough, substandard margins, and improper alignment can adversely affect reproduction.

In the unlikely event that the author did not send UMI a complete manuscript and there are missing pages, these will be noted. Also, if unauthorized copyright material had to be removed, a note will indicate the deletion.

Oversize materials (e.g., maps, drawings, charts) are reproduced by sectioning the original, beginning at the upper left-hand corner and continuing from left to right in equal sections with small overlaps. Each original is also photographed in one exposure and is included in reduced form at the back of the book.

Photographs included in the original manuscript have been reproduced xerographically in this copy. Higher quality 6" x 9" black and white photographic prints are available for any photographs or illustrations appearing in this copy for an additional charge. Contact UMI directly to order.

UMI

A Bell & Howell Information Company
300 North Zeeb Road, Ann Arbor MI 48106-1346 USA
313/761-4700 800/521-0600

A Linear, Stochastic, Dynamical Model of El Nino/Southern Oscillation

by

Christopher J. Thompson

A dissertation submitted in partial fulfillment
of the requirements for the degree of

Doctor of Philosophy

University of Washington

1998

Approved by Ka-Kit Tung
(Chairperson of Supervisory Committee)

Program Authorized
to Offer Degree Department of Applied Mathematics

Date 19 March 1998

Doctoral Dissertation

In presenting this dissertation in partial fulfillment of the requirements for the Doctoral Degree at the University of Washington, I agree that the Library shall make its copies freely available for inspection. I further agree that extensive copying of this dissertation is allowable only for scholarly purposes, consistent with "fair use" as prescribed in the U.S. Copyright Law. Requests for copying or reproduction of this dissertation may be referred to University Microfilms, 1490 Eisenhower Place, P.O. Box 975, Ann Arbor, MI 48106, to whom the author has granted "the right to reproduce and sell (a) copies of the manuscript in microform and/or (b) printed copies of the manuscript made from microform."

Signature CT Thompson

Date 19 March 1998

University of Washington

Abstract

A Linear, Stochastic, Dynamical Model of

El Nino/Southern Oscillation

by Christopher J. Thompson

Chairperson of the Supervisory Committee: Professor K.K. Tung

Department of Applied Mathematics

Much research has been devoted to physical models of the interannual SST variability in the Pacific known as El Nino/Southern Oscillation (ENSO). The Zebiak-Cane model (ZCM, 1987) has established the dominate view of ENSO as being a coupled ocean-atmosphere phenomenon that is chaotic and linearly unstable. Recently, the idea that ENSO irregularity might be caused by stochastic forcing has gained support. Here, a variant of the ZCM is developed which is linear and stable, but displays ENSO-like variability under moderate external forcing.

A linearized version of the Battisti (1988) variant of the ZCM is developed. This linear ocean-atmosphere model (LOAM) has time invariant background states, and is subject to singular vector analysis. The principle singular vector for time periods, τ, (the τ-optimals) show the following characteristics. (1) The τ–optimals grow more quickly than the most unstable mode (the ENSO mode). (2) The τ–optimals develop into the ENSO mode by 90 days. (3) Optimals were produced which used only the SST (T-optimals) and which used only the ocean dynamics (r-optimals.) For τ greater than 60 days, both optimals produce ENSO modes (of the same phase). A T-optimal pattern with a 0.1 degree anomaly maximum produces the same size ENSO as a r-optimal pattern

with a 1.2 meter maximum thermocline anomaly. (4) The full optimal is the linear combination of these two sub-optimals, where their relative sizes are determined by their relative weights in the norm. (5) Neutral and damped versions of LOAM show these same properties, and still display transient growth.

A version of LOAM (with an annual cycle added) is subjected to parameter studies to find plausible parameter regimes that damp the ENSO mode while preserving the transient growth of the τ-optimals. Increasing the ocean mechanical damping and decreasing the western boundary reflection has the desired effect. Four candidate models ranging from slightly damped to heavily damped are run in simulation and their output analysis. A moderately damped version, T.80, emerges as the candidate with a power spectrum and annual cycle of variance (of the Nino3 index) that are most like those from observations. The predictability limits are calculated, and display a similar pattern to the "spring barrier" of ENSO. The T.80 predictability limit ranges from 12 to 18 months, depending on the season. A stochastic differential equation version of LOAM (with an annual averaged background) is developed to check some of the results of the stochastic simulations.

TABLE OF CONTENTS

LIST OF FIGURES

LIST OF TABLES

ACKNOWLEDGEMENTS

Most of this work was supported by a grant for the NOAA/Office of Global Programs to the Stanley P. Hayes Center of the University of Washington. Many thanks to Ed Sarachik and David Battisti for many years of scientific guidance, and to all the denizens of the Climate Palace and the graduate students of Applied Math.

I would also like to thank my family and friends for their emotional support throughout my graduate student years, without which this dissertation would not have been completed. In particular, I thank Mom, Dad, MaryEllen, Joe, Casey, Shea, Ray, Deni, Tommy, Brian, Ed, CarolAnne, Franz, Dorothy, Zachary, Richard, Janice, Mark, Sarah, Donna, Caitlin, Wendy, Rebecca, Anna, Dave, Margaret, and all the Amath Class of 1990.

Chapter 1: Introduction and Summary

A revolution in our ability to predict the weather is taking place. Over the past five decades the forecast "horizon" has gradually been extended from only a few hours to several days. But now we are on the verge of a whole new kind of forecasting: short term climate prediction. We can foretell not only what the weather will be like tomorrow, but what it will be like next year, (at least some aspects of the weather). Success so far has been achieved through the prediction of the interannual sea surface temperature cycle known as ENSO (El'Nino/Southern Oscillation). Weather patterns are short lived and chaotic, so how can they be predicted one year in advance? In fact, they can't. However, ocean behaviour exists on a much longer time scale, and in some regions can be predicted up to a year in advance. Weather patterns are strongly influenced by the sea surface temperature (SST), and so if the SST can be predicted, then the *statistics* of the weather can be predicted.

It will never be possible to say if it will rain or not on a particular Thursday a year in advance. But it should be possible, in some cases, to predict the average rain fall next spring, or the average temperature next summer. If you are trying to schedule the company picnic, this may not be very useful. But if you are a farmer, a rancher, or even a city manager, the value of this information cannot be overstated. Already, with just limited prediction capability, substantial improvement in crop yields has been achieved in Northeastern Brazil and elsewhere (Moura 1994). ENSO has its most dramatic effects in the tropical Pacific, South America and Australasia, but also effects weather in North America. Of particular importance, ENSO is one of the predictors of the Asian monsoon, which causes both flooding and drought in India and east Asian countries like China and Japan.

Much work has been done recently in constructing models of the tropical Pacific

ocean and atmosphere system in order to simulate the ENSO physics. These models range from concise analytical models (e.g. Suarez and Schopf 1988) to large numerical coupled GCMs (e.g. Philander et al. 1992). The simplest models that have achieved some success in prediction are of the intermediate type. In particular, the model due to Zebiak and Cane (1987) has demonstrated skill up to a year in advance (Cane et al. 1986). The predictive capability of this model has recently been improved through more refined initialization (Chen et al. 1995).

Nonetheless, many questions remain to be addressed, including both the mechanisms that produce ENSO and the best methods for predictions. The specific questions of interest to this study are:

1) Are the ENSO warm and cold phases the reflection of an unstable system whose size is controlled by non-linearities, or is it a stable system occasionally stimulated into growth by external stochastic forcing? Currently the best ENSO predictor is the Zebiak-Cane model (ZCM) which has a self-sustaining ENSO cycle. However, other models (e.g. Miyakoda's GFDL model) also have predictive skill when initialized with data, but the models do not support ENSO oscillations.

2) Which physical fields (SST, winds, thermocline depth etc...) are the most important for initializing the coupled models for use in forecasting? Are there specific patterns in these fields, which, if more accurately resolved would minimize the error growth in the model?

Both of these questions can be addressed, at least in part, by the relatively new tool of optimal initial condition (OIC) analysis. Traditionally, stability analysis focuses on the eigenmodes of the linearized system. If the system has at least one eigenmode which is unstable (i.e. which grows), then the system is unstable. An infinitesimal perturbation will cause the most unstable eigenmode to grow until the system saturates non-linearly. If the system has no unstable eigenmodes then it

traditionally has been assumed that nothing in the system will "naturally" grow, and that significant growth can only be achieved through significant external forcing.

It has been shown (e.g. Farrell 1988b) that if a linear system has the mathematical property of being non-self adjoint, significant transient growth may be achieved even if the system is asymptotically stable. Finding the set of conditions which transiently grows the fastest and calculating their rate of growth is what OIC analysis is all about. For the remainder of this study, the optimal initial conditions will be referred to simply as "optimals."

As pointed out by Blumenthal (1991), the Zebiak and Cane model (ZCM) is not self-adjoint, and therefore it may be possible to find structures in the system that grow faster than the eigenvalues, at least for a limited time. A series of papers by Farrell (1988b, 1989 and others) point out the value of searching for these optimal growth structures in stability analysis. Also Farrell (1990) and Lacarra and Talagrand (1988) discuss their effect on error growth and predictability. The basic idea is that if the structure that grows fastest can be identified, then the error in the system can be minimized by resolving this structure as accurately as possible.

This study develops a linear version of the coupled ocean-atmosphere equatorial model by Battisti (1988) which is very similar to the ZCM. This linear ocean-atmosphere model (LOAM) is used to generate the singular vectors of the linear propagator of the system for a fixed time period, τ. The principle right singular vector represents the initial condition which will grow the fastest over the time period. This optimally growing structure will be called the τ–optimal.

The study is divided into 8 chapters. Following the introduction, Chapter 2 describes the basic equations of the Battisti model, shows how these equations are linearized for use in LOAM, and outlines the mathematics of their solution. The details of how the equations were non-dimensionalized, discretized, and put into matrix form

are presented in Appendices A through D.

Chapter 3 explores the shape and behaviour of the optimals for the special case in which there is no seasonal cycle in the model, i.e. where the background states are time-invariant (see also Chapter 7). In this chapter the following material is covered: (i) two different methods for computing optimals are presented: the adjoint method and singular value decomposition; (ii) the optimals are computed and it is shown that they grow much faster than the ENSO mode of the system; (iii) it is demonstrated that optimization of the ocean dynamics and thermodynamics can be considered separately under most conditions; (iv) the various fields of the optimals are examined and physical explanations for their structure are given; (v) the background states are modified to produce a neutral ENSO mode, and then a damped ENSO mode, and the previous results are shown to remain valid; (vi) the optimals produced in this study are compared with those calculated in several other recent studies; and (vii) some of the numerical difficulties that arose in the analysis are discussed. The bulk of the material presented in Chapter 3 has already been published by the author in Thompson (1997).

In Chapter 4, the model is generalized to include background states that evolve following the annual cycle. The effect of the annual cycle on both the ENSO mode and the optimals is explored. With the inclusion of the annual cycle, the singular values have a second dimension, the starting month, in addition to growth time, τ. It is observed that for almost all possible starting months and growth times, the optimals, when allowed to evolve, tend to peak during boreal winter months. This is noted to be consistent with observed ENSO events, which tend to peak during the boreal winter. All research in Chapters 5 and 6 is performed with the annual cycle included.

In Chapter 5, a series of parameter studies is carried out in order to modify the model to do two things: 1) to make the ENSO mode damped so that the LOAM can be driven stochastically without growing indefinitely, and 2) to achieve this damping

while preserving as much of the transient growth as possible, so that only moderate noise is required to drive the model. In other words, the desired model is designed to have diminished eigenvalues, while preserving the amplitude of its singular values. From the parameter studies, four candidate models are developed. These models are then tested to determine which models (if any) can be considered plausible models of ENSO. These models are the linear damped stochastic models, which will be shown to be a credible alternative to the nonlinear unstable chaotic models that have so far dominated ENSO research and prediction. The first test for these models is a set of hindcasts on the available SST observations. The models are shown to have reasonable predictive capability. The novel method of data assimilation, which uses only SST, is presented in detail in Appendix E.

In Chapter 6, the candidate models are driven stochastically and their output is statistically compared with observations. Three different types of perturbations are used to drive the system: 1) Normally distributed SST perturbations that are uniform in time, 2) a truncated series of Empirical Orthogonal Functions (EOFs) of the SST observations, and 3) a thermocline perturbation, non-uniform in time, inspired by the Madden-Julian Oscillation (MJO). It is shown that one of the candidate models outperforms the others in its ability to mimic the observations, and indeed appears to be a plausible ENSO model. Finally, in this chapter the candidate models are used to estimate the limits of predictability of the ENSO system, and the seasonal structure of predictability is examined.

In Chapter 7 a more analytic approach was taken to characterizing the systems response to noise forcing. In Chapter 6, LOAM was run as a simulation and perturbed randomly, but in Chapter 7 the LOAM is reformulated as a set of stochastic differential equations (SDE). These SDE are derived and solved for the time-invariant background case. This stochastic analysis is compared to the output from a randomly perturbed simulation (the method of Chapter 6) of the same, time-invariant background model,

and the equivalence of these two approaches is demonstrated.

Finally, Chapter 8 summarizes the research performed in this document, discusses its implications about the nature and predictability of ENSO, and suggests directions for further research.

Chapter 2: Model Description

2.1 LOAM: Linear Ocean-Atmosphere Model

The Zebiak-Cane model (hereafter ZCM) of the equatorial Pacific is well established and has been used successfully to simulate the interannual variability of ENSO (Zebiak and Cane 1987), and to make predictions about the occurrence of El Nino events up to a year in advance (Latif et al. 1994). A model almost identical to Zebiak-Cane was developed by Battisti (1988, hereafter B88M), and has been studied extensively (Battisti and Hirst 1989). The model used in this study is a linearized version of these models called LOAM (Linear Ocean-Atmosphere Model). Throughout this paper LOAM is configured to the Battisti version because (i) the behaviour of B88M is more regular than ZCM, and so is more straightforward to analyse and, (ii) a large part of this study is to see if the optimal initial conditions for SST can be computed separately from the other model variables as was done by Chen et al. (1997) with B88M. The differences between the ZCM and B88M are covered in depth by Mantua and Battisti (1995).

The model consists of a prognostically evolving ocean coupled to a diagnostically determined atmosphere. It is an anomaly model, and so all variables are calculated as perturbations superposed on user supplied background fields, which were derived from Rasmusson and Carpenter (1982) follow an annual cycle. The details and characteristics of the Battisti model are covered in depth by Battisti (1988), and details of the linearization used in this study are included in Appendix A. Unlike the full Battisti model, (in Chapters 3 and 7) LOAM is run with a time invariant, annually averaged background state. The annually averaged backgrounds for the SST, winds and upwelling are shown in Fig. 2.1.

In the Battisti model, a regular ENSO cycle develops and persists (Battisti 1988). It was believed that the ENSO cycle is the most rapidly growing eigenmode of the linear

portion of the model equations, while the non-linearities serve primarily to limit the growth of this ENSO mode. A linearized version of the Battisti model was built by Battisti and Hirst (1989) and run as an initial-value problem, which seemed to confirm this idea. More recently Chen et al. (1997), ran the full Battisti model and found that the model is essentially linear for small perturbations over time periods of at least 9 months. Of course, any system can be considered linear for small enough time periods and perturbations, but some of the results of this paper involve time periods greater than 90 days, and some justification that the system is linear this long is required.

In LOAM, the ocean equations, (A5) - (A7), are discretized spectrally in y by projecting them onto Rossby wave space, and discretized in x using finite differences. The details of the projection onto Rossby space are presented in Appendix B. The atmosphere and SST equations are projected onto Hermite function space in y and likewise discretized in x using finite differences. It is important to note that in the coupled model, the winds and Ekman current are diagnostically determined by the SST, i.e. these fields are automatically consistent with SST. The term "T-fields" will be used to refer to SST, winds, and Ekman currents altogether. Likewise, "r-fields" will refer to the Rossby (and Kelvin) wave amplitudes, which include the thermocline depth along with its dynamically consistent upper layer currents. In matrix form, the model can be written:

$$\begin{bmatrix} \mathbf{M}_{11} & \mathbf{M}_{12} \\ \mathbf{M}_{21} & \mathbf{M}_{22} \end{bmatrix} \begin{bmatrix} \underline{r} \\ \underline{T} \end{bmatrix} = \frac{d}{dt} \begin{bmatrix} \underline{r} \\ \underline{T} \end{bmatrix}, \tag{2.1.1}$$

where $\underline{r}$, and $\underline{T}$, are the r-field and T-field discretizations, respectively. Defining

$$\underline{\varphi}(t) \equiv \begin{bmatrix} \underline{r}(t) \\ \underline{T}(t) \end{bmatrix}, \text{ then } \frac{d}{dt}\underline{\varphi} = \mathbf{M}\underline{\varphi}. \tag{2.1.2}$$

Given a set of initial conditions, the solution to this system can be determined at any time by

$$\underline{\varphi}(t) = \exp(\mathbf{M}t) \cdot \underline{\varphi}(0). \tag{2.1.3}$$

where

$$\exp(\mathbf{M}t) \equiv \mathbf{I} + \mathbf{M}t + \frac{1}{2}\mathbf{M}^2t^2 + \ldots \equiv \mathbf{R}(t), \tag{2.1.4}$$

is called the matrix exponential or propagator. A second way to express the solution to (2.1.1) uses the eigenmodes of the system. For solutions of the form

$$\underline{\varphi} = \underline{e}(x,y)\cdot\exp(-i\sigma t), \tag{2.1.5}$$

where $i = \sqrt{-1}$, and σ is a complex number, (2.1.1) becomes

$$\mathbf{M}\underline{e} = -i\sigma\underline{e}. \tag{2.1.6}$$

This equation has a set of N linearly independent solutions $(\underline{e}_j, \sigma_j)$ called the eigenvector-eigenvalue pairs (or the eigenmodes), and where N is the number of columns (or rows) in the matrix $\mathbf{M}$. The time dependent solution to the original problem (2.1.1) can be written as the sum of these eigenmodes.

$$\underline{\varphi}(t) = \sum_{j=1}^{N} \alpha_j \underline{e}_j \exp(-i\sigma_j t). \tag{2.1.7}$$

where the α_j are the magnitudes of the projection of the initial condition onto the eigenvector. In other words,

$$\underline{\alpha} = \mathbf{E}^{-1}\underline{\varphi}(0), \tag{2.1.8}$$

where $\underline{\alpha}$ is a vector of the initial condition coefficients, and $\mathbf{E}$ is a matrix whose columns are the eigenvectors.

From (2.1.7) it can be seen that the eigenvector associated with the eigenvalue having the largest imaginary part will grow the fastest and dominate the solution at sufficiently long times. In general, $\underline{e}$ and σ can be either complex or real. Because the operator matrix, $\mathbf{M}$, is real for this system, complex $\underline{e}$ and σ will occur only in complex conjugate pairs. That is, if there is a eigenmode $(\underline{e}_r + i\underline{e}_i, \sigma_r + i\sigma_i)$ in the solution set, then the eigenmode $(\underline{e}_r - i\underline{e}_i, \sigma_r - i\sigma_i)$ will also be in the solution set. For our system, the eigenmodes of interest will usually be of this type. Since this is a model of the physical world, only real solutions are meaningful. In terms of the evolution of an eigenmode, this problem can be resolved be considering only the portion of the

eigenmode that projects onto the real plane. In other words, $\underline{\varphi}_j(t) = \mathrm{Re}\left(\underline{e}_j \exp\left(-i\sigma_j t\right)\right)$ would represent the evolution of mode j, where Re(•) takes the real part of the parenthetical quantity. Looking at it this way, an eigenmode then has a real part and an imaginary part, between which it oscillates with a frequency determined by $\mathrm{Re}(\sigma)$. Mathematically speaking, though, a more rigorous way to view these oscillating modes of the systems is as pair of complex conjugate eigenmodes acting together. That is, $\underline{\varphi}(t) = (\underline{e}_r + i\underline{e}_i)\exp\left(-i(\sigma_r + i\sigma_i)t\right) + (\underline{e}_r - i\underline{e}_i)\exp\left(-i(\sigma_r - i\sigma_i)t\right)$. A little algebra shows that the imaginary parts of this mode cancel, and so the mode is always real, and in fact evolves exactly like taking the real part of the eigenmode.

For this model the most unstable mode resembles the ENSO cycle, and will be referred to as the ENSO mode. Figure 2.2 shows the real and imaginary parts of the ENSO mode produced by LOAM. The real part is at the peak of a warm event, while the imaginary part shows the fields halfway between warm and cold events. The cold phase in this linear model is identical to the warm phase but with the signs reversed. The period of this ENSO mode is 1055 days which is in good agreement with Battisti and Hirst (1989).

2.2 Model Equations

The equations for the coupled ocean-atmospheric model and their linearization is shown in this section. First the Zebiak-Cane/Battisti model is linearized and then non-dimensionalized. Details of the derivation of the full model equations are covered exhaustively in the literature. See in particular Zebiak and Cane (1987) and Battisti (1988).

The full model consists of an atmosphere model coupled to an ocean model through the SST and winds. The atmospheric winds are driven by the SST. The winds in turn drive the ocean currents, while the ocean currents force SST evolution. The model

covers the equatorial wave guide in Pacific from Indonesia to the coast of South America. The independent variables are: x- the east/west coordinate, y- the north/south coordinate, and t, which is time.

2.2.1 Atmosphere

The atmosphere is the anomaly model of Gill (1980) as modified by Zebiak (1986). The atmosphere is modeled as a single vertical baroclinic mode on an equatorial β plane. It is considered to be in steady state with the SST, and is linear with mechanical and thermodynamic damping. The dependent variables for the atmosphere are, the meridional and zonal surface wind velocities: $U = U(x,y,t)$, $V = V(x,y,t)$ and the geopotential perturbation, $\varphi = \varphi(x,y,t)$.

The atmospheric equations are:

$$AU - \beta yV + \frac{\partial \varphi}{\partial x} = 0, \tag{2.2.1}$$

$$\beta yU + AV + \frac{\partial \varphi}{\partial y} = 0, \tag{2.2.2}$$

$$c_a^2 \frac{\partial U}{\partial x} + c_a^2 \frac{\partial V}{\partial y} + A\varphi = -Q_0 + Q^{(n)}, \tag{2.2.3}$$

where the damping, $A = 1.576 \cdot 10^{-5} s^{-1}$, and c_a is the characteristic wind velocity. The Battisti model heating is given by

$$Q_0 = \gamma c_a^2 (2\beta / c_a)^{1/2} T \left[\frac{T_{ref}}{\overline{T}(x,y)} \right]^2 \exp\left(b \left(\frac{1}{T_{ref}} - \frac{1}{\overline{T}(x,y)} \right) \right), \tag{2.2.4a}$$

with $\gamma = 1.4 m K^{-1} s^{-1}$, $T_{ref} = 303K$, $b = 5400K$, and $\overline{T} = \overline{T}(x,y)$ =mean annual SST. The Zebiak-Cane model (ZCM) gives the heating as

$$Q_0 = \gamma c_a^2 (2\beta / c_a)^{1/2} T \exp\left(\frac{b}{T_{ref}} \left(\overline{T}(x,y) - T_{ref} \right) \right), \tag{2.2.4b}$$

where the constants are the same except $\gamma = 1.6 m K^{-1} s^{-1}$.

The model has a wind convergence feedback which is given by

$$Q^{(n)} = \alpha c_a^2 \left[\Delta\left(-\nabla \cdot \left(\vec{U} + \overline{\vec{U}} \right) \right) - \Delta\left(-\nabla \cdot \overline{\vec{U}} \right) \right], \tag{2.2.5}$$

where

$$\Delta(x) \equiv \begin{cases} 0 & when \quad x < 0 \\ x & when \quad x \geq 0 \end{cases}, \tag{2.2.6}$$

and where $\alpha = 0.75$ is an efficiency factor.

All of the atmospheric equations are already linear except the convergence feedback which can be linearized as (see Battisti and Hirst 1989, BH89 hereafter)

$$Q^{(n)} = -\alpha c_a^2 \left[\frac{\partial U}{\partial x} + \frac{\partial V}{\partial y}\right] H\left(-\frac{\partial \overline{U}}{\partial x} - \frac{\partial \overline{V}}{\partial y}\right), \tag{2.2.7}$$

where $H(x)$ is the Heavyside function defined by

$$H(x) \equiv \begin{cases} 0 & when \quad x < 0 \\ 1 & when \quad x \geq 0 \end{cases}. \tag{2.2.8}$$

Defining the following constants,

$$K_Q(x,y) = \gamma c_a^2 (2\beta / c_a)^{1/2} \left[\frac{T_{ref}}{\overline{T}(x,y)}\right]^2 \exp\left(b\left(\frac{1}{T_{ref}} - \frac{1}{\overline{T}(x,y)}\right)\right) \text{ for B88M, or} \tag{2.2.9a}$$

$$K_Q(x,y) = \gamma c_a^2 (2\beta / c_a)^{1/2} \exp\left(\frac{b}{T_{ref}}\left(\overline{T}(x,y) - T_{ref}\right)\right) \text{ for ZCM, and} \tag{2.2.9b}$$

$$K_C(x,y) = -\alpha c_a^2 H\left(-\frac{\partial \overline{U}}{\partial x} - \frac{\partial \overline{V}}{\partial y}\right), \tag{2.2.10}$$

equation (2.2.3) may be written:

$$c_a^2 \frac{\partial U}{\partial x} + c_a^2 \frac{\partial V}{\partial y} + A\varphi = -K_Q T + K_C \left(\frac{\partial U}{\partial x} + \frac{\partial V}{\partial y}\right). \tag{2.2.11}$$

2.2.2 Ocean dynamics

The ocean model consists of two layers: an upper layer and a motionless lower layer. The upper layer is modeled with the linear shallow water equations on an equatorial β plane. Separate from the dynamics of the these two layers, an Ekman layer of fixed depth is imbedded in the upper layer. The Ekman layer is considered to be in steady state with the surface winds and will be covered in Section 2.2.3. The dependent variables for the ocean are, the meridional and zonal surface wind velocities: $u = u(x,y,t)$, $v = v(x,y,t)$ and the thermocline perturbation, $h = h(x,y,t)$.

The ocean equations are:

$$au - \beta yv + g' \frac{\partial h}{\partial x} = -\frac{\partial u}{\partial t} + \tau^x / \rho_o H_0, \tag{2.2.12}$$

$$\beta yu + av + g' \frac{\partial h}{\partial y} = \tau^y / \rho_o H_0, \tag{2.2.13}$$

$$H_0 \frac{\partial u}{\partial x} + H_0 \frac{\partial v}{\partial y} + ah = -\frac{\partial h}{\partial t}. \tag{2.2.14}$$

where $H_0 = 150m$ = mean upper layer depth, $g' = c_o^2 / H_0$ = reduced gravity, and τ^x and τ^y are the surface wind stress in the zonal and meridional directions respectively. The oceanic damping time is $a^{-1} = 2.5\ years$. A linear representation of the wind stress must be used, and so following BH89:

$$\tau^x = \rho_o H_0 \left(K_S^x U + K_S^c V \right), \tag{2.2.15}$$

and

$$\tau^y = \rho_o H_0 \left(K_S^y V + K_S^c U \right), \tag{2.2.16}$$

where

$$K_S^x(x,y) = \frac{2\overline{U}^2 + \overline{V}^2}{\left(\overline{U}^2 + \overline{V}^2\right)^{1/2}} \cdot \frac{\rho_a C_D}{\rho_o H_0}, \tag{2.2.17}$$

$$K_S^y(x,y) = \frac{\overline{U}^2 + 2\overline{V}^2}{\left(\overline{U}^2 + \overline{V}^2\right)^{1/2}} \cdot \frac{\rho_a C_D}{\rho_o H_0}, \tag{2.2.18}$$

$$K_S^c(x,y) = \frac{\overline{U}\,\overline{V}}{\left(\overline{U}^2 + \overline{V}^2\right)^{1/2}} \cdot \frac{\rho_a C_D}{\rho_o H_0}. \tag{2.2.19}$$

Here $C_D = 2.51 \cdot 10^{-3}$ is a constant, $\rho_o = 1.026 \cdot 10^3\ kg m^{-3}$ =sea water density, and $\rho_a = 1.275\ kg m^{-3}$ = atmospheric density. $\overline{U}$ and $\overline{V}$ are the annual mean surface wind fields.

2.2.3 Ekman layer

A thin surface (Ekman) layer is included in the model which is determined by the surface winds. The ocean upper layer has an Ekman layer imbedded according to:

$$H_0 = H_1 + H_2, \tag{2.2.20}$$

$$H_0 u = H_1 u_1 + H_2 u_2, \text{ and} \tag{2.2.21}$$

$$H_0 v = H_1 v_1 + H_2 v_2. \tag{2.2.22}$$

The shear between these two layers is determined from simplified Ekman theory as:

$$r_s u_s - \beta y v_s = \tau^x / \rho_o H_1, \tag{2.2.23}$$

$$r_s v_s + \beta y u_s = \tau^y / \rho_o H_1, \tag{2.2.24}$$

where

$$u_s \equiv u_1 - u_2, \text{ and} \tag{2.2.25}$$

$$v_s \equiv v_1 - v_2, \tag{2.2.26}$$

and where $r_s^{-1} = 2\ days$ is the damping constant.

2.2.4 Thermal Equation

The thermal equation determines the dynamics of the SST, and is given in B88 by

$$\begin{aligned} \frac{\partial T}{\partial t} = & -u_1 \frac{\partial}{\partial x}(\overline{T} + T) - v_1 \frac{\partial}{\partial y}(\overline{T} + T) - \overline{u}_1 \frac{\partial T}{\partial x} - \overline{v}_1 \frac{\partial T}{\partial y} \\ & - \overline{T}_z \delta \left[\Delta(\overline{w}_1 + w_1) - \Delta(w_1) \right] - \delta \Delta(\overline{w}_1 + w_1) \left[\frac{T - T_s(h)}{H_m} \right] - \alpha_s T \end{aligned} \tag{2.2.27}$$

where the overbars denote annual mean fields, $H_m = H_1 = 50m$ in B88 or $H_m = 100m$ in ZC87, $\alpha_s^{-1} = 125\ days$ is a thermal damping coefficient, and $\delta = 0.75$ is an efficiency factor. The surface layer upwelling is defined as

$$w_1 = H_1 \left(\frac{\partial u_1}{\partial x} + \frac{\partial v_1}{\partial x} \right). \tag{2.2.28}$$

Here the subsurface temperature anomaly is defined as

$$T_s = \Theta(h) \left\{ \tanh\left[\lambda \left(\overline{h} + \xi |h| \right) \right] - \tanh\left(\lambda \overline{h} \right) \right\}, \tag{2.2.29}$$

where

$$\begin{cases} \Theta = +28K \text{ and } \lambda^{-1} = 80m & \text{when} \quad h > 0 \\ \Theta = -40K \text{ and } \lambda^{-1} = 33m & \text{when} \quad h \le 0 \end{cases} \tag{2.2.30}$$

and $\xi = 1.5$ in B88 or $\xi = 1$ in ZC87.

The equation (2.2.27) can then be linearized first by discarding the quadratic

terms and then by linearizing the subsurface temperature expression in a Taylor series expansion:

$$T_s(h) = T_s|_{h=0} + h\frac{\partial T_s}{\partial h}\bigg|_{h=0} + \frac{1}{2}h^2\frac{\partial^2 T_s}{\partial h^2}\bigg|_{h=0} + \ldots \tag{2.2.31}$$

Dropping second and higher order terms, and noting that $T_s(h=0)=0$, leaves

$$T_s(h) = h \cdot T_s'(\bar{h}), \tag{2.2.32}$$

where

$$T_s'(\bar{h}) = \frac{1}{2}\left\{\left[\frac{\partial T_s}{\partial h}\right]_{h=0^+} + \left[\frac{\partial T_s}{\partial h}\right]_{h=0^-}\right\} = \frac{\xi}{2}\left\{\frac{28}{80}\cosh^{-2}(\bar{h}/80) + \frac{40}{33}\cosh^{-2}(\bar{h}/33)\right\} \tag{2.2.33}$$

approximates the first derivative of $T_s(h)$. Equation (2.2.27) is linearized as

$$\left[K_w\frac{\partial}{\partial x} + \bar{T}_x\right]u_1 + \left[K_w\frac{\partial}{\partial y} + \bar{T}_y\right]v_1 - K_T h + \left[\bar{u}_1\frac{\partial}{\partial x} + \bar{v}_1\frac{\partial}{\partial y} + d(x,y)\right]T = -\frac{\partial T}{\partial t} \tag{2.2.34}$$

where

$$K_w(x,y) = \delta H_1 \bar{T}_z H(\bar{w}_1). \tag{2.2.35}$$

$$K_T(x,y) = \delta\frac{\Delta(\bar{w}_1)}{H_m}T_s', \text{and} \tag{2.2.36}$$

$$d(x,y) = \alpha_s + \delta\frac{\Delta(\bar{w}_1)}{H_m}. \tag{2.2.37}$$

2.2.5 Backgrounds and Constants

For reference, the constants and constant background fields used by LOAM in Chapters 2 and 3 of this study are listed in Table 2.1. Four of the important background fields can be found in Figures 2.3(a) through (d). Shown in this figure are (a) the upwelling cooling coefficient, (b) the thermocline heating coefficient, (c) the temperature damping coefficient, and (d) the background zonal surface currents.

Table 2.1 - Values of Model Equation Constants. Values of the constants and constant background fields for various parameters used by LOAM.

Symbol	Value	Parameter
A	$1.576 \cdot 10^{-5} s^{-1}$	Atmospheric damping
β	$2.2915 \cdot 10^{-11} m^{-1} s^{-1}$	Meridional gradient of Coriolis force
(c_a, c_o)	$(60, 2.9)\ ms^{-1}$	Gravity wave speed (atmosphere, ocean)
γ	$1.4 mK^{-1} s^{-1}$	Coupling coefficient
(T_{ref}, b)	$(303K, 5400K)$	Reference Temperatures
$\overline{T}(x,y)$	Figure 2.1(b)	Background SST
α	0.75	Efficiency factor
$(\overline{U}, \overline{V})$	Figure 2.1(b)	Background winds (zonal, meridional)
H_0	$150m$	Mean upper layer depth
g'	$5.6\ cm$	Reduced gravity
a^{-1}	$2.5\ years$	Oceanic damping
(ρ_a, ρ_o)	$(1.275, 1.026 \cdot 10^3)\ kg m^{-3}$	Density of (atmosphere, ocean)
C_D	$2.51 \cdot 10^{-3}$	Coupling coefficient
(H_1, H_2)	$(50, 100)\ m$	Depth of (surface,subsurface) layer
r_s^{-1}	$2\ days$	Surface layer damping
$K_w(x,y)$	Figure 2.3(a)	Upwelling heating coefficient
$K_T(x,y)$	Figure 2.3(b)	Thermocline cooling coefficient
$d(x,y)$	Figure 2.3(c)	Temperature damping coefficient
$(\overline{T}_x, \overline{T}_y)$	See B88	Background SST gradients
$\overline{u}_1$	Figure 2.3(d)	Background zonal surface current
$\overline{v}_1$	See B88	Background meridional surface current

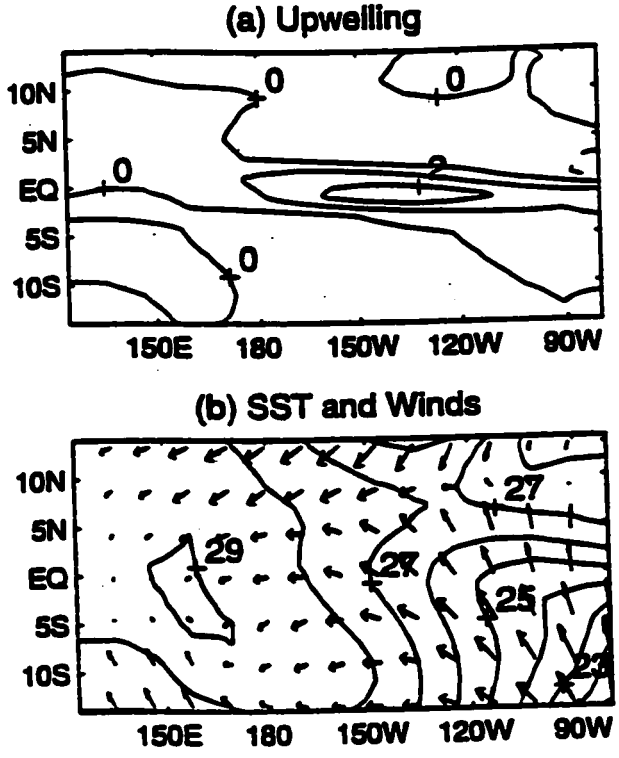

Figure 2.1 - Annually Averaged Backgrounds for Upwelling, SST and Winds. Graph (a) shows the upwelling with a 1 m/day contour increment. Graph (b) shows the SST contours with a 1K increment, and also shows the surface winds as arrows with a maximum velocity of 7.0 m/s.

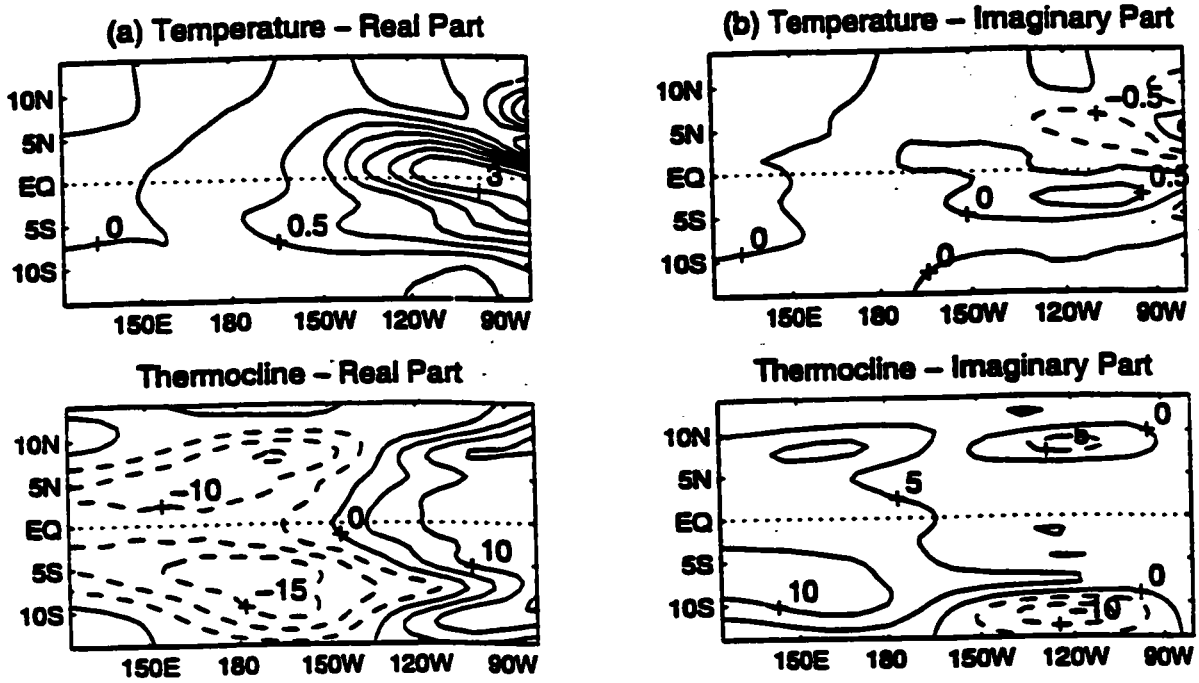

Figure 2.2 - ENSO Mode. Real and imaginary parts of the ENSO mode produced by LOAM. Temperature increment is 0.5 degrees/contour and the thermocline is 5 meters/contour. The real part of the ENSO mode is at the peak of a warm event. Since this is an eigenvector, it has no particular amplitude, but has been normalized so that the peak temperature is 3.5 degrees C.

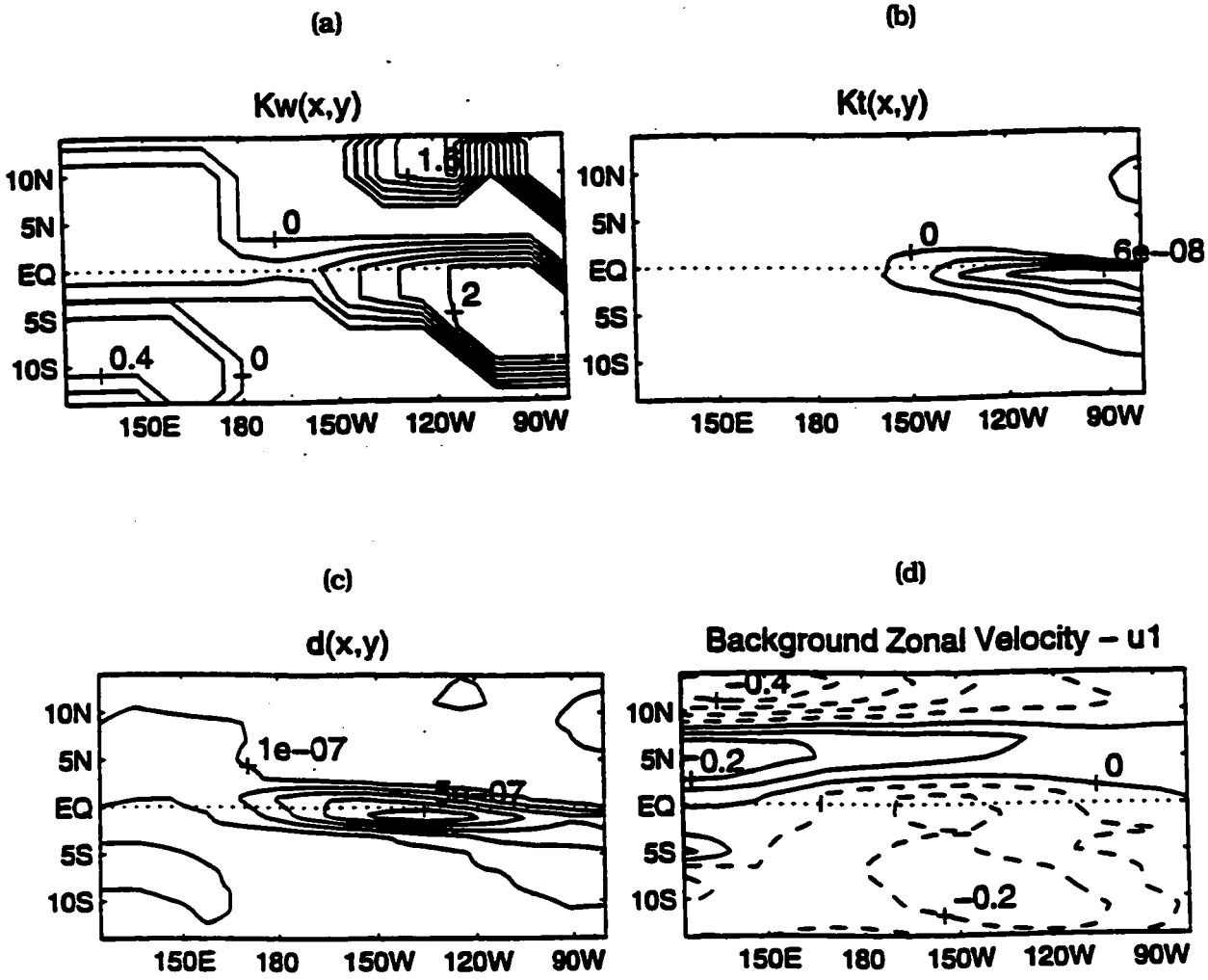

Figure 2.3 - Various Background Fields for LOAM. (a) shows K_w, the coefficient of cooling due to upwelling. Contour increments are $0.4\ K$. (b) shows K_t, the coefficient of heating due to thermocline movement. Contour increments are $2.0 \cdot 10^{-8}\ K \cdot m^{-1} \cdot s^{-1}$. (c) shows d, the coefficient of cooling due to SSTA. Contour increments are $1 \cdot 10^{-7}\ s^{-1}$. (d) shows $\overline{u}_1$, the Background zonal currents. Contour increments are $0.2\ m \cdot s^{-1}$.

Chapter 3: Annually Averaged Case

3.1 Interpretation of Optimals and Adjoints

Two different ways of computing the optimal initial conditions (or simply "optimals") are used in this Chapter. The first method is the adjoint method, which computes the adjoint of the fastest growing eigenmode. The second method uses singular value decomposition (SVD) of the propagator to find the optimal that produces the largest amplification in a fixed period of time (See Buizza and Palmer 1995). Optimals of the first type will be called adjoints, while the second type will be referred to either as singular vectors or as "τ-optimals" where τ is the period for which amplification is optimized.

3.1.1 Adjoint Method - The Optimal for Long Term Growth

For any optimization method, a norm must be defined that measures the size of the vector to be optimized. In our case, the state vector is $\underline{\varphi} = \begin{bmatrix} \underline{r} \\ \underline{T} \end{bmatrix}$, a combination of the r-fields and T-fields. How should these two subvectors be combined? Our interest is in the optimal growth patterns in the noise, so the L_2 norm is a good choice since the L_2 norm of either of the subfields is proportional to the RMS amplitude in that subfield. The RMS amplitude being the typical measure of noise. Simply adding the r and T fields together is problematic, though, since the relative weights of the two subfields will be determined, possibly arbitrarily, by the non-dimensionalization scheme. This difficulty is addressed in the following way: the norm will be defined as a weighted L_2 norm, that is

$$\|\underline{\varphi}\|_{2w} = \left(\begin{bmatrix} w_1 \underline{r} \\ w_2 \underline{T} \end{bmatrix}^H \begin{bmatrix} w_1 \underline{r} \\ w_2 \underline{T} \end{bmatrix} \right)^{1/2}, \qquad (3.1.1)$$

where "H" is the Hermite transpose. This norm will be referred to as the L_{2w} norm, or as the L_2 norm when the weights are at their nominal value of one. A more formal derivation of this norm can be found in Appendix F. Appendix F also includes a discussion of the alternative "perturbation energy" norm, along with a survey of the norms used in comparable research.

Later it will be shown that the relative weights do not matter much in the determination of the optimal fields, and so the nominal values will frequently be used. In the case when the nominal values are used, the relative weighting here is not arbitrary: the non-dimensionalization of the SST has been pick such that the amplitude of the r-field and T-field portions of the L_2 norm are approximately equal over the ENSO cycle (See Fig. 3.4). The L_2 norm of $\underline{r}$ closely tracks the L_2 norm of the thermocline over the ENSO cycle (not shown).

The initial vector $\underline{\varphi}(0)$ of unit norm that has the largest projection along a given eigenvector of the system is the normalized adjoint of that eigenvector (Farrell 1988a). From (2.1.7) it can be seen that to achieve the greatest long term (asymptotic) growth, the optimal will be the initial state that projects most strongly onto the fastest growing eigenvector. For this system, finding the long term optimal (or the ∞-optimal) is the same as finding the adjoint of the ENSO mode. In general, for matrices (Farrell 1988a):

$$adjoints(\mathbf{M}) = eigenvectors(\mathbf{M}^T), \tag{3.1.2}$$

where "T" is the matrix transpose.

Like the eigenvalues of the system, the adjoint field is complex and has phases. Figure 3.1 shows various phases of the adjoint of the ENSO mode (or just "adjoint") produced by LOAM. Keep in mind that while the phases of the ENSO mode correspond to a field advancing through time, the phases of the adjoint each represent different initial fields. The interpretation of this complex adjoint is discussed in Section 3.1.3, while the physical interpretation of the fields is discussed in Section 3.3.

3.1.2 Singular Value Decomposition or Tau-optimals

For a given time period, τ, the optimal can be computed (on the L_2 norm) using the SVD of $\mathbf{R}(\tau)$, the propagator. Singular value decomposition breaks $\mathbf{R}(\tau)$ into three matrices:

$$\mathbf{R} = \mathbf{U}\mathbf{S}\mathbf{V}^T, \tag{3.1.3}$$

where $\mathbf{U}$ and $\mathbf{V}$ are orthonormal matrices, and $\mathbf{S}$ is a diagonal matrix. The columns of $\mathbf{V}$ and $\mathbf{U}$ are called the right and left singular vectors, respectively. (Hereafter, the right singular vectors will be called simply the "singular vectors.") The diagonal elements of $\mathbf{S}$ are the singular values. The column of $\mathbf{V}$ with the largest corresponding singular value is the optimal initial field. Its L_2 norm grows by a factor equal to its singular value (in time τ), and its final shape after time τ is given by the corresponding column of $\mathbf{U}$. This can be seen by noting that since $\mathbf{V}$ is orthogonal it has the property that $\mathbf{V}^T\mathbf{V} = \mathbf{I}$, where $\mathbf{I}$ is the identity matrix. Equation (3.1.3) can be rewritten as $\mathbf{R}\mathbf{V} = \mathbf{U}\mathbf{S}$ or $\mathbf{R}\underline{v}_i = s_i\underline{u}_i$ where $\underline{v}_i$ and $\underline{u}_i$ are the ith columns of $\mathbf{V}$ and $\mathbf{U}$, and s_i is the ith diagonal element of $\mathbf{S}$. Since $\mathbf{R}(\tau)$ is the propagator, it takes the field of shape $\underline{v}_i$, to a field of shape $\underline{u}_i$, and size s_i, at time τ. More details about SVD can be found in Noble and Daniel (1988).

Since for this system, $\mathbf{R}(\tau)$ is always real, the SVD method produces real fields, rather than the complex fields of the adjoint method, but there is a direct correspondence between the methods. As τ increases, the τ-optimal converges to some phase of the adjoint. Figure 3.2 shows the correlation coefficient between the τ-optimal and the adjoint for τ going from zero to 180 days. The correlation coefficient used is the maximum coefficient comparing the optimal to all phases of the adjoint. Shown in Fig. 3.3 is the phase of the adjoint to which the τ-optimal is most highly correlated. In Fig. 3.3 the time axis is extended out to 1200 days (a little longer than the period of the ENSO mode). After an initial period of about 60 days, the τ-optimals converge to the adjoint.

One might expect the τ-optimal to converge to a single field as $\tau \to \infty$, but in fact it converges to a cycle.

The explanation for this behavior is that the L_2 norm of the r and T-fields fluctuates over the ENSO cycle. It peaks twice per cycle, once at the warm event, and then half a cycle later at the cold event. (See Fig. 3.4). In this linear model these peak events are identical in shape, but with opposite signs. The τ-optimals use the strategy of trying to get the ENSO mode which they generate to peak right at time τ. Figure 3.3 shows that the optimal phase of the adjoint progresses though one cycle for every period of the ENSO.

3.1.3 Interpretation of Optimals

This system can be viewed as having three "sources" of growth: 1) the exponential growth of the ENSO mode, 2) the periodic growth seen leading into the warm and cold events, and 3) the transient growth associated with short term effects (see Borges and Sardeshmukh 1995). The exponential growth is easy to quantify since it is given by the imaginary part of the ENSO mode eigenvalue. This accounts for the growth rate at longer times, but only causes a portion of the growth for periods less than a year. Figure 3.4 shows values of the L_2 norm of the r and T-fields over one ENSO period, with the exponential growth removed. Also shown is the portion of the total L_2 norm contributed by the T-fields, and the portion contributed by the r-fields. Depending on the values of the weighting factors, w_1 and w_2, the L_{2w} norm will vary, but throughout this chapter, unless otherwise stated, $w_1=w_2=1$. With the nondimensionalization used, this makes the contribution to the norm about the same for the T-fields as for the r-fields. The graph shows that the norm is cyclic, with a period of one half the period of the ENSO mode. The two peaks of the L_2 norm correspond to the peak warm event and the peak cold event in the ENSO cycle. By starting at a minimum

point in the cycle, the norm can grow by more than a factor of 2 over a 260 day period.

Owing to the instability of the ENSO mode, and the cyclic nature of the L_2 norm on the ENSO mode, large growth can be achieved without resorting to adjoints or singular vectors. How much more growth can we achieve using our optimization techniques? Figure 3.5 shows the growth that can be achieved by four different schemes. The bottom curve (scheme 1) shows the maximum growth that can be achieved over n-days by starting with a pure ENSO mode at the optimal phase where the instability growth is removed. The second curve (scheme 2) adds in the instability growth, i.e. the natural exponential growth of the ENSO mode. The top curve (scheme 4) shows the growth that the 360 day-optimal gives, while the next to top curve (scheme 3) shows the growth that can be achieved starting with the best phase of the adjoint. The last curve marked "filtered SVD" shows the growth achieved by the optimal fields presented in the graphs below, which have been filtered to remove some grid noise. This is covered in depth in Section 3.5.

For scheme 1, maximum growth of about a factor of 2 occurs for a period of one quarter the ENSO period. This scheme just starts the ENSO mode somewhere on the upward slope of the L_2 norm as shown in Fig. 3.4. If Fig. 3.5 were extended to show growth periods as long as one half an ENSO period, it would show that this scheme would be unable to produce growth at that time. Wherever it starts on the L_2 norm cycle it ends up at the same magnitude half a cycle later. At 3/4 of a cycle it would achieve its maximum growth again, and so on. The second curve shows the amount of growth that the first curve achieves if its natural exponential growth is not suppressed, which is more realistic especially for small perturbations. At 360 days, the instability more than doubles the growth compared to scheme 1, but it has only a small effect for the shorter time periods. The figure also shows that the τ-optimal (scheme 4) produces a significant improvement in growth: it is twice as effective as the unstable ENSO mode

(scheme 2) for periods as short as 90 days, and almost three times as effective at one year. The growth of the adjoint is included to demonstrate that not only does it look very similar to the τ-optimals (see Fig. 3.2) but that the small differences do not have a large effect.

Figure 3.6 shows the growth over time for five different τ-optimals. Each produces the largest possible value at its target time, but notice that the 30, 90 and 180 day optimals continue to grow, each peaking at around 300 days. In section 3.2 it will be shown that the optimals develop quickly (by about 90 days) into the ENSO mode. They produce the model ENSO more efficiently than if started with a pure ENSO mode. Examination of Fig. 3.6 shows that as τ increases from 30 days to 360 days, the first peak (the first warm event) occurs later, and is larger. The 540-day optimal, however, peaks before its target day and produces an ENSO mode with smaller amplitude than the 360-day optimal. Is there an optimal τ? Since the system is unstable, as $\tau \to \infty$ the growth of the τ-optimals must go to infinity, but maybe the system has a local maximum.

Figure 3.7 shows the time and magnitude of the first peak for τ-optimals with τ ranging from 20 to 1000 days. This graph shows that there is indeed a local maximum at τ at 360 day, and then another at 880 days. The time period, τ, where the first local maximum occurs will be called τ_{max}. This local maximum is essentially the unstable equivalent of the absolute maximum for τ found in damped systems (See Section 4 of Penland and Sardeshmukh, 1995).

But what about the second peak? The second peak is not coincidentally 1/2 an ENSO period after the first: remember that the τ-optimals are periodic (see Fig. 3.3). Figure 3.7(b) provides the explanation. Given 360 days, the optimal is able to spin off its largest ENSO. In order to optimize for a smaller τ, the optimal shifts the warm event to an earlier and earlier time, but loses efficiency by doing so. For τ greater than 360 days, the warm event is delayed, likewise with a loss of magnitude. At a certain point, as τ

gets even larger, it becomes more effective to use the second peak of the L_2 norm's cycle (the cold event). Thus the first peak is made as early as possible so that the second peak will occur closer to τ. This transition shows up clearly in Fig. 3.7b as being somewhere between 520 and 540 days. Interestingly, it also shows up in Fig. 3.3 as an area in the phase of the adjoint that the τ-optimals move through very quickly.

3.2 Optimizing on SST vs. Optimizing on Dynamics

The optimal fields calculated above use both the SST and ocean dynamics combined (somewhat arbitrarily) together to define the norm. Others, such as Chen et.al. (1997), have avoided this problem by ignoring the ocean dynamics altogether, and instead have looked for the optimals that maximize the SST growth over a fixed period of time, with the constraint that the ocean dynamics be zero initially. In the above notation this means the SVD of $\mathbf{R}_{22}$, where the propagator is divided as

$$\begin{bmatrix} \underline{r}(t) \\ \underline{T}(t) \end{bmatrix} = \begin{bmatrix} \mathbf{R}_{11} & \mathbf{R}_{12} \\ \mathbf{R}_{21} & \mathbf{R}_{22} \end{bmatrix} \begin{bmatrix} \underline{r}(0) \\ \underline{T}(0) \end{bmatrix}. \tag{3.2.1}$$

[Note that this is not the same as taking the SVD of $\mathbf{R}$ while using $w_1 = 0$ in the L_{2w} norm. This formulation would leave out the constraint that the ocean dynamics initially be zero and would lead to an ill posed problem whose solution would be to make the ocean dynamics (r-fields) initially infinite while leaving the initial SST zero.] The first singular vector of $\mathbf{R}_{22}$ will be referred to as the T-optimal, while the first singular vector of $\mathbf{R}_{11}$ will be called the ocean dynamics optimal or r-optimal.

Chen et al. (1997) computed $\mathbf{R}_{22}$ by running the full Battisti model with small perturbations on the SST field, but found the method too computationally expensive to apply to the full set of fields. Using LOAM, finding the optimals is relatively easy, so the T-optimal can be checked against the SST portion of the full optimal for various time periods. The r-optimal can also be compared to the full optimal. Intuition would suggest

that the shape of the T-optimal should become similar to the full optimal for longer times - long enough to give the SST time to interact with the ocean dynamics. From (2.1.4) and (3.2.1) an expression for $\mathbf{R}_{22}$ can be found,

$$\mathbf{R}_{22} = \mathbf{I} + \mathbf{M}_{22}t + \left(\mathbf{M}_{21}\mathbf{M}_{12} + \mathbf{M}_{22}^2\right)\frac{t^2}{2!} + \left[\left(\mathbf{M}_{21}\mathbf{M}_{22} + \mathbf{M}_{22}\mathbf{M}_{21}\right)\mathbf{M}_{12} + \left(\mathbf{M}_{21}\mathbf{M}_{12} + \mathbf{M}_{22}^2\right)\mathbf{M}_{22}\right]\frac{t^3}{3!} + \cdots \tag{3.2.2}$$

From this it is clear that $\mathbf{R}_{22}$ will be affected by all parts of the evolution operator $\mathbf{M}$ at longer times. Figure 3.8 gives a plot of the spacial correlation between the full optimal and each of the two partial optimals. This figure shows that after about 60 days the T-optimal and r-optimals look like their respective parts of the full optimal, both having a correlation greater than 85%.

Which is the more important part of the full optimal - the ocean dynamics or the thermodynamics? Figure 3.4 showed their relative sizes in the full optimal for $w_1 = w_2 = 1$, but what if these weights are changed? The fact that the *shapes* of the subfield optimals are essentially independent of the weighting after 60 days, indicates that the r-optimal and the T-optimal might be linearly combined to give the full optimal. Because our system has a single growing mode, the ENSO mode, - any initial condition will eventually lead to this mode. Let

$$\underline{\beta}_\tau(t) = \mathbf{R}(t)\underline{\alpha}_\tau \tag{3.2.3}$$

where $\underline{\alpha}_\tau$ is a full τ-optimal, and $\underline{\beta}_\tau(t)$ is the field that results after time t has elapsed. Defining $\underline{\beta}_{ENSO}$ as the (normalized) shape of the ENSO mode, then for large enough t,

$$\mathbf{R}(t)\underline{\alpha}_\tau \cong \sigma(t)\cdot\underline{\beta}_{ENSO},\ \mathbf{R}(t)\begin{bmatrix}\underline{\alpha}_\tau^r \\ \underline{0}\end{bmatrix} \cong \sigma^r(t)\cdot\underline{\beta}_{ENSO},\ \text{and}\ \mathbf{R}(t)\begin{bmatrix}\underline{0} \\ \underline{\alpha}_\tau^T\end{bmatrix} \cong \sigma^T(t)\cdot\underline{\beta}_{ENSO}, \tag{3.2.4}$$

where $\underline{\alpha}_\tau^r$, and $\underline{\alpha}_\tau^T$ are the r-optimal and T-optimal respectively, and the σ are real scalars.

But how long a time is required for this, and will the phase of the ENSO mode be the same for each? Figure 3.9 gives the correlation coefficient between $\underline{\beta}_\tau(t)$ and $\underline{\beta}_{ENSO}$

for the full optimal, as well as the T-optimal and r-optimal for τ equals 90 and 360 days. Figure 3.10 gives the phase of the ENSO for the same parameters. Figure 3.9 shows that for periods of time as short as 90 days, (3.2.4) is approximately true, with a correlation of greater than 85% between the optimals after 90 days of growth and the ENSO mode. Figure 3.10 shows that the ENSOs produced by the different optimals are almost in phase, to within 5 degrees by time τ. However, these phases do not converge. The explanation can be found back in Fig. 3.4: the norm of the T-fields and the norm of the r-fields peak at slightly different times. Since the T-optimal is optimizing the T-fields only, it will try to make an ENSO where the T-field norm peaks at the chosen time, whereas the r-optimal will try to place the ENSO so that the r-field peaks at the chosen time.

Nevertheless, for some sufficiently large fixed time, it is approximately true that

$$\mathbf{R}_t\left[a_1\begin{bmatrix}\underline{\alpha}_\tau^r\\ \underline{0}\end{bmatrix}+a_2\begin{bmatrix}\underline{0}\\ \underline{\alpha}_\tau^T\end{bmatrix}\right]=\left(a_1\sigma_t^r+a_2\sigma_t^T\right)\cdot\underline{\beta}_{ENSO} \tag{3.2.5}$$

where a_1 and a_2 are real scalars. Then the "mixture" of the T-optimal and r-optimal that produce the maximum ENSO can be computed from a simple optimization problem. But first choose the time $t=\tau$, large enough so that, (i) equation (3.2.4) is valid, and so that (ii) the shapes of the T-optimal and r-optimal are the same as their respective parts of the full optimal. If weighting factors are included then (3.2.5) can be used to compute the full optimal,

$$\underline{\alpha}_\tau\equiv\begin{bmatrix}a_1\underline{\alpha}_\tau^r\\ a_2\underline{\alpha}_\tau^T\end{bmatrix}. \tag{3.2.6}$$

The optimization problem becomes

$$\max\left(a_1\sigma_\tau^r+a_2\sigma_\tau^T\right)\quad s.t.\quad \left(a_1^2w_1^2+a_2^2w_2^2\right)^{1/2}=1, \tag{3.2.7}$$

which has the solution,

$$a_1=\frac{w_2\sigma_\tau^r}{w_1\left((w_2\sigma_t^r)^2+(w_1\sigma_t^T)^2\right)^{1/2}},\ \text{and}\ a_2=\frac{w_1\sigma_\tau^T}{w_2\left((w_2\sigma_t^r)^2+(w_1\sigma_t^T)^2\right)^{1/2}}. \tag{3.2.8}$$

In order to check this result, the full optimal was computed using LOAM, and the

results are plotted against (3.2.8) for a wide range of weights. The results found in Fig. 3.11 show good agreement between the two. Examining (3.2.8) or Fig. 3.11 shows that the weights essentially act as a penalty against their respective subfields. Note that this figure is not intended as a practical method for computing the optimal, but merely as a demonstration that the approximations leading to (3.2.8) are valid.

Table 3.1 - Relative Growth of Subfield Optimals. Size of the SST field grown over τ days started from either the T-optimal (first column) or the r-optimal (second column) of unit size. All field sizes are measured as the maximum of the field.

τ (days)	T-final/T-initial (deg/deg)	T-final/h-initial (deg/meter)
90	2.7	0.20
180	5.2	0.39
360	7.2	0.61

Equation (3.2.5) suggests a straightforward way to evaluate the relative importance of the two different subfields. Since both the T-optimal and r-optimal produce a field (at time τ) of the same shape, the maximum SST of the final field is an adequate description of its size. Table 3.1 shows the maximum SST produced by the T-optimal scaled to have an initial maximum SST of one degree, along with the maximum SST produced by an r-optimal with a maximum thermocline perturbation of 1 meter. Assuming the worst case, that errors in knowledge of each of the initial fields are in the shape of their respective optimal, what is needed is a judgement about the "value" of the initial fields. A hypothetical forecaster who wanted equal amounts of possible error coming from inaccuracies in the measurement of the thermocline and SST would need to resolve the thermocline field to about 1.2 meters if her SST resolution were 0.1 degrees (at 360 days). Figure 3.12 shows the initial fields and the final fields for the 90 day and 360-day optimals, respectively.

3.3 Physical Interpretion of Optimals

For the physical explanation of the optimal initial conditions, the 360-day optimal will be examined in more depth. For didactic purposes, the optimal will be divided into four subfields: the symmetric SST, the antisymmetric SST, the symmetric thermocline and the antisymmetric thermocline. As before, the SST fields also include the implied wind and the Ekman component of the currents, while the thermocline fields include the dynamically consistent geostrophic currents. Figure 3.13a shows the growth of the L_2 norm for the full field, starting with each of the of the four different suboptimals. Figure 3.13b shows the correlation between the field produced by each of the suboptimals and the field produced by the full optimal. From this figure it can be seen that even though the suboptimals are initially linearly independent, they become collinear as they grow. That is, as time goes on they all develop into the ENSO mode at the same phase. The total growth at 360 days of the full optimal is then simply the sum of the amplitudes of each of the suboptimals after 360 days. The symmetric part of the T-optimal accounts for 68% of the final amplitude of the 360 day T-optimal, and the antisymmetric part accounts for 32%. For the 360 day r-optimal the symmetric and antisymmetric parts account for 80% and 20% of the final amplitude, respectively.

3.3.1 Symmetric Part of T-Optimal

The symmetric SST portion of the T-optimal is shown in Fig. 3.14a, along with the surface winds which accompany it in Fig. 3.14b. The warm water in the Eastern Pacific and cold water in the Western Pacific induce strong westerly winds near the equator at around 120W. The effect of these temperature and wind fields can be broken up into two parts: their effect on the SST and their effect on the ocean dynamics.

Figure 3.14c shows the derivative of the SST. Most of the heating in the western central Pacific is from two sources: about half of it is due to the $d(x,y)\cdot T$ term of

(2.2.34). The other half is due to relaxation of the anomalous upwelling caused by the westerly surface winds, the $K_w \partial v_1 / \partial y$ term of (2.2.34). Notice how the SST pattern avoids putting positive SST on the equator in the eastern Pacific. Examining Fig. 2.3c shows why: the thermal damping term peaks along the equator in the central and eastern Pacific. By putting negative temperature values in the central equatorial Pacific, and avoiding positive values in the eastern Pacific, the optimal achieves a net heating from this term, while still producing the needed westerly winds. In the ENSO cycle the westerly winds are likewise caused by a west to east gradient in the temperature, but the positive SST is right on the equator, reducing its effectiveness. The T-optimal thus gets an initial boost from the $d(x,y) \cdot T$ term, but as soon as day 30 it becomes a damping factor as the warm anomalies move equatorward.

Figure 3.14d shows the effect of the initial wind field on the first three symmetric ocean components, i.e. the Kelvin wave and Rossby waves one and three. The winds force a downwelling Kelvin signal, and upwelling Rossby signals in the east-central Pacific. The downwelling Kelvin signal will grow and propagate eastward, suppressing the thermocline and causing heating in the east around the equator. This "secondary" source of heating will eventually provide most of the heating to counteract the damping of the $d(x,y) \cdot T$ term. The upwelling Rossby signals grow and propagate westward where they will have relatively little effect on the SST since the heating coefficient K_T is small there. See Fig. 2.3b. These upwelling Rossby signals will eventually reflect off the western boundary into an upwelling Kelvin signal which will switch off the warm ENSO event being built by this optimal, but this will not occur until just after the warm event peaks at the 360 day mark (see Battisti 1988).

3.3.2 Antisymmetric part of T-optimal

The antisymmetric portion of the T-optimal is shown in Figs. 3.14e and 3.14f.

The SST field consists of a cold anomaly in the NE Pacific and a warm anomaly in the SE Pacific, with a weaker warm anomaly over the central and western Pacific in the North, and its opposite in the south. The primary effect on the winds is to cause a strong northerlies near the equator in the east, but it also causes easterlies in the NE Pacific and westerly winds in the SE Pacific. These westerlies are not insignificant, with a peak velocity of about half the peak velocity of the westerlies in the symmetric T-optimal.

Figure 3.14g shows the derivative of the SST produced by these antisymmetric fields. Initially only modest overall heating is achieved, with a tendency as in the symmetric case to move the warm anomaly to the equator. About half of this initial heating comes from the background meridional currents acting on the large meridional SST gradient in the east, i.e. the $\bar{v}_1 \partial T/\partial y$ term of (2.2.34). Most of the rest comes from relaxation of the upwelling as before. The thermal damping term acts primarily to cause the cooling in the southeast. Figure 3.14h shows the effect of the surface winds on the ocean dynamics, giving the derivative of the Kelvin and first two symmetric Rossby waves. The effect is almost identical to that in the symmetric case, but with about one third the amplitude. As before, these perturbations are self-reenforcing and promote ENSO growth.

3.3.3 Symmetric part of r-Optimal

The initial thermocline and zonal current for the symmetric 360 day r-optimal are shown in Figs. 3.15a and 3.15b. The thermocline is the more important of these two fields and consists of a trough extending the length of the Pacific Basin along the equator, deepening at the eastern boundary. The deep thermocline in the eastern equatorial Pacific causes heating there, as shown in Fig. 3.15c which gives the rate of change of the SST. Almost all of this heating is due to the $K_T h$ term in (2.2.34), which acts in the eastern equatorial Pacific (see Fig. 2.3b). As before, this heating causes

westerly winds in the eastern and central equatorial Pacific which will further deepen the thermocline there.

Why doesn't the optimal ignore the rest of the basin and maximally deepen the thermocline in the east to maximize the SST heating? A look at the time evolution of the ocean dynamics shows what is going on. Figure 3.16 gives the magnitude of the Kelvin wave, K, and of the first two symmetric Rossby waves, R1 and R3, at 50 day intervals starting with the symmetric r-optimal. K has nearly a constant positive magnitude across the basin, as does R1, except R1 has an extra "kick" near the eastern boundary. This kick is effective in R1 since the thermocline profile of this Rossby wave peaks slightly off the equator, near where the coefficient K_T peaks. However it is also a inefficient feature, since the SST and winds that it stimulates work against it. Examining Figs. 3.16a to 3.16c, it can be seen that this initially positive peak gets pushed down as it propagates westward, and is in fact negative, by day 100. Remember that the L_2 norm is being maximized here, so quantities that increase in magnitude contribute to the growth. Looking at Fig. 3.16, it can be seen that R3 starts out negative in the east, and grows under the influence of the winds. The thermocline structure of R3 is such that its negative value produces a modest positive perturbation to the thermocline at the equator (and therefore heating), but this modest heating effectively contributes to growth since the winds reinforce rather than fight R3.

The initial Kelvin profile reflects the same type of trade off as the R1 profile. An unforced Kelvin signal propagates eastward, and then reflects off the eastern boundary as westward-bound Rossby signals. If the initial K profile were to have all of its amplitude near the eastern boundary, it would indeed produce a larger SST in the east, but the reflected Rossby signals it generated would be squashed by the westerly winds caused by the SST. As K is initially positive across the entire basin, the thermocline perturbation in the east is supported by positive amplitude propagating from the west over the course of the 360 days. At first it does this on its own, but later it uses the the

positive amplitude that the Rossby waves start out with in the western Pacific, which reflect off the western boundary into the Kelvin wave. See Fig. 3.16.

3.3.4 Antisymmetric part of r-Optimal

The antisymmetric part of the r-optimal is not so complicated. Since the antisymmetric Rossby waves are not strongly influenced by the growing warm anomaly in the east, and since they do not reflect off the western boundary, nor are they produced by Kelvin reflection at the eastern boundary, heating is their primary effect. Figures 3.15d and 3.15e show the initial thermocline displacement and the accompanying zonal currents. The heating is shown in Fig. 3.15f. About half of the heating is caused by the thermocline suppression at about 5S and 100W, while the remainder comes from downwelling, and the surface currents produced which advect along mean temperature gradients (not shown).

3.3.5 The Subfields Recombined

Since the system is linear, and since τ is sufficiently large (see Fig. 3.9b), these four subfields are simply added together to form the complete initial conditions. The evolution of the full initial conditions is just the sum of the fields produced by the separately evolving subfields. Since the subfields are initially linearly independent, the initial size of the L_2 norm is the square root of the sum of the squares of their individual amplitudes. By the end of the period τ the subfields are collinear, so the L_2 norm of the complete field is just the sum of the L_2 norms of the subfields.

3.4 Neutral and Damped Cases

The above sections show that for an annually averaged background, the Battisti model has the following properties: (i) there is a correspondence between the phases of

the adjoint of the ENSO mode and the τ-optimals (Fig. 3.3) and that the τ-optimals essentially become the adjoint at a relatively small τ of about 180 days (Fig. 3.2), (ii) that the initial growth rates of the τ-optimals are significantly greater than the growth rate of the ENSO mode (Fig. 3.5), (iii) that the optimals quickly develop into the ENSO mode (Fig. 3.9), (iv) that there exists a τ_{max} (at 360 days) whose optimal out performs those around it (Figs. 3.6 and 3.7), and (v) that r-optimals and T-optimals have the same shape as their respective parts of the full-optimal (Fig. 3.8). Several of these properties seem as though they may result from the robust growth rate of the ENSO mode when using the annual averaged background.

For comparison, two other background fields were tested: one which produced a nearly neutral ENSO mode, and one for which the ENSO mode is damped. The annual average background fields were obtained by averaging the monthly fields from Battisti (1988). Table 3.2 shows the growth rate and period of the ENSO mode using the background fields for each month individually. For each month the ENSO mode is also the most unstable (or least damped) eigenmode. The damped ENSO was constructed from a mean field that is the average of three stable months, i.e. from a perpetual spring. The neutral ENSO background was constructed as the average over 5 consecutive months that included December through March, plus some percentage of both November and April. The percentage of the unstable November and stable April was varied until a (nearly) neutral ENSO was obtained. Table 3.2 also shows the growth and period of the ENSO mode for these two cases plus for the nominal background. Note that the values in Table 3.2 are consistent with Fig. 13 from Battisti and Hirst (1989) which shows the results of a similar calculation.

Table 3.2 - Period and Growth Rate of ENSO Mode for Various Backgrounds. Growth rates are e-folding times. The first twelve are average fields over the months named. The Annual Average field is the nominal background used throughout Chapter 3. The Damped case is the months of February to April averaged. The Neutral case is a five month average starting with 7% of November though 93% of April. For the Neutral case to be truly neutral, it would need an infinite period of growth, in fact it is slightly damped with a e-folding time of 23 centuries.

Month	Period (years)	Growth (years)
JAN	3.10	9.78
FEB	3.37	-4.75
MAR	3.49	-2.75
APR	3.66	-3.34
MAY	3.37	1.83
JUN	4.20	0.73
JUL	3.41	0.70
AUG	2.82	0.66
SEP	2.70	0.90
OCT	2.18	1.13
NOV	2.34	1.25
DEC	2.36	2.25
Year Average	2.89	1.21
Neutral Case	2.82	$-2.3 \cdot 10^3$
Damped Case	3.53	-4.48

The neutral and damped backgrounds were then run through the same tests as the annual average. Qualitatively the optimals produced by these backgrounds have the same characteristics as listed above, although there are quantitative differences. The most important similarity is that the pattern of the optimals are alike for all three cases, while the most important difference is that the transient growth rates are smaller for the neutral and damped cases. Figure 3.17 shows the 240-day optimal for the

neutral case, both initially and after 240 days. A 240 day period is picked since this is the value of τ_{max} for this case. It looks very similar to Fig. 3.12c, the τ_{max}–optimal for the nominal case. However, it produces less growth, with a 4.9-fold increase in the L_2 norm. For comparison, the 240-day optimal for the nominal case grows by a factor of 9 (see Fig. 3.5). The damped case, at its τ_{max} of 180 days, only produces a 3-fold growth in the L_2 norm, compared to about 7.5 for the nominal case 180-day optimal. But the shape of the damped optimal (shown in Fig. 3.18) is still very similar to the others.

The figures describing the five properties listed above will not be reproduced here for the two new cases, but they will be described. (i) The τ-optimals do converge to the adjoint, but not as quickly as for the nominal case. For instance, the nominal case reaches 85% correlation by τ equals 45 days (see Fig. 3.2), but the neutral case takes 100 days and the damped case takes 150 days. (ii) As mentioned above, while the neutral and damped cases do not produce as much initial growth as the nominal case, they do significantly out perform their respective ENSO modes. Even the system where the ENSO mode is damped has an optimal which can produce 3-fold growth in 180 days. (iii) In all cases the optimals grow into the ENSO mode. Figs. 3.17b and 3.18b show their respective optimals after τ days of growth. Each is at a peak warm event of ENSO. (iv) Graphs of the type in Fig. 3.7 were produced for the neutral and damped cases, which were qualitatively similar, but with smaller peak growths. The most effective growth periods shifted, being 240 days and 180 days for the neutral and damped cases, respectively. (v) Like the nominal case, the r-optimal and T-optimal can be computed independently for large enough τ. The value of that "large enough" τ becomes greater. The 85% correlation from Fig. 3.8 is reached for the nominal case by τ = 60 days, whereas for the neutral and damped cases, it takes 90 days and 120 days, respectively.

The experiments with different background states indicate that the instability of the ENSO mode is not the primary reason that the optimals are able to produce growth. The fact that the qualitative results are not sensitive to the details of

background state also helps to justify the use of an annual averaged background instead of a changing background. The neutral and damped cases also demonstrate another idea: that it is possible to grow ENSO-like warm and cold events even if the system is stable. The ZCM and B88M imply that the ENSO peak events are one phase of an unstable, interannual coupled basin mode, but others (in particular Penland and Sardeshmukh 1995, hereafter PS95) have suggested that the ENSO peak events are instead the transient growth caused by stochastic forcing in a stable system. The implications of the results of this section to PS95 are discussed in Section 3.6.4.

3.5 Numerical Concerns

As stated in Section 2.1, the model equations were solved by finite differencing in x and by a spectral method in y. For all the results in this study, the LOAM ocean used 15 grid points in x, 8 Hermite functions for the SST in y, and 9 Rossby waves for the ocean dynamics in y. (LOAM automatically uses one less function in SST than ocean dynamics to avoid a truncation problem). The atmosphere automatically uses the same grid size in x as the ocean, but extends around the Earth. In y, the atmosphere was projected onto 14 Hermite functions.

To check the resolution, runs where made at double the resolution in x, with no substantial change in the shape of the ENSO mode or the principle singular vector. The results of the spectral resolution test in y were a little more complicated. The model was able to simulate ENSO with as few as two waves: the Kelvin and gravest symmetric Rossby wave. The optimals produced from this minimalist ENSO were symmetric since only symmetric functions were used. By adding the first antisymmetric mode to the ocean and SST expansions, the optimal fields produced took on all the basic characteristics of the higher resolution runs. However, the ENSO mode produced at this coarse resolution is only slightly unstable because it only has one symmetric Rossby

mode to carry energy from east to west. When the Kelvin wave reflects off the eastern boundary, it generates the westward traveling Rossby waves, with only about half the amplitude being carried by the first Rossby mode (Clarke 1983). The fewer the number of Rossby modes used, the "leakier" the eastern boundary becomes. The number of Rossby modes used in the model runs was picked in part to make sure that the growth rate of the ENSO mode converged. The other condition would be that the optimals have converged. Increasing the number of Rossby waves from 9 to 19 increased the growth of the 360-day optimal by about 20%, but increased the run time too much to be practical for all the parameter studies done here. However, a single high resolution (19 Rossby mode) 180-day optimal is presented in Fig. 3.19 which shows that the primary effect is to extend poleward the meridional extent of the warm water in the SE Pacific, relative to that in Fig. 3.12c.

The optimals produced by the model consistently had one numerical resolution problem. Examining the background field for the zonal surface currents, Fig. 2.3d, a strong eastward current can be seen, peaking in magnitude at 5N on the western boundary. This current acts on the *gradient* of the anomalous SST field in the thermal equation, (2.2.34), to produce change in the temperature field. In trying to maximize the gradient of SST right on the boundary, the optimals force a 2 delta-x wave which propagates across the whole basin. Doubling or tripling the number of gridpoints in x does not help: the grid noise remains. A simple 1-2-1 filter was applied to smooth the optimals. This removed the noise but also degraded their performance slightly. Figure 3.5 gives curves for the growth of both the filtered and unfiltered optimals. It shows that the degradation in performance is at most 15%. Throughout this study all pictures of the optimal or adjoint fields are filtered, but all the parameter studies use the unfiltered fields. This noise does not appear in the ENSO mode, only in the optimals.

This noise may be an indication of a real phenomenon, but if so, it is on a

smaller scale than this model can resolve. Furthermore, the equations are long wavelength approximations, and so do not model small scale processes. Therefore, small scale effects that appear are probably not physical. In fact, the background field that causes the problem is not valid on short spacial scales: it has current going into and out of the western boundary. The long wavelength boundary condition for the western boundary is that the integral of the zonal velocity over the boundary is zero (Cane and Sarachik 1976), and is met by this background. However, the more general boundary condition, that the zonal current be zero everywhere, is not met. For this reason it was felt that this phenomenon could be safely ignored.

3.6 Comparison with other Studies

In this section the results of four other recent papers will be compared with the results of this study. Two papers are devoted to finding the optimal initial conditions for the Battisti model (B88M) or the Zebiak-Cane model (ZCM). These two studies, Chen et. al. (1997, hereafter C97) and Xue et. al. (1996a, hereafter X96a), use different methods for calculating the optimals, and explore different aspects of the problem, but nevertheless produce optimals that can be directly compared to those here. The third study, Moore and Kleeman (1996, hereafter MK96), computes the optimals for another intermediate coupled equatorial Pacific model by Kleeman (1993). The fourth paper, Penland and Sardeshmukh (1995, hereafter PS95), find the optimals of a Markov model created from SST observations. The model used by PS95 is different enough from B88M that one should not expect the optimals to be the same, however, it is still interesting to compare some of the general characteristics of the optimals for the two different models.

3.6.1 Chen et al.

C97 takes B88M and calculates the linear tangent model using the method suggested by Lorenz (1965). The model is first run over a set period of time, τ, to establish a reference trajectory. The model is then run repeatedly, each time perturbing the initial field a small amount on a single element of the state vector. The change in the reference trajectory for each perturbation is recorded, and then the (linear tangent) resolvent, $\mathbf{R}(\tau)$, can be approximated. Due to computational restrictions, the resolvent was restricted to the SST, and therefore is similar to the $\mathbf{R}_{22}$ matrix used here. Since C97 ran the full model, dynamic consistency of the initial conditions is not required. However, in this study a perturbation to the SST field automatically causes the associated winds to exist, so the full model will take time to spin up the winds. Theoretically this spin up time is short. Questions about the effect of computing the T-optimal independently of the r-optimal, as is done in C97 was the impetus for much of this chapter. A major difference between the two studies is that C97 computed the resolvent with changing background states, whereas here a constant background state was used.

Despite these differences there is good agreement between the SST part of τ-optimals in this paper and the T-optimals from C97. Figure 2 from C97 shows the 180-day optimal starting at four different months. All four of these optimals have the east-west dipole pattern across the basin and the north-south dipole in the eastern Pacific, similar to Fig. 3.19. The warm anomaly in the southeast has a maximum about twice the size of the minimum of the broad cool anomaly in the western central Pacific, similar to Fig. 3.19. The main difference is the meridional extent of the warm anomaly. C97 shows it extending out to at least 11S, whereas in Fig. 3.19 it extends to about 18S. Because of computational limits, C97 did not look beyond about 11 degrees from the equator, so the optimals are consistent at least as far as they are shown. Some

meridionally extended runs where done by the authors of C97 which show that the warm water does extend farther south, but these were not included in their paper (Y.-Q. Chen, personal communications, 1996).

Table 3.3 - Comparison of Growth Rates of SST-optimals. Shown are growth rates from this study, from C97, and from X96a. Growth rates from LOAM are for a annually averaged background state, whereas the growth rates from X96 and C97 are growth rates for changing background states averaged over runs starting at each month of the year. N.A. stands for not available.

Time Period (days)	T-optimal Growth from LOAM	T-optimal Growth from C97's Fig. 1	T-optimal Growth from X96's Fig. 19
90	2.4	2.0	N.A.
180	4.7	4.0	6.5
270	5.8	5.5	N.A.

The growth rates from C97 can also be compared, at least approximately, against this model's growth rates. C97 computes the T-optimals with an annual averaged background for only a few τ, but the average growth rates can also be estimated from C97's Fig. 1. Table 3.3 gives these growth rate estimates, alongside the growth rates for same period T-optimals as computed by LOAM. The growth rates for the same τ agree to within 20%.

3.6.2 Xue et al.

X96a took a different approach to reducing the dimension of the problem while using a similar approach to C97 for linearization. X96a first created a reduced EOF space from a series of two year hindcasts using the ZCM. The tangent linear operator was then generated by perturbing the model with each of these EOFs. The optimal initial conditions were then taken as the first singular vector of these resolvents. Like C97, X96a created resolvents that reflected changing background states - but likewise found

that it did not make much difference in the shape of the optimal fields. Unlike C97, X96a's optimals are for the full set of fields.

Despite using a different model than this study (ZCM vs. B88M), and despite using a very different analysis technique, the optimals produced by X96a are similar to those found here. Figure 6 from X96a shows a composite average of the first singular vectors of twelve 6-month resolvents, each starting at a different month of the year. This is roughly the equivalent of the 180-day optimal with an annually averaged background, and so will be compared to Fig. 3.19. The SST field has a qualitatively similar structure, with a warm anomaly in the south-east Pacific, and a cold anomaly in the western-central Pacific. On the other hand, X96a's warm anomaly is more equatorially confined, extending down to only about 5S, as opposed to 18S here. Also, the cold anomaly is smaller and more intense: it has roughly the same magnitude as the warm anomaly and is confined to the area between the dateline and 130W, instead of extending all the way to the western boundary. X96a's thermocline is also similar to Fig. 3.19, with a valley along the equator from about 5N to 5S crossing the entire basin. Similar to Fig. 3.19, the valley narrows slightly at 120W and is broader at the eastern and western boundaries.

X96a also performs an experiment where an SST-only optimal is produced in an attempt to reproduce the fields from C97. The optimal produced (see X96a Fig. 19) more closely resembles both the T-optimals of C97 and the T-optimal calculated here. The warm anomaly extends further south to at least 11S. Also, the cold anomaly in the central Pacific extends almost to the western boundary. The average of the growth rates of X96a's 180 day T-optimals from X96a's Fig. 19 are shown in Table 3.3 for comparison against the 180 T-optimal growth as calculated by LOAM. X96a's growth rate is about 40% larger, but considering the growth rate's sensitivity to different background conditions, this should be considered good agreement.

3.6.3 Moore and Kleeman

The coupled model used by MK96 consists of a two level atmosphere coupled to a two layer baroclinic ocean through SST and surface winds. The model is similar to B88M or ZCM with the exception that: (i) there is no Ekman layer, and (ii) the equation governing SST evolution is simpler. The SST anomalies in MK96 are governed by,

$$\frac{\partial T}{\partial t} = \eta(x)h - \varepsilon T + \kappa \frac{\partial^2 T}{\partial x^2}, \tag{3.6.1}$$

where ε ,and κ are constants and $\eta(x)$varies zonally. MK96 finds the singular vectors by constructing a linear tangent model, and along with it the adjoint model. Then using the iterative techniques of Lanczos and Arnoldi, MK96 is able to compute the singular values and singular vectors without explicitly computing the resolvent or its adjoint.

MK96 computes 90-day optimals over each of the four seasons. Like in the other studies, it reports that while the growth rates are sensitive to the background conditions, the shape of the optimals are not. The 90-day optimal, for the period of April through June, is shown in MK96's Fig. 8. Both the thermocline and SST fields are given. The thermocline field of MK96 is broadly similar to those produced here. It consists of a narrow trough centered on the equator, running the length of the basin. Its width is from 5N to 5S over most of the basin, but then spreads to a range of 10N to 10S near the western boundary, where it also deepens by about 50%. Compare this description to the 90-day optimal of Fig. 3.12a from this chapter. The most apparent difference between the two thermocline fields is that the MK96 field is nearly symmetric, whereas the optimal here has a significant antisymmetric component. The reason that MK96's thermocline lacks the antisymmetric component is clear from Section 3.3.2. In LOAM, about half the heating comes from suppression of the thermocline in the off-equatorial upwelling zone, but the MK96 model uses a thermocline heating coefficient, η, that is meridionally constant. According to Section 3.3.2, the other half of the heating comes from downwelling and the surface currents

acting on mean temperature gradients. However, the MK96 thermal equation (3.6.1) does not include any advection terms, and so ignores these avenues of growth.

The SST portion of MK96's 90-day optimal (MK96's Fig. 8d) looks nothing like the optimal SSTs produced here. MK96's SST field is symmetric about the equator, has a high frequency component in the zonal direction (noise perhaps), and has its extremum centered on the equator. MK96 tries several ways to filter out the high frequency component (see MK96's Fig. 13), but at best arrives at a SST that consists of a warm anomaly in the Eastern equatorial Pacific. Because of the simple thermal equation used by MK96, even without the noise problems, it would not be possible to arrive at the SST optimal fields calculated here. The antisymmetric portion of the T-optimals produced here is due to advection and downwelling, neither of which are included in (3.6.1). While MK96's SST field does have a warm anomaly in the east (in order to produce westerly winds), their warm anomaly is not divided into two parts like Fig. 3.14a. The warm anomaly avoids the equatorial region in this model to avoid the excessive cooling which would occur in the upwelling zone near the equator. The cooling coefficient, d(x,y), in LOAM has structure (Fig. 2.3c), whereas in the MK96 model it is uniform.

3.6.4 Penland and Sardeshmukh

PS95 advances the hypothesis that the ENSO cycle is not a linearly unstable system that is constrained in size by nonlinearities, as implied by B88M and ZCM. Instead, PS95 suggests that the Pacific basin is linearly stable, and that the warm and cold events are transients that grow when an optimal structure is randomly created by noise. To demonstrate that this is possible, PS95 takes 40 years of SST observations for the tropical Indo-Pacific basin and builds a linear Markov model. Because of the nature of this empirical modelling, all the eigenmodes of the linear Markov model are damped. PS95 then finds the singular vectors of the model for various time periods, τ.

The PS95 model is obviously quite different from LOAM. Even if B88M were an exact model of the real Pacific SST, the PS model would not necessarily produce the same optimals as LOAM due to its inclusion of the Indian Ocean. However, since PS95's model is the first order autoregression of the 7 month transition, its 7 month optimals are its models equivalent of LOAM's 7 month T-optimals.

Like this study, PS95 found that the shape of the τ–optimal was not overly sensitive to τ, at least in the range of 3 months to 15 months. For comparison note the similarity between the T-fields of the 90-day and 360-day optimals in Fig. 3.12 of this study. PS95 found the maximum growth occurred for the 7 month optimal (i.e . τ_{max} =7 months). Figure 6a of PS95 shows its 7 month optimal. Like optimals found here it has a large warm anomaly in the SE Pacific forming a N-S dipole across the equator in the east. It also displays the E-W dipole along the equator which produces the westerly wind in the eastern Pacific. However, PS95's optimal also has features not found in any of the studies discussed here. On the equator in the western Pacific is a second large warm anomaly, and further west, the Indian Ocean is cold. Also, a band of warm water extends from the warm anomaly in the western Pacific to Baja California. Figure 6b of PS95 shows the state of the SST after 7 months of growth starting from the optimal. This figure shows the SST at its peak, and consists of a large warm anomaly in the eastern equatorial Pacific, similar to an ENSO warm event. PS95's Fig. 6b also shows that the Indian Ocean has changed from cold to warm during the 7 months.

The results of the neutral and damped background experiments explained in Section 6 are not inconsistent with the PS95 hypothesis that ENSO warm and cold events could be the product of transient growth in a stable system. PS95 finds an optimal that grows an ENSO-like warm event in 7 months in a damped system, and here optimals are found that grow ENSO-like warm events in 6 and 8 months for a damped and neutral system, respectively. The growth here is somewhat less: the PS95 optimal achieves a 5-fold increase in the L_2 norm (of SST), whereas the T-optimals for the

damped and neutral cases here achieve 2-fold and 3-fold increases in the L_2 norm of the T-fields, respectively. However, the nominal case of this study would also support an alternate hypothesis: that the Pacific has a linearly unstable periodic mode limited in size by nonlinearities. In this hypothesis the optimals, induced randomly by noise, would either cancel or intensify the otherwise regular warm and cold events.

3.7 Summary of Annually Averaged Case

The properties of the optimal growth structure for a linearized version of the Battisti coupled model of the equatorial Pacific with a constant background state were explored in this chapter. It was found that the first singular vector of the linear propagator (the τ-optimal) grows significantly faster than the most unstable eigenmode (the ENSO mode) of the system. It was shown that the τ-optimals grow rapidly into the ENSO mode (around 90 days). For τ less than 500 days a local maximum, τ_{max}, was found that outperformed the τ-optimals around it, and has the characteristic that the ENSO mode it produced peaked at time τ. This τ_{max} is 360 days for the annually averaged background case, 240 days for a 5 month average (neutral ENSO) case, and 180 days for a 3 month average over the dynamically stable months of February through April (damped ENSO). While the growth rates of the optimal fields for these different background fields are very different, the shape of the optimal fields are quite similar.

Experiments were run to compare the shape of the optimals produced by looking at (i) the propagator of the r-fields alone, or r-optimals, (ii) the propagator of T-fields alone, or T-optimals, and (iii) the propagator of both fields, or the full-optimal. It was demonstrated that when optimizing for a sufficiently long period, the sub-optimals take on the same shape as their respective parts of the full-optimal. The value of this "sufficiently long period" changes depending on the background fields. The nominal case achieved 85% correlation between both of the sub-optimals and the full-optimal by

τ=60 days, whereas it took 90 days and 120 days for the neutral and damped cases, respectively. It was shown that for a given τ, initializing the linear model with either one of the sub-optimals by itself produced an ENSO mode of the same phase as the full-optimal. For the nominal case, it was shown that the T-optimal pattern with an amplitude of 0.1 degrees is about as efficient for generating a mature ENSO as the r-optimal pattern with a 1.2 meter amplitude.

Finally, the optimal initial conditions calculated here were compared with optimals from the work of Xue et al. (1996), Chen et al. (1997), and Penland and Sardeshmukh (1995). PS95 used a very different model, computing a Markov model from SST observations, but its optimals are at least qualitatively similar to those calculated here. C97 used the same model as this study, but linearized in a different manner and then considered only the SST. Nevertheless, the T-optimals produced here are almost the same as the SST-optimals of C97. X96a used the ZCM, a very similar model to B88M. Even though they employed a very different technique to compute the linear tangent propagator, their optimals and their growth rates, are in good agreement with those produced here.

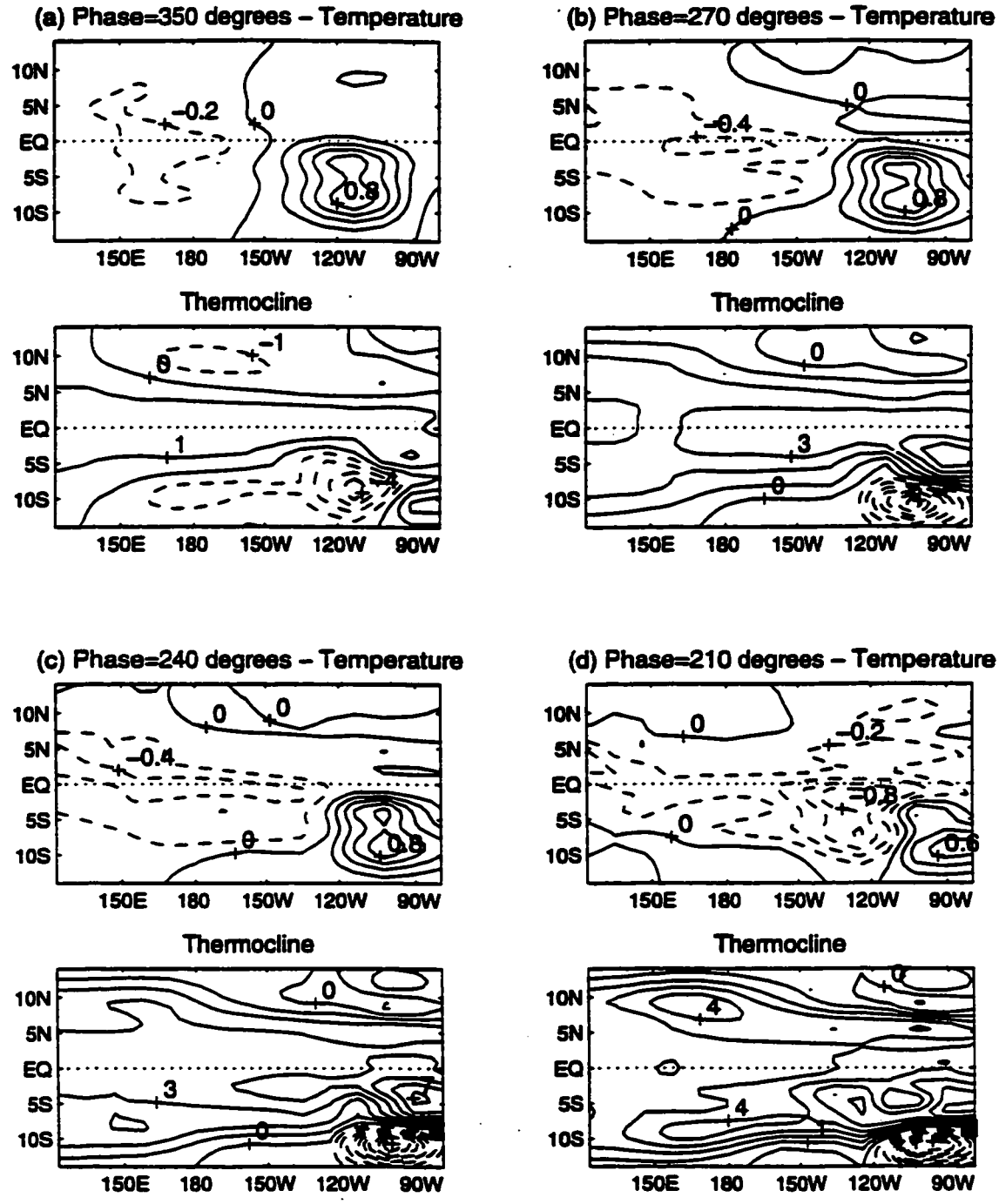

Figure 3.1 - SSTA and Thermocline Field of Adjoint at Various Phases. Temperature and thermocline depth fields for the adjoint of the ENSO mode at four different phases. All graphs have contours of 0.2 C for the temperature and 1 meter for the thermocline. The patterns in the range of 180 to 0 degrees, are the same as those in the range of 360 to 180, except the signs of the fields are reversed.

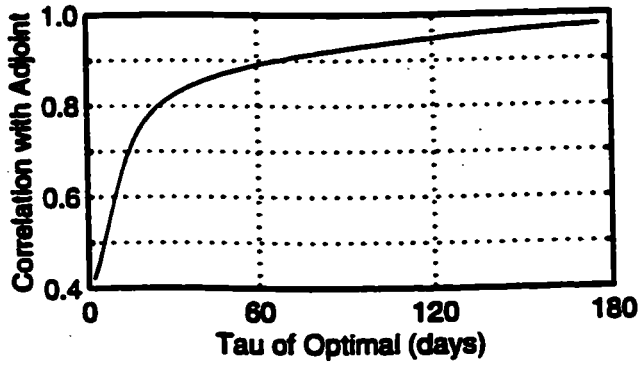

Figure 3.2 - Correlation Between tau-Optimals and Adjoint. Correlation coefficient between the τ-optimal, for a given τ, and the adjoint. The correlation shown is the maximum between the τ-optimal and all phases of the adjoint.

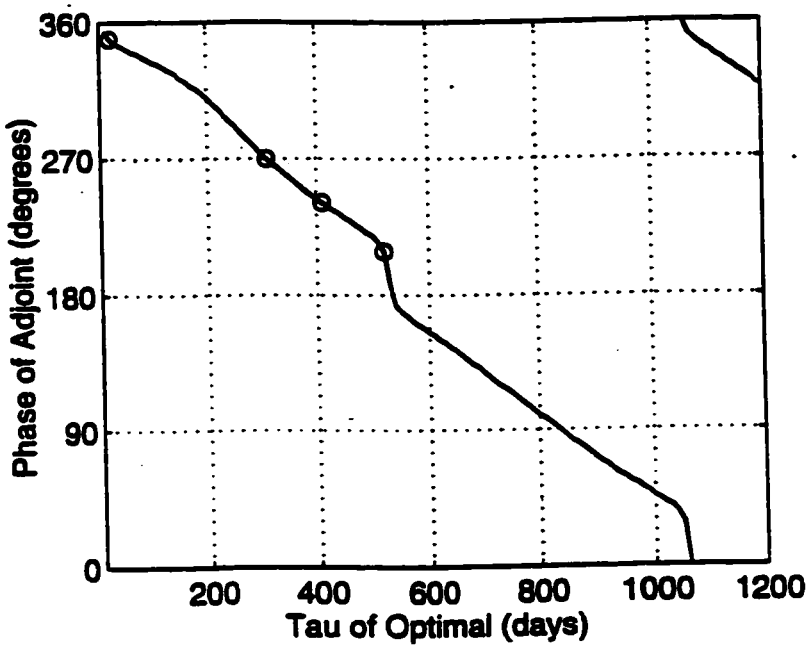

Figure 3.3 - Phase Relationship Between tau-Optimals and Adjoint. The phase of the adjoint which has the highest correlation with the τ-optimal, at a given τ. Correlations are greater than 0.95 for all periods larger than 180 days. Correlation coefficients for shorter periods are shown in Fig. 3.2. Since the τ-optimal does not distinguish between warm and cold events (in terms of their size) the phase of the adjoint with max correlation is arbitrary by 180 degrees. The circles which appear on the plot correspond to the phases of the adjoint which are pictured in Fig. 3.1.

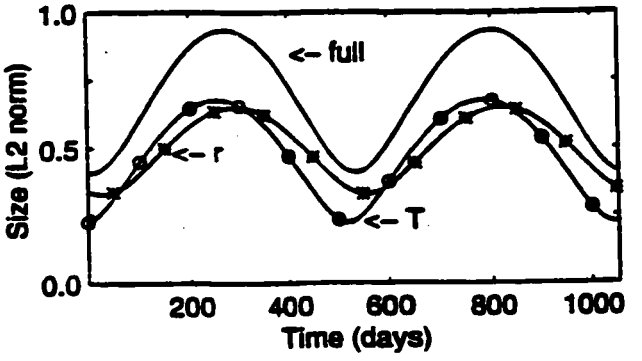

Figure 3.4 - Size of L2 Norm over ENSO Cycle. Size of the L_2 norm over one cycle of the ENSO mode, where the exponential growth of the mode has been suppressed. The solid line is sum of both the SST and ocean dynamics, i.e. the full norm. The line with circles shows the T-field portion the L_2 norm, and the line with stars shows the r-field portion

Key	
Solid line	All fields
Stars	T-field
Asterisks	r-field

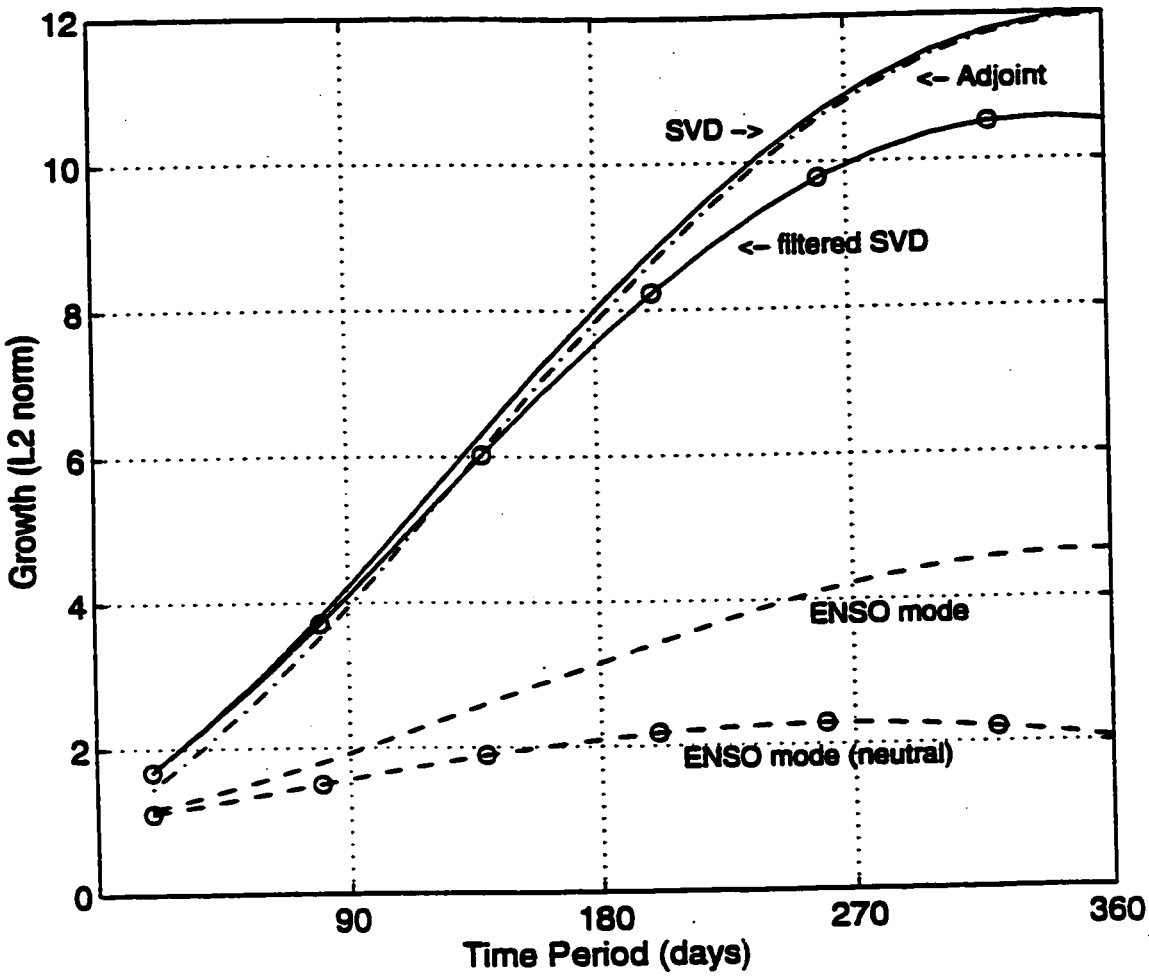

Figure 3.5 - Growth of Various Optimizing Schemes. Growth achieved over a fixed time period for various optimization schemes. The different schemes are described in text.

Key	
Solid line	SVD
Dot-dash line	Adjoint
Circles and line	filtered SVD
Dashed line	ENSO mode
Circles and Dashes	neutral ENSO

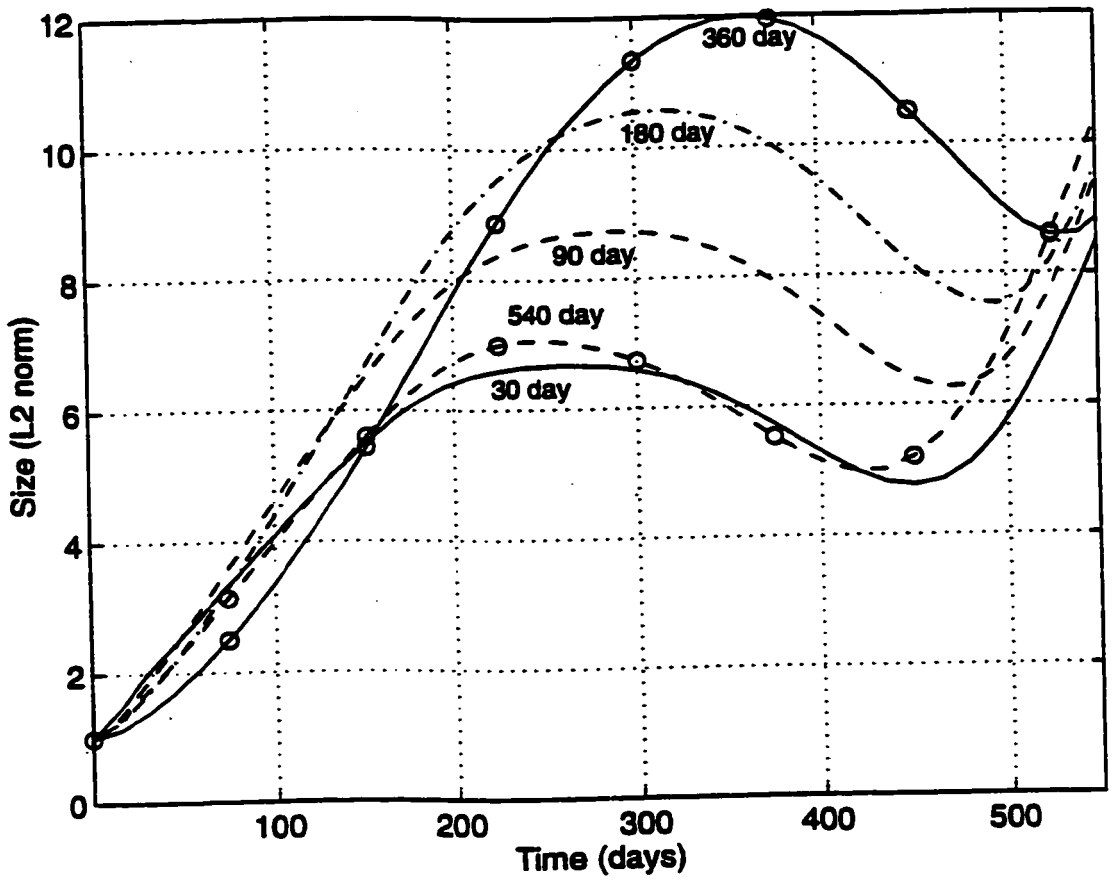

Figure 3.6 - Growth over Time of Various tau-Optimizing. This chart shows the growth of the L_2 norm starting with various different τ-optimals.

Key	
Solid line	30-day optimal
Dashed line	90-day optimal
Dot-Dash line	180-day optimal
Circles and line	360-day optimal
Circles and Dashes	540-day optimal

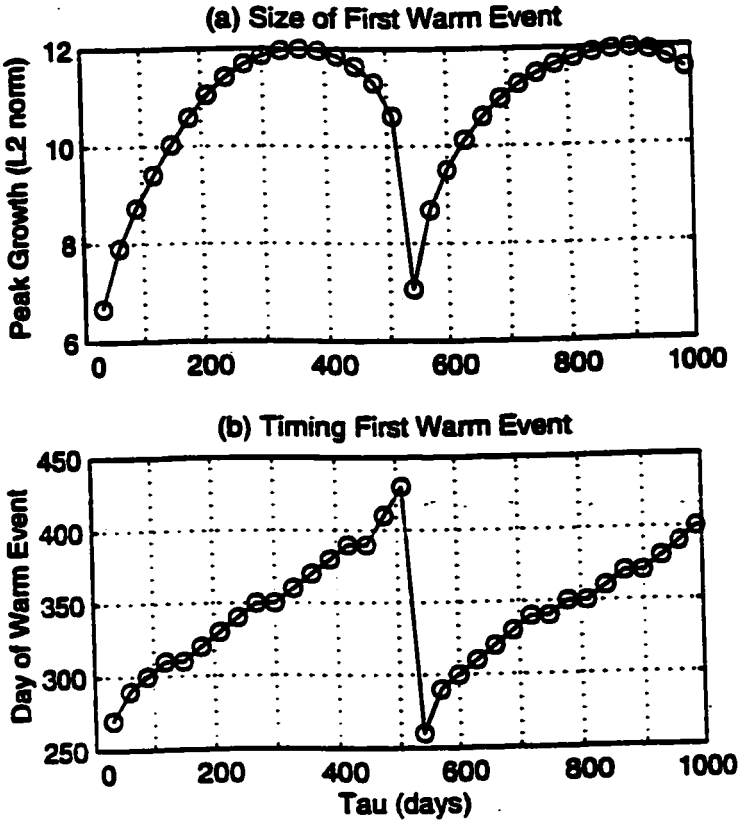

Figure 3.7 - Size and Timing of First Warm Event. (a) shows the size of the first maximum produced by a range of τ-optimals. The first maximum of the L_2 norm corresponds to an ENSO peak warm event. (b) shows the time of first maximum produced by the same range of τ-optimals. Notice that only for τ=360 days, does the ENSO produced actually peak at time τ. (Note: in (b) it appears as if some pairs of subsequent events peaks at the same time- this is not necessarily the case. They just both peak within the 10 day resolution of the model run.)

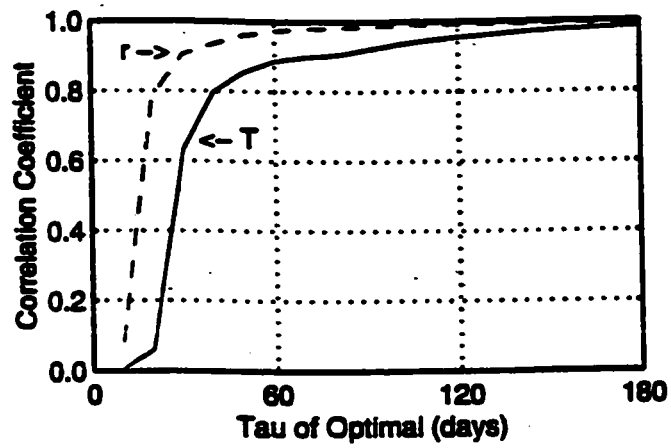

Figure 3.8 - Correlation between Sub-optimals and Full-optimal. Correlation coefficient between the T-optimal and the full-optimal, along with the correlation between the r-optimal and the full-optimal over a range of τ.

Key	
Solid line	T-optimal
Dashed line	r-optimal

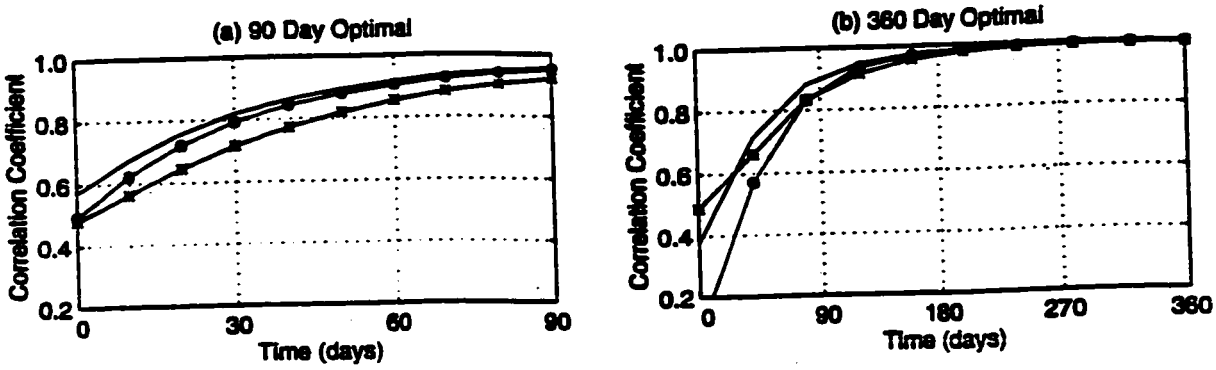

Figure 3.9 - Correlation between Evolving tau-optimal and ENSO mode. Graph (a) shows the correlation coefficient between the different types of 90-day optimals and the ENSO mode. Graph (b) shows the same but for the the 360-day optimals.

Key	
Solid line	full-optimal
Circles and line	T-optimal
Asterisks and line	r-optimal

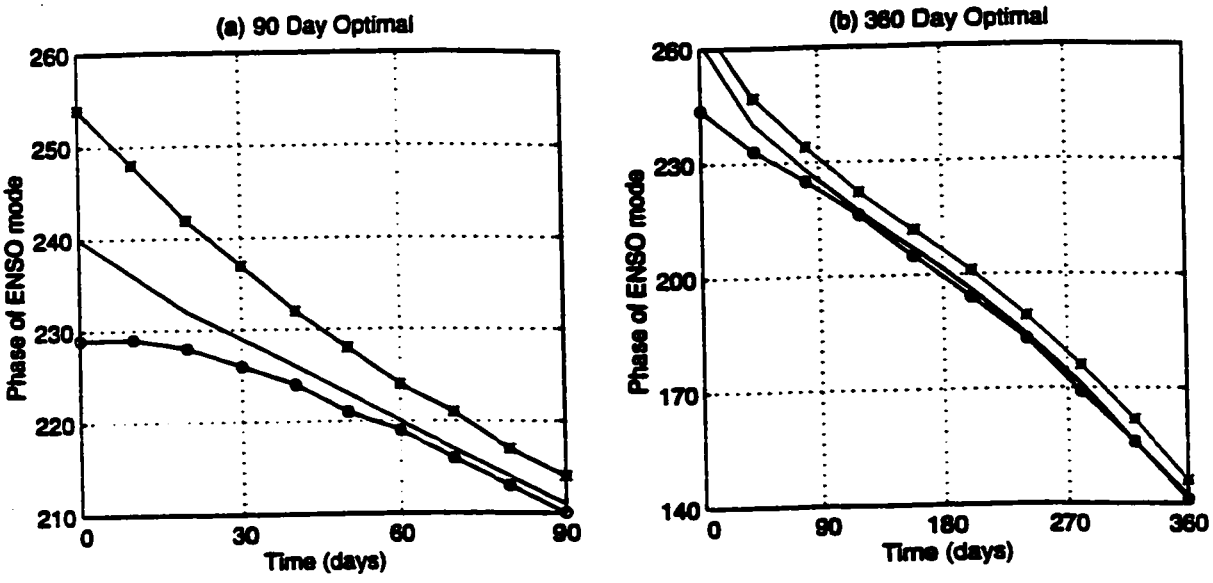

Figure 3.10 - Phase of ENSO with Highest Correlation to Optimals. The evolving optimal initial condition is compared to all phases of the ENSO mode and the one with the highest correlation is given. This is a companion figure to Fig. 3.9. which gives the values of the correlation. Graph (a) shows the 90-day optimals, while (b) shows the 360-day optimals.

Key	
Solid line	full-optimal
Circles and line	T-optimal
Asterisks and line	r-optimal

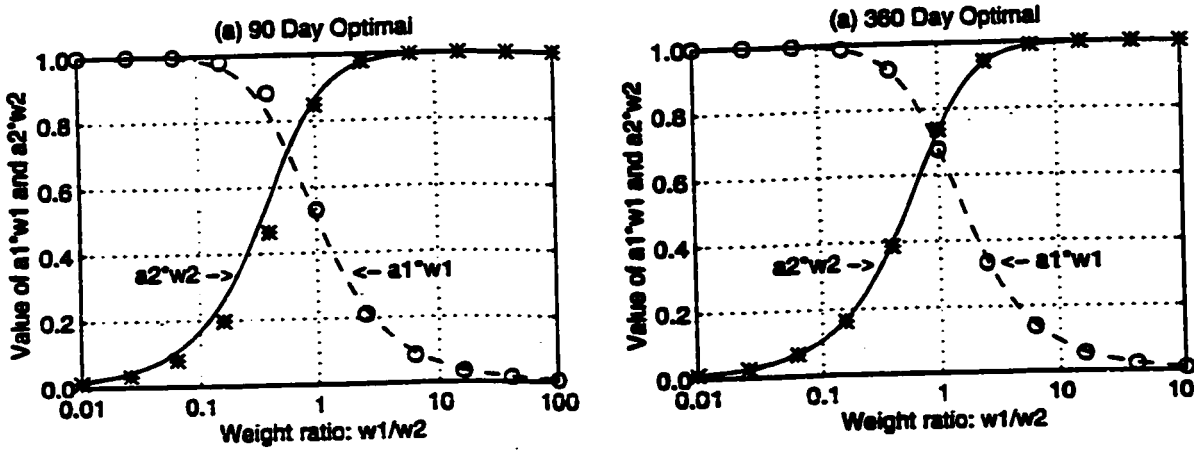

Figure 3.11 - Relative Weighting of Sub-optimals. Plots of the value of $a_1 \cdot w_1$ and $a_2 \cdot w_2$ against w_1 / w_2. In other words the amplitude of the r-optimal and T-optimal versus their relative weighting in the L_{2w} norm. The dashed line and solid lines give the values as predicted by Equ. (3.2.8). The circles and asterisks give the actual values as calculated by LOAM. The (a) graph is for the 90-day optimal and the (b) graph for the 360-day optimal

Key	
Solid line	$a_2 \cdot w_2$ (Equ. 3.2.8)
Asterisks	$a_2 \cdot w_2$ (LOAM)
Dashed line	$a_1 \cdot w_1$ (Equ. 3.2.8)
Circles	$a_1 \cdot w_1$ (LOAM)

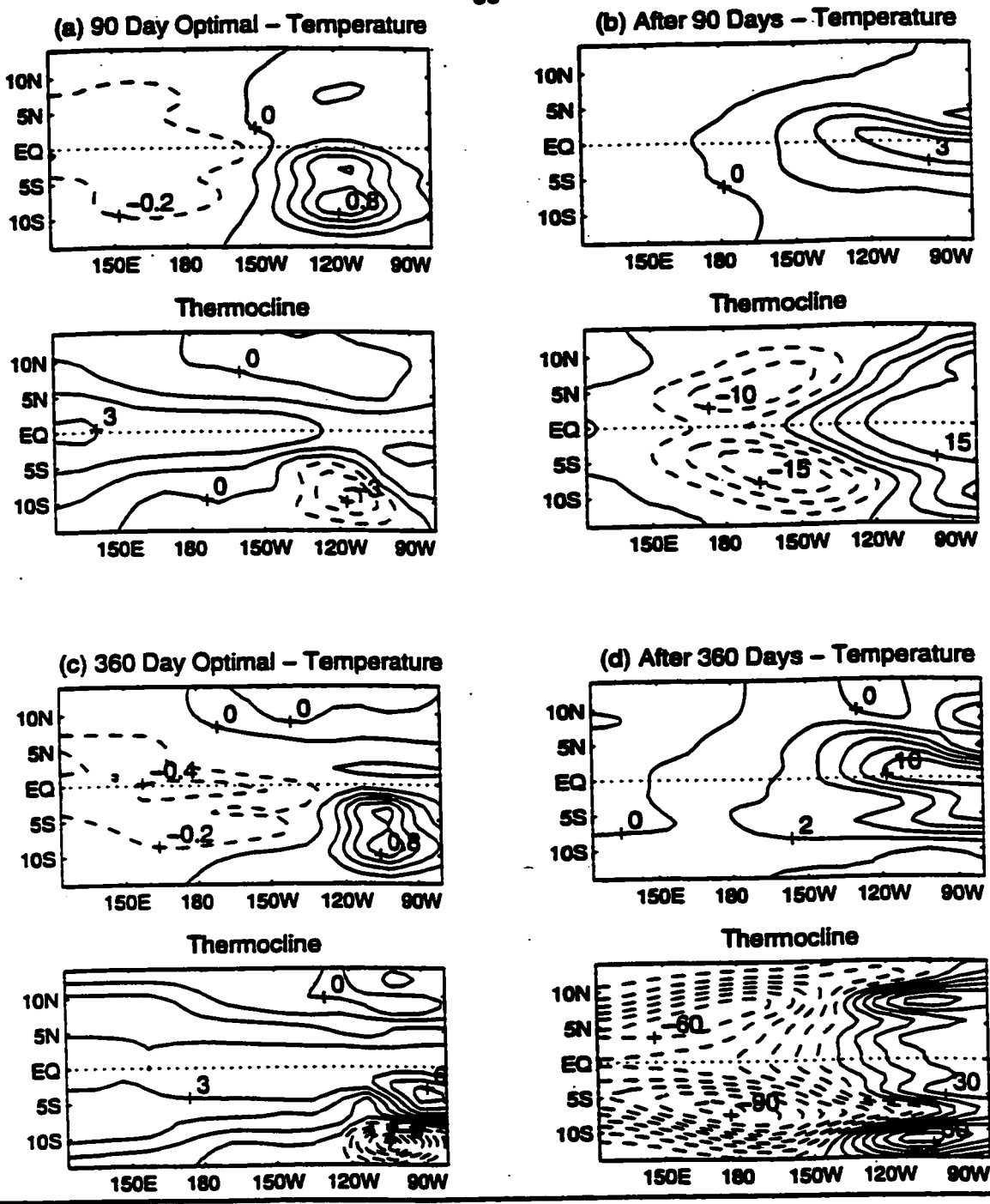

Figure 3.12 - SSTA and Thermocline of Optimals. Contour plots of the SST and thermocline fields for 90 day and 360-day optimals, both initially and after τ days. Graph (a) is the 90-day optimal and has increments of 0.2 C and 1 meter for SST and thermocline respectively. Graph (b) is the 90-day optimal after 90 days growth with increments of 1 C and 5 meters. Graph (c) is the 360-day optimal with increments of 0.2 C and 1 meter. Graph (d) is the 360-day optimal after 360-days of growth with increments of 2 C and 10 meters.

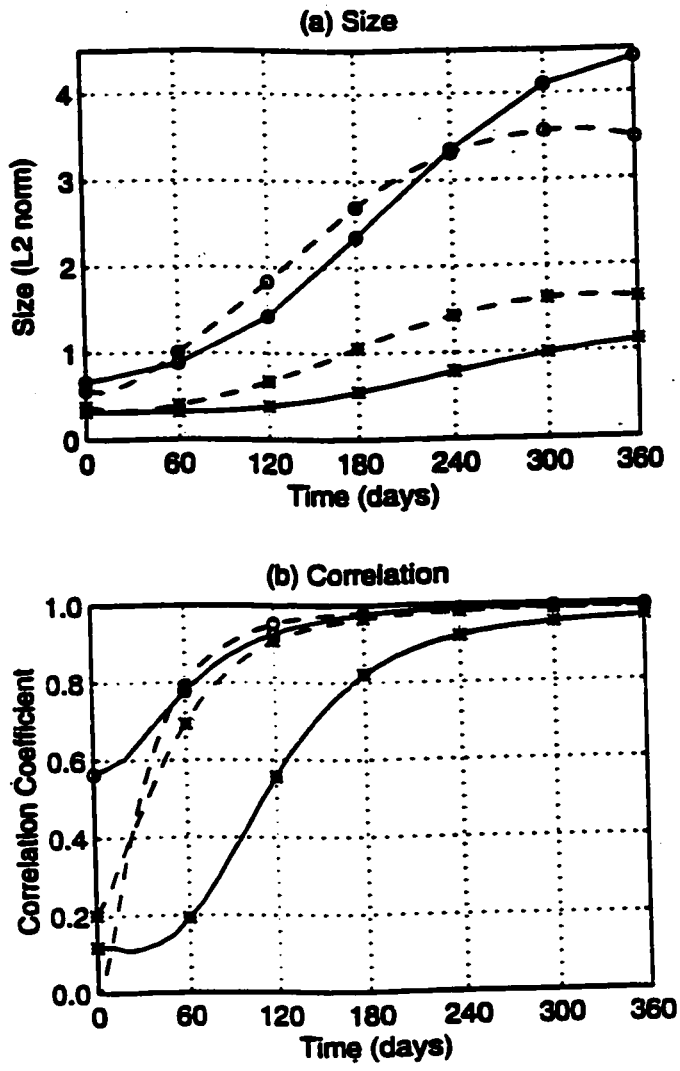

Figure 3.13 - Relative Growth of Subfields. Growth and correlation with the full optimal of various subfields of the 360-day optimal. Graph (a) shows the growth over 360 days of the symmetric and antisymmetric T-fields, and the symmetric, and antisymmetric r-fields. Graph (b) shows the correlation over time of each of the subfields with the full-optimal.

Key	
Dashed w/Circles	Sym T-field
Dashed w/Stars	Antisym. T-field
Solid w/Circles	Sym. r-field
Solid w/Stars	Antisym. r-field

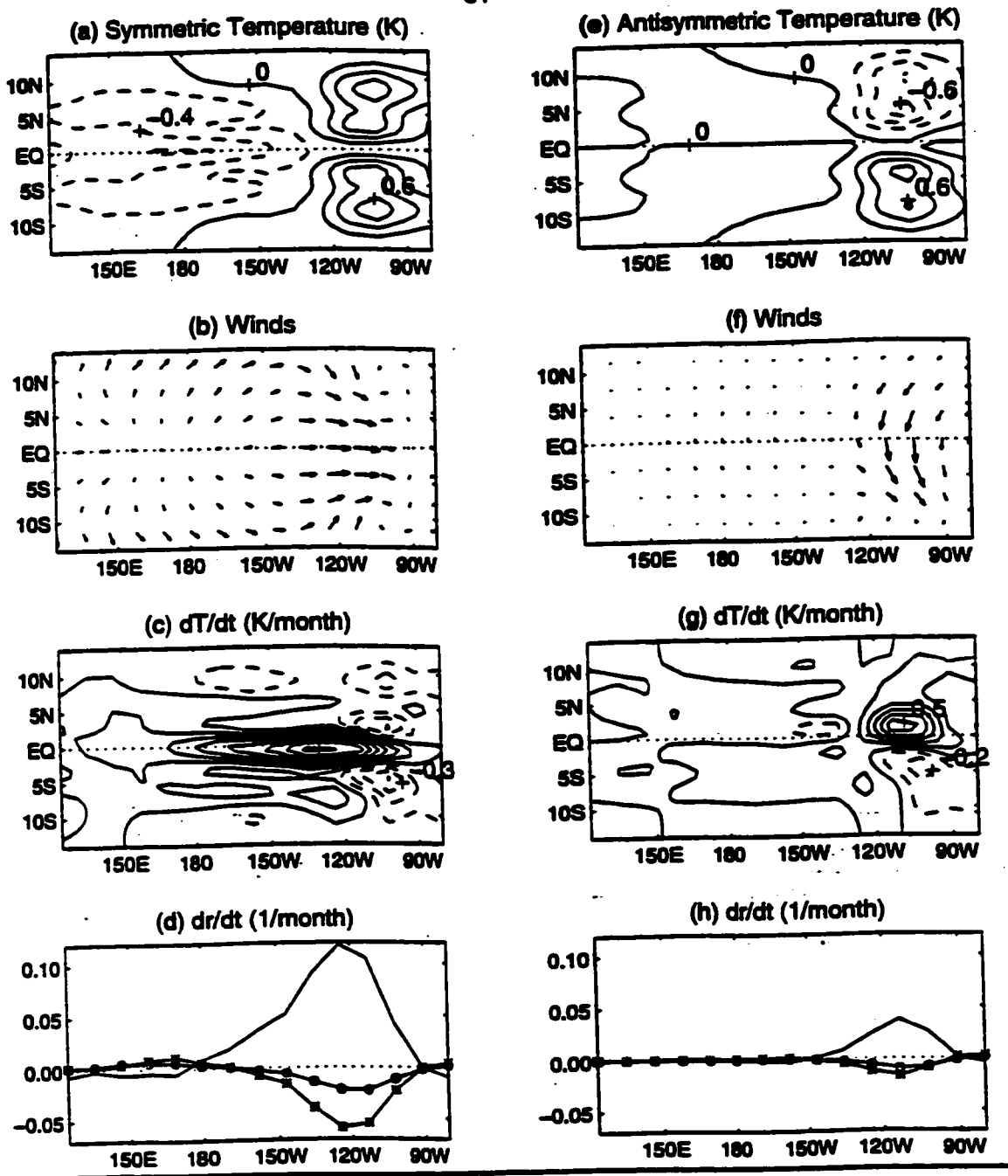

Figure 3.14 - Initial Fields and Selected Derivatives for the Symmetric and Antisymmetric T-fields of the 360-day Optimal. Graphs (a)-(d) are for the symmetric case and (e)-(g) are for the antisymmetric case. Graphs (a) and (e) are the SST fields with a 0.2 C increment.Graphs (b) and (f) are the wind fields. The maximum wind speed in graph (b) is 0.27 m/s and the maximum wind speed in (f) is 0.19 m/s. Graphs (c) and (g) show the derivative of the SST field with an increment of 0.2 C/month. Graphs (d) and (h) show the derivatives of the Kelvin wave (solid line) and first two symmetric Rossby wave (stars and circles) in units of 1/months.

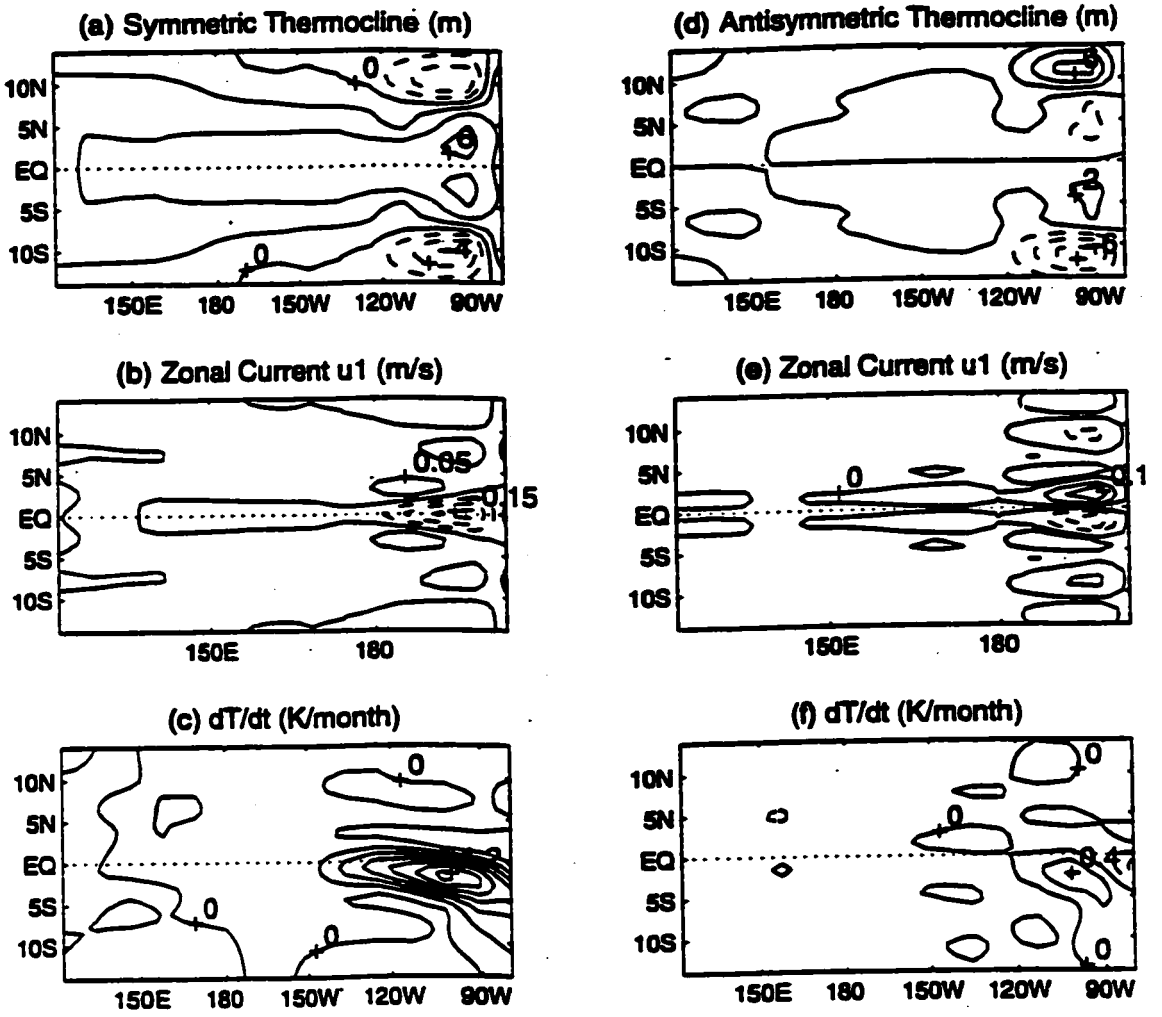

Figure 3.15 - Initial Fields and SST Derivative for the Symmetric and Antisymmetric r-fields of the 360-day Optimal. Graphs (a) -(c) are for the symmetric case and (d)-(f) for the antisymmetric case. Graphs (a) and (d) show the thermocline depth with a 5 meter increment. Graphs (b) and (e) show the zonal surface currents with a 0.1 m/s increment. Graphs (c) and (d) show the derivative of the SST field with an increment of 0.5 C/month.

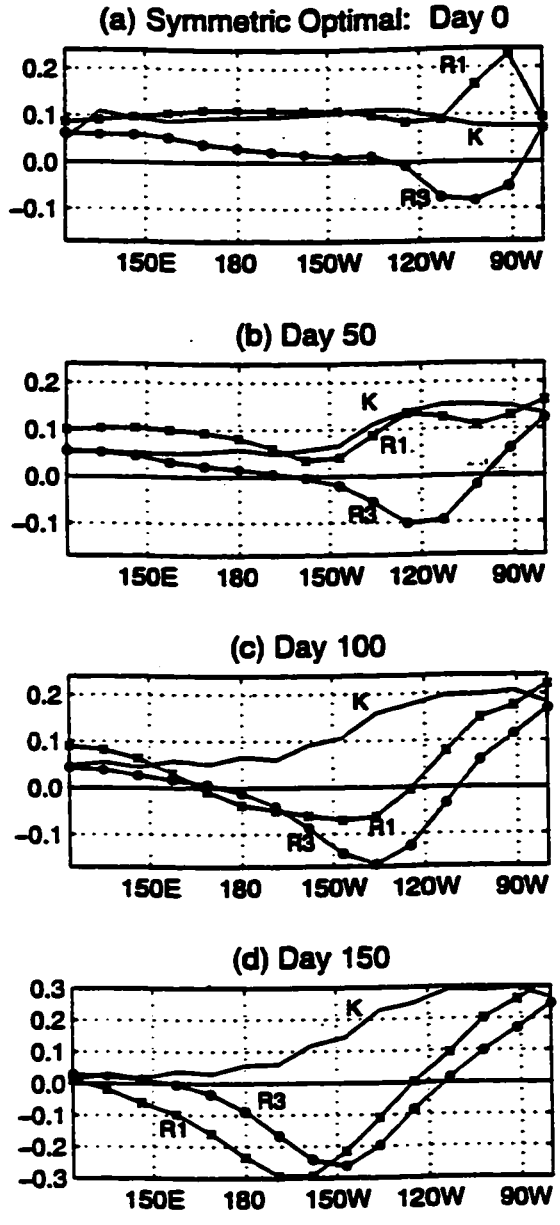

Figure 3.16 - Evolution of Primary Ocean Waves. Evolution of the Kelvin and first two symmetric Rossby waves starting with the symmetric r-fields of the 360-day optimal. Graphs (a)-(d) are the values of the Rossby coefficients at day 0, day 50, day 100 and day 150, respectively. The amplitude is the value of the non-dimensional coefficient of the waves.

Key	
Line w/Stars	1st Rossby wave
Line w/Circle	3rd Rossby wave
Solid line	Kelvin wave

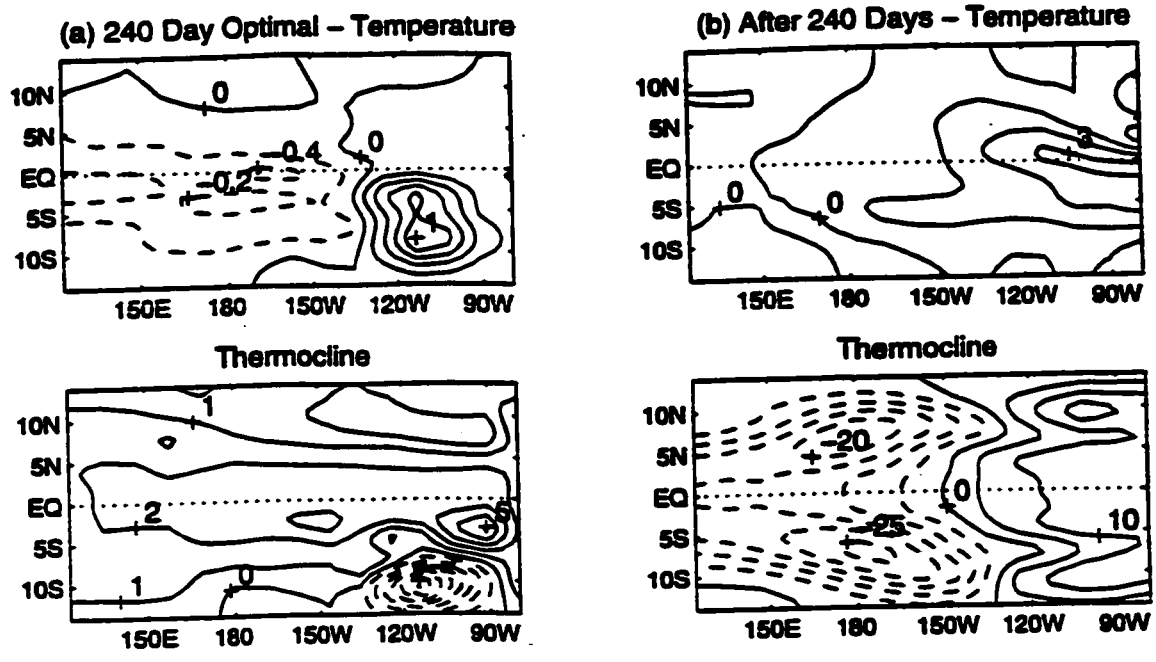

Figure 3.17 - Initial and Final Fields for Neutral Case Optimal. Contour plot of the 240-day optimal for the neutral case background fields. Graphs (a) show the SST and thermocline initially, with increments of 0.2 K and 1 meter, respectively. Graphs (b) show the SST and thermocline after 240 days, with increments of 1 K and 5 meters.

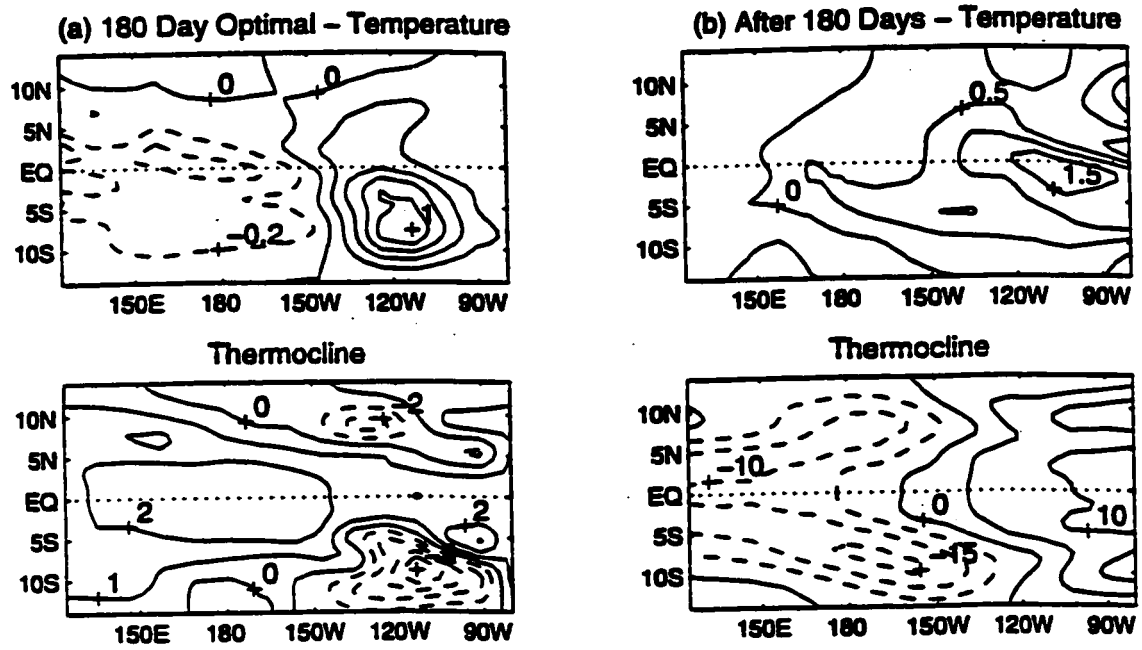

Figure 3.18 - Initial and Final Fields for Damped Case Optimal. Contour plot of the 180-day optimal for the damped case background fields. Graphs (a) show the SST and thermocline initially, with increments of 0.2 K and 1 meter, respectively. Graphs (b) show the SST and thermocline after 180 days, with increments of 0.5 K and 5 meters.

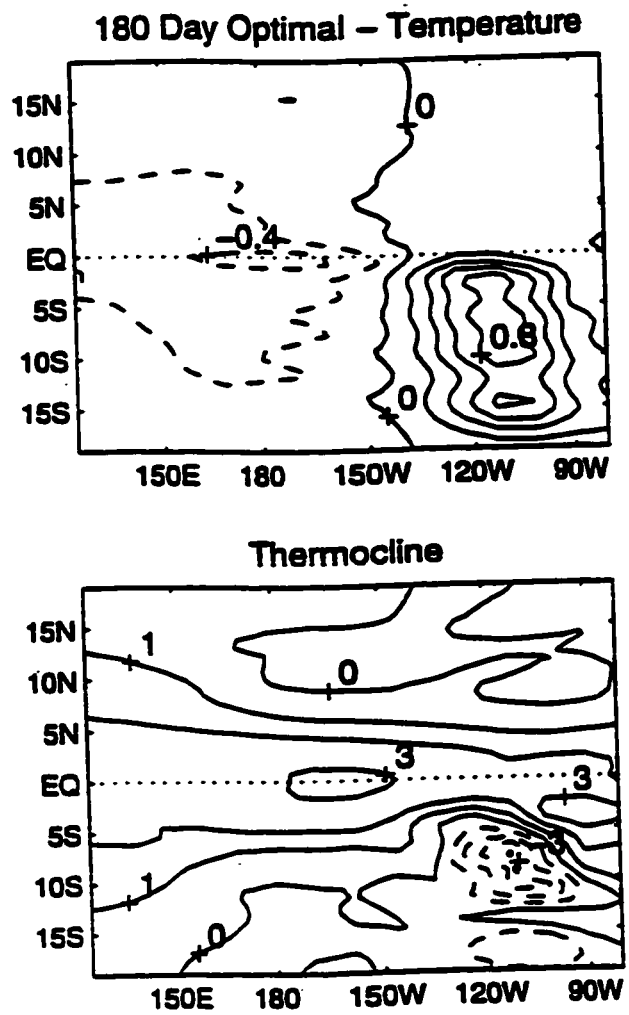

Figure 3.19 - Initial Fields for High Resolution Nominal Case Optimal. Contour plot of the 180-day optimal for the annually averaged background. This graph was done at about twice the resolution of the other optimals appearing in this paper. Notice that the graph runs from 19N to 19S. The SST and thermocline contours are in increments of 0.2K and 1 meter, respectively.

Chapter 4: Annual Cycle Case

4.1 LOAM with Changing Backgrounds

In Chapters 2 and 3 the singular vectors, eigenvectors, and adjoints of LOAM were found assuming a constant background. Specifically, the annual cycle was approximated by its average value. This proved to be an adequate simplification to find the general shape and mechanism of the optimal patterns, but it obviously tells nothing about the seasonal dependence of the optimals. In this and subsequent chapters, LOAM is generalized to include an annual cycle in the background states.

The basic matrix equation controlling the dynamics, (2.1.2) then becomes

$$\frac{d}{dt}\underline{\varphi} = \mathbf{M}(t)\underline{\varphi}, \text{ where } \underline{\varphi}(t) = \begin{bmatrix} \underline{r}(t) \\ \underline{T}(t) \end{bmatrix}. \tag{4.1.1}$$

Unlike the case where the linear matrix operator, $\mathbf{M}$, is invariant in time, this equation cannot in general be solved with a simple matrix exponential, but must be integrated in time. Also, unlike the constant background case, this system does not have the simple eigenvalue decomposition. However, an analysis similar to Chapters 2 and 3 can still be carried out with the use of Floquet theory which is a generalization of eigenvalue analysis for a system with either periodic forcing or a periodic matrix operator (Iooss and Joseph 1980).

To solve (4.1.1), the problem will be discretized in time by holding the matrix operator constant over each month and finding the linear propagator for each month. These propagator matrices are then multiplied in order to get the propagator matrix between any two times. In other words,

$$\mathbf{R}_1 = \exp(\mathbf{M}_1 t_m),\ \mathbf{R}_2 = \exp(\mathbf{M}_2 t_m),\ \ldots.\ \mathbf{R}_{12} = \exp(\mathbf{M}_{12} t_m) \tag{4.1.2}$$

where $\mathbf{M}_1$ is the matrix operator with the January climatological background, $\mathbf{M}_2$ has the February background, etc., and where t_m is one month. (In this model all months are

365.25/12 days long). The linear propagator for one year from January through December is therefore:

$$\mathbf{R}_{year} = \mathbf{R}_{12} \cdot \mathbf{R}_{11} \cdot \ldots \cdot \mathbf{R}_{1}. \tag{4.1.3}$$

The eigenvalues of this matrix $\mathbf{R}_{year}$ are called the Floquet multipliers of $\mathbf{M}(t)$ and indicate the frequency and growth rate of the eigenvectors of $\mathbf{R}_{year}$, which are the modes of the system (4.1.1). Recall the definition of eigenvalues

$$\mathbf{R}_{year} \cdot \underline{e}_j = \lambda_j \underline{e}_j, \tag{4.1.4}$$

where $\underline{e}_j$ is the jth eigenvector and λ_j the jth eigenvalue of $\mathbf{R}_{year}$. From (4.1.4) it can be seen that

$$\left\{ \begin{array}{l} \text{if } \|\lambda_j\| > 1 \text{ then } \underline{e}_j \text{ is unstable} \\ \text{if } \|\lambda_j\| = 1 \text{ then } \underline{e}_j \text{ is neutral} \\ \text{if } \|\lambda_j\| < 1 \text{ then } \underline{e}_j \text{ is stable} \end{array} \right\}. \tag{4.1.5}$$

Keeping in mind that both λ_j and $\underline{e}_j$ are complex quantities, the frequency of the mode is determined by $\mathrm{mod}(\lambda_j)$, which is the angle through which $\underline{e}_j$ rotates in one year.

Since this eigenvector is determined by the one year propagator - it only indicates what the fields look like at one year intervals. From just an eigenvalue analysis of $\mathbf{R}_{year}$, nothing can be said about the states that the fields go through in getting from $\underline{e}_j$ to $\lambda_j \underline{e}_j$. In fact, a yearly propagator going from July to June,

$$\mathbf{R}'_{year} = \mathbf{R}_{6} \cdot \mathbf{R}_{5} \cdot \ldots \cdot \mathbf{R}_{1} \cdot \mathbf{R}_{12} \cdot \ldots \cdot \mathbf{R}_{8} \cdot \mathbf{R}_{7}, \tag{4.1.6}$$

will have (in general) eigen*vectors* that are different than those of the January to December propagator. However, the eigenvalues are the same for both systems - it certainly would not be reasonable for the ENSO mode to grow at a different exponential rate when going from July to July than when going from January to January.

To illustrate examine Fig. 4.1, which shows the Nino3 index for a pure ENSO mode propagating freely and where the exponential growth has been suppressed. In Fig. 4.1, Nino3 has been calculated in three different ways, all starting from the same initial state. The solid line indicates Nino3 as calculated by multiplying the current state by

the appropriate monthly linear propagators. The circles show the Nino3 index at yearly intervals where the state is found by multiplying the previous year's state by the eigenvalue (and taking the real part of the resulting complex fields). The dashed lines show Nino3 calculated as if the intermediate fields could be found simply by rotating the ENSO eigenvector continuously at the frequency of the eigenvalue. The later is *not* the correct way to calculate the fields for this system. It would be the correct way if the background fields were time invariant and so is only shown for reference.

As can be seen from the solid line in Fig. 4.1, the ENSO mode is more complicated with an annual cycle than the simple periodic ENSO mode from Chapters 2 and 3. The Nino3 signal contains several frequencies and the states through which it passes cannot be fully described by a single complex eigenvector. However, it does have a dominant frequency which is determined by (any one of) the yearly propagators. The period of this dominant frequency will be considered to be the period of the ENSO mode.

Similar to the annually averaged case, LOAM now produces a single unstable mode which looks like ENSO. This ENSO mode has a period of 2.7389 years and grows at a rate of 1.8188 times per year. Figure 4.2 shows the SSTA and thermocline fields of the most unstable eigenvector for the January to December linear propagator of (4.1.3). Figure 4.3 shows the same information but for the July to June propagator of (4.1.6). The two figures show both the real and imaginary parts of the eigenvectors. In both figures the eigenvector has been rotated so that the real part shows the ENSO at the peak of a warm event. As stated before, the shape of the ENSO mode changes for the different yearly propagators, but as can be seen from Figs. 4.2. and 4.3, the eigenmodes are still recognizably versions of ENSO.

4.2 Optimals with a Cyclic Background

The singular values now take on a dimension that they did not have with the

constant background case. Not only is the time period of the optimization a factor but so is the starting month. Figure 4.4a shows a contour map of all the first singular values for the τ-optimals with τ between 3 and 15 months, starting at each month of the year (for the B88M). This kind of graph will be called an SV map. From this figure it can be seen that, like the annually averaged case, there exists a local maximum in the transient growth. This maximum occurs at around the 9 month optimal starting at the beginning of May. Hereafter the notation (m, τ)-optimal will be used, where "m" is the starting month and τ the time period. Note that the maximum value of the SV is about 12, the same as the maximum SV for the annually averaged case.

As before the optimal patterns suffer from the same grid noise explained in some depth in section 3.5. Figure 4.4b is the same as Fig. 4.4a, except that the SV's are replaced by the growth achieved over time τ by the τ-optimal which has been modified by a 1-2-1 meridional filter. As can be seen from this second figure, the filter degrades the optimals' performance by about 10%. Note also that the SV map and the contour map of the filtered growth has the same pattern. The significance of this pattern will be discussed later in this section. In general, throughout this study, the SV maps will be unfiltered, whereas (m, τ)-optimal fields, or the evolution of those fields will be filtered.

The optimals produced are very similar to those of the annually averaged case. Figure 4.5 shows the optimal pattern for the (5,9)-optimal. Compare with Fig. 3.12c, the τ_{max}-optimal from Chapter 3. The SST field shows the characteristic E-W dipole along the equator, and the same N-S dipole in the eastern Pacific. The thermocline field shows the same trough extending across the basin along the equator, spreading slightly at the western boundary. Both thermocline fields also display the dipole located near the eastern boundary and south of the equator. The similarity in the patterns indicates that while the cyclic background effects the magnitude of the growth, the mechanisms of growth are the same as detailed in Section 3.3.

Figure 4.6 shows a contour map of the correlation coefficients between the (m,τ)-optimals for all m and τ and the (5,9)-optimal, i.e. the $(m,\tau)_{max}$-optimal. This figure is intended to show that the shape of the optimals are not particularly sensitive to the time of year or period of growth. Over most of the figure the correlation is greater than 0.8. The exception is in the area near (m,τ)=(9,15) where the correlation drops precipitously. This area corresponds to the location where the optimal changes from producing a warm event to producing a cold event- the pattern (not shown) looks very much like the adjoint in the annually averaged case at phase=210 degrees - see Fig. 3.1d.

Returning to Fig. 4.4a, an interesting feature should be pointed out. Appearing on the SV map is a dashed line which marks the locations where the starting month plus the time period τ yields January 1st. Notice that for a fixed start month, the location of the τ_{max}-optimal for that month is close to the dashed line. In other words, whatever time of year the system is perturbed, the system has a tendency to peak during the (northern) winter months.

This seems to agree with the tendency of the real ENSO system to peak during the winter months. To demonstrate this, Figure 4.7 shows the evolution of the Nino3 index for 6 different warm ENSO events from the COADS data between 1950 and 1992. The warm events chosen were all those with a peak SSTA of greater than 1.0 degrees. As can be seen, in all six of these events, the ENSO matures around December. Not shown are two ENSO warm events which do not show this characteristic, but rather start in the winter of one year and then extend to the next winter. Another way to view this tendency to peak during winter is to view the standard deviation of the monthly averaged temperatures which are shown in Figure 4.8. From this figure it can seen that November and December show the greatest temperature variation.

In LOAM, the tendency for transient growth to produce peaks during the winter months is even more pronounced than indicated by Fig. 4.4. Recall from Section 3.1.3

that a τ-optimal does not necessarily peak at time τ. For example, Fig. 4.9a shows the growth of the (May, τ)-optimals for various τ. The circles indicate the value of the L_2 norm at time τ for each curve. As can be seen from this figure, each optimal produces a mature ENSO event in December, January or February, regardless of the value of τ. Figure 4.9b shows the same diagram for the (Sep., τ)-optimals. Here the results are similar except for the larger τ's where the optimals start to peak in the *following* winter. Figure 4.9c shows the same set of curves (with the circles removed) for (m, τ)-optimals over τ=3,6,9,12 and 15 months, starting every other month. This graph clearly shows the tendency for the optimals to peak during winter regardless of the starting month or optimization period.

Comparing Fig. 4.9 with Fig. 4.8, it might appear that the model peaks 2 or 3 months late relative to the real system. At least part of this discrepancy is due to Fig. 4.7 using the Nino3 index, while Fig. 4.9 uses the L_2 norm. The Nino3 index of the model ENSO peaks about 1 month earlier than the L_2 norm. The rest may be due to deficiencies in the model, or else due to the structure of the noise which drives the real system. In Chapter 6 a version of LOAM will be forced stochastically to better determine the validity of the model.

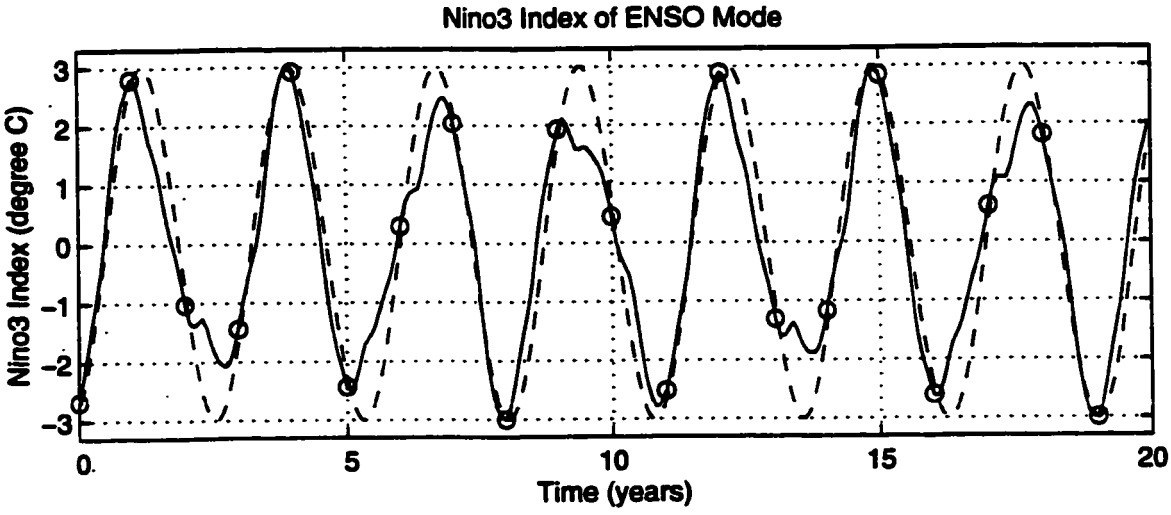

Figure 4.1 - Nino3 Index of ENSO Mode. Solid line shows the Nino3 index of SSTA produced by the ENSO mode, but with the exponential growth removed. Circles show the Nino3 index if January to December eigenvector is multiplied by its eigenvalue. In other words, the circles show the value of Nino3 for each January 1st. Dashed line shows Nino3 for same eigenvector rotated continuously.

Key	
Solid line	Simulation (LOAM)
Circles	Eigenvalue times Eigenvector
Dashed line	Rotated Eigenvector

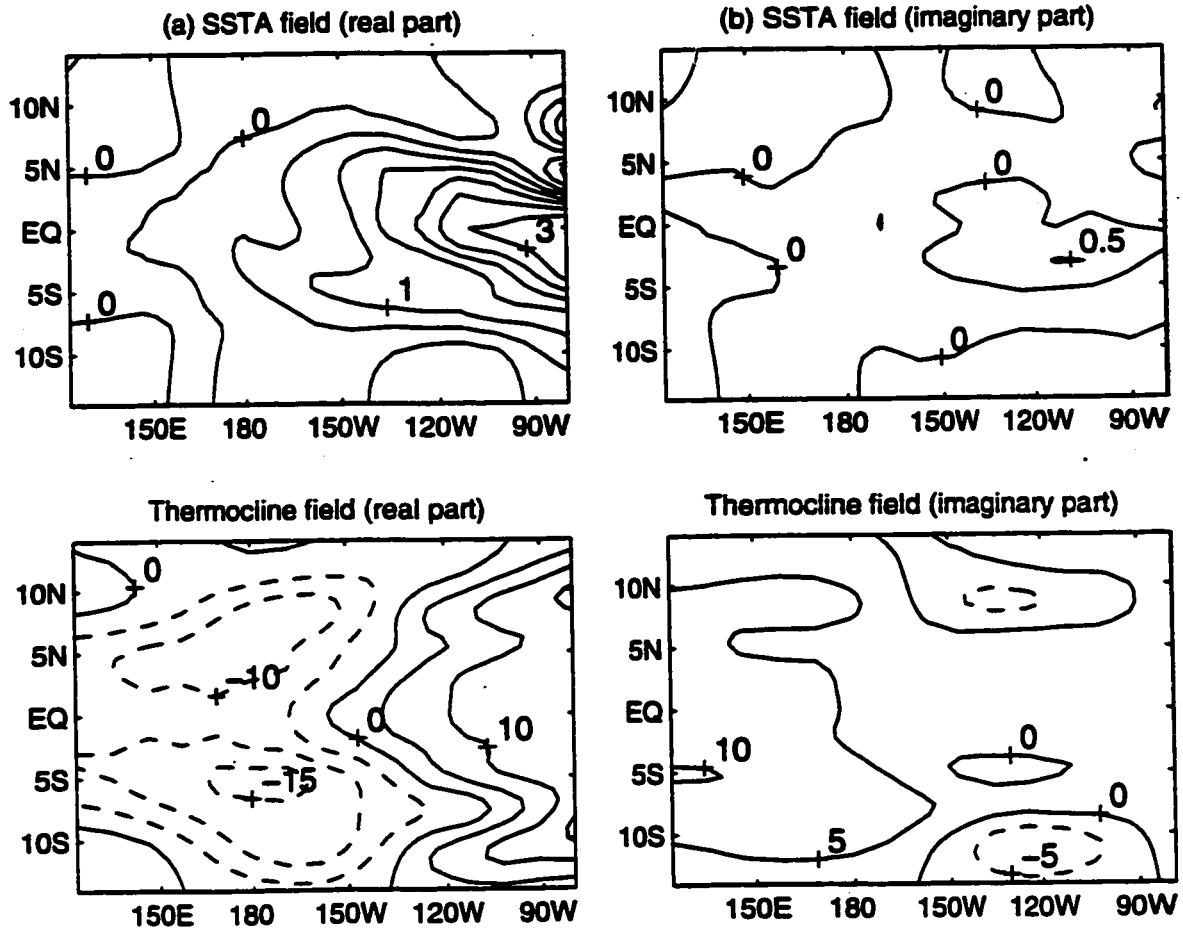

Figure 4.2 - Real and Imaginary parts of January to December ENSO mode. (a) shows the SSTA and thermocline fields of the real part of the most unstable eigenmode (the ENSO mode) for the January to December resolvant. (b) shows the imaginary part of the same.

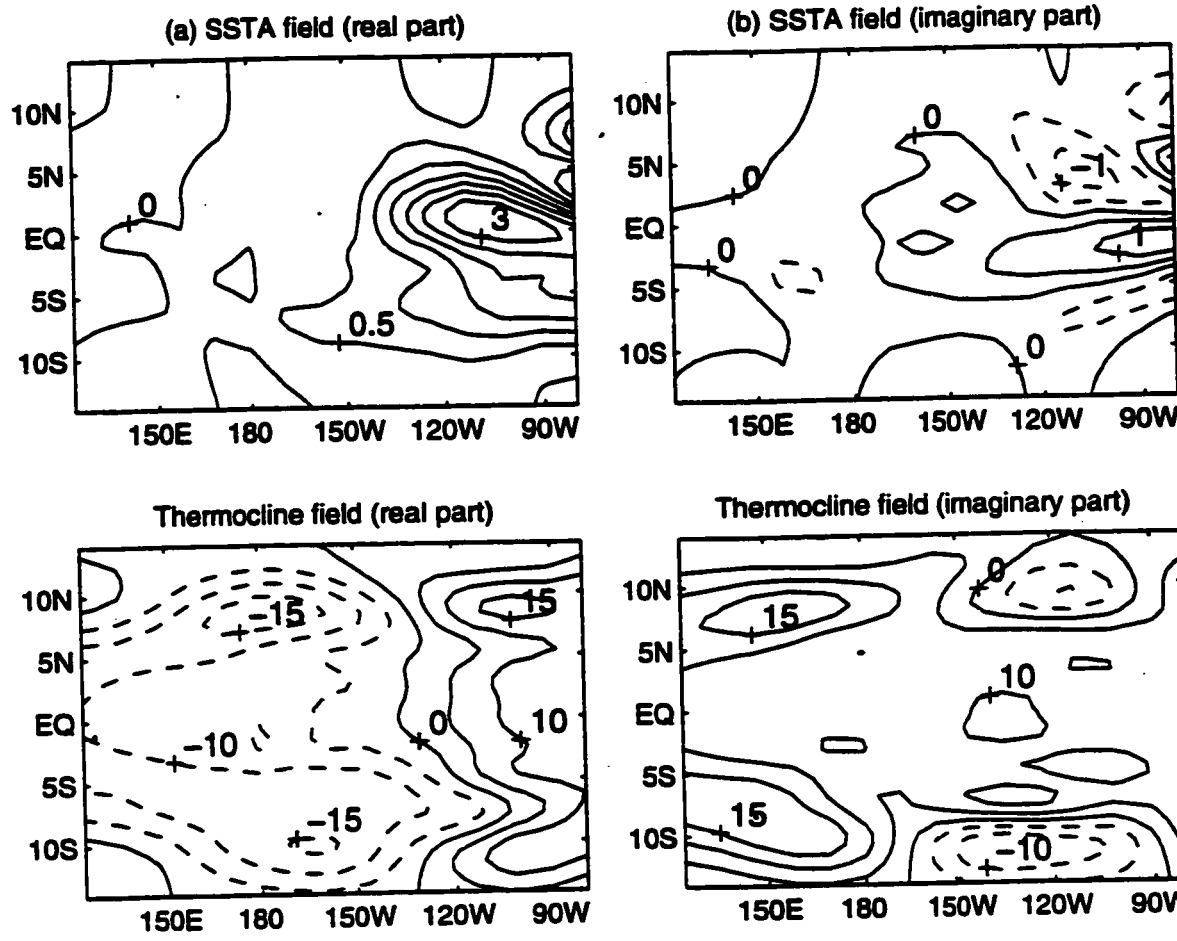

Figure 4.3 - Real and Imaginary parts of July to June ENSO mode. (a) shows the SSTA and thermocline fields of the real part of the most unstable eigenmode (the ENSO mode) for the July to June resolvant. (b) shows the imaginary part of the same.

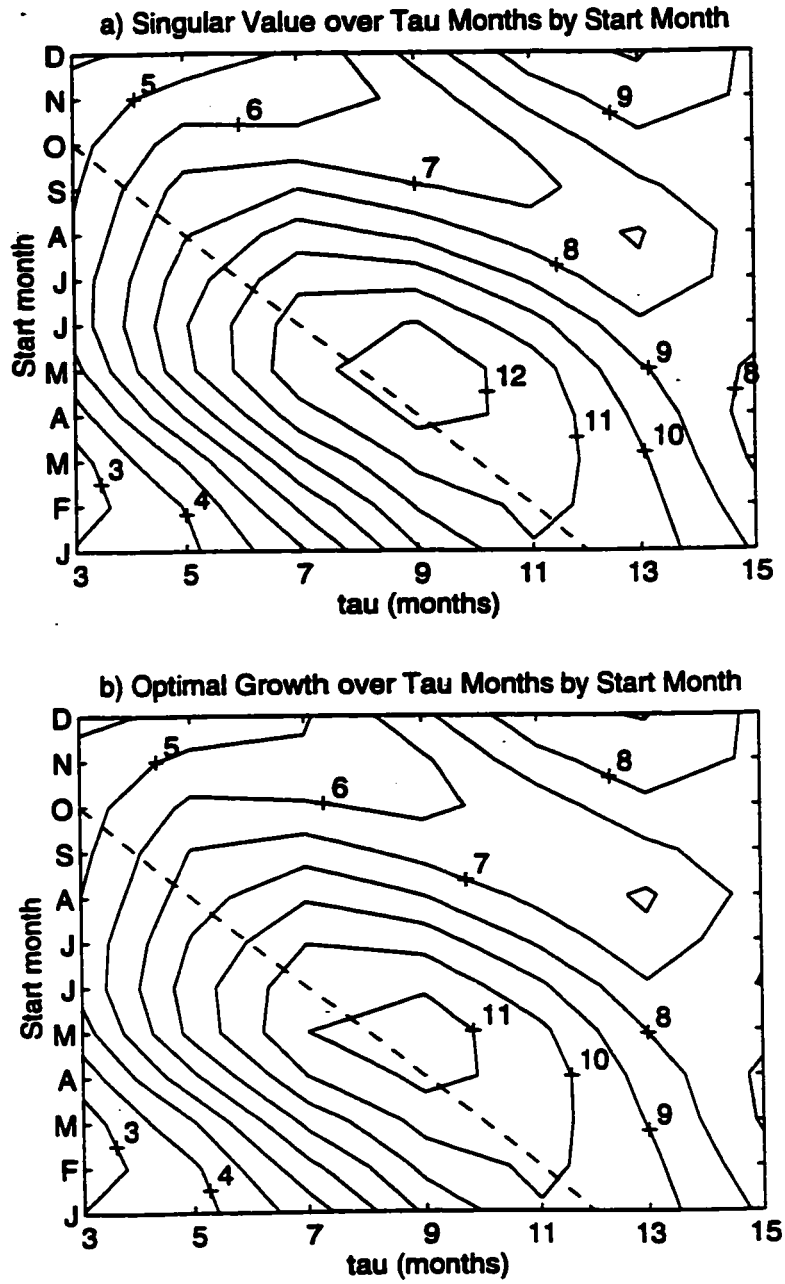

Figure 4.4 - Singular Value Maps. (a) contour map of the first singular values of LOAM with the B88M parameters. For each start month, SV1 is plotted for τ between 3 and 15 months. (b) same as (a) except that instead of plotting SV1, the growth after τ months starting from the *filtered* τ-optimal is shown. For both graphs the contour interval is one. The dashed line shows the location where the start month plus τ yields the target date of January 1st.

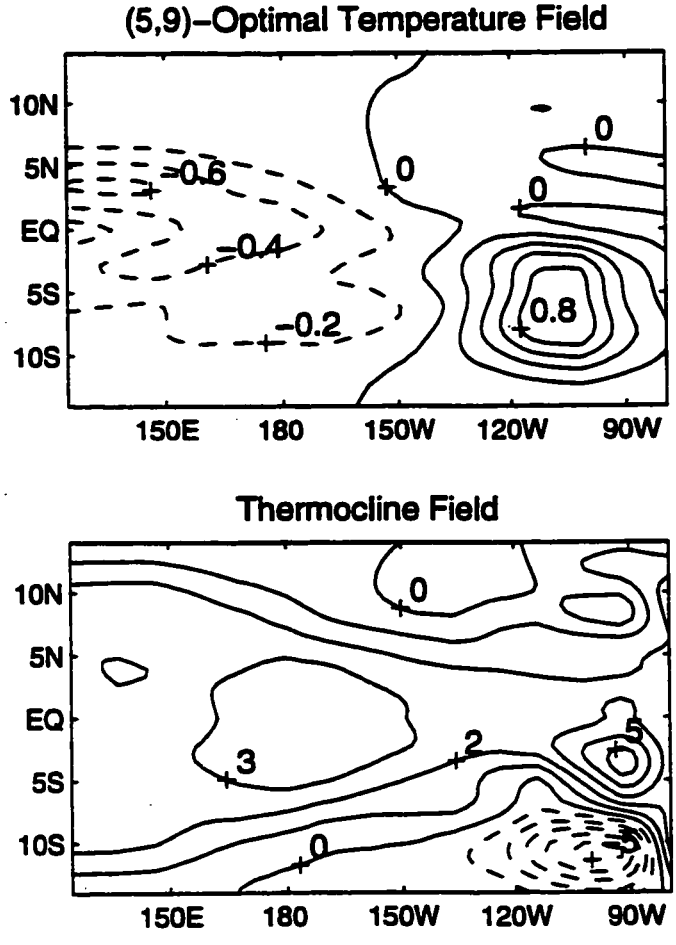

Figure 4.5 - (May,9 month)-Optimal Initial Conditions. Contour map of the SST and thermocline fields of the (5,9)-optimal. Contour intervals are 0.2 degrees C and 1 meter for the SST and thermocline, respectively.

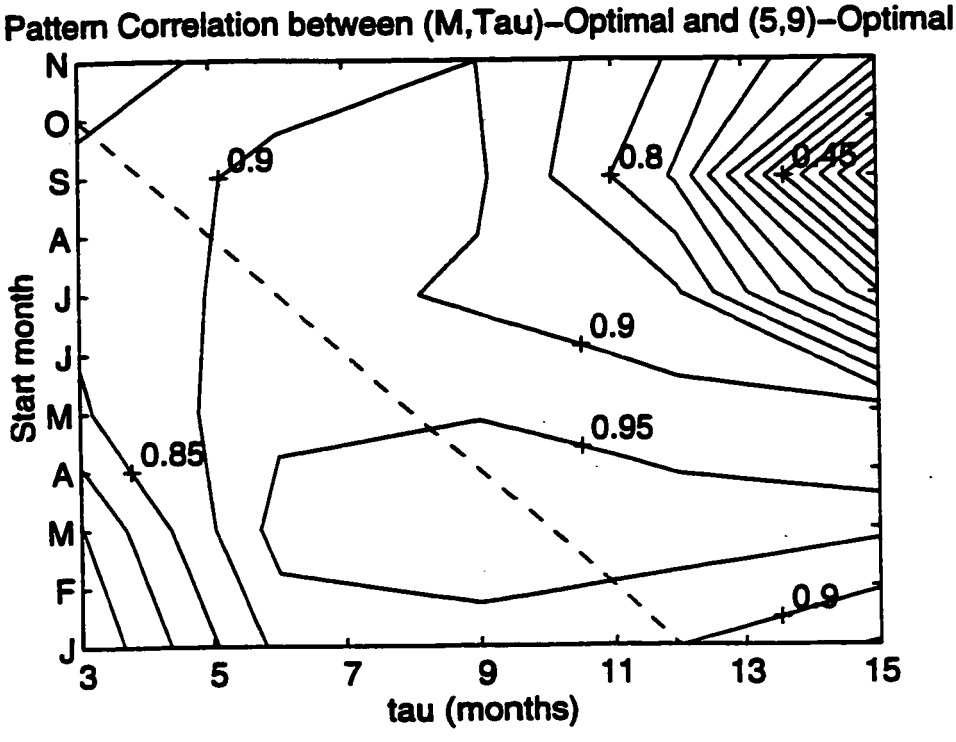

Figure 4.6 -Correlation between (M,tau)-Optimals and (5,9)-Optimal. This contour plot is on the same domain as Fig. 4.4, but shows the correlation coefficient between the (May, 9 mo.)-optimal pattern (shown in Fig. 4.5) and the optimal pattern for all other (M, τ) (which are not shown).

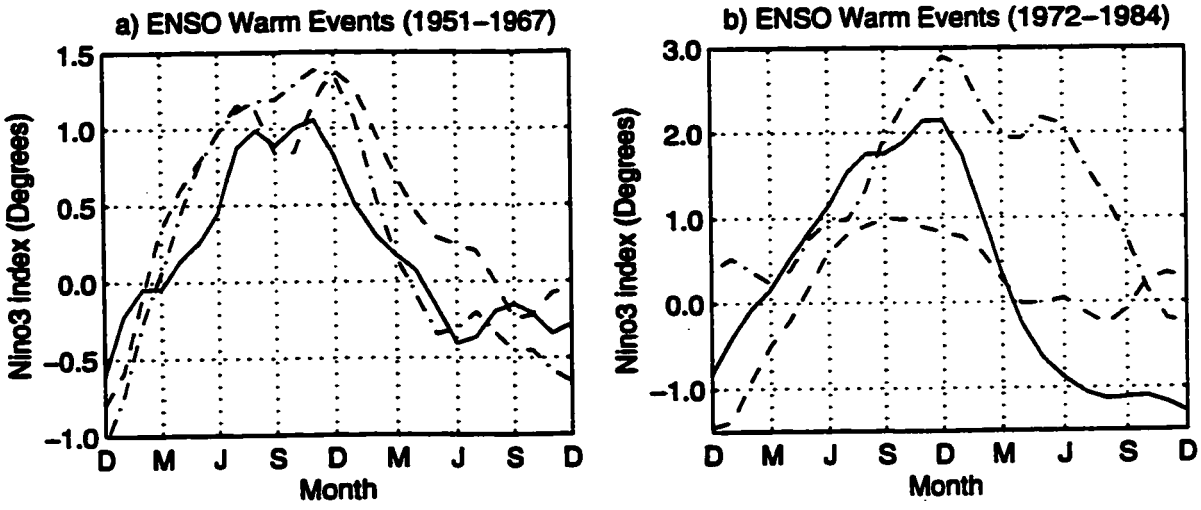

Figure 4.7 Sampling of Warm ENSO Events between 1950 and 1990. Plots of the Nino3 index for 6 of the warm events in the COADS data.

Key for Fig. 4.7(a)		Key for Fig. 4.7(b)	
Solid	1953-1954	Solid	1972-1973
Dashed	1957-1958	Dashed	1976-1977
Dash-Dot	1963-1964	Dash-Dot	1983-1984

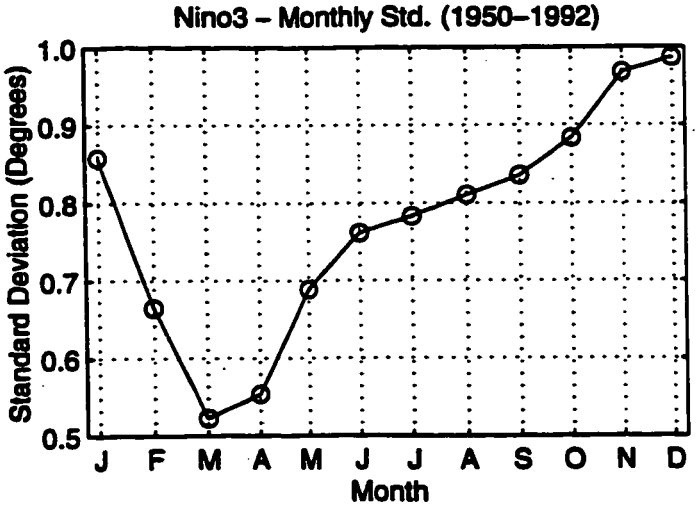

Figure 4.8 - Standard Deviation of Nino3. Standard deviation in degrees C of Nino3 index by month for COADS data between 1950 and 1992.

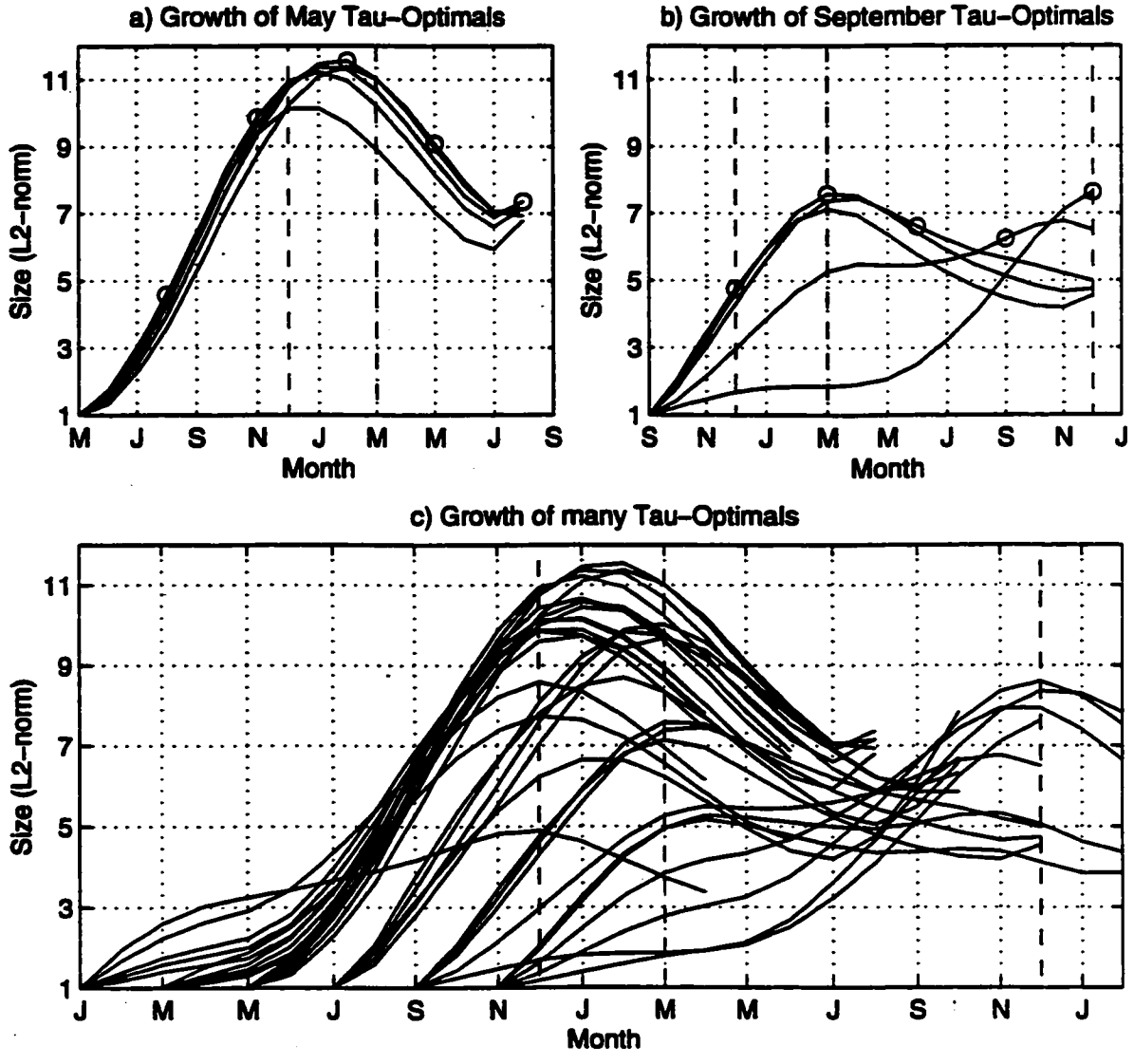

Figure 4.9 - Growth of Various Optimals. The growth over time of the L_2 norm of various optimals. (a) the growth of the (May, τ)-optimals for τ=(3,6,9,12,15) months. The circles mark the L_2 values at time τ for each optimal. (b) same as (a) except for the September start month. (c) the growth for the same set of τ, but for 6 different start months. The dashed lines delineate the winter months where all optimals have tendency to peak.

Chapter 5: Transient Growth vs. Modal Growth

5.1 Competing Hypothesis for ENSO Variability

Since Zebiak and Cane 1987, the most credible hypothesis to explain ENSO is that it is a large scale deterministic system, the seemingly random behaviour of which can be explained by non-linear dynamics. That is, ENSO can be characterized by a set of unstable equations where the growth of the ENSO mode is limited by non-linearity and the erratic behaviour is caused by chaos. Much literature has been devoted to studying the chaotic behaviour of the ZCM. See for example Jin, et al. (1994) or Tziperman, et al. (1994).

However, an alternate hypothesis is now gaining favor: that the ENSO dynamical system is approximately linear, and that its erratic behaviour is caused by external stochastic forcing. For example, Penland and Sardeshmukh (1995) built a statistical model of the Indian and Pacific basins and drive it stochastically as a simulation of ENSO. Also, Chang et al. (1997) runs several computer models, some of which are unstable and chaotic, and others which are stable and stochastically driven. The model statistics are then compared with the statistics of Pacific SST data.

The results of Section 3.4 of this study lend credence to the stochastic hypothesis in that it gives a mechanism by which ENSO-like warm and cold events can be produced even in a damped or neutral model. Four possible scenarios are: (i) ENSO is an unstable chaotic mode. (ii) ENSO is an unstable, saturated mode where external noise causes transient growth which either cancels or reinforces the warm and cold events so that they take on their irregular appearance. (iii) ENSO is a neutral or slightly damped mode where noise alters the phase and amplitude of the peaks so that they take on their irregular appearance. (iv) ENSO is a highly damped mode where noise and transient growth create all warm and cold events.

What is meant by the terms "highly" damped vs. "slightly" damped in scenarios (ii) and (iii)? A slightly damped system would be one where an ENSO mode which is initiated will last for a least a few cycles, unless modified by subsequent noise. In a highly damped system, transient growth leading to an event would not last beyond that event. This points out a difficulty with scenario (iv). If the time spectrum of the noise is white, ENSO events would occur independently of each other, which is not the case in the real system. Scenario (iv) would therefore require the external forcing to provide this correlation.

Scenario (i) and (ii) intrinsically require non-linearities, and so cannot be addressed using LOAM. Scenarios (iii) and (iv) can be addressed using a linear model. However LOAM will need to be made stable in order to study those scenarios. This can be achieved by simply decreasing the coupling between the ocean and atmosphere, but a more deliberate approach will be taken. Previous studies using intermediate class ENSO models undoubtedly tuned the models in order to put them in an unstable regime.[1] Why not tune LOAM in order to increase the strength of transient growth relative to the growth of the ENSO mode? The degree to which this can be done will increase the plausibility of a stochastic explanation for ENSO variability, since the amplitude of the external perturbations required to produce an event will be reduced. In any case, some parameter studies will covered in the next section and will be useful in trying to control the statistics of a stochastic model.

5.2 Transient Growth vs. Modal Growth: Parameter Studies

Since the class of models being studied here are highly parameterized, there are

[1]This class of models is distinguished by the use of steady state atmospheric models, either physically based (e.g. Gill (1980) and Linzen and Nigam (1987) models) or empirically based. As a result these models are devoid of atmospheric noise and therefore produce the ENSO cycle by normal mode growth and not by transient growth.

many coefficients within the basic equations that are known only approximately. The objective of the parameter studies in this section will alter LOAM in such a way as to maximize the transient growth while neutralizing the fastest growing mode. For this purpose a ratio will be defined:

TMR = (9 month growth of (May,9)-optimal)/(growth of ENSO mode in 1 year). (5.2.1)

By itself, this "Transient growth to Modal growth Ratio" is not completely meaningful. The optimal growth is over a 9-month period and the modal growth is over a year. The modal growth shows the growth of the complex vector which represents the ENSO mode, but as discussed in Section 3.1.3, the growth of the real part of the mode varies over the different phases of the mode. However, it does give a good estimate of the relative strengths of these two avenues of growth, and is straightforward to calculate.

The TMR for the linearized B88M is 6.97, which will be considered the baseline. For all of the parameter studies, the TMR will not be listed directly, but rather the percent change in the TMR from the baseline. From the definition of the TMR, it would seem that it has been assumed that the maximum growth in LOAM is always at (m, τ)=(May, 9 months). This assumption has been made to avoid calculating all the SVs for each point of the parameter studies. This assumption has been shown to be reasonable by checking the full SVmap at the extremes of the parameter ranges - the maximum optimal remains consistently at (May, 9 months) to within the resolution of the SVmaps. The SVmaps have a resolution of 2 months for the starting time, and 3 months for τ.

5.2.1 Modifying Coupling Strength

The most straightforward way to suppress the growth in LOAM is to reduce the coupling strength between the ocean and atmospheric components of the model. Specifically, the constant γ in (2.2.4a) or (2.2.4b) controls the strength of the heating

and therefore the amplitude of the atmospheric reaction to a given SST field. Alternatively, the constant C_D in equations (2.2.17) to (2.2.19) controls the strength of the forcing of the ocean to a given wind field. Changing either of these coefficients has the same effect on the model.

Table 5.1 shows the period and growth of the ENSO mode, the (May,9)-optimals growth, and the TMR as the coupling is reduced from its nominal value. As might be expected, both the strength of the optimal and the growth rate of the ENSO mode are reduced. Note that the two are reduced at about the same rate. By interpolation, it is found that the ENSO mode becomes neutral at a coupling multiplier of about 0.76. At this neutral point the TMR is reduced by a factor of about 0.92. So reducing the coupling, while neutralizing the model as desired, does not increase the TMR, but reduces it slightly. This result is not surprising, since reducing the coupling damps the model, but without targeting any particular mechanism. In the next two sections, coefficients which damp the modal growth more than the transient growth will be sought.

Table 5.1 - Effect of Coupling Strength on LOAM. Coupling between the ocean and atmosphere (either C_D or γ is reduced) and the changes in the ENSO mode and singular values are listed. TMR is the ratio of the transient growth to modal growth. The modal growth is given as the amount of exponential growth achieved in one year. Numbers greater than one indicate an increase in the transient growth relative to the ENSO growth. The italicized entry is interpolated, the bold entry is the nominal.

Coupling ($\gamma \cdot C_D$)	ENSO Period (years)	ENSO Growth per year	Sing. Value (m=5, τ=9)	TMR change (factor)
1.0	2.74	1.82	12.68	1.00
0.9	2.79	1.43	9.61	0.97
0.8	2.85	1.11	7.18	0.94
0.758	*2.88*	*1.00*	*6.39*	*0.92*
0.7	2.93	0.85	5.30	0.90
0.6	3.02	0.64	3.87	0.88

5.2.2 Modifying Ocean Dynamics

One characteristic of the transient growth vs. modal growth difference that should be exploitable is the time scale difference. The τ-optimal experiences its growth over a 9 month period, too short a period of time for reflection from the western boundary to have much effect. Both the B88M and ZCM use a 100% reflective boundary, yet Clarke (1991) and du Penhoat and Cane (1991) have estimated that the western boundary may have a reflection coefficient in the neighborhood of 0.8. Since du Penhoat and Cane (1991) shows that the eastern boundary reflection coefficient is close to 1.0 and since the τ-optimals use this reflection for growth (see Section 3.3), only the western boundary coefficient was varied.

Table 5.2 shows the effect on LOAM of reducing the reflection efficiency of the western boundary. As expected, the ENSO growth rate is reduced, while the SV remains essentially unchanged. However, in light of du Penhoat and Cane (1991), decreasing the reflection beyond 0.7 is probably not realistic, and so the model cannot be neutralized using this coefficient alone.

Table 5.2 - Effect of Western Boundary Reflection on LOAM. Same as Table 5.1 except the reflection of waves reflected off the western boundary is varied. The italicized entry is interpolated, and the bold entry is the nominal.

Western bndry (WBR)	ENSO Period (years)	ENSO Growth per year	Sing. Value (m=5, τ=9)	TMR change (factor)
1.0	2.74	1.82	12.68	1.00
0.9	2.87	1.70	12.73	1.08
0.8	3.03	1.58	12.78	1.17
0.775	*3.08*	*1.50*	*12.80*	*1.20*
0.7	3.24	1.46	12.86	1.27

A second modification to the ocean equations which should effect the TMR positively would be to increase the mechanical damping of the ocean. The damping, a^{-1} from equations (2.2.12) through (2.2.14), is set to 2.5 years in the ZCM and B88M, but

this damping time is probably too long. Picaut et al. (1993) fits an intermediate ocean model, driven by observational winds, to tide gauge, moorings and GEOSAT data, and finds a damping time of 6 months. While increasing the damping will effect both types of growth, it should effect modal growth more owing to its longer timescale and since it is made up of equatorial waves which propagate back and forth across the basin.

Table 5.3 shows the effect of the increased mechanical damping on LOAM in a range for the mechanical damping from 2.5 years to 6 months. As expected, the ENSO mode is damped more quickly than the optimal, with the TMR increasing by 77% for the 6 month damping coefficient. The ENSO mode goes neutral when $a^{-1} = 0.703$ years, at which point the transient growth still retains 77% of its strength.

Table 5.3 - Effect of Ocean Damping on LOAM. Same as Table 5.1 except that the mechanical damping of the ocean, a^{-1}, is reduced. The italicized entry is interpolated, and the bold entry is the nominal.

Damping (a^{-1}) (years)	ENSO Period (years)	ENSO Growth per year	Sing. Value (m=5, τ=9)	TMR change (factor)
2.5	2.74	1.82	12.68	1.00
1.9	2.78	1.68	12.25	1.05
1.5	2.82	1.54	11.78	1.10
1.1	2.91	1.33	11.05	1.20
0.9	2.98	1.18	10.48	1.28
0.703	*3.10*	*1.00*	*9.79*	*1.42*
0.7	3.12	0.97	9.68	1.44
0.5	3.41	0.69	8.44	1.77

5.2.3 Modifying Thermal Equation, Part I

The thermal equation (2.2.34) contains several terms with unknown efficiency factors in the upwelling process (nominally set to 0.75) which might be exploited to move LOAM into a desirable regime. These efficiency factors were each varied over a range from 1.0 to 0.50 and tables similar to those above were produced.

Table 5.4 shows the effect on LOAM of varying the upwelling efficiency, δ in K_w, from (2.2.36). This coefficient has a moderate effect on both kinds of growth, with the growth increasing as δ increases. However, the TMR is not as strongly affected as with the western boundary reflection in Table 5.2. From the interpolation in Table 5.2, when the ENSO growth rate reaches a factor of 1.50 per year, the TMR has increased by 20%, whereas there is only a 5% increase in the TMR for the same ENSO growth rate in Table 5.4.

Table 5.5 shows the affect of varying the thermocline heating efficiency, δ in K_T, from (2.2.37). This coefficient effects both kinds of growth similar to the previous coefficient: increasing modal and transient growth as δ is increased. Over most of the range of the efficiency parameter there is little change in the TMR, except as the efficiency approaches one. This extreme is in the opposite direction of where we want to send the ENSO growth, but it increases the TMR by 17% and might be useful in conjunction with another parameter which strongly reduces the ENSO growth such as the mechanical damping of Table 5.3.

Table 5.4 - Effect of Upwelling Efficiency on LOAM. Same as Table 5.1 except that the upwelling efficiency, δ for K_w is varied. See equation (2.2.36). The nominal value is 0.75.

δ for K_w (efficiency)	ENSO Period (years)	ENSO Growth per year	Sing. Value (m=5, τ=9)	TMR change (factor)
1.00	2.55	2.20	14.73	0.97
0.88	2.65	2.00	13.66	0.98
0.75	2.74	1.82	12.68	1.00
0.63	2.82	1.65	11.77	1.02
0.50	2.90	1.50	10.92	1.05

Table 5.5 - Effect of Thermocline Heating Efficiency on LOAM. Same as Table 5.4 except that the thermocline heating efficiency, δ for K_T is varied. See equation (2.2.37). The nominal value is 0.75.

δ for K_T (efficiency)	ENSO Period (years)	ENSO Growth per year	Sing. Value (m=5, τ=9)	TMR change (factor)
1.0	3.06	2.70	22.07	1.17
0.9	2.92	2.33	17.77	1.09
0.8	2.80	1.99	14.21	1.03
0.75	2.74	1.82	12.68	1.00
0.7	2.68	1.65	11.31	0.98
0.6	2.58	1.34	9.01	0.97
0.5	2.49	1.03	7.22	1.00

Table 5.6 shows the effect on LOAM of varying the upwelling damping efficiency, δ in $d(x,y)$, from (2.2.38). Since this is a damping term, its effect is in the opposite direction of the other two terms discussed in this section. That is, decreasing the value increases the modal growth. The model is fairly sensitive to this term- decreasing the efficiency by just 30%, for instance, almost doubles the growth rate of both the ENSO mode and the τ-optimal. However, it seems to affect both kinds of growth almost equally. The TMR does not change by more than 6% over a large range of model stability in which the ENSO yearly growth varies by almost 300%.

Table 5.6 - Effect of Upwelling Damping Efficiency on LOAM. Same as Table 5.4 except that the upwelling efficiency, δ for $d(x,y)$ is varied. See equation (2.2.38). The nominal value is 0.75.

δ for $d(x,y)$ (efficiency)	ENSO Period (years)	ENSO Growth per year	Sing. Value (m=5, τ=9)	TMR change (factor)
1.00	2.66	1.18	8.06	0.98
0.87	2.69	1.44	9.93	0.99
0.75	2.74	1.82	12.68	1.00
0.63	2.80	2.38	16.91	1.02
0.50	2.85	3.30	23.75	1.04

5.2.4 Modifying Thermal Equation, Part II

Two further parameters in the thermal equation will also be explored. The first is the time invariant background thermal damping time, α_s^{-1}, from (2.2.37). The second is the manner in which the non-linearity in the subsurface temperature is linearized.

Table 5.7 shows the effect of varying the background thermal damping in LOAM. The damping varies from about 2 month to 1 year, with the nominal value at 125 days. The strength of both types of growth are increased as the damping is decreased, with the optimal growth being slightly more sensitive than modal growth. The TMR grows as the damping is reduced, increasing by 17% at the minimum damping of 375 days. However, at this point the ENSO mode is growing by a factor of 3.22 times per year.

Table 5.7 - Effect of Background Damping on LOAM. Same as Table 5.4 except that the background thermal damping, α_s^{-1}, is varied The nominal value is 125 days.

α_s^{-1} (days)	ENSO Period (years)	ENSO Growth per year	Sing. Value (m=5, τ=9)	TMR change (factor)
63	2.11	0.59	3.90	0.95
83	2.39	1.05	6.68	0.91
125	2.74	1.82	12.68	1.00
167	2.99	2.41	18.04	1.08
375	3.33	3.22	26.09	1.17

Returning to the subsurface temperature parameterization, it can be seen from (2.2.33), that in LOAM the derivative of $T_s(h)$ at zero is approximated by the average of the derivative from the left-hand and right-hand sides. Remember that the function is discontinuous at this point. See (2.2.29) and (2.2.30). Alternatively, the derivative could have been assumed to be the left or right derivative, or any weighted combination of the two. Xue et al. (1996), for example, used the derivative of $T_s(h)$ from the positive side when linearizing. For this parameter study, (2.2.29) will be generalized to:

$$T_s'(\bar{h}) = \left\{ R_{ss}\left[\frac{\partial T_s}{\partial h}\right]_{h=0^+} + (1-R_{ss})\left[\frac{\partial T_s}{\partial h}\right]_{h=0^-} \right\}, \qquad (5.2.1)$$

where R_{ss} varies between 0 and 1.

Table 5.8 shows the effect on LOAM by varying the subsurface temperature linearization. As expected, growth increases as the linearization moves to the "warm water" parameterization. The TMR increases as the model grows more unstable, reaching a 13% increase when R_{ss} reaches one.

Table 5.8 - Effect of Subsurface Temperature Linearization on LOAM. Same as Table 5.4 except that the manner in which the subsurface temperature parameterization is made is varied. See equation (5.2.1). In the nominal case R_{ss}=0.5.

R_{ss} (ratio)	ENSO Period (years)	ENSO Growth per year	Sing. Value (m=5, τ=9)	TMR change (factor)
0.00	2.69	1.27	8.46	0.96
0.25	2.70	1.51	10.25	0.97
0.50	2.74	1.82	12.68	1.00
0.75	2.83	2.18	16.03	1.06
1.00	3.00	2.62	20.65	1.13

5.3 Stochastically driven ENSO Models

As discussed in Section 5.1, and using the parameter studies from Section 5.2, several alternative ENSO models will be designed and tested. Figs. 5.1a and 5.1b use the data from Tables 5.1 through 5.8, and plot the change in the TMR against the ENSO growth rate for all the parameters studied. In general, the objective will be to alter the B88 model parameters in such a way as to stabilize the model while increasing the TMR as much as possible. An examination of Fig. 5.1 shows that there are only three parameters of the eight studied which accomplish this: the western boundary reflection (WBR), the ocean mechanical damping (a^{-1}), and the upwelling efficiency (δ in K_w).

Of course, varying the parameters in conjunction with each other may lead to the same effect. For instance, it might be possible to raise the TMR using the subsurface temperature parameterization (R_{ss}) and thermal damping (α_s^{-1}), and then compensate for the increased ENSO growth rate using the upwelling damping efficiency (δ in $d(x,y)$) and/or the coupling strength. However these contortions probably are not necessary since a^{-1} and WBR have the strongest effect on the TMR while sending the modal growth in the correct direction.

Four different candidate models will be developed. Table 5.9 shows the parameter values for each model, and the basic characteristics of each model such as the ENSO growth rate and the model singular values. The shapes of the ENSO modes and τ-optimals are basically the same as before and are not shown. The SVmaps for all four models are presented in Fig. 5.2. Explanations of how each model was designed are given below.

Table 5.9 - Transient Growth Model Characteristics. Parameter values and derived characteristics of the four candidate models from Section 5.3. The bold entries are the B88M values.

Model Designation	N.97	T.97	T.80	T.60
Coupling ($\gamma \cdot C_D$)	0.75	**1.00**	**1.00**	**1.00**
Western Boundary (WBR)	**1.0**	0.8	0.7	0.7
Ocean Damp (1/month)	**30**	10	8.7	7
Upwelling Eff (δ in K_T)	**0.75**	**0.75**	**0.75**	0.6476
ENSO Growth per year	0.97	0.97	0.80	0.60
ENSO Period (years)	2.89	3.42	3.85	4.54
1st Singular Value, max	6.2	10.3	9.9	8.6
(Start month, τ) of SV1	May, 9 mo.	May, 9 mo.	May, 9 mo.	May, 9 mo.
2nd Singular Value, max	2.6	2.7	2.4	2.1

The first model will be the nominal model. All parameters will be left at their nominal B88M values, except that the coupling between the ocean and atmosphere will be reduced until the model is slightly damped. This model will be called N.97 - "N" for "nominal", and ".97" since that is the yearly growth of the ENSO mode. Remember that these models are to be driven stochastically (Section 5.6) and so the B88M parameters could not be used without lowering the coupling - an unstable linear model would just grow indefinitely.

The second model was built to match the ENSO growth rate of N.97, but the transient growth will be kept as large as possible. To do this, the WBR, which preserves the transient growth most effectively, is set to a reasonable value of 0.8. The ocean mechanical damping is then increased until the ENSO growth reaches 0.97 per year. The proper damping turns out to be 10 months. This model will be called T.97 where "T" is for "transient growth".

The last two models are designed to explore the region where the ENSO mode is not approximately neutral, but instead somewhat damped. Both models are built to enhance the transient growth. The third model, designated T.80, has an ENSO growth rate of 0.8 per year. It was built by first setting the WBR to its smallest plausible value of 0.7, and then the ocean mechanical damping was increased. The proper damping to reach a growth of 0.8 per year turned out to be 8.7 months. The fourth model has an ENSO growth of 0.6 per year. This was achieved by reducing the WBR to 0.7, the lowest plausible reflection coefficient, and increasing ocean damping to 7 months, the greatest plausible damping. The upwelling efficiency, δ in K_w, was then lowered until the desired growth rate was achieved.

It should be noted that all these models were built with the primary design criteria of manipulating the transient and ENSO growth rates. Unfortunately, it is not possible to hold all other characteristics constant. Specifically, the period of the ENSO

mode ranges from 2.9 years in N.97 up to 4.5 years in T.60. An examination of the parameter study (Tables 5.1, 5.2, 5.3 and 5.4) shows that all the parameters which were varied in producing the models above have the characteristic of lengthening the period as they lower the growth rate. In fact, none of the parameters had the property of shortening the period while both lowering ENSO growth and enhancing the TMR. Therefore, it was not possible to control the ENSO period.

5.4 Hindcasting with Candidate Models

The four models were used to make hindcasts on the COADS data set of SSTA data for the equatorial Pacific for the years 1950 through 1990. For details regarding this data set, see Woodruff et al. (1993). Note that LOAM is not intended as a forecast model. Forecasts using each of these models demonstrate that: (i) instability is not a requirement for a plausible ENSO model, (ii) the decreased ocean damping and western boundary reflection models are just as plausible as the "nominal" model, and (iii) the limit of how damped the ENSO mode can be made before it is no longer a reasonable model. It will be seen in the next section that, due to the data assimilation method that is used, the importance of transient growth cannot be assessed.

5.4.1 Assimilation of Temperature Data

LOAM is limited in its capability as a hindcast/forecast model because of its inability to assimilate wind data. When the ZCM or B88M are run in "forecast mode" the thermocline state at time zero can be determined in whole or in part by using the measured surface winds up to time zero. The best hindcasts using the ZCM are made by spinning up the model using a weighted average of the wind data and the model winds. A detailed explanation is given in Chen et al. (1995). However, LOAM is unable to drive its ocean with arbitrary wind forcing, that is, forcing that is inconsistent with the winds produced by the current LOAM SSTA. In fact, LOAM is not set up to be driven by external

forcing at all - so how is the data assimilated?

The data assimilation was done by selecting a set of thermocline and SSTA fields which, when allowed to evolve freely, most closely match (in a least squared sense) the SSTA fields given by the COADS data. Specifically, the thermocline and SSTA fields at time zero are determined by selecting a set of fields at time zero minus two years which best fits the SSTA data over the two year interval. The mathematics of the assimilation process are covered in detail in Appendix E. Unfortunately, this method makes no use of the available windstress data in estimating the state of the thermocline.

Since this assimilation method works by freely evolving the model over a two year period before time zero - *no information about the importance of transient growth* can be inferred from the hindcasting in this section. In fact, since the standard techniques of data assimilation for the ZCM involve forcing by data right up to time zero, the ZCM forecasts are more likely to capture the noise which is proposed here to be the cause of transient growth-induced ENSO events.

5.4.2 Comparison of Candidate Models by Forecast Skill.

All four candidate models were used to make a series of forecasts using the 40 years of COADS data from 1950 to 1990. Forecasts were made starting every 3 months from January of 1952 through January of 1989. Forecasts were made up to 12 months and the predicted Nino3 index was compared to the actual Nino3 index. Figure 5.3 shows the correlation coefficient and the RMS error for each of the models averaged over the 40 years as a function of forecast length. Also included for comparison is the same data for the persistence forecast.

Looking first at the correlation in Fig. 5.3a, it can be seen that all 4 models eventually surpass the persistence skill. Model T.60 does better than persistence after 5

months, while the other three models achieve this after only 3 months. In general, after 3 months, the two models T.97 and T.80 perform similarly, with N.97 performing slightly worse and T.60 performing noticeably worse. None of the models are reasonably accurate after the 9 month mark, where they all have less than a 0.4 correlation between their predictions and the data. The RMS errors are found in Fig. 5.3b. Here all four models do better than persistence after about 3 months. The T.80 and T.60 perform almost identically. They outperform T.97 in the longer forecasts by less than 0.1 degrees C, and outperform N.97 by about 0.15 degrees C.

In order to get some intuition about the models, some plots of their forecasts will be examined. Figure 5.4 shows the 0 month forecasts (i.e. the nowcasts) for model T.97. As could be expected from the RMS and correlation graphs, the nowcasts look quite good. The nowcasts for the other models (not shown) look similar. Matching the Nino3 index at time zero may not seem like much of a feat - after all the time zero fields are included in the assimilation data set. But recall that the time zero fields are those that develop after two years of model evolution, where the initial fields (at time equals minus two years) are chosen to agree optimally with all the fields in the assimilation period. The time zero fields are not weighted any more heavily than the others.

Figure 5.5 shows the six month forecasts of the T.80 model over the 40 years of data. At the six month level, T.80 is slightly better than the other models - doing better in correlation and RMS error. Figure 5.5 shows that it does reasonably well -though it is fooled in several places. Most notably, T.80 seriously underpredicts the 82-83 event, which is typical of ENSO forecast models. The T.97 and N.97 models' 6 months forecasts of Nino3 SSTA look similar to Fig. 5.5, and are not shown. Only the T.60 model's forecasts are perceptibly worse.

Figure 5.6 shows the 12 month hindcasts made by the T.60 model, and demonstrates some of the model's problems. Primarily, it seems that the ENSO mode is

too damped. Notice that the T.60 model never produces a ENSO event with a magnitude greater than 1 degree C. Also, it would seem that the model's ENSO mode has too long a period. For example, T.60 predicts a warm peak event in the middle of 1974, presumably because of the cold event (in 1971-1972) during the assimilation period. This cold event *is* followed by a warm event, but the real event occurs a year earlier. Likewise, the cold event predicted in reaction to the 1973 warm event is a year too late. This out-of-phase behavior occurs in many places, particularly in the years from 1964 through 1980.

Figure 5.7 shows the 12 month projections made by the N.97 model. This model has very different difficulties than the T.60 for the 12 month forecasts. Since the model is nearly neutral, it produces predictions of about the right magnitude. Of course when it errs, the errors are larger. For example, it fails to predict the 82-83 warm event just like T.60, but unlike T.60, it predicts a large cold event in reaction (which does not occur). N.97, which has a much shorter ENSO period than T.60, does not seem to have the out-of-phase problem found in T.60. For instance, the cold-warm-cold sequence in 1964 to 1967 is predicted by T.60 as warm-cold-warm, whereas N.97 gets it right.

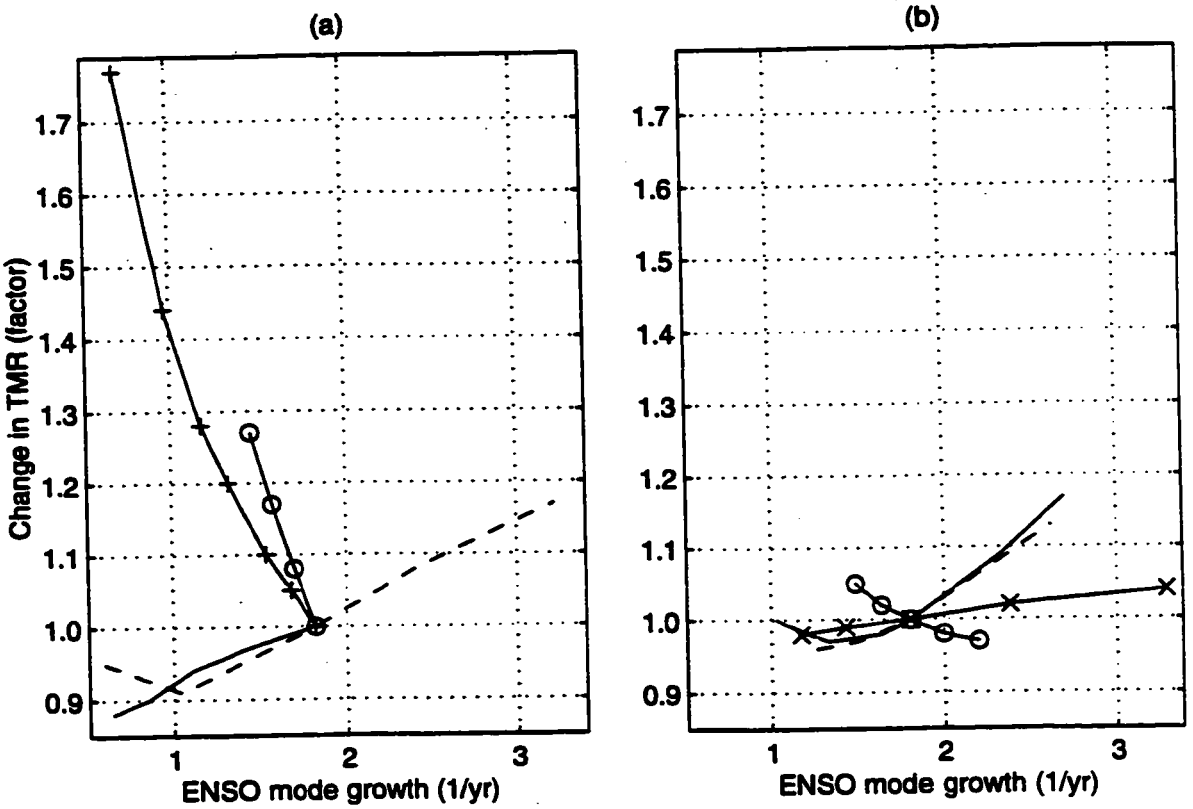

Figure 5.1 - Change in TMR against ENSO growth. Plot of data from parameter studies in Tables 5.1 through 5.8. the 8 lines were plotted on two separate graphs for clarity. The scales are the same for both.

Key 5.1(a)		**Key 5.1(b)**	
Circles	WBR	Circles	δ of K_w
Pluses	Ocean Damping	Crosses	δ of $d(x,y)$
Solid line	Coupling Coef.	Solid line	Thermal Damping
Dashed line	δ of K_T	Dashed line	R_{ss}

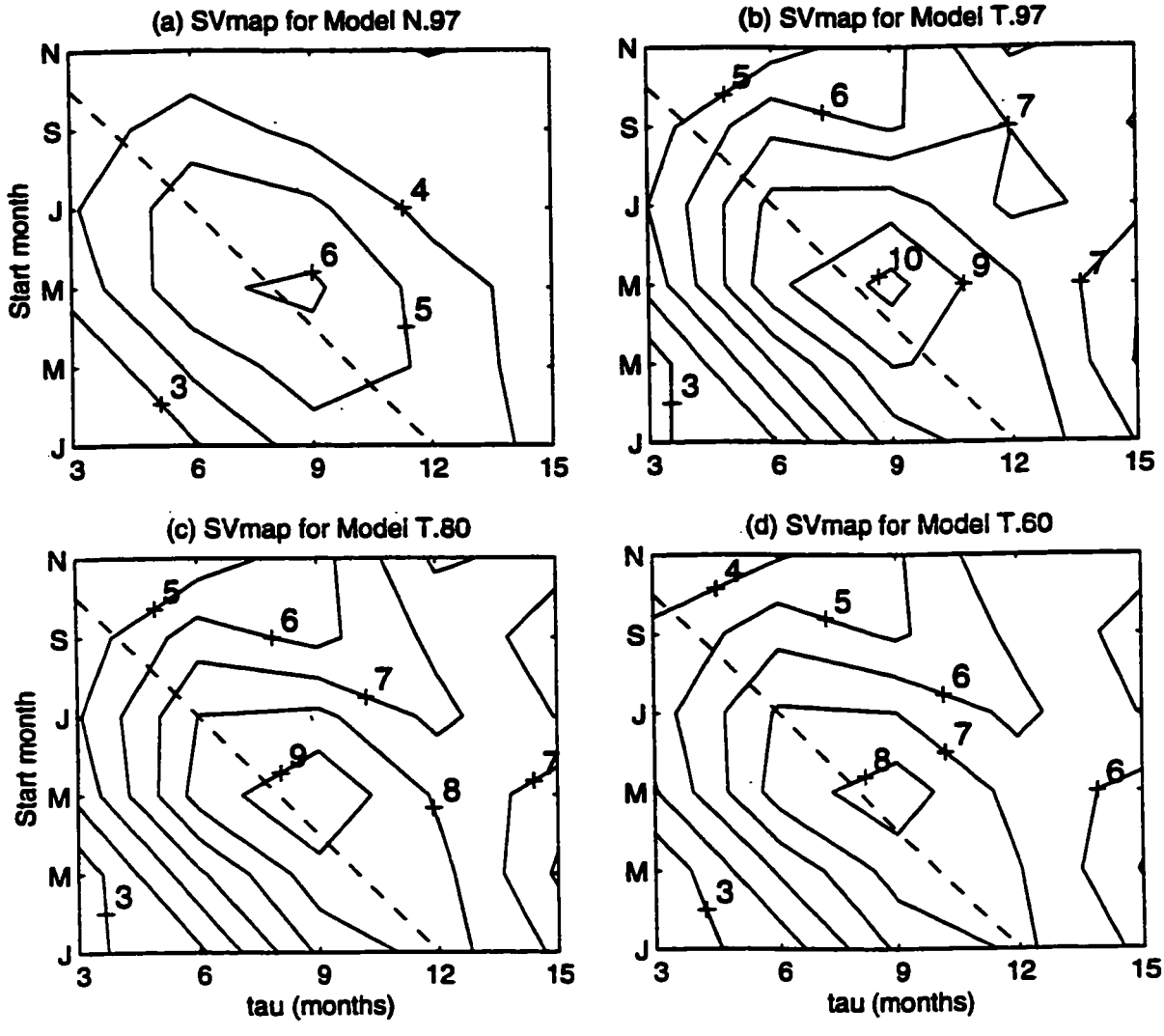

Figure 5.2 - Singular Value Maps of Candidate Models. These are contour maps of the first singular values of the various models starting at every month of the year for periods between 3 months and 15 months. The contour interval is one, and the dotted line on each graph shows which combinations of start month and period add up to optimizing the L2 norm in January.

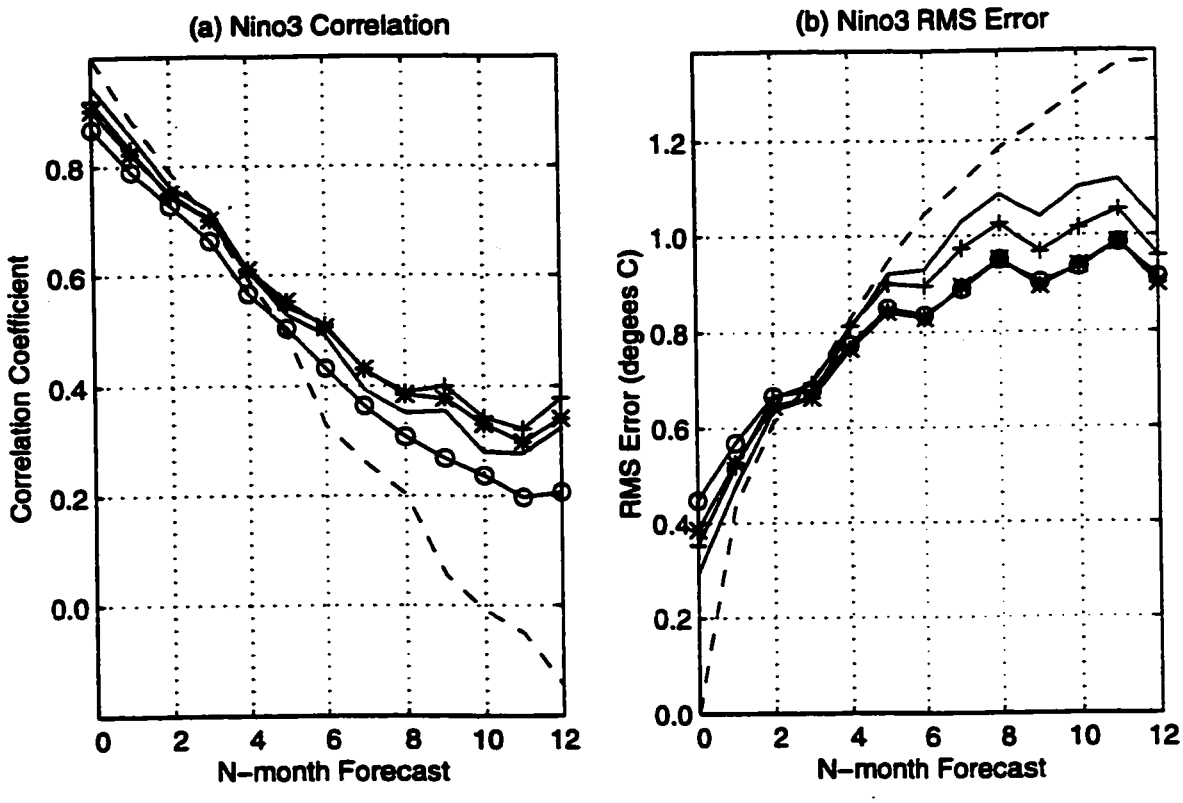

Figure 5.3 - Correlation and RMS Error of Model Hindcasts. The average correlation coefficient (a), and average RMS error (b) of hindcasts made by each candidate model on COADS data from 1950 to 1990 as a function of the length of the forecast. The persistence forecast averages are included.

Key	
Dashed line	Persistence
Solid line	N.97
Pluses	T.97
Asterisks	T.80
Circles	T.60

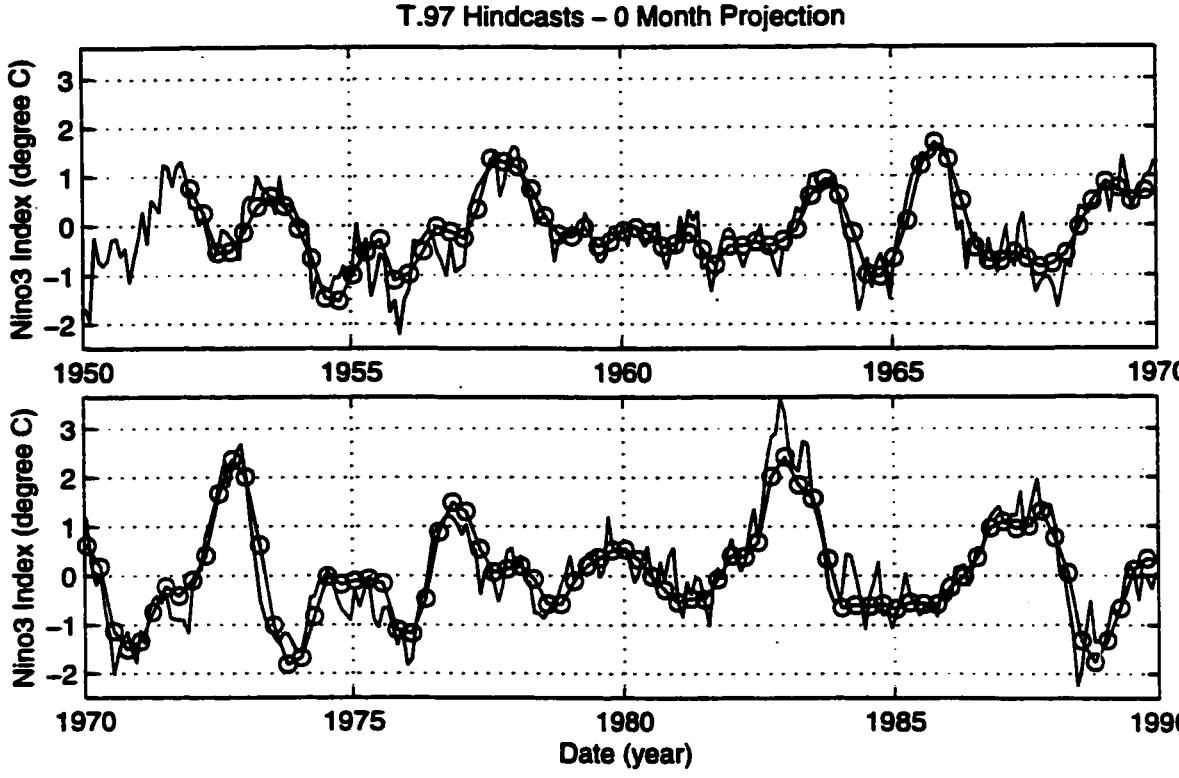

Figure 5.4 - T.97 Model Nowcasts vs. Data. Plot of Nino3 index for COADS data and for the nowcasts of the T.97 model. The circles show the actual forecasts and the lines between them are to provide visual continuity.

Key	
Solid line	COADS data
Circles	Nowcasts

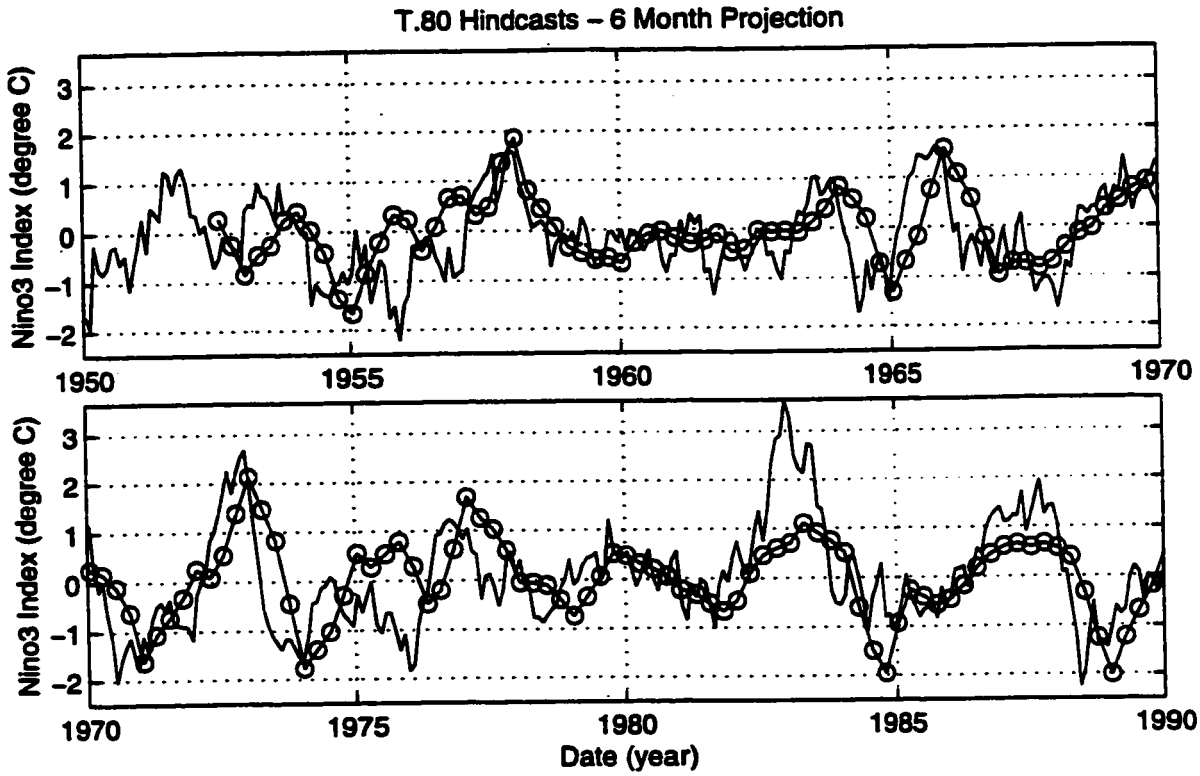

Figure 5.5 - T.80 Model 6 Month Hindcasts vs. Data. Plot of Nino3 index for COADS data and for the 6 month hindcasts of the T.80 model. The circles show the actual forecasts and the lines between them are to provide visual continuity.

Key	
Solid line	COADS data
Circles	6 month Hindcast

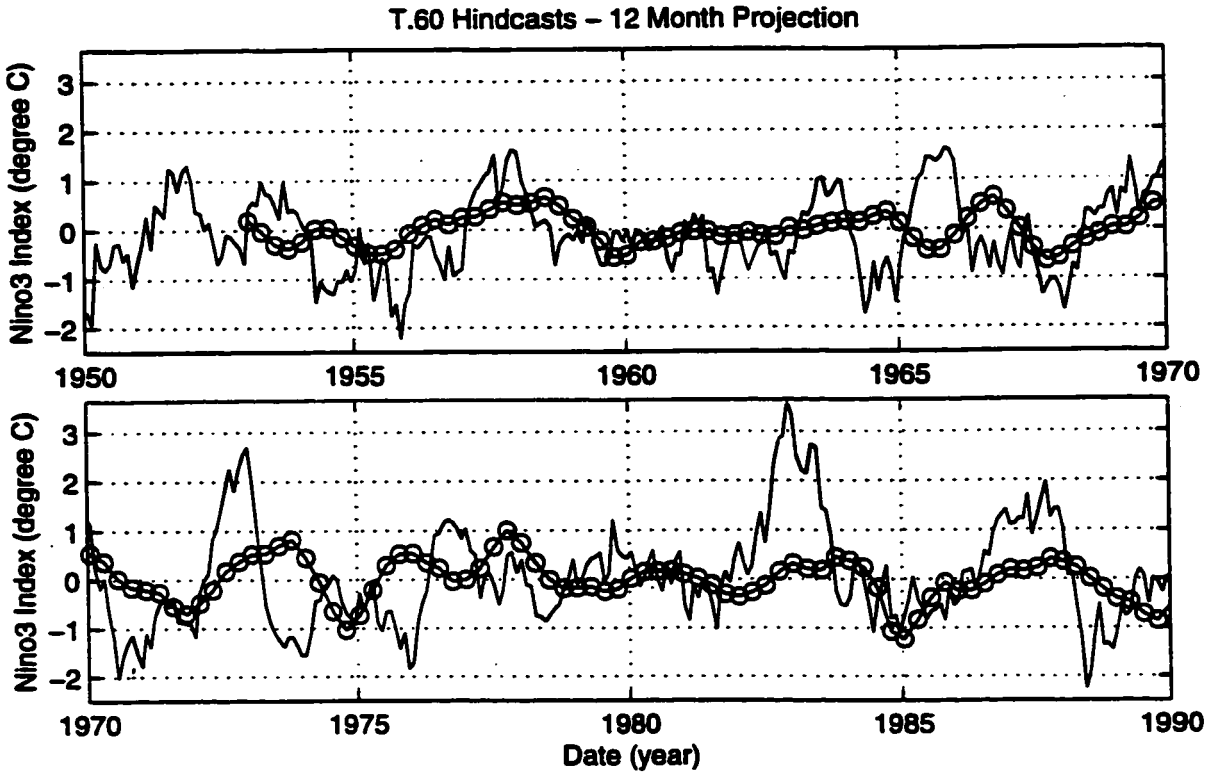

Figure 5.6 - T.60 Model 12 Month Hindcasts vs. Data. Plot of Nino3 index for COADS data and for the 12 month hindcasts of the T.60 model. The circles show the actual forecasts and the lines between them are to provide visual continuity.

Key	
Solid line	COADS data
Circles	12 month Hindcast

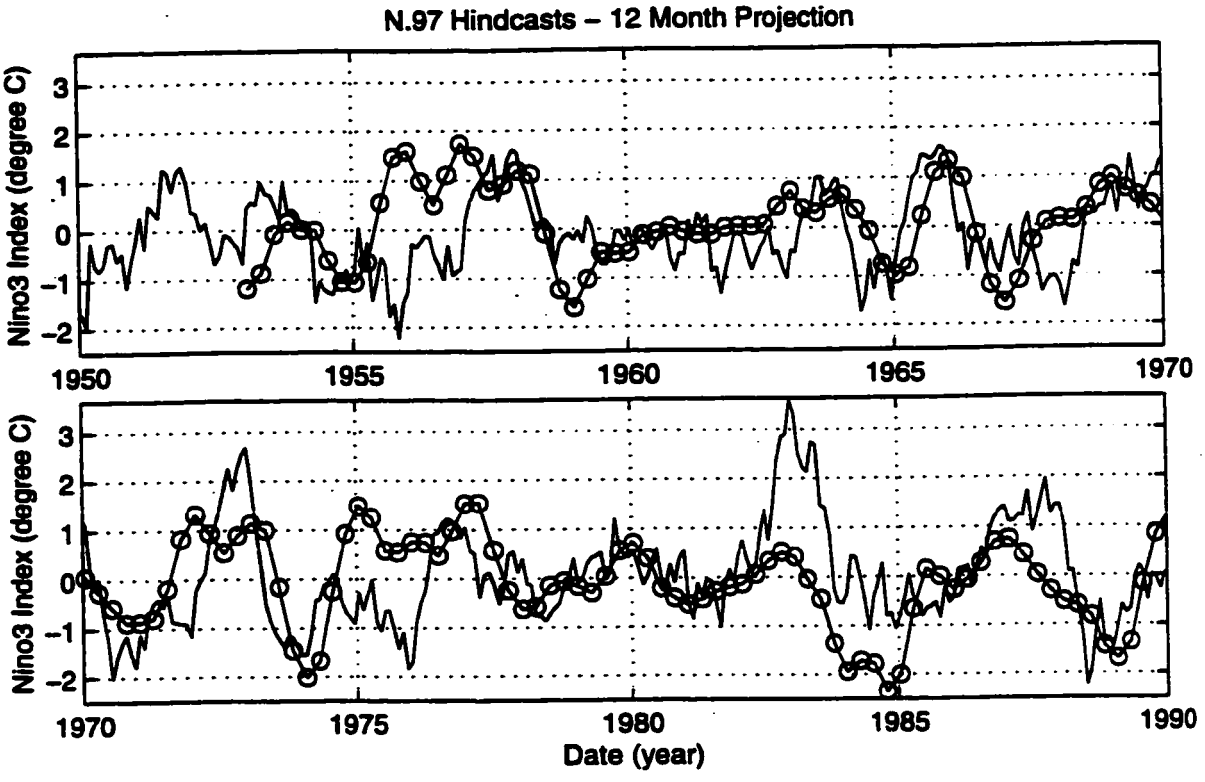

Figure 5.7 - N.97 Model 12 Month Hindcasts vs. Data. Plot of Nino3 index for COADS data and for the 12 month hindcasts of the N.97 model. The circles show the actual forecasts and the lines between them are to provide visual continuity.

Key	
Solid line	COADS data
Circles	12 month Hindcast

Chapter 6: Stochastic ENSO Simulations

6.1 Stochastically Perturbed Runs

The four different models will now be driven stochastically, and the results examined, to show whether or not they produce irregular ENSO events in a manner similar to the real Pacific ocean. Three different methods will be used to generate the noise perturbations. (i) The components of the spectral decomposition of the SSTA field will be perturbed with a random normal distribution. (ii) The EOFs of the COADS SSTA data will be determined from 42 years of observational data, and a "noise" time series will be generated by discarding the higher order EOFs. The model is then perturbed by choosing *at random* from the "noise" time series. (iii) A patch of ocean in the western Pacific is perturbed with a random magnitude Kelvin wave (normally distributed).

In all cases, the model is randomly perturbed - not randomly forced. At every timestep, the new state is first determined by the model, and then a random field is added to it. In the first two cases above, only the SSTA field is perturbed, while in the third case only the ocean is perturbed. Remember that in LOAM, the winds are always in equilibrium with, and determined by, the SSTA, and thus are also perturbed. Likewise, the ocean perturbation includes both the thermocline and currents.

6.1.1 SSTA Noise - Normal Distribution

Each of the four candidate models was run through a 200 year simulation, where at each timestep of 15 days, the SSTA field was perturbed through the addition of a randomly generated SSTA field. Several tests where then performed on the time series produced by each model, and the results compared with the same tests done on the COADS data.

The random perturbations in this case are produced by setting each of the

(spectrally and spacially discretized) components of the model's SST field to a random number with a normal distribution. See Appendix D for the discretization scheme. The amplitude of the random numbers was set differently for each model, depending on the model's sensitivity to the noise. First, the 200 year run was made with an arbitrary scaling for the random numbers, and then the scaling was changed so that the maximum amplitude of the Nino3 index would be exactly 3 degrees for the sample run. For all four models (and the sample runs) the random number generator was started with the same seed. So for all the runs, the random fields which generated them have exactly the same shapes, but different amplitudes as determined by each model's sensitivity. All runs were started with all fields initially set to zero.

Table 6.1 - Standard Deviation of Normally Distributed Noise. The standard deviations of the noise used to drive each of the candidate models. The distribution in space of the standard deviation will be of the form found in Fig. 6.1b. These numbers represent the spacial maxima of the standard deviations from Fig. 6.1b.

Model	N.97	T.97	T.80	T.60
Max Std. (deg.)	0.19	0.11	0.18	0.27

Figure 6.1a gives an example random SSTA field (for the T.97 model). Figure 6.1b shows the spacial distribution of the standard deviation for the noise over the 200 year run for the T.97 model. Since the same random numbers were used for each of the four different models, the distribution of the other models will have the same shape as the T.97 distribution. The maximum amplitude of the standard deviation for each of the models is shown in Table 6.1. From Figure 6.1b it can be seen that the noise is distributed uniformly over most of the basin, and drops off poleward of 10 degrees (where the Hermite functions start decaying to zero). As seen from Table 6.1, none of the models require much noise to produce ENSO events of realistic amplitude. The least

sensitive of the models, T.60, requires noise with a maximum standard deviation of only 0.27 degrees C to achieve a maximum ENSO event with a peak temperature of 3 degrees C.

The time series of the Nino3 index for the first 100 years of the simulations are shown in Fig. 6.2, along with the 42 years of COADS data. Even without any sophisticated tests, the increasing irregularity of the models from N.97 to T.60 is apparent. That is, the irregularity increases with increasing TMR - see Table 5.9. Note that all of the models, which start at rest, "spin-up" fairly quickly, producing their first ENSO event within 7 years.

As might be expected because of their nearly neutral ENSO modes, both N.97 and T.97 display unrealistically long periods of regular ENSO events. Around year 45, both the N.97 and T.97 models enter long lasting quasi-regular ENSO oscillation regimes. In the N.97 model this regime persists at least 55 years, while in the T.97 model the regime persists for about 20 years. The more damped models, T.80 and T.60, show no such long term ENSO oscillation regimes, but do show individual events that persist through at least two years.

Looking at the 100 year sample, it might appear that the linear models produce a similar bias toward warm events as the real Pacific ocean. This *is not* the case - the slight bias toward warm events in this sample is coincidental. LOAM is by definition linear and therefore unable to incorporate the warm bias built into other intermediate models. The other obvious difference between the candidate models and the COADS data is the high frequency component (noise maybe) in the Nino3 index. LOAM intentionally emphasizes the long wavelength, low frequency physics of the coupled system and so none of the candidate models will show an internally generated high frequency signals. The twice-monthly imposed noise in the LOAM simulations is required to produce a high frequency signal. And much effort has been expended to reduce the size of that

imposed noise. See the parameter studies in Chapter 5. Also, LOAM has no measurement noise, which might account for the COADS noise, and is not of interest to this modeling study.

Figure 6.3 shows the power spectra of the Nino3 index for the four different simulations and the COADS data. The spectral analysis of the four models was performed on the second 100 years of the test runs. As might be expected from the time series, Fig. 6.2, the N.97 and T.97 show a strong peak at (or near) the period of the ENSO mode for each model. Table 6.2 gives the periods for the peak frequencies for comparison with the ENSO mode periods listed in Table 5.9. Models N.97 and T.97 also show a distinct secondary peak (local maximum) at around 1.5 years. This secondary peak is part of the ENSO mode and will be discussed more in Section 6.2.

Table 6.2 - Normal Power Spectra Peak Values. The period of the peak frequency in the power spectrum (Fig. 6.3) for each model plus the COADS data. Also included are the periods of the second local maximum for N.97, T.97 and T.80, and the second highest peak for the T.60 model. See text for explanation.

Model	N.97	T.97	T.80	T.60	COADS
Peak Period (yrs)	2.90	3.39	3.63	6.06	3.50
2nd Local max (yrs)	1.53	1.41	1.38	N.A.	2.10
2nd and 3rd highest Peaks (yrs)	N.A.	N.A.	N.A.	3.64 4.88	N.A.

The spectrum of model T.60 is quite different from T.97 and N.97. It is broad, lacking the distinct peaks of the first two models. Its peak period is 6.06 years - somewhat longer than its ENSO period of 4.54 years. However, the second and third highest peaks, which are almost as large as the first, are at 3.64 and 4.88 years, respectively. So T.60 can be interpreted as having a spectrum which broadly straddles the ENSO mode period. There is no obvious secondary local maximum as found in T.97

and N.97.

The spectrum of T.80 is a mixture of the broad spectrum of T.60 and the "peakier" spectrum of T.97 and N.97. The highest peak is near its ENSO mode period of 3.85 years, but the peak is not nearly as distinctive as it is in T.97 and N.97. The secondary local maximum is there also, but it too is not as distinctive as in T.97 and N.97. Altogether the T.80 model seems to do the best job of the four candidate models at the matching the COADS spectrum. While T.80 does not have as broad a spectrum as COADS, they both peak at about the same frequency. T.60 peaks at too low a frequency.

As discussed in Section 4.2, the real ENSO system has a tendency to peak during the winter months, and this tendency can be quantified by taking the standard deviation of the monthly mean SSTA in Nino3. Figure 6.4 shows the standard deviation of the Nino3 index for each of the candidate models by month. As was hypothesized in Section 4.2, the LOAM models show greater variation during the winter months even though they are uniformly forced (perturbed) in time. All of the models have qualitatively the same standard deviation curves - with a maximum in January and a minimum in June. The COADS curve is included for reference. The COADS data peaks in December, and has its trough in March/April. All of the models except T.80 have too high a variability over most of the year. T.80 has about the correct average variability, but its trough is not located at the correct time of year. Of course, the total variability of any of these models can be changed by altering the amplitude of the noise forcing which was (somewhat) arbitrarily set so that the maximum ENSO event over the 200 year simulations would be exactly 3 degrees.

6.1.2 SSTA Noise - Higher Order EOFs

Another set of 200 year simulations was run using noise derived from the COADS dataset. The noise fields were derived by first finding the Empirical Orthogonal

Functions, EOFs, of the COADS time series and then recreating the time series with the higher order EOFs removed. This time series of the lower order EOFs was taken to be noise. When the candidate models were run, a perturbation to the SSTA was made once a month by selecting, at random, from the noise time series. Note that the COADS data set gives the SST in monthly increments. For each model, the number of EOFs removed was the number that caused that model to produce a maximum ENSO event of around 3 degrees C. For consistency, the simulations were then rerun with the noise multiplied by a constant which made the maximum SSTA reach exactly 3 degrees.

Table 6.3 - Standard Deviation of EOF Noise. Shown here is the number of EOFs dropped from the COADS data to generate the noise time series for each model, and the percent variance explained by those EOFs, along with the multiplier required to make the maximum SSTA exactly 3. The last row is maximum standard deviation contained in a pattern similar to Fig. 6.5b, which is for the T.97 case in particular.

Model	N.97	T.97	T.80	T.60
EOFs Dropped	12	14	10	9
% Variance of Dropped EOFs	93.1	94.9	90.8	89.4
Multiplier	0.99	0.89	0.84	1.01
Max Std. (deg.)	0.21	0.16	0.25	0.30

Table 6.3 shows the number of EOFs dropped for each candidate model, along with the percent variance explained by those EOFs. In all cases, the dropped EOFs explained about 90 to 95 percent of the total variance, and so the remainder of the EOFs can reasonably be considered noise. Even though the same sequence of random numbers was used for all runs, and unlike the normal noise distribution (NND) case from Section 6.1.1, the different models were not perturbed using the same noise patterns. This is a consequence of eliminating a different number of EOFs for each model.

Figure 6.5a shows an example noise field (for the T.97 model) and Fig. 6.5b shows a contour map of the standard deviation over the basin for noise used in the 200 year simulation (for T.97). Since the COADS data was first projected onto the Hermite functions used to discretize LOAM, the noise amplitude drops to zero outside the equatorial region- similar to the NND case. The noise is distributed less uniformly than in the NND case, but the average value of the standard deviation in the equatorial region is about the same - compare with Fig. 6.1b. The maximum standard deviation over the entire basin is listed in Table 6.3 to give an idea of the size of the noise fields for the different models.

Table 6.4 - EOF Noise Power Spectra Peak Values. The period of the peak frequency in the power spectrum (Fig. 6.7) for each model plus the COADS data. Also included are the periods of the second local maximum for N.97, T.97 and T.80, and the 2nd and 3rd highest peaks for the T.60 model.

Model	N.97	T.97	T.80	T.60	COADS
Peak Period (yrs)	2.86	3.39	3.77	7.41	3.50
2nd Local max (yrs)	1.54	1.41	1.36	N.A.	2.10
2nd and 3rd highest Peaks (yrs)	N.A.	N.A.	N.A.	5.26 4.44	N.A.

The Nino3 index for the first 100 years of the simulations is shown in Figure 6.6. Qualitatively, this set of runs is similar to the NND runs of Section 6.1.1, with the irregularity increasing with increasing TMR. The spectra for the EOF noise runs are shown in Fig. 6.7, and Table 6.4 lists the periods of various peaks for the spectra. All the models produce a spectrum very similar to the ones generated by the NND cases. N.97 and T.97 show the same primary and secondary local maxima as in Fig. 6.3a and 6.3b. As in the NND case, the T.60 model has a much broader peak in its spectra with no

obvious 2nd local maximum. From the table it can be seen that the range of the broad maximum in the spectrum of T.60 (as quantified by the periods of the three highest peaks) is at lower frequency than in the NND case. The T.80 case once again displays a mixture of the characteristics of the other models, with discernible primary and secondary local maxima, and having much broader peaks than N.97 and T.97.

Figure 6.8 shows the standard deviation of Nino3 by months for the 200 year simulations driven by EOF noise. The result is qualitatively similar to the NND case, except that here all the models have nearly the same standard deviation. All four models peak at about 1.1 degrees C, as does the COADS data. However, unlike the COADS data which has its minimum standard deviation of about 0.5 degrees in March, the LOAM models have their minima in June with magnitudes around 0.7 degrees.

6.1.3 Ocean Noise - (Structured Noise Forcing)

The previous two simulations used SST perturbations to drive the model. In this section the ocean (i.e. the r-fields) will be perturbed to drive the four candidate models. With the SST, a large historical set of data allows for some statistical analysis to determine reasonable noise forcing - as was done in the EOF noise runs. No such data set yet exists of the thermocline. The TOGA-TAO array has been producing some sparse data, but only for about the last 10 years (Hayes et al., 1991). There is, however, the suggestion that the winds of the Madden-Julian Oscillation (MJO - Madden and Julian, 1971), by stimulating Kelvin waves in the western equatorial Pacific, may have an effect on ENSO .

The LOAM models were therefore forced by adding Kelvin wave perturbations to the western Pacific during the 5 months when MJO is thought to be most active - from December through April. (See Salby and Hendon, 1994). What is needed is an estimate of the variability of the *anomalies* from the average annual cycle of the Kelvin waves produced by the MJO. Lacking this data, it has been assumed that the variability of the

anomalies will follow the variability of the MJO itself. The models were perturbed by adding a Kelvin wave of fixed shape, but random amplitude, once a month during the five active months. The random amplitudes were normally distributed, and all models were run with the same sequence of random numbers. As before, the perturbations were scaled individually for the candidate models such that the maximum amplitude on the Nino3 index would be 3 degrees C over a 200 year period. The shape of the thermocline portion of the perturbation is shown in Fig. 6.9. The scaling used for each model is given in Table 6.5 as the maximum of the standard deviation which would be found in Fig. 6.9b for that model.

Table 6.5 - Standard Deviation of Thermocline Perturbation. Shown for each model is the standard deviation of the peak thermocline perturbation (in meters) for the noise used in the ocean noise simulations.

Model	N.97	T.97	T.80	T.60
Max Std. (m)	4.7	4.4	7.1	9.3

The Nino3 index for the first 100 years of the simulations are shown in Fig. 6.10. As before, the models increase in irregularity from N.97 to T.60, although T.80 and T.60 look quite similar. The power spectra of the Nino3 index for the simulations are shown in Fig. 6.11, while Table 6.6 lists some of the important peaks for the spectra. Despite the very different forcing used for these runs, the spectra share almost all the same characteristics of the two previous noise schemes. One interesting exception is that the peak period for T.80 has gone down, while the peak period for T.60 has increased - making the two models look similar. The T.60 model still has a broader peak than T.80, although for both models the six highest peaks cluster over almost the same range, (See Table 6.6).

One interesting difference between the ocean noise forcing and the previous

forcing regimes is found in the monthly standard deviation of Nino3 - Fig. 6.12. Unlike the COADS data, the NND and EOF forcing produce monthly standard deviations which peak in January or December and bottom out in June. The ocean forcing, which is not uniform in time, peaks instead in November and bottoms out in May - at least for the T.80 and T.60 models. The monthly standard deviation of the N.97 model looks like those of previous models, while T.97 has its peak and trough somewhere between the N.97 and T.80. The shifted graphs do not more closely resemble the COADS monthly standard deviation which is asymmetric - with its maximum in December and minimum in March - but this shift does demonstrate that the model statistics are being affected by the forcing. The models with an increased sensitivity to noise (i.e. with a larger TMR) shift by a larger amount.

Table 6.6 - Ocean Noise Power Spectra Peak Values. The period of the peak frequency in the power spectrum (Fig. 6.11) for each model plus the COADS data. Included are the periods of the second local maximum for N.97, T.97 and T.80. Also listed is the range of the six highest peaks when applicable.

Model	N.97	T.97	T.80	T.60	COADS
Peak Period (yrs)	2.94	3.45	4.26	5.71	3.50
2nd Local max (yrs)	1.55	1.41	1.35	N.A.	2.10
Range of 6 Highest Peaks (yrs)	N.A.	N.A.	3.64 5.71	3.84 5.71	N.A.

6.2 Analysis of Stochastic Simulations

In Section 6.1, the results of stochastic runs of the four candidate models were compared using three different types of forcing. In general, a given candidate model responded similarly to each of the different types of forcing. A much greater variation

in behaviour was found between the different models, even when those models were forced with the same perturbations. In this section, the reaction of the models to the noise will be explored in more depth.

6.2.1 Nino3 Index Irregularity

Figures 6.2, 6.6 and 6.10 all show the Nino3 index for each of the models over 100 years of simulation. Each of the models shows some degree of irregularity - T.80, and T.60 in particular show variability similar to the COADS Nino3 index. Just looking at the Nino3 index, however, does not provide a sense of how the imposed perturbations cause the irregularity. Is a warm event caused by a single perturbation which just happens to be at the right time of the year and projects strongly onto the first singular vector? Or is the growth more likely to be the result of many perturbations added together? How important is the first singular vector pattern to the overall response of the model?

Since LOAM is linear, the exact contribution of each noise perturbation can be calculated: the amplitude of Nino3 and any point in time is just equal to the sum of all the perturbations that came before it. Figure 6.13 shows Nino3 for the first 12 years of the EOF noise-driven T.80 model (see Fig. 6.6d). The dotted line shows the Nino3 index of the total fields - i.e. it is the same as the first 12 years from Fig. 6.6d. The solid lines show the evolution of each of the monthly perturbations, propagated forward individually. When all of the solid lines are added together, the result is the dashed line.

From Fig. 6.13 it can clearly be seen that any given ENSO event is the result of many of the preceding perturbations. For example, the cold event occurring in year 3 has a magnitude of nearly 2 degrees, but no single perturbation contributes more than 0.5 degrees to the total. The warm events peaking in years 5 and 7 might be seen as counterexamples: they both have fairly large individual contributors, but notice that in year seven two large amplitude negative contributions counteract the large positive

perturbation. Here, the warm event occurs because in the mess of lines with amplitude below 0.5 C, there are a few more warm events than cold.

Another interesting example from Fig. 6.13 is the pair of cold events in years 9 and 10. The ENSO modes produced by LOAM are capable of producing events of the same sign in consecutive years - even in the pure ENSO modes. Look, for example, back at Fig. 4.1 in years 3 and 4, where a cold event spans two consecutive Januarys. However, the long cold event in Fig. 6.13 does not seem to be formed by one (or more) of these cold events - but rather by unrelated cold events occurring in subsequent years. One other interesting feature in Fig. 6.13 is the lack of a cold event in year 11. In that year the largest individual perturbation grows to a minus 1 degree C cold event, but it is more than offset by a number of individual warming perturbations.

Figure 6.14 shows the same type of graph as Fig 6.13, but this time for the first 12 years of the ocean perturbations regime. Recall that in this case, perturbations are added only in the months December through April, and that all the perturbations are of the same shape. While the total Nino3 signal looks irregular - the individual perturbations are quite uniform in shape. Their amplitudes vary, but the shape and spacing of the solid lines in Fig. 6.14 are relatively regular. Notice in Fig. 4.9c, that the optimals which are started in the first several months of the year all grow uniformly and peak between January 1st and February 1st. This is in contrast to September starts shown in Fig. 4.9b, which can peak as late as March, or even skip forward to the next December.

The second question of interest in this section is how important the singular vectors (or optimal structures) are to the stochastically forced models. To explore this, a simple experiment was performed. All the simulations from Section 6.1 were run again, but this time the perturbations were projected onto the τ-optimal before being added to the current model state. To simplify the calculations, the noise was projected onto a

single pattern, the (9,5)-optimal, instead of recalculating the pattern for each month. This is justified since in Chapter 4 it was shown that the shapes of the optimals for different months and τ are very similar. The seeds in the random number generators were kept consistent, so the SV-projected run could be compared directly to the nominal runs.

Figure 6.15 shows the results for the T.80 model driven by EOF noise. Shown are the original Nino3 index, as it appears in Fig. 6.6d, along with the SV projected Nino3 index. As can be seen in Fig. 6.15, the curves are nearly the same. This is despite the fact that all errors over the 200 years run are cumulative. Table 6.7 shows the correlation coefficient and the RMS error for all the models and noise schemes. Most of the correlation coefficients are around 0.90 or above and the RMS errors are 0.4 or below. This table indicates that the optimal initial conditions are the primary factor in determining the evolution of the stochastic models.

In general, in the more highly damped models the correlations are higher, and the RMS errors lower. This makes sense, since in the more highly damped models, any errors that occur will damp out more quickly. The other noticeable trend in Table 6.7 is that the NND has a lower correlation. The NND has the least structure in its noise forcing, and so likely projects on to the second singular vector more than the other two noise schemes. Note that the ocean forcing noise scheme perturbs the thermocline in the equatorial western Pacific which is a portion of the τ-optimal pattern for the thermocline (See Fig. 4.5).

Table 6.7 - Correlation and RMS Error of Noise Projected onto Tau-Optimal Below, for each of the different stochastic forcing cases, the correlation between the original 200 years Nino3 index, and the Nino3 index where only the noise projected onto the first singular value, is listed. Also the RMS errors for the SV projected runs are shown.

Correlation	**N.97**	**T.97**	**T.80**	**T.60**
NND	0.87	0.75	0.83	0.87
EOF Noise	0.96	0.92	0.96	0.98
Ocean Noise	0.95	0.94	0.97	0.97
RMS Error (deg C)				
NND	0.54	0.67	0.46	0.48
EOF Noise	0.26	0.40	0.25	0.22
Ocean Noise	0.32	0.28	0.21	0.19

6.2.2 Power Spectra

Figures 6.3, 6.7, and 6.11 show the power spectra produced by each of the models under the different forcing regimes. In each case, the N.97 and T.97 models showed a distinct pattern with a primary peak at almost the ENSO period for the model, along with a secondary peak at about 1.55 and 1.41 years respectively. T.80 showed the same general pattern, with the secondary peak at around 1.35 years, though the peaks were not as pronounced. An examination of a typical Nino3 index for a pure (neutralized) ENSO mode, as is given in Fig. 4.1, shows that even in a pure ENSO mode, more than a single frequency exists. (This was discussed in Chapter 4, and is in contrast to the time invariant background case from Chapter 3).

To see if the secondary peaks are just part of the ENSO mode, the ENSO mode for each of the models was run for 200 years and the power spectrum calculated. For this

calculation the ENSO modes were "neutralized" - that is, at every timestep the amplitude of the mode was increased just enough to compensate for the exponential decay in these damped models. The dashed lines in Figure 6.16 show the results. All three of the models show primary and secondary maxima at the same periods as the stochastically driven models. But interestingly enough, the T.80 and T.60 ENSO modes show the most distinct peaks, whereas the spectra of their simulations show the least distinct peaks.

The solution to this apparent paradox is found in a second experiment. The spectra of the same ENSO modes were determined, but in this experiment the ENSO modes were allowed to decay at their normal rates. In each case, the ENSO mode was initiated at the peak of a warm event and run for twenty years with no stochastic forcing. The spectra produced are shown as the solid lines in Fig. 6.16. While the spectra for T.97 and N.97 do not change very much, the peaks of the T.80 spectrum are greatly reduced and the peaks of the T.60 spectrum are almost completely gone. In fact, the decaying spectra of Fig. 6.16 look remarkably like their respective spectra from the stochastic runs. Since the stochastic runs consist mostly of decaying ENSO modes, this should not be surprising. Remember from Chapter 3 that the optimal initial conditions which drive these models develop quickly (3 months or less) into the ENSO mode.

6.2.3 Monthly Standard Deviations

Figures 6.4, 6.8 and 6.12 all show the standard deviation of the Nino3 index over the 200 year simulations, on a month by month basis. In Section 4.2 it was proposed that the tendency of the optimals to produce peaks during the winter months would cause the stochastic models to have larger variance during the winter. In Section 6.1 it was indeed shown that the stochastic models tended to peak during the winter - but is the nature of the optimals the reason? Referring back to Fig. 4.1, notice that like the

stochastically perturbed cases, the pure neutralized ENSO mode also has a tendency to peak in magnitude during winter. (Each January 1st is marked with a circle in Fig. 4.1).

To test this idea, a monthly standard deviation graph was produced for the neutralized ENSO mode of each of the four candidate models. Figure 6.17 shows the results. All four of the models have their highest standard deviation in November/December, and their lowest in June. The shape of the curves in Fig. 6.17 is about the same as for the stochastic runs, except the magnitude is about double. Since the pure ENSO modes produce events regularly, their variance should be higher than the variance of the stochastic simulations.

So what is the explanation for the annual variation of standard deviation graphs. Is it mostly due to the nature of the ENSO mode, or the nature of the transient growth? In fact, the reason is probably more fundamental: both the optimals and the ENSO mode tend to peak in the winter months due to favorable growth conditions from June through November (see Table 3.2).

6.2.4 Which Candidate Model Wins?

The four models derived in Chapter 5 and driven stochastically in Section 6.1 have been referred to as candidate models - but no judgement has yet been made about which model most closely matches observations. The choice of T.80 is fairly straightforward.

Both T.97 and N.97 are much too regular compared to observations, even with the added noise. This does not prove conclusively that a good stochastic model could not be nearly neutral, or even unstable. The main factor in determining the level of noise input to the models here was making sure that the models produced ENSO events of a reasonable size. Because the models produced by LOAM are linear, doubling the amplitude of the perturbations would only serve to double the amplitude of the output -

without increasing the irregularity. With a base model that had a regular, but unstable ENSO mode limited in size by non-linearities, it is plausible that irregularity could be increased by increasing the amplitude of the stochastic perturbations without necessarily making the ENSO events unrealistically large.

In choosing between T.60 and T.80, a decision is not as clear. Both produce reasonable-looking irregularity. Both produce spectra that look similar to the COADS spectrum. The T.80 spectrum is a bit too peaked, but has approximately the correct period for its ENSO mode. The T.60 spectrum is broad, like the COADS spectrum, but seems to have too long a period for its ENSO mode. The main factor in favor of T.80 as a more realistic parameterization is the hindcast results from Chapter 5, in which the T.80 model significantly outperforms T.60.

Of course, four models is hardly an exhaustive search of the infinite parameter space. Comparing the pure damped spectra from Fig. 6.16, to the COADS spectrum shown in Fig. 6.11a, it would seem that a model better than T.80 or T.60 would have damping somewhere between the two models, but with the spectral peak shifted to a higher frequency - perhaps even a little higher than T.80.

6.3 Limits of Predictability

Assuming that the above models reflect some of the physics of the real system, they can be used to estimate the predictability of the real system. Most of the studies on ENSO predictability have emphasised the idea that error in the initial conditions is the main source of forecast error (Chen, D. et al., 1995, or Chen Y.-Q., et al. 1997). However, Fig. 6.13 and Fig. 6.14 suggest something else: that the primary source of error is the random forcing which occurs between the prediction time and the forecast time. (This is also suggested by Kirtman and Schopf, 1997). This difference in emphasis can be explained by the differences in the models used by the researchers. Most previous

research has been done with the ZCM - a model in which the system irregularity is attributed to chaos, hence the concern about the sensitivity of the initial conditions. Kirkman and Schopf, however, use a slightly unstable non-linear intermediate model, which produces a regular periodic, ENSO mode. This model is made irregular by imposed random forcing.

6.3.1 Overall Predictability

A predictability experiment is conducted as follows, (i) generate a long sample run using each of the four models, (ii) use that same model to do hindcasts on the data where the data is "assimilated" perfectly by just taking the known state at the initial forecast time, (iii) do enough hindcasts to resolve the forecast skill. Using this method, a set of predictability limits can be generated: the model physics is perfect, the initial conditions are perfect- forecast errors are caused only by the noise, which is assumed to be unpredictable. In this study the same 200 year runs from the NND models of Section 6.1 were used.

Figures 6.18a and 6.18b show the correlation coefficient of the Nino3 index and the RMS error for each of the candidate models for prediction periods of up to 36 months. As it might be expected, the predictability is lower for the more damped (and therefore more irregular) models. At 24 months, for instance, the correlation coefficients for N.97 and T.97 are still both greater than 0.9, but T.80's correlation has dropped to about 0.6 and T.60's correlation has dropped to about 0.35.

These numbers can be compared to the correlation coefficients found by Chen et al. (1995) using the ZCM on the COADS data from 1972-1992 (their Fig. 3). Chen et al. were able to achieve about a 0.6 correlation at 24 months over this time period. This is almost the same predictive skill as the T.80 theoretical limit, and much greater skill than the T.60's theoretical limit of 0.35. This is another strike against the T.60 model. While it is possible that the ZCM might exceed the theoretical limit of predictability

over a short period of time, it is unlikely that chance would make the ZCM this much more successful at prediction than the T.60 estimate.

In the other measure of predictability, the RMS error, the Chen et al. (1995) forecasts are not as good. Over the same time period, their 24 month forecasts have an RMS error of a little over 1 degree C. The estimates of the predictability limit for RMS error at 24 months are 0.65 C and 0.92 C for the T.80 and T.60 models, respectively.

Figures 6.18c and 6.18d show the same RMS error data as in Fig. 6.18b except the data is normalized in two different ways. In Fig. 6.18c the RMS error for each model is divided by the RMS amplitude of the Nino3 index over the simulation. This correction is made in order to counteract the fact that the variance of the models is somewhat different - see Fig. 6.4. From Fig. 6.18c it can be seen that this correction does not change the order of the relative predictablities, though it does increase the RMS error of T.80 model relative to the other models. The second normalization is to divide the forecast length by the period of the ENSO mode for each model. This will correct the tendency for a longer period model to be more persistent, and therefore more predictable. Figure 6.18d shows that this correction does not change the relative order of predictability, in fact it increases the separation of the relative RMS errors since the longer period models are also the least predictable models (see Table 5.9).

6.3.2 Seasonal Predictability

Looking at the singular value maps of Chapters 4 and 5, the non-uniformity of the SVs suggests that there may be more to the story of these model's predictability than the long term average of predictability. The transient growth varies considerably throughout the year - shouldn't the predictability also vary? The "self forecasting" experiments from the previous section are further analysed in this section. The seasonal cycle of the predictability is studied by examining the RMS errors and

correlation coefficients as a function of start month and forecast length. This produced RMS error maps and correlation maps in the same vein as the SV maps. Figures 6.19 through 6.22 show the correlation maps for the four different models, while Figs. 6.23 through 6.26 show the RMS error maps. Note that the eight lines in the overall predictability Figs. 6.18a and 6.18b could be reproduced by taking these eight figures, and averaging the correlation and RMS error, respectively, over all the start months.

Looking at Fig. 6.19, quite a bit of structure is evident. Specifically, the correlations of forecasts that end in winter months are much higher than forecasts of the summer months. The dotted lines on Fig. 6.19a mark the combinations of start month and forecast length add up to a forecast of January 1st. Examine the June cross section - that is the cross section of forecasts that *start* in June. Here, the predictive capability starts at about 0.94 for a one month prediction and then increases to about 0.98 by months 3 and 4. It stays somewhat level between months 3 and 9, before declining steeply into month 12. This pattern repeats, but with the overall predictability dropping steadily. Note from the contour graph that any other start month would show this same basic pattern, except that peaks and valleys are shifted to correspond with winter and summer months, respectively.

So why this pattern? The answer lies more with the nature of the ENSO cycle than with the non-uniformity of the SV maps. Since ENSO mode tends to peak in winter, to get a good *correlation* in the winter it is important to get the sign of the prediction right - if the amplitude is close, then the correlation will be high. However, in this model during the late spring/early summer, the ENSO mode is generally in transition between warm and cold events. Here the amplitude will be close to zero, and the slope of the Nino3 index will be at its greatest. A minor misprediction of the timing of the transition will lead to a large misprediction of the amplitude with possibly even the opposite sign.

Although this effect is very obvious in the N.97 model, it is nonetheless a subtle effect. It is only because N.97 is so (unrealistically) predictable that this effect becomes apparent. The same effect can be observed in T.97 in Fig. 6.20, but the overall loss of predictability as the forecast length increases begins to mask the effect. For T.80, the most realistic model, the effect appears only as a single "cliff" in the correlation contour map shown in Fig. 6.21. The periodicity of the effect can be barely discerned in the second summer, and probably would not be observed anywhere but in a modelling study. Even in Fig. 6.22, the correlation map for T.60, the cliff is apparent, but it is completely gone by the second summer.

A structure in the RMS maps can also be accounted for by the annual cycle structure in the SV maps. Examine Fig. 6.26 which shows the RMS map for the T.60 model. For the longer forecast times, a yearly cycle is discernible: the predictability gets better for forecasts ending in the summer and worsens for forecasts ending in the winter. The explanation can be found in Fig. 6.18. By the time this model gets out to 18 months and beyond, it is making essentially random predictions, but because the variance of both the data and the model is small during the summer, the RMS error will be smaller. The effect is subtler for shorter forecast times, since the slope of the overall increase in RMS error is large. This effect is still obvious in the T.80 RMS error contour map shown in Fig. 6.25. Notice that the relatively steep slope of the overall RMS predictability loss during the first winter causes the peak of the seasonal RMS error cycle to appear shifted back by several months. The cycle still appears in the T.97 and N.97 RMS error maps shown in Fig. 6.24 and 6.23, respectively. However, it is mostly hidden until after the second winter.

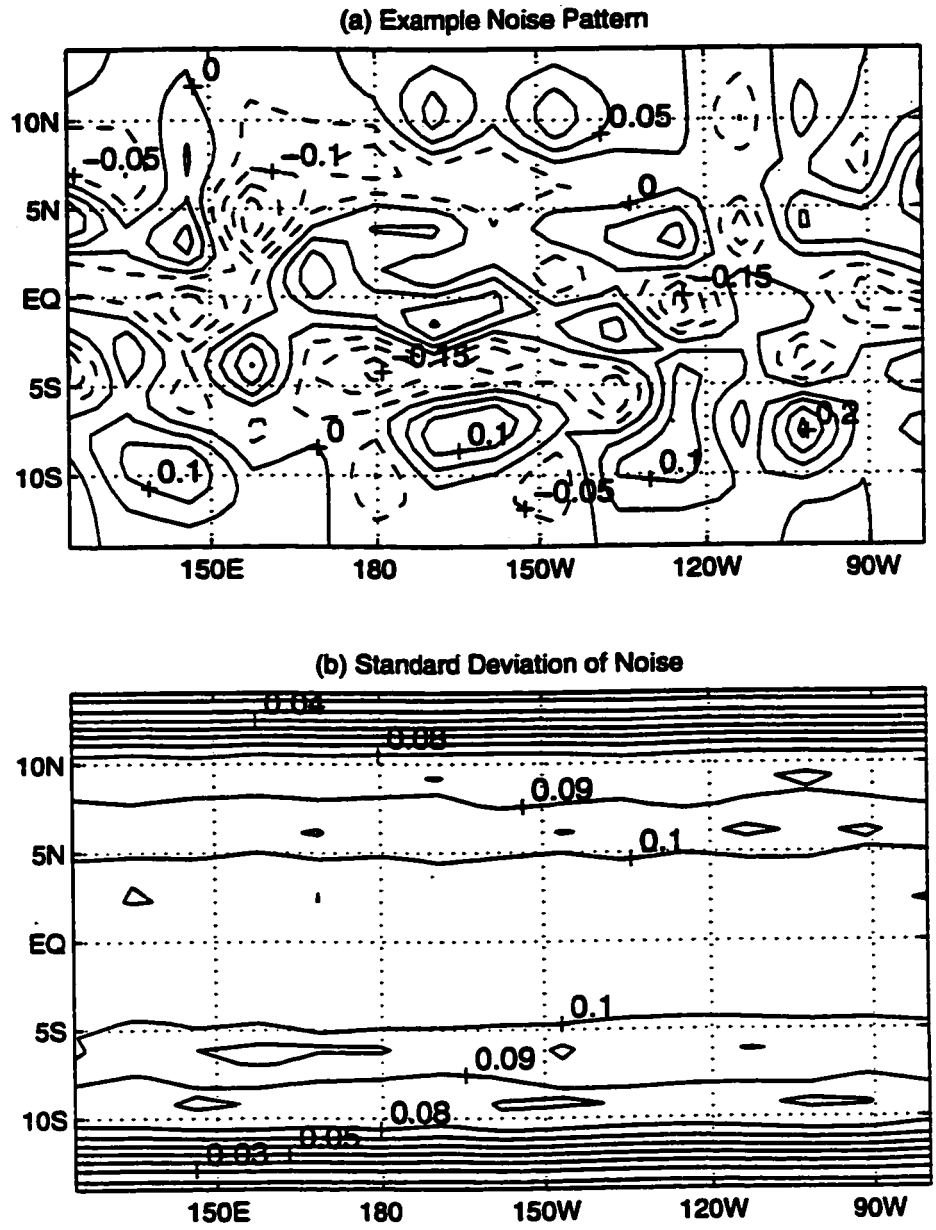

Figure 6.1 - Normal Distribution Noise Perturbation. Graph (a) shows a random example of noise perturbation field used for the normal distribution case. The field shown is of the correct amplitude for the T.97 model. Contour spacing is 0.05 degrees C. Graph (b) shows the spacial variation of the standard deviation of the noise used in the 200 year simulations, also for the T.97 model. Contour spacing is 0.01 degrees C.

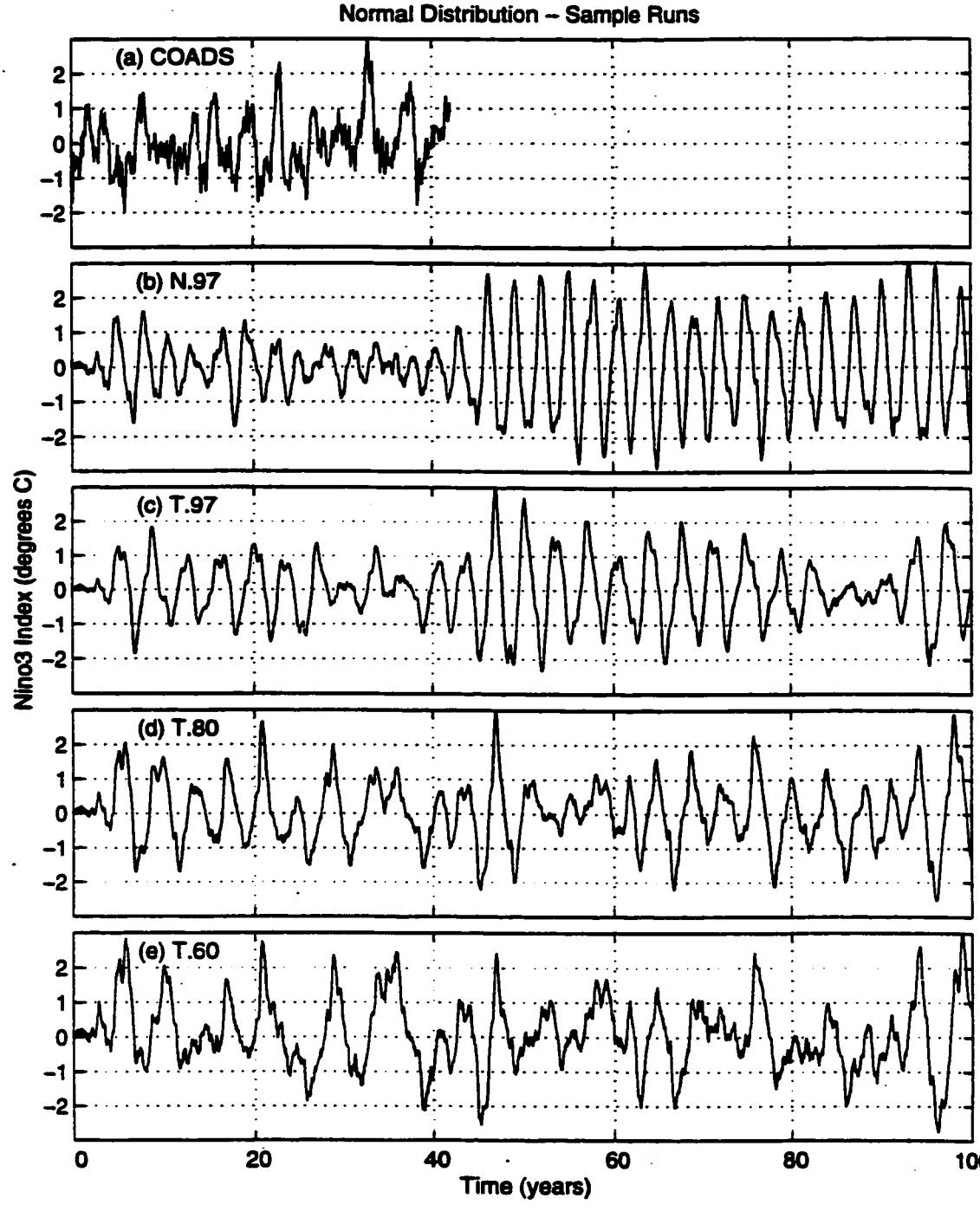

Figure 6.2 - Normal Distribution Simulation Runs. Graphs (b) through (e) show the Nino3 index of the four candidate models for the first 100 years of the simulation runs. Graph (a) shows the Nino3 index of the COADS data for reference.

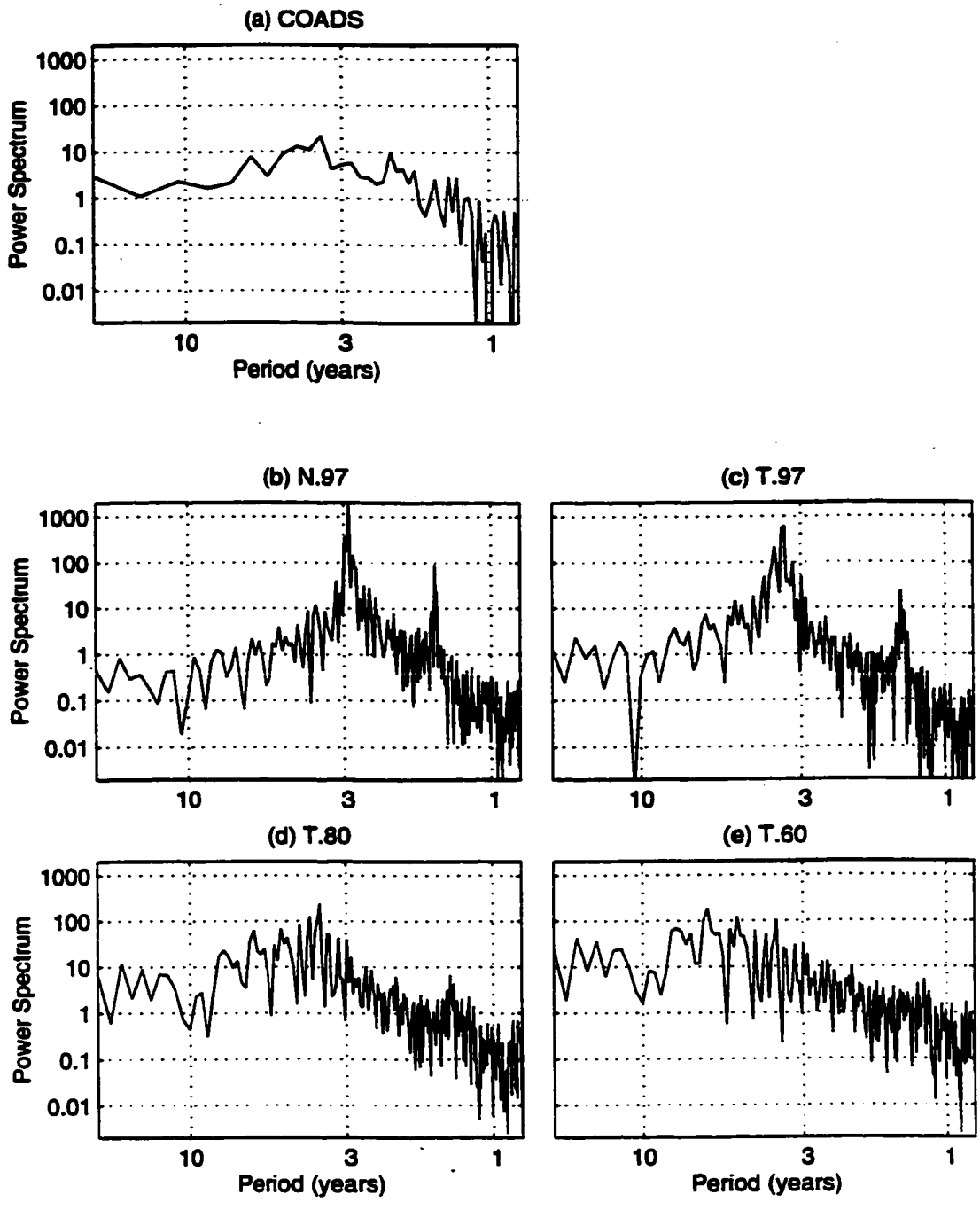

Figure 6.3 - Normal Distribution Power Spectra. Graphs (b) through (e) show the power spectrum of the Nino3 index of the four candidate models for the second 100 years of the simulations runs. Graph (a) shows the power spectrum of the COADS data for reference.

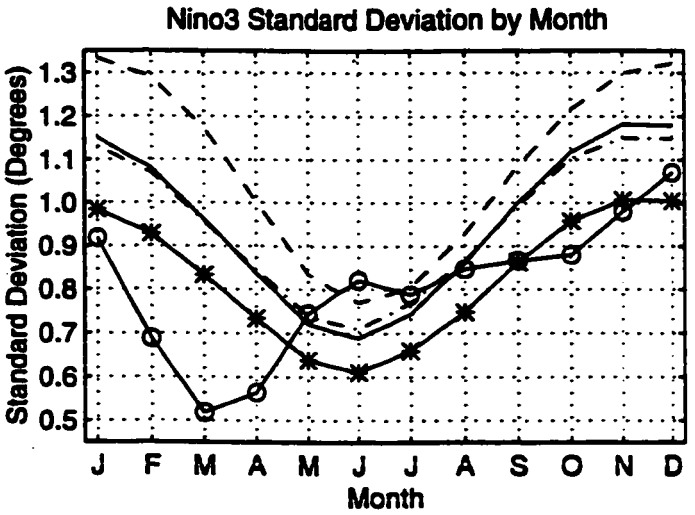

Figure 6.4 - Normal Distribution Standard Deviation by Month. The monthly standard deviation of the Nino3 index for each candidate model for the 200 year simulation. Also shown for reference is the same information for COADS.

Key	
Circles	COADS data
Dashed line	N.97
Solid line	T.97
Asterisks	T.80
Dot-dash line	T.60

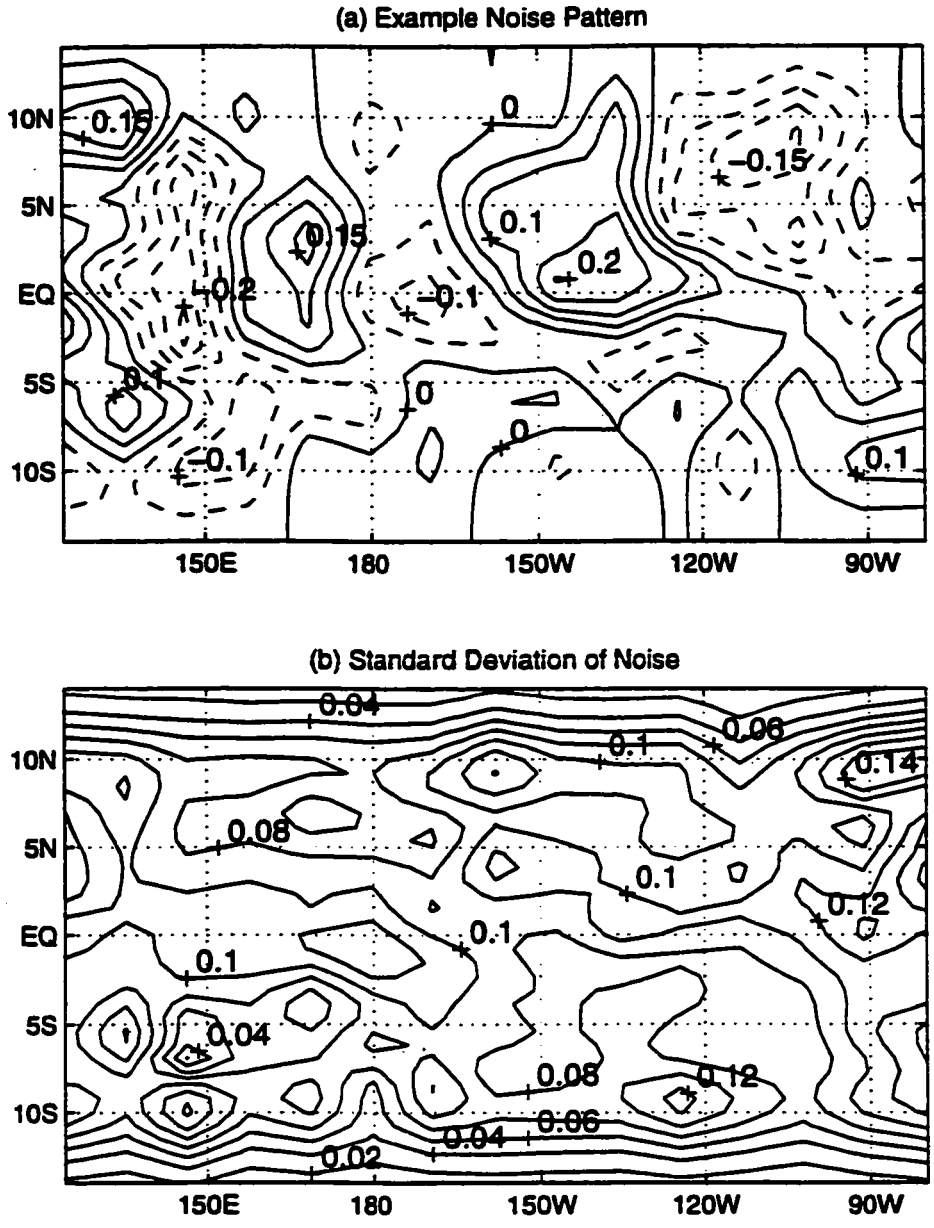

Figure 6.5 - EOF Noise Perturbation. Graph (a) shows a random example of a perturbation field used for the EOF noise case. The field shown is from the T.97 model simulation. Contour spacing is 0.05 degrees C. Graph (b) shows the spacial variation of the standard deviation of the noise used in the 200 year simulation, also for the T.97 model. Contour spacing is 0.02 degrees C.

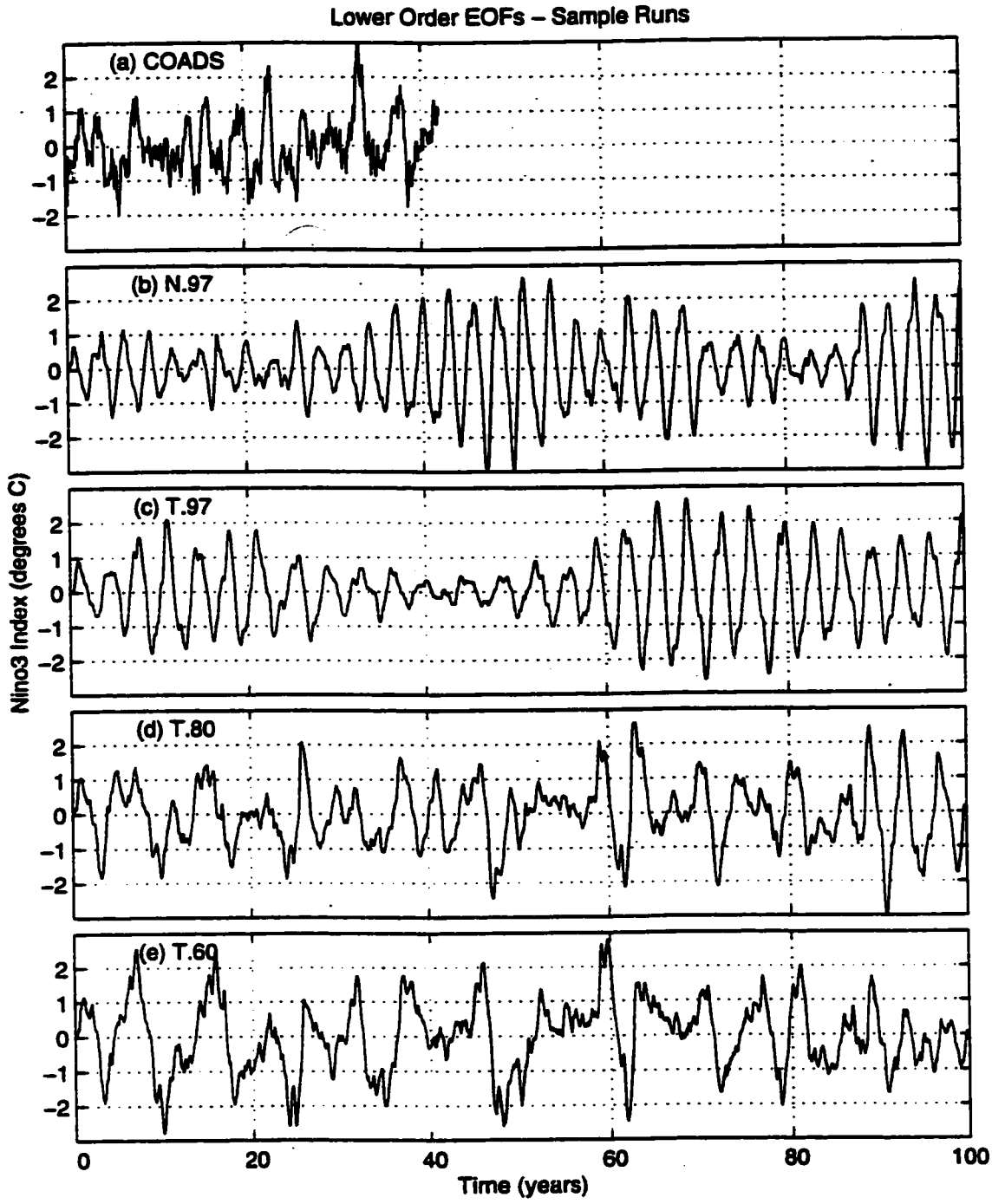

Figure 6.6 - EOF Noise Simulation Runs. Graphs (b) through (e) show the Nino3 index of the four candidate models for the first 100 years of the EOF noise simulation runs. Graph (a) shows Nino3 for the COADS data for reference.

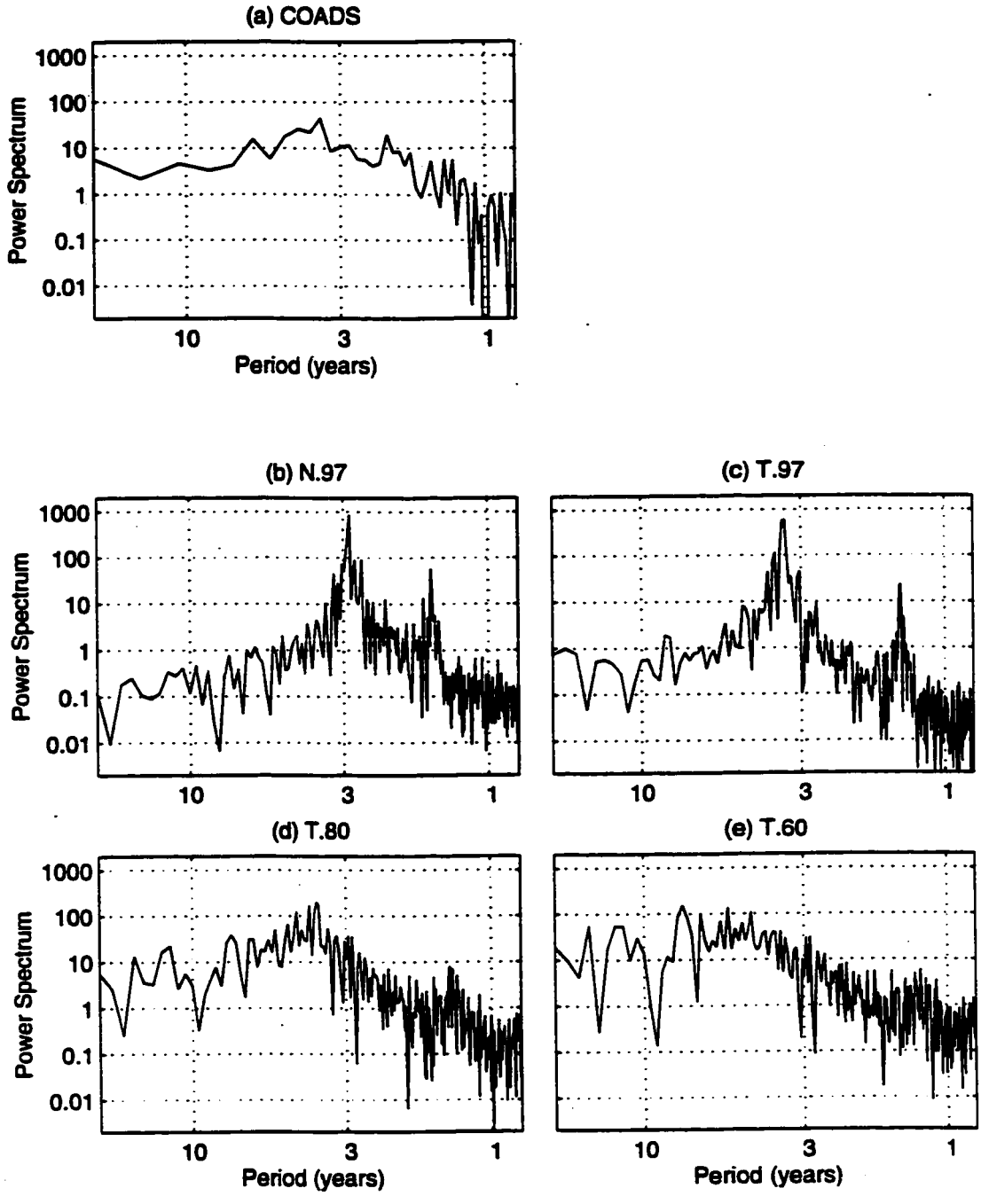

Figure 6.7 - EOF Noise Power Spectra. Graphs (b) through (e) show the power spectrum of the Nino3 index of the four candidate models for the second 100 years of the EOF noise simulations runs. Graph (a) shows the power spectrum of the COADS data for reference.

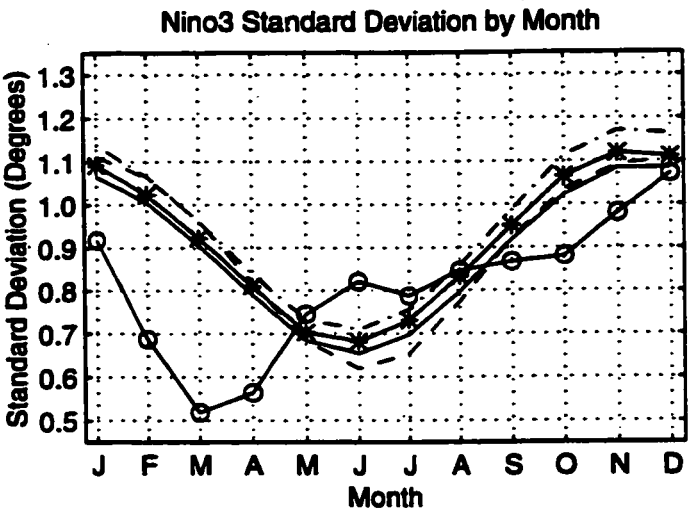

Figure 6.8 - EOF Noise Standard Deviation by Month. Shows the monthly standard deviation of the Nino3 index for each candidate model for the 200 year EOF noise simulation. Also shown for reference is the same information for COADS.

Key	
Circles	COADS data
Dashed line	N.97
Solid line	T.97
Asterisks	T.80
Dot-dash line	T.60

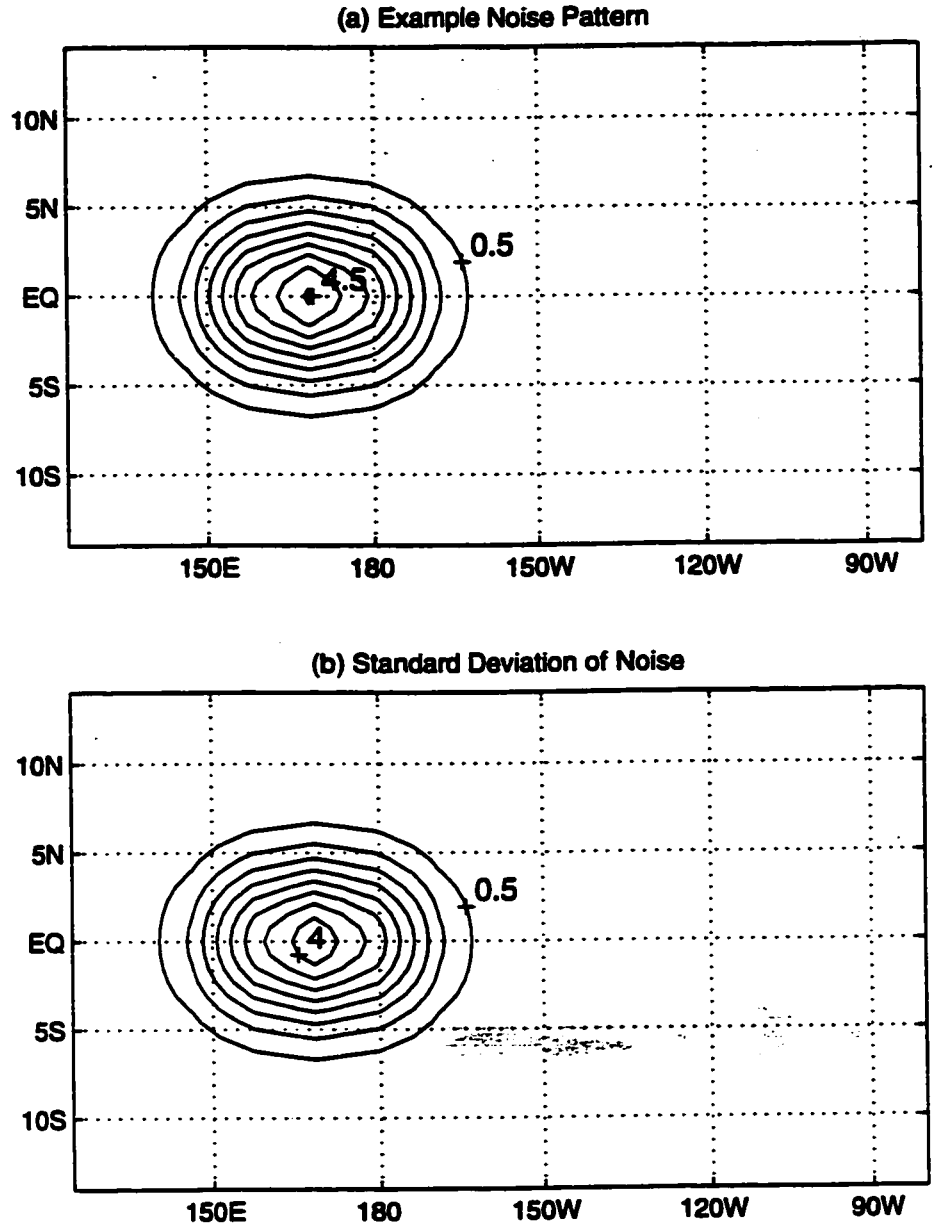

Figure 6.9 - Ocean Noise Perturbation. This figure shows the equivalent fields for the Ocean noise case as in Fig. 6.1 and Fig. 6.5 for the NND and EOF noise cases, respectively. Since only the magnitude of the field is random, and not the shape, both the "typical field" of graph (a) and the "standard deviation" of graph (b) look the same. The graphs shown are the correct size for the T.97 model. Contour spacing is 0.5 meters.

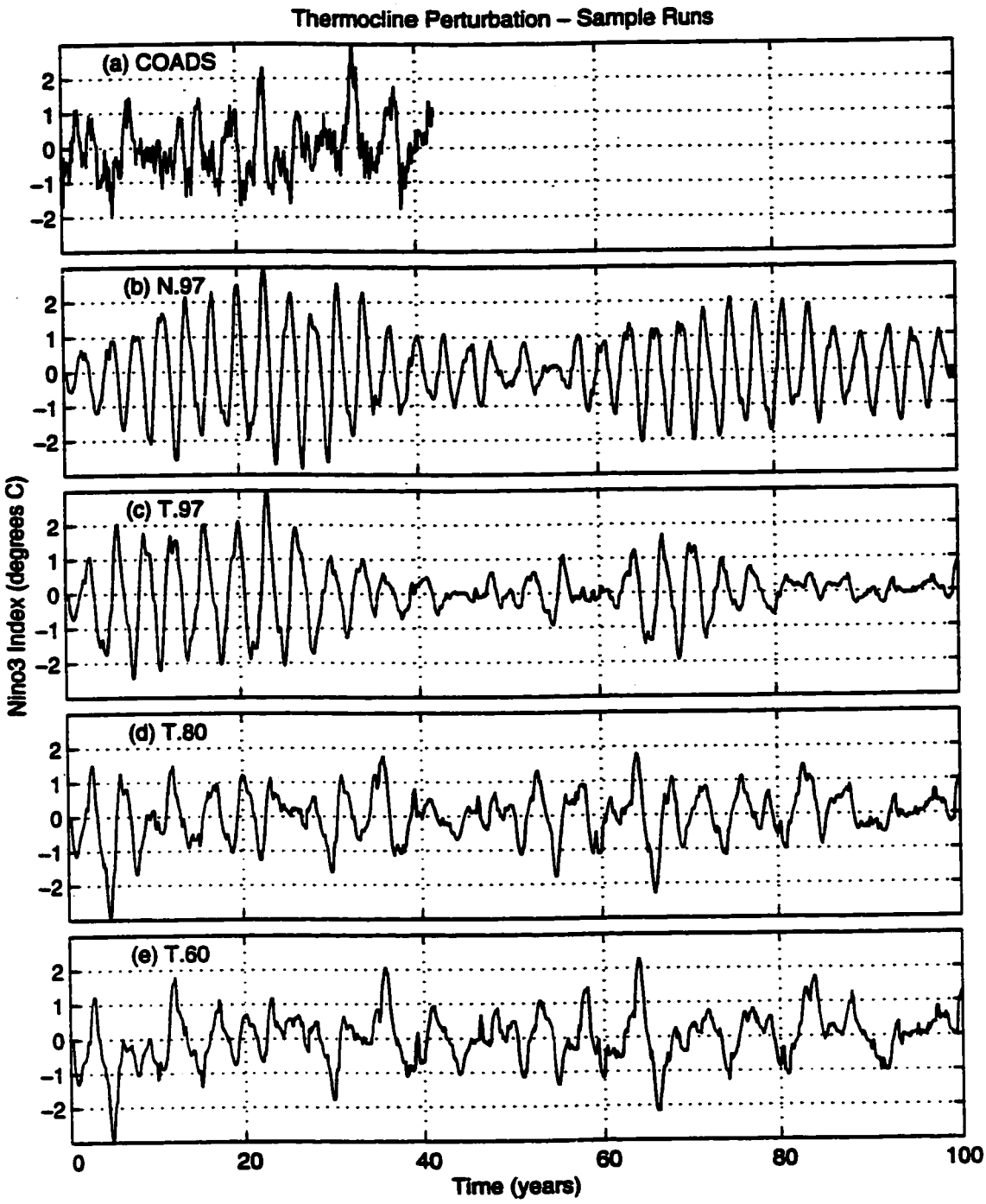

Figure 6.10 - Ocean Noise Simulation Runs. Graphs (b) through (e) show the Nino3 index of the four candidate models for the first 100 years of the Ocean noise simulation runs. Graph (a) shows Nino3 for the COADS data for reference.

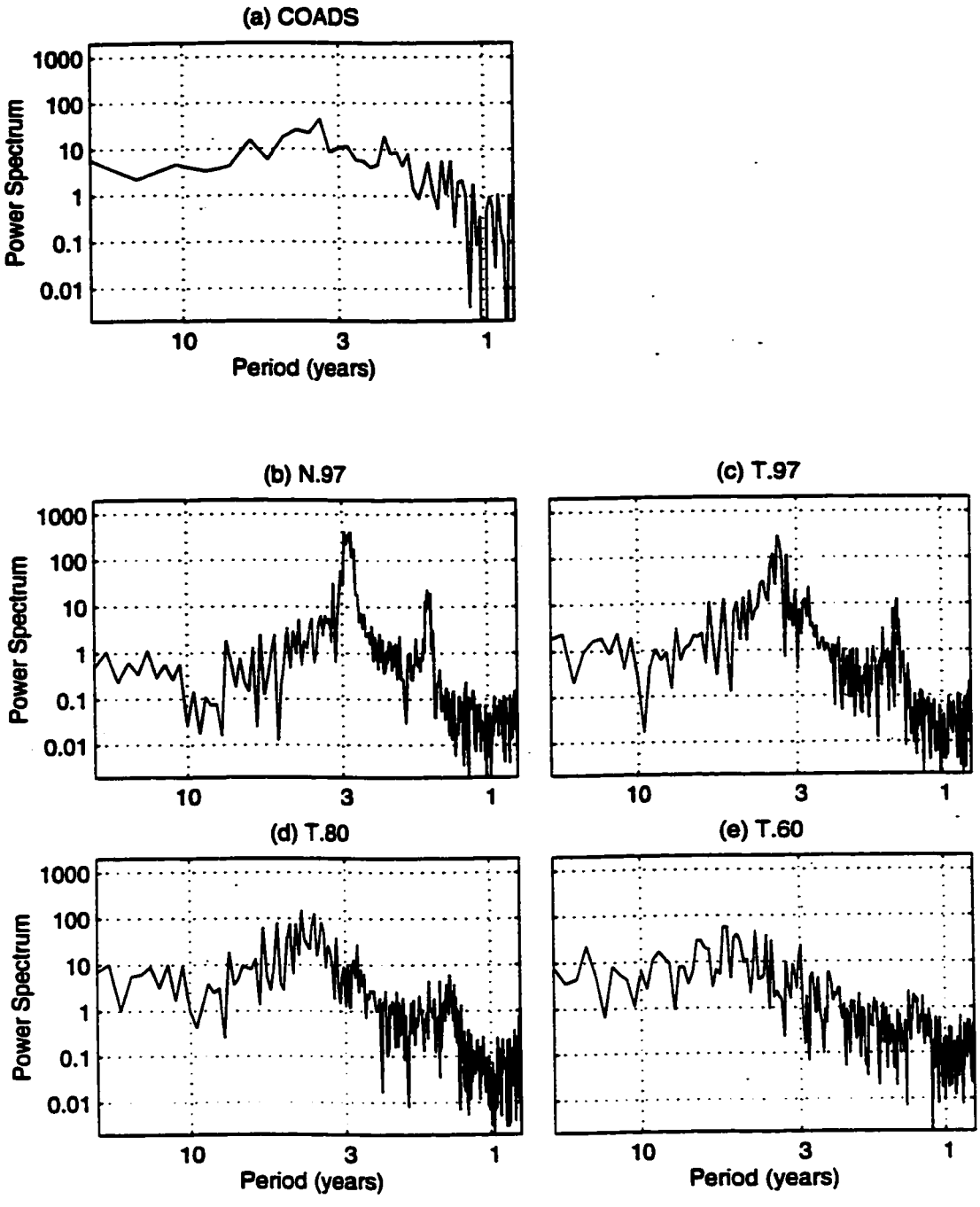

Figure 6.11 - Ocean Noise Power Spectra. Graphs (b) through (e) show the power spectrum of the Nino3 index of the four candidate models for the second 100 years of the Ocean noise simulations runs. Graph (a) shows the power spectrum of the COADS data for reference.

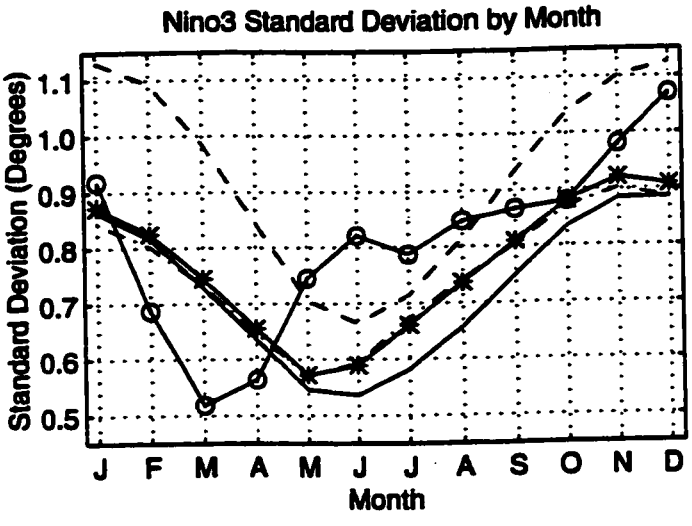

Figure 6.12 - Ocean Noise Standard Deviation by Month. Shows the monthly standard deviation of the Nino3 index for each candidate model for the 200 year Ocean noise simulation. Also shown for reference is the same information for COADS.

Key	
Circles	COADS data
Dashed line	N.97
Solid line	T.97
Asterisks	T.80
Dot-dash line	T.60

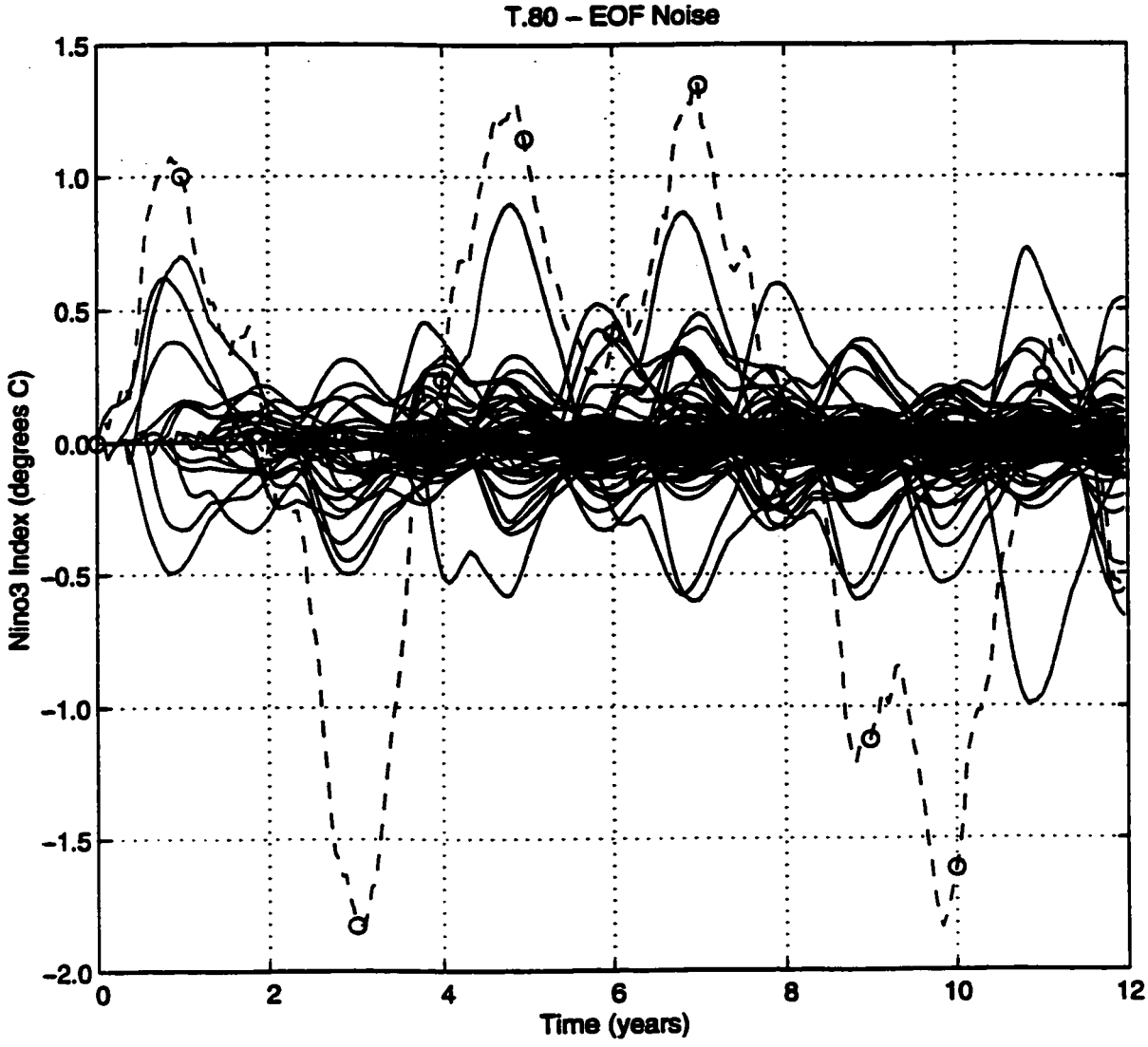

Figure 6.13 - T-80 - EOF Noise Components of Total Nino3 Signal. This graph shows the first 12 years of the EOF noise simulation for T.80, where in addition to the Nino3 index, the contribution to this index by each of the monthly perturbations is shown.

Key	
Dashed line	Total Nino3
Solid lines	Components

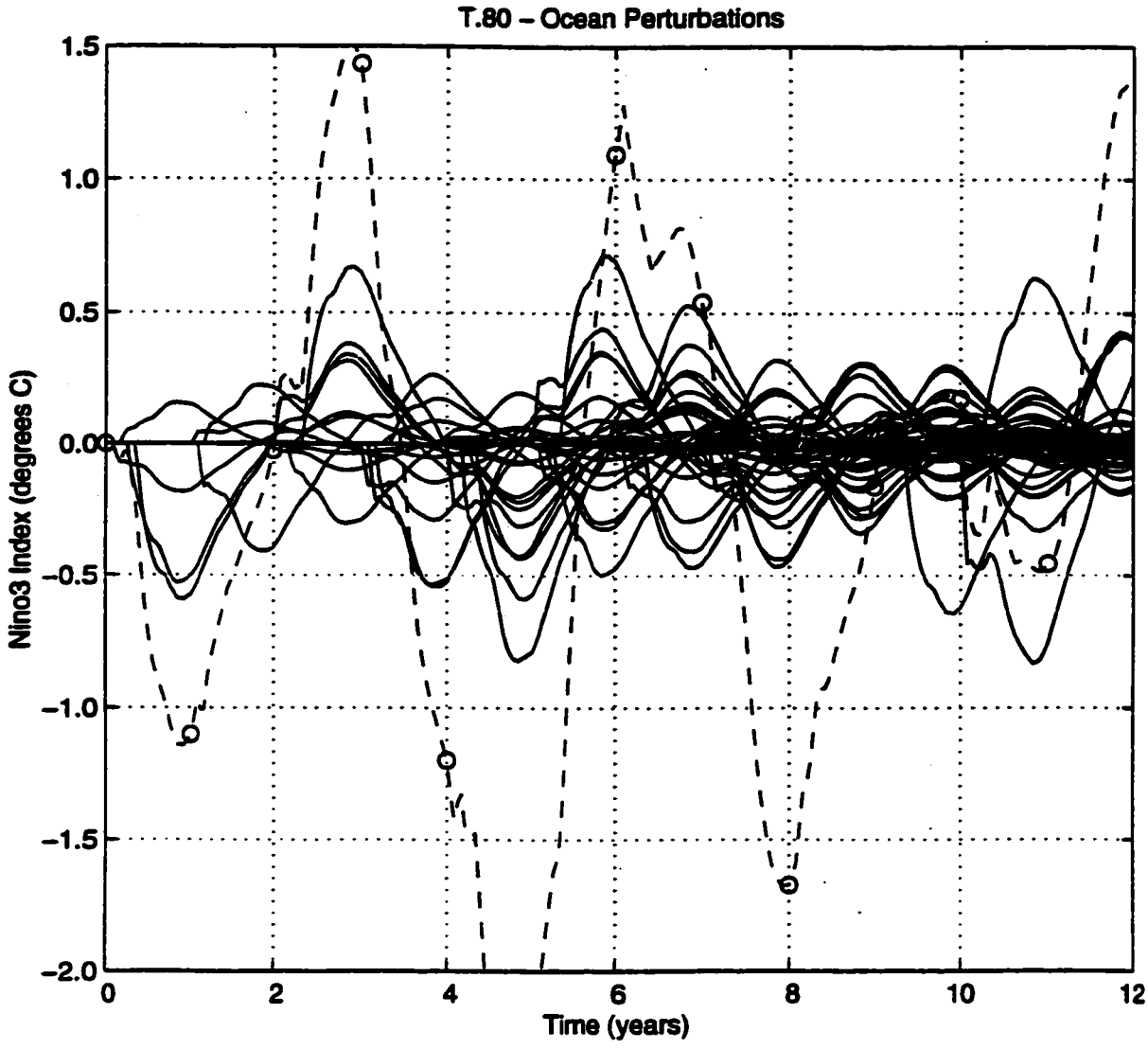

Figure 6.14 - T-80 - Ocean Perturbation Components of Total Nino3 Signal. Same as Fig. 6.13, except this time for the ocean noise case.

Key	
Dashed line	Total Nino3
Solid lines	Components

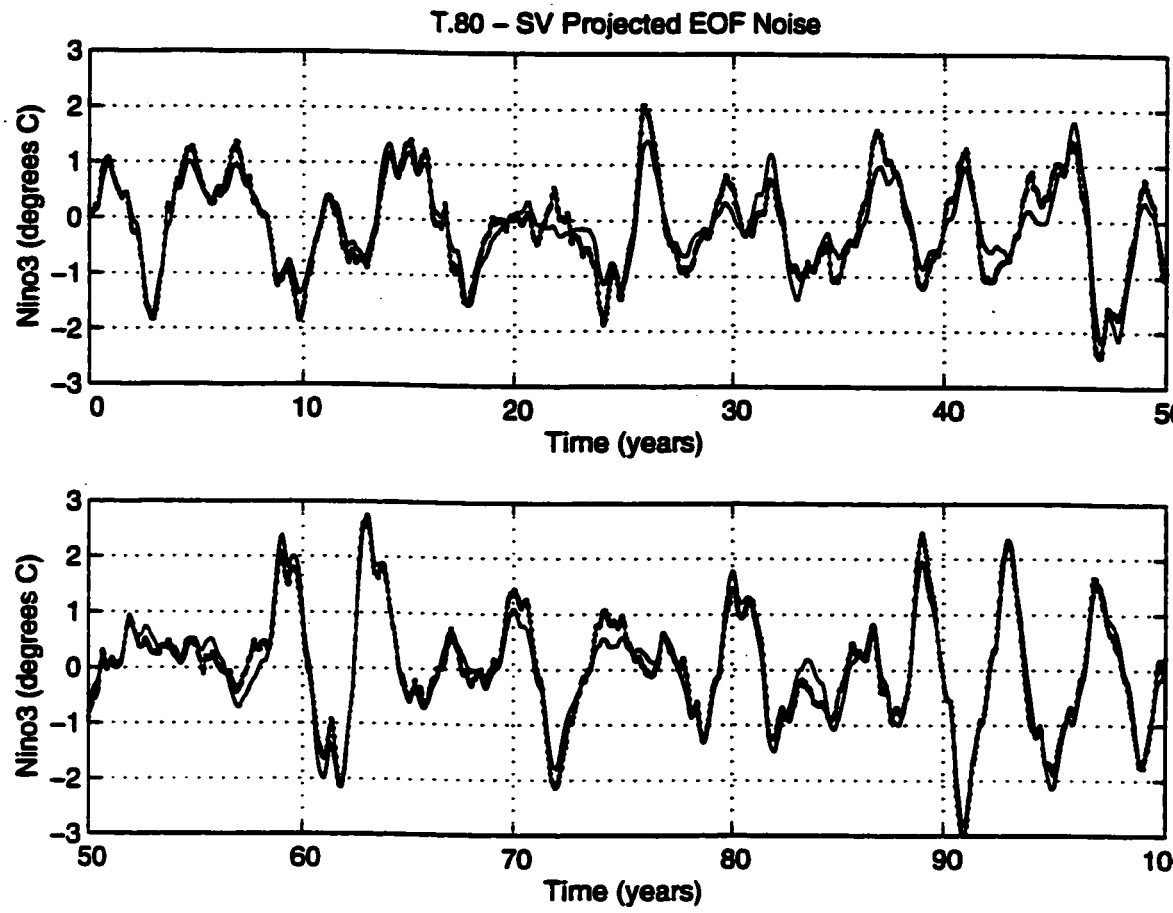

Figure 6.15 - T-80 - SV Projected Noise Run and EOF Noise Run. Shown is the Nino3 index for the first 100 years of the T.80 EOF noise simulation- the same information as in Fig. 6.6(d). Also shown is the Nino3 for the same model, driven by the same noise patterns, except this time only that portion of the noise which projected onto the first singular value was used.

Key	
Line with Dots	EOF Noise
Solid line	SV Projected

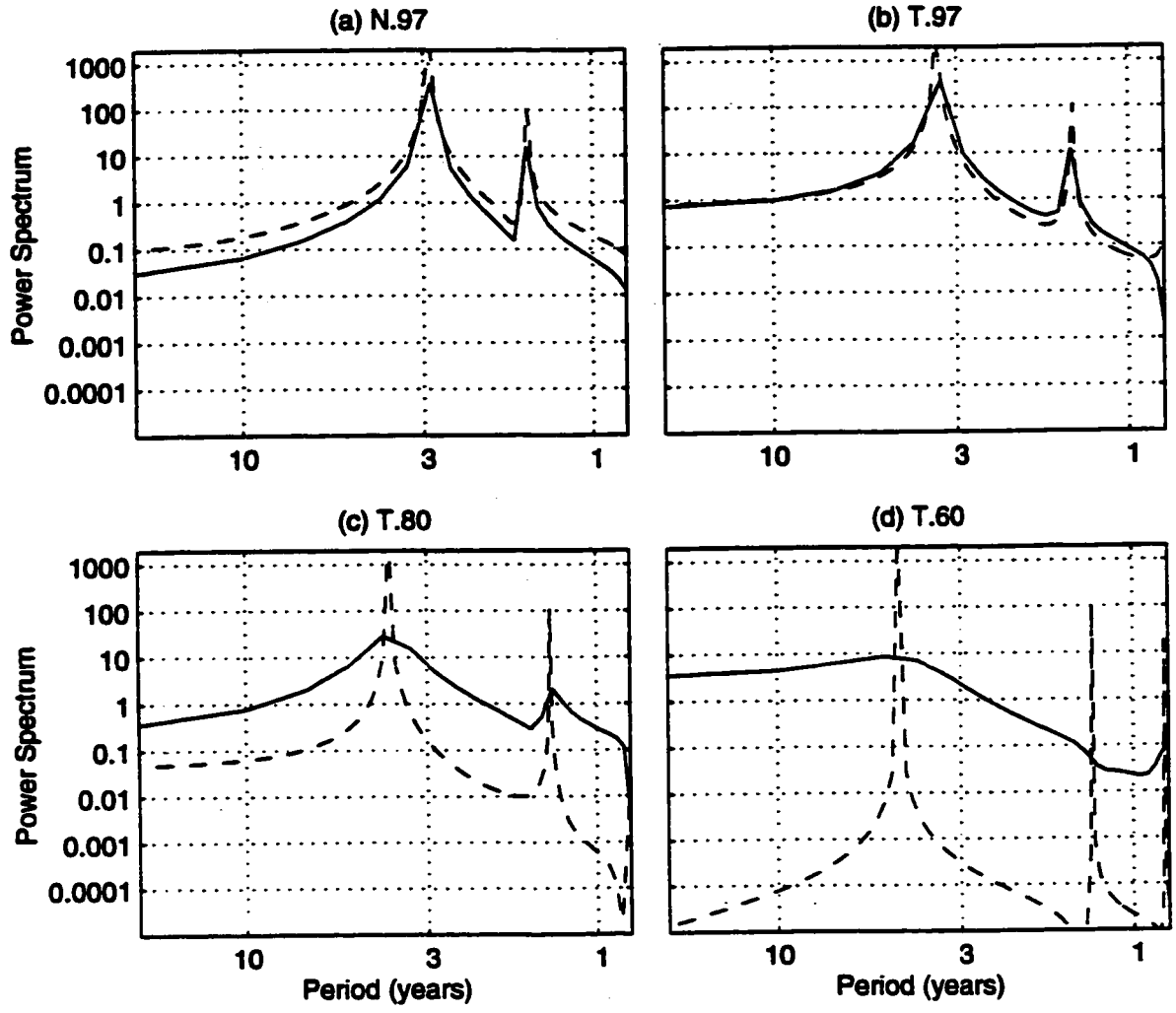

Figure 6.16 - Spectrum of Pure ENSO Modes for Models. Shown are the power spectra for each model for two different cases. One is for each model's ENSO mode where the exponential decay has been removed, and the other is with the normal exponential decay. Note that the vertical scale on these graphs has been extended in comparison to Figs. 6.3, 6.7,and 6.11.

Key	
Dashed line	"Neutralized"
Solid lines	Normal Damping

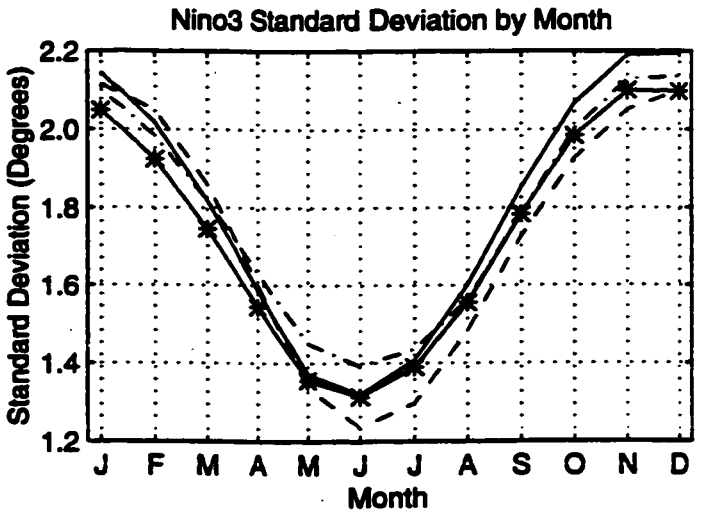

Figure 6.17 - Pure ENSO Mode Standard Deviation by Month. Shows the monthly standard deviation of the Nino3 index for the ENSO mode of each candidate model. The ENSO modes have been made neutral (see text) and their maximum SST is set to 3 degrees C.

Key	
Dashed line	N.97
Solid line	T.97
Asterisks	T.80
Dot-dash line	T.60

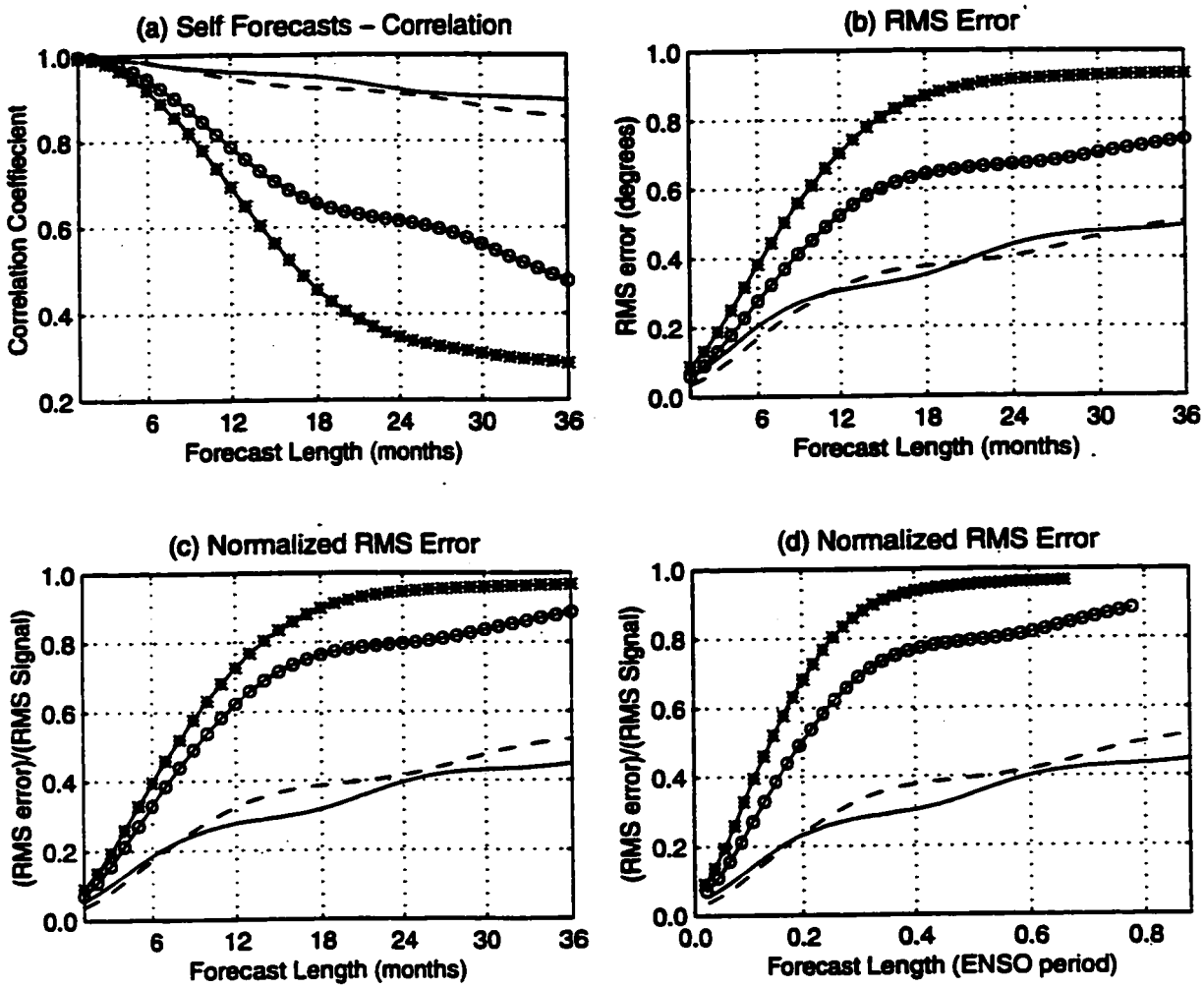

Figure 6.18 - Predictability Limits for Various Models. (a) shows the correlation coefficient of the Nino3 index between a control run and a forecast for each model. (b) shows the RMS errors found using the same scheme. (c) is the same a (b) except RMS error is normalized by the RMS of the Nino3 index for each model. (d) is the same as (c) except that time is normalized by the period of the ENSO mode.

Key	
Solid line	N.97
Dashed line	T.97
Circles	T.80
Asterisks	T.60

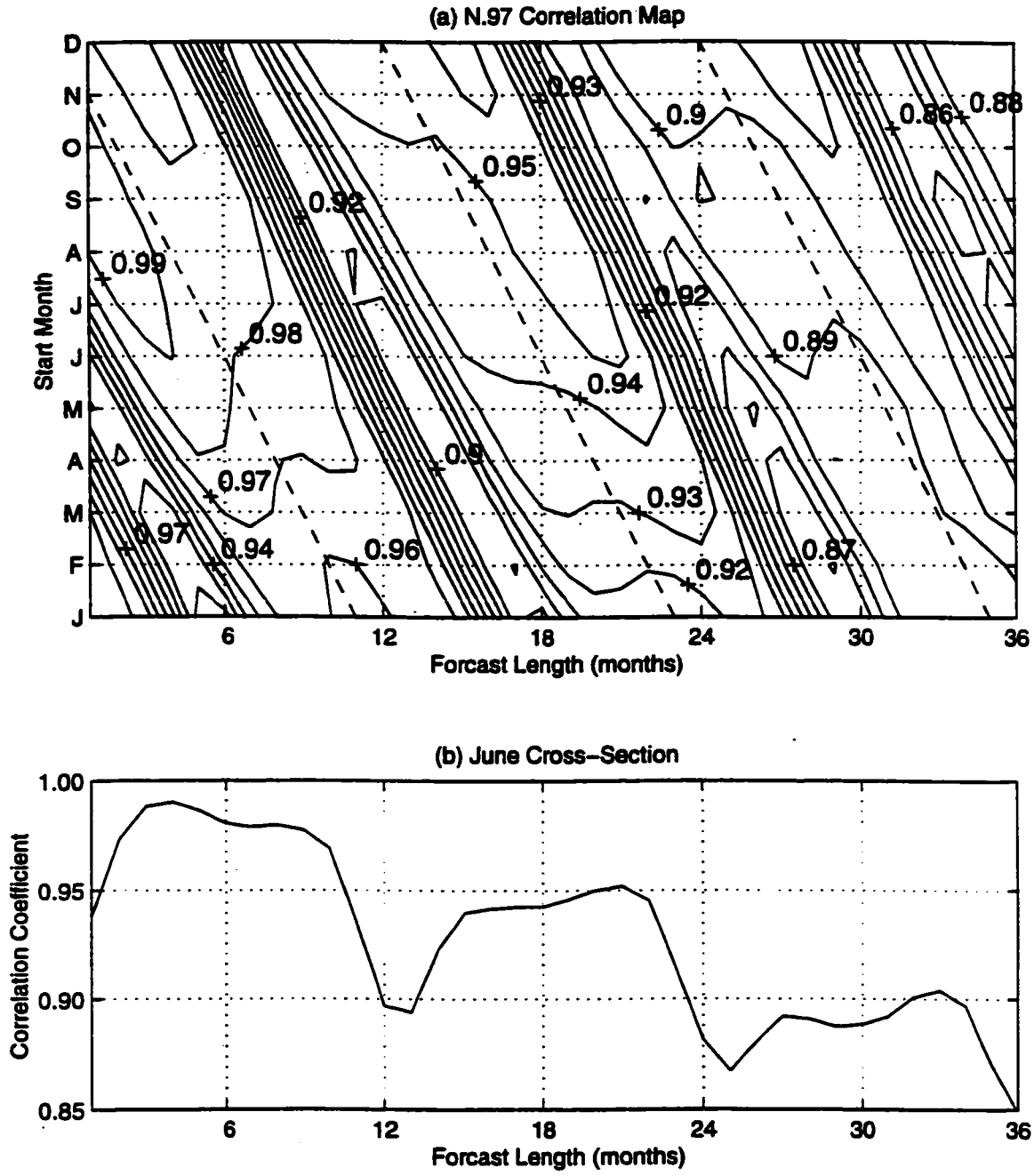

Figure 6.19 - N.97: Forecast Correlation by Lead time and Start Month. (a) Shows the same information as Fig. 6.18(a) except that correlations are composited for every month instead of averaged over the entire year. (b) shows the June cross-section to aid in interpreting the contours.

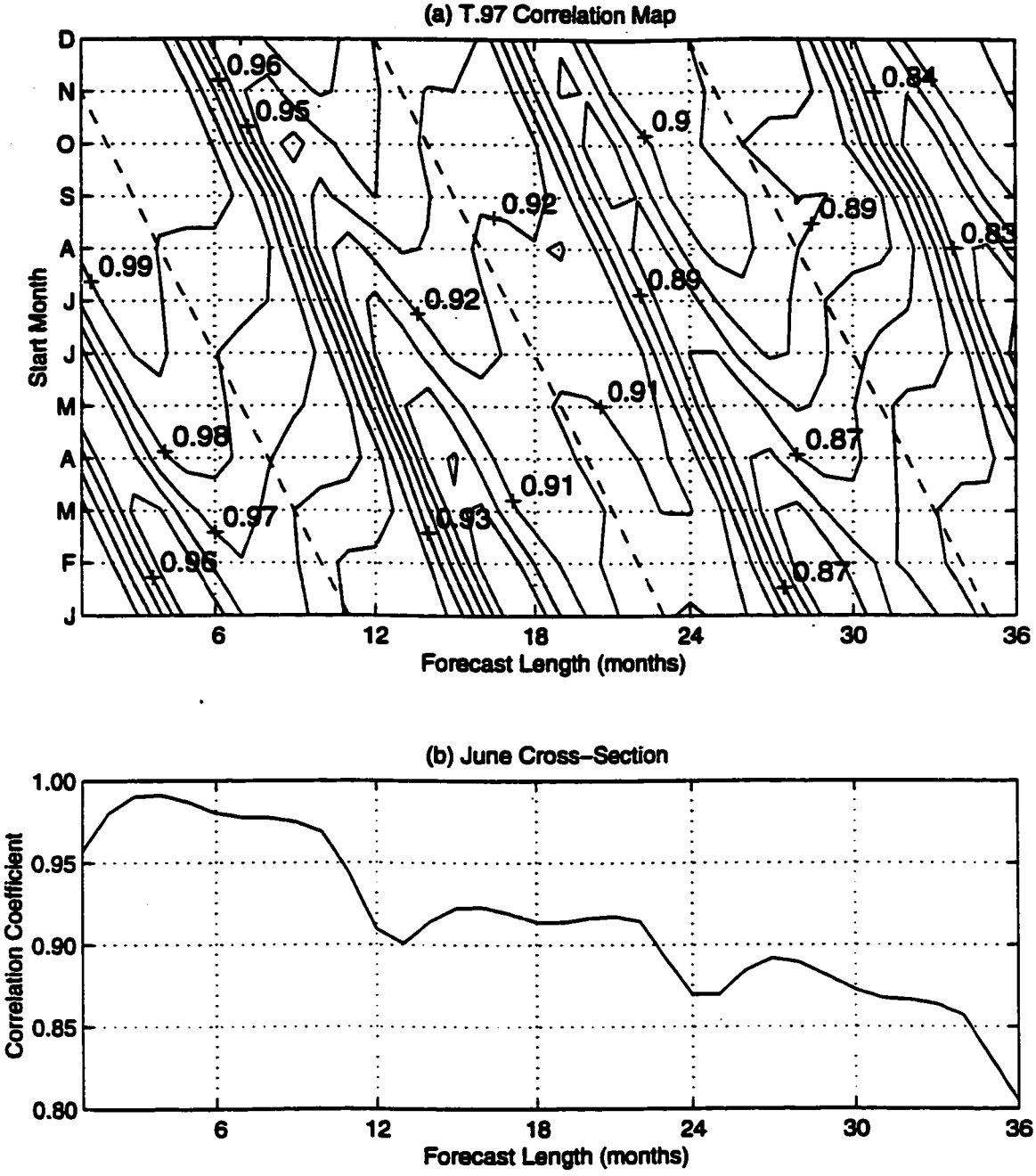

Figure 6.20 - T.97: Forecast Correlation by Lead Time and Start Month. Same as Fig. 6.19 except using the T.97 model.

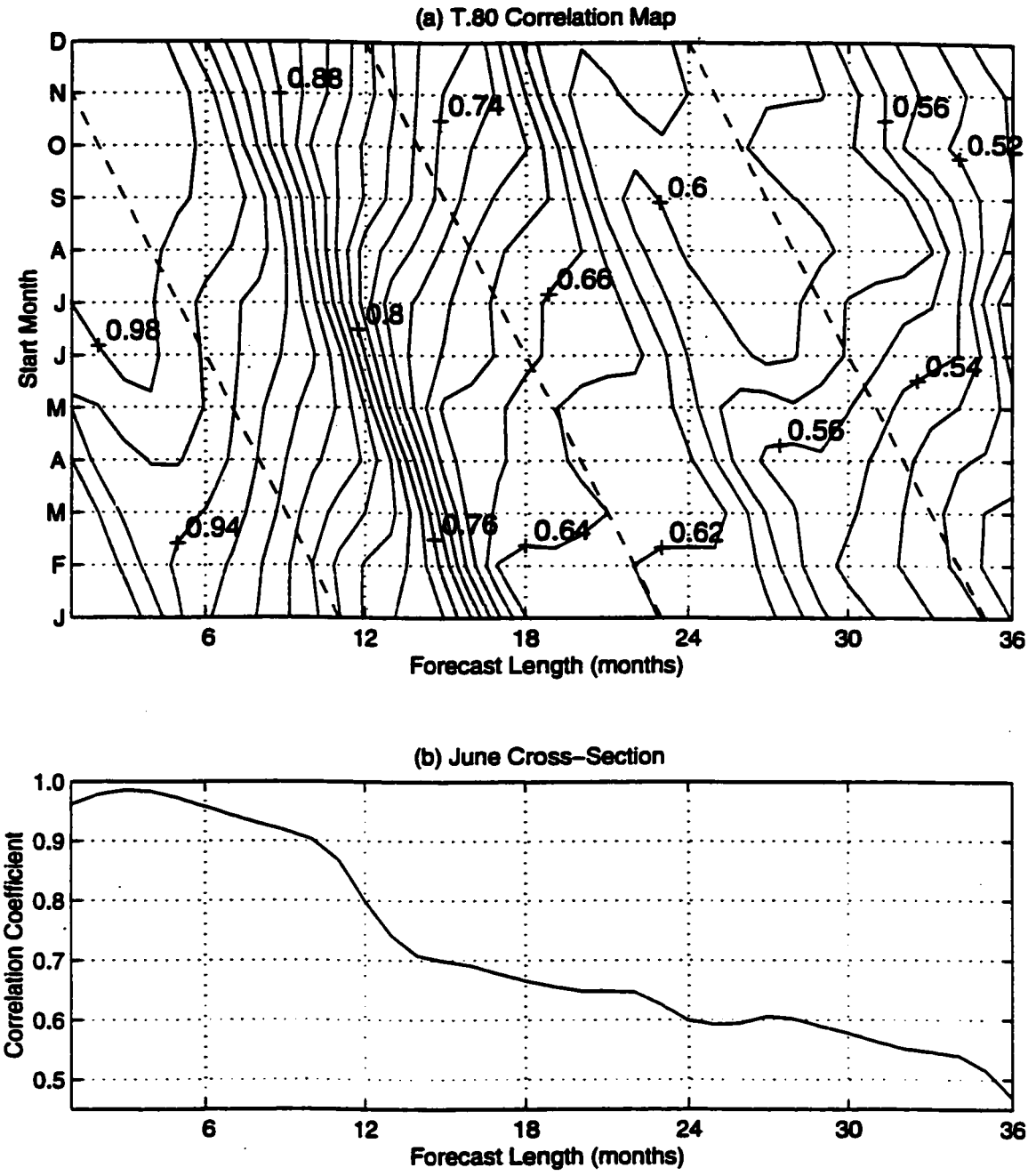

Figure 6.21- T.80: Forecast Correlation by Lead Time and Start Month. Same as Fig. 6.19 except using the T.80 model.

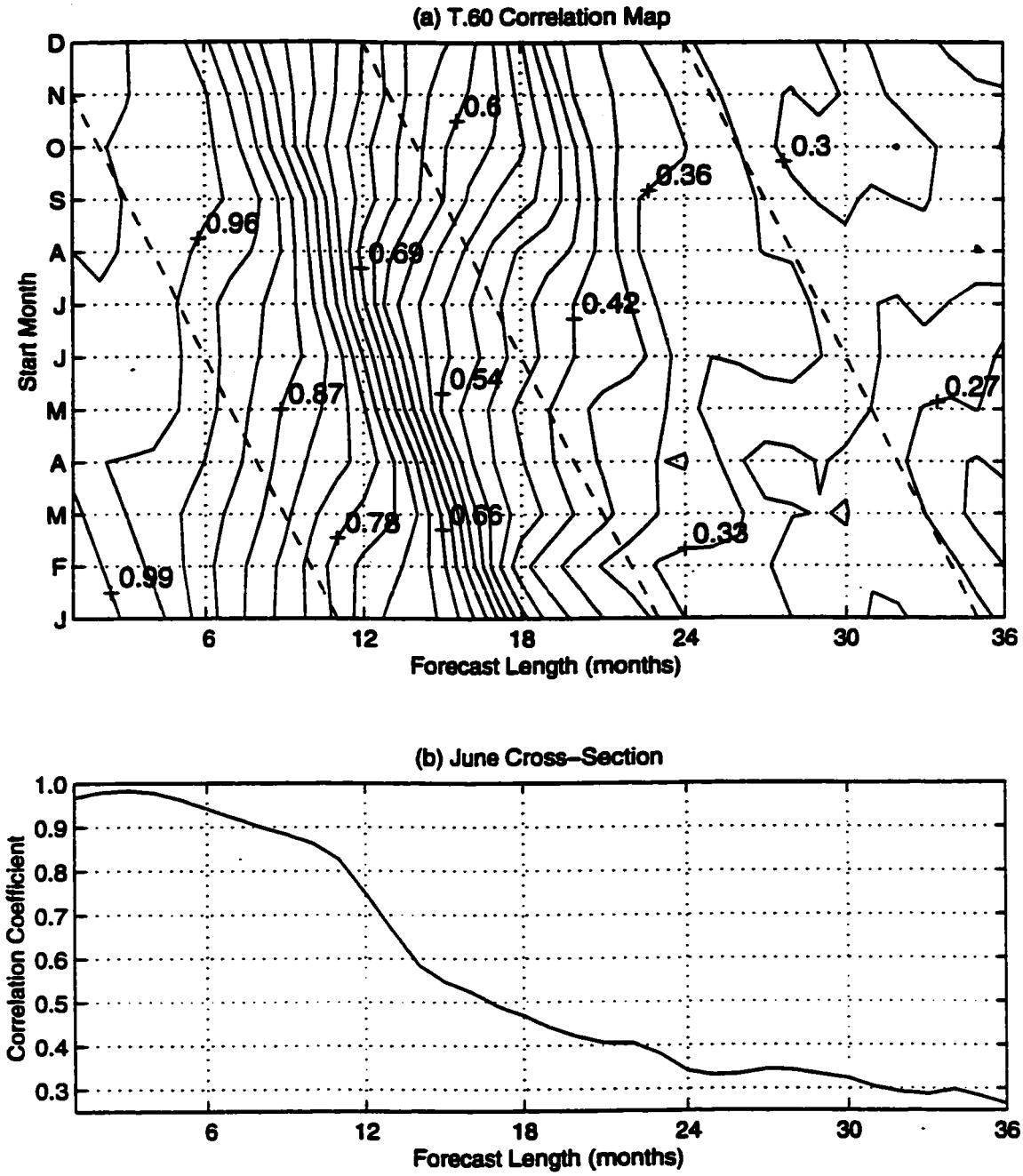

Figure 6.22- T.60: Forecast Correlation by Lead Time and Start Month. Same as Fig. 6.19 except using the T.60 model.

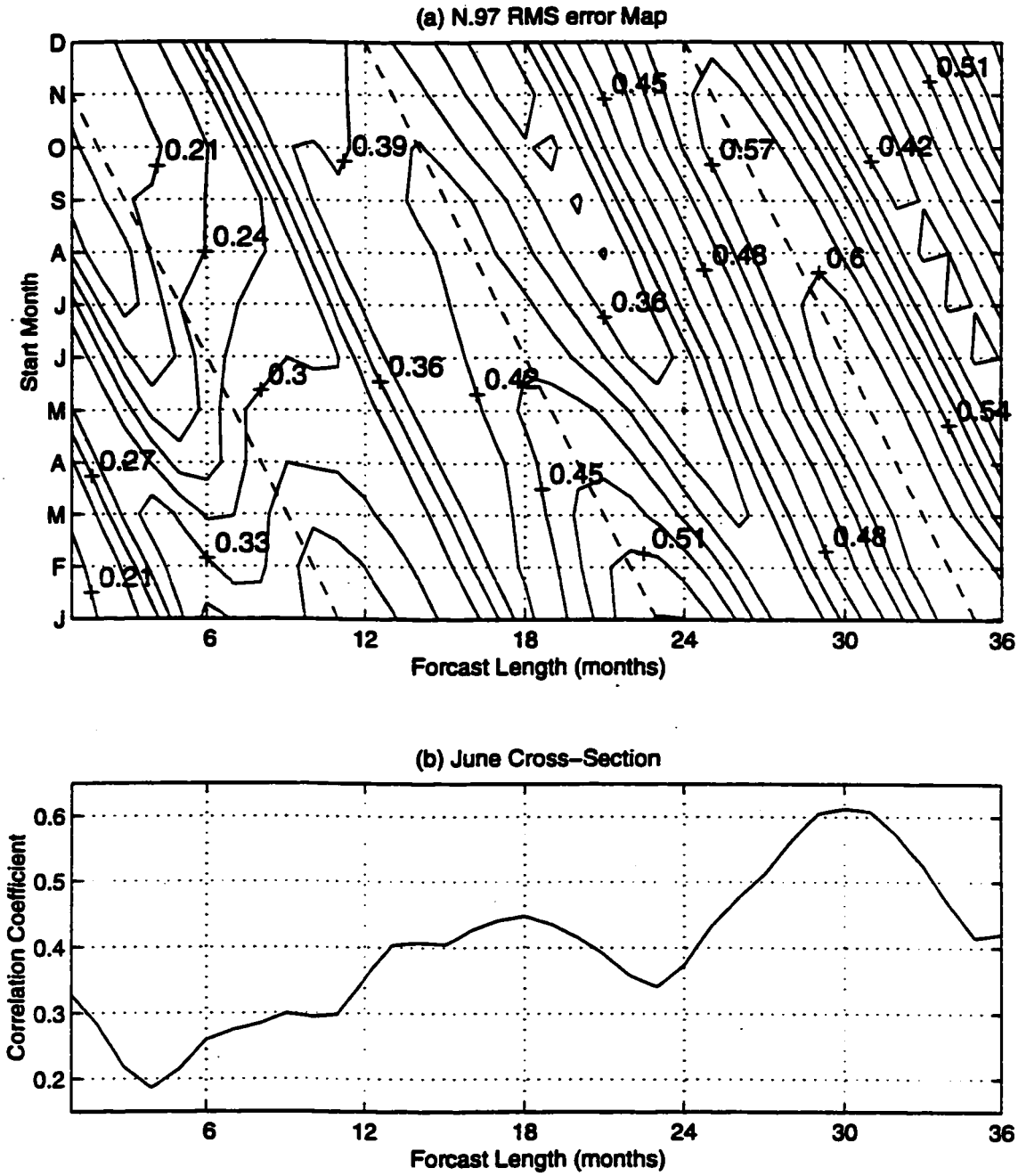

Figure 6.23- N.97: Forecast RMS Error by Lead Time and Start Month. Same as Fig. 6.19 except that it shows the RMS error.

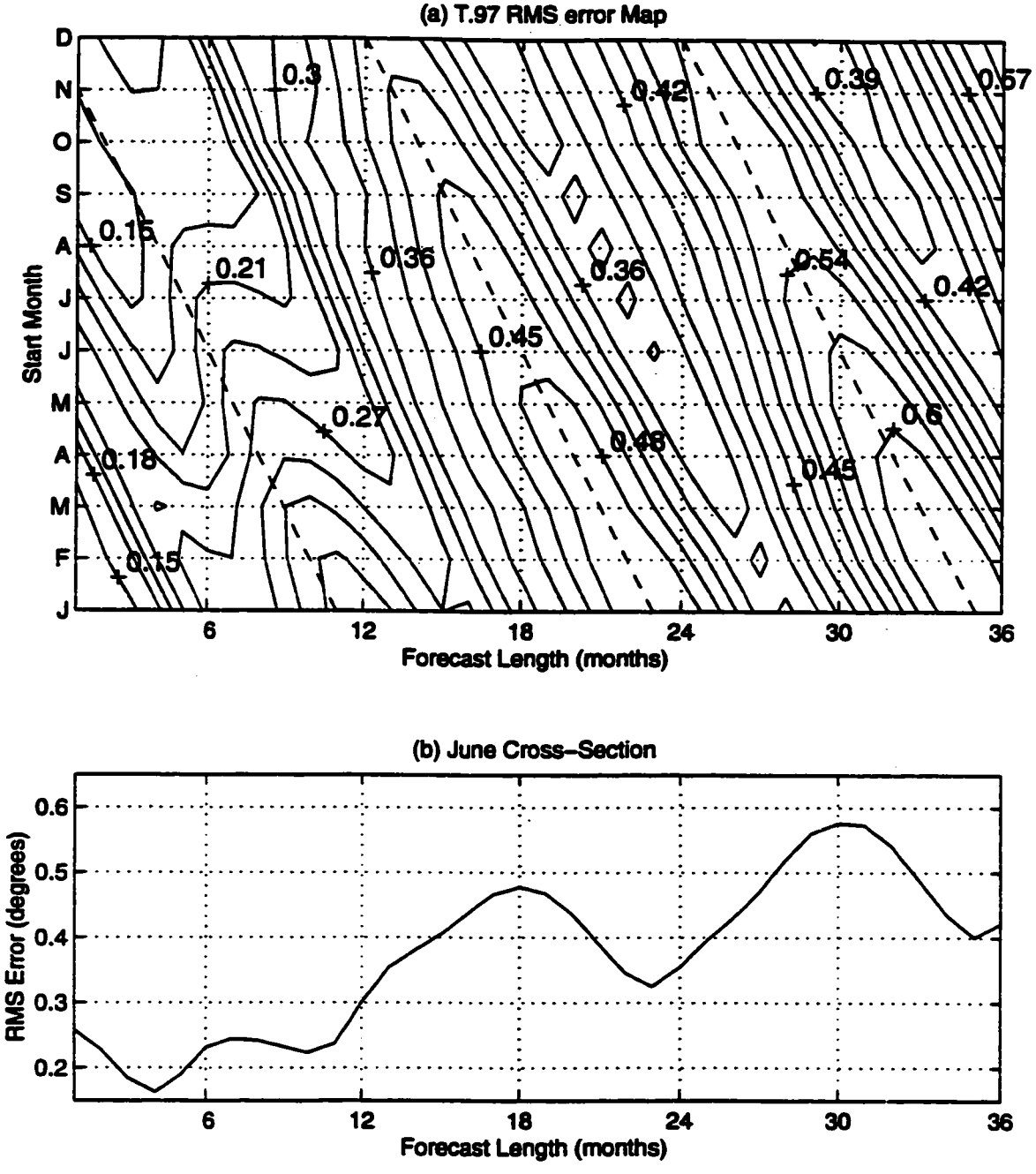

Figure 6.24- T.97: Forecast RMS Error by Lead Time and Start Month. Same as Fig. 6.23 except using the T.97 model.

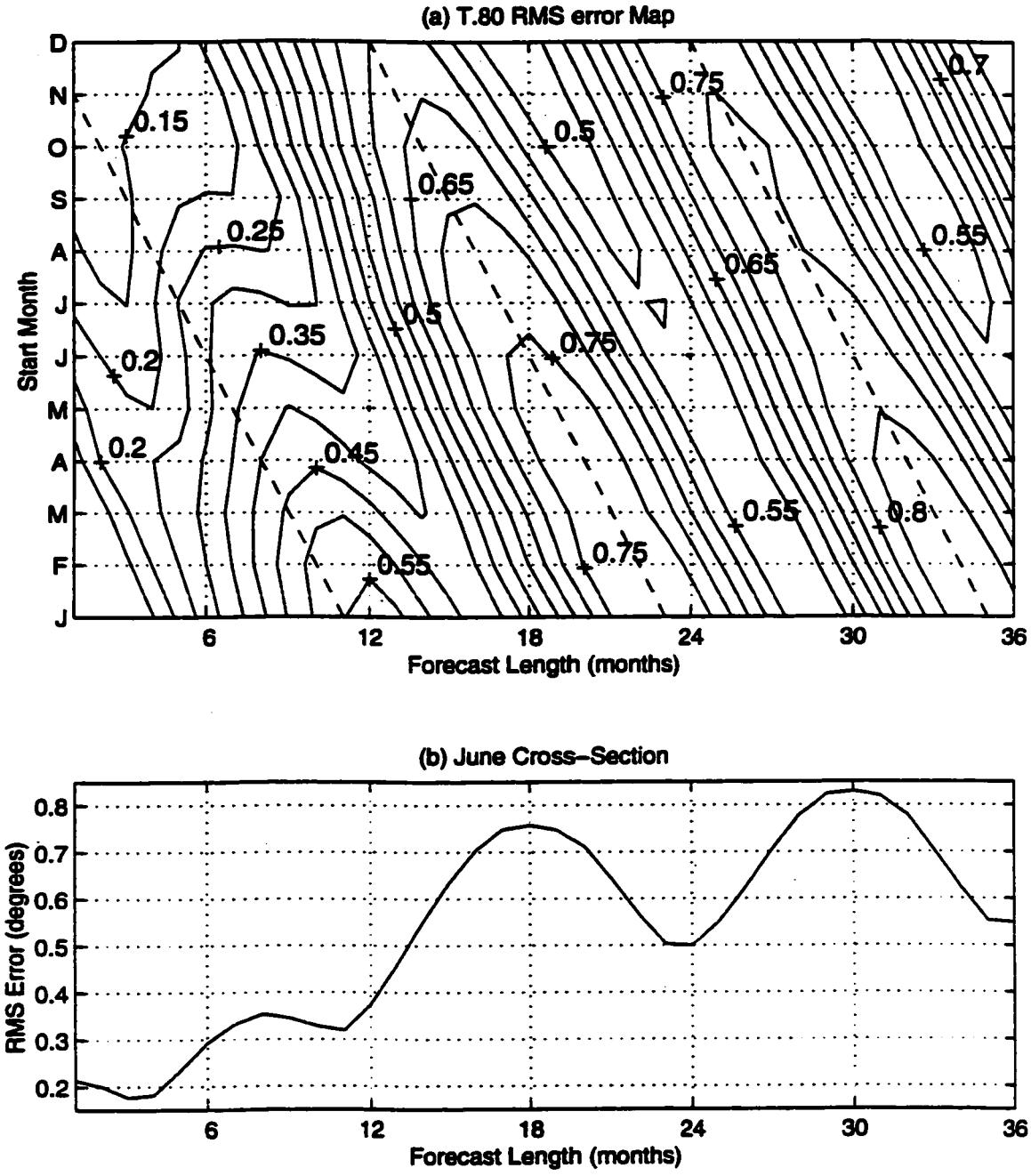

Figure 6.25- T.80: Forecast RMS Error by Lead Time and Start Month. Same as Fig. 6.23 except using the T.80 model.

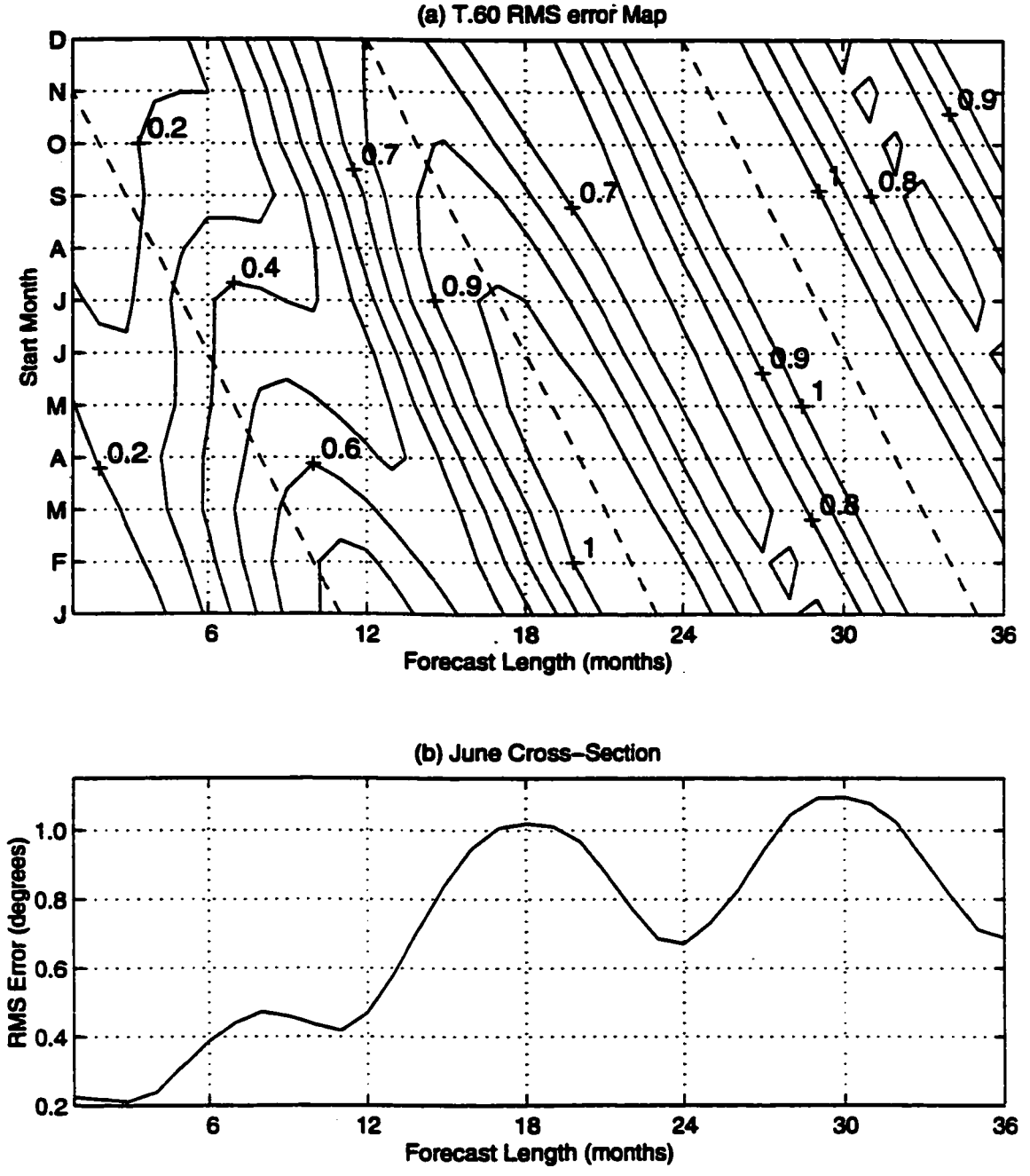

Figure 6.26- T.60: Forecast RMS Error by Lead Time and Start Month. Same as Fig. 6.23 except using the T.60 model.

Chapter 7: Stochastic Analysis: Annually Averaged Case Revisited

7.1 Introduction

In Chapter 6 the behaviour of the four candidate models when driven by random perturbations was explored. This analysis was carried out by running the models as simulations, and then analysing the model output. However, analysis of a stochastically forced system can also be carried out more elegantly using the tools of stochastic calculus. Farrell and Ioannou (1993, hereafter FI93) point out the utility of stochastic calculus in the study of non-normal, linearly stable dynamic systems. Specifically, FI93 analyses the Navier-Stokes equations, linearized about a mean shear flow. The dominant forcing functions and the dominant response functions are found as solutions of related Lyapunov equations.

In this chapter, the time invariant background version of LOAM will be examined with stochastic forcing using random perturbations as in Chapter 6, and also using stochastic calculus as in FI93. There are two objectives. First, to demonstrate that the bimonthly random perturbations of the NND scheme is a good approximation to white noise forcing. (Or conversely, that the white noise forcing is a good approximation to forcing on synoptic weather time scales.) Second, to point the way toward a more complete stochastic analysis which could include the time dependent cases covered in Chapter 6.

7.2 Stochastic Forcing of a Linear System

The matrix operator equation governing LOAM, (2.1.2), can be written as a stochastic differential equation (SDE):

$$\frac{d}{dt}\underline{\varphi} = \mathbf{M}\underline{\varphi} + \mathbf{F}\underline{\xi} \tag{7.1}$$

where $\mathbf{F}\underline{\xi}$ is the stochastic forcing term. This type of SDE is known as the Ornstein-Uhlenbäck equation (Gardiner, 1985). The columns of $\mathbf{F}$ represent the patterns being forced by the stochastic vector $\underline{\xi}$. In this chapter, the matrix $\mathbf{F}$ will generally be set to the identity matrix (i.e. each component of the spectral decomposition used to discretize LOAM will be forced independently). The components of $\underline{\xi}$ are assumed to be a δ-correlated Gaussian white noise process with zero mean:

$$\langle \xi_i \rangle = 0, \text{ and} \tag{7.2}$$

$$\langle \xi_i(t)\xi_j(t') \rangle = \varepsilon_i \delta_{ij} \delta(t-t'), \tag{7.3}$$

where $\langle \bullet \rangle$ denotes ensemble averaging. As in the NND case, the magnitude, ε_i, of the forcing on each component will be taken to be equal. Furthermore, ε_i will be set to one, which can be done without loss of generality due to the linearity of the system.

The solution of (7.1) is given by:

$$\underline{\varphi}(t) = e^{\mathbf{M}t}\underline{\varphi}(0) + \int_0^t e^{\mathbf{M}(t-s)}\mathbf{F}\underline{\xi}\,ds \tag{7.4}$$

where $\underline{\varphi}(0)$ is the initial condition. Since the solution is linearly dependent on a Gaussian random variable, $\underline{\xi}$, the solution will also have a Gaussian distribution. The solution statistics are therefore fully characterized by the first two moments.

7.2.1 The First Moment

Since the mean value of the random forcing is zero, the first moment of the solution of (7.1) is simply

$$\langle \underline{\varphi}(t) \rangle = e^{\mathbf{M}t} \langle \underline{\varphi}(0) \rangle. \tag{7.5}$$

Because the systems under study here are all damped, this leads to

$$\lim_{t\to\infty} \langle \underline{\varphi}(t) \rangle = 0. \tag{7.6}$$

Even for cases other than the asymptotic case, the mean will often be zero. The mean solution is zero when the mean initial condition is zero (e.g. when the initial conditions are Gaussian with zero mean). Also, when looking at predictability limits, (7.1)

describes the error growth, and so will have a zero initial condition.

7.2.2 The Second Moment: Derivation of Matrix B

This section derives the second moment (the ensemble average variance) of the solution, closely following the derivation from FI93. The second moment

$$\begin{aligned}\langle \varphi_i(t)\varphi_i(t)\rangle &= \int_0^t\int_0^t \left[e^{\mathbf{M}(t-s)}\right]_{ia}\mathbf{F}_{ab}\langle \xi_b(s)\xi_d(s')\rangle\left[e^{\mathbf{M}(t-s')}\right]_{ic}\mathbf{F}_{cd}\,ds'ds \\ &= \mathbf{F}^H_{ba}\left(\int_0^t\left[e^{\mathbf{M}(t-s)}\right]^{\mathrm{T}}_{ai}\left[e^{\mathbf{M}(t-s)}\right]_{ic}ds\right)\mathbf{F}_{cb} \\ &= \sum_b f_a^{\mathrm{T}(b)}\mathbf{B}^t_{ac}f_c^{(b)}\end{aligned} \tag{7.7}$$

where $f^{(b)}$ is defined as the b-th column of $\mathbf{F}$, and therefore $f_a^{(b)} = \mathbf{F}_{ab}$. Also the matrix $\mathbf{B}$ has been defined:

$$\mathbf{B}^t \equiv \int_0^t e^{\mathbf{M}^{\mathrm{T}}(t-s)}e^{\mathbf{M}(t-s)}\,ds. \tag{7.8}$$

This matrix will prove to be useful, and so a method for its calculation will be developed. Setting $\tau = t-s$, gives $\mathbf{B}^t = \int_0^t e^{\mathbf{M}^{\mathrm{T}}\tau}e^{\mathbf{M}\tau}\,d\tau$, and then differentiating with respect to time yields

$$\frac{d}{dt}\mathbf{B}^t = e^{\mathbf{M}^{\mathrm{T}}t}e^{\mathbf{M}t}. \tag{7.9}$$

For this system $\mathbf{M}$ is asymptotically stable, and so from (7.9) comes

$$\lim_{t\to\infty}\frac{d}{dt}\mathbf{B}^t = 0. \tag{7.10}$$

Since the derivative of $\mathbf{B}^t$ vanishes as $t\to\infty$, and since (7.9) is integrable, the existence of the limit $\mathbf{B}^\infty = \lim_{t\to\infty}\mathbf{B}^t$ is assured (FI93). Differentiating (7.8) with respect to time yields an evolution equation for $\mathbf{B}^t$:

$$\frac{d}{dt}\mathbf{B}^t = \mathbf{I} + \mathbf{M}^{\mathrm{T}}\mathbf{B}^t + \mathbf{B}^t\mathbf{M}, \tag{7.11}$$

where $\mathbf{I}$ is the identity matrix. The evolution equation is solved using the initial condition $\mathbf{B}^0 = 0$, which can be seen from (7.8). Taking the limit as $t\to\infty$, (7.11) and (7.10) yield:

$$\mathbf{M}^{\mathrm{T}}\mathbf{B}^{\infty}+\mathbf{B}^{\infty}\mathbf{M}=-\mathbf{I}, \tag{7.12}$$

which is called the backward Lyapunov equation, and can be solved for $\mathbf{B}^{\infty}$ using standard methods. The steady state (asymptotic) variance maintained by stochastic forcing is simply the trace of $\mathbf{F}^{\mathrm{T}}\mathbf{B}^{\infty}\mathbf{F}$. For the case here, where $\mathbf{F}=\mathbf{I}$, the variance is the trace of $\mathbf{B}^{\infty}$. Using the value of $\mathbf{B}^{\infty}$, the solution of (7.11) can be found:

$$\mathbf{B}^{t}=\mathbf{B}^{\infty}-e^{\mathbf{M}^{\mathrm{T}}t}\mathbf{B}^{\infty}e^{\mathbf{M}t}. \tag{7.13}$$

7.2.3 Derivation of the Covariance Matrix

Another matrix that will prove useful is the covariance matrix (called the correlation matrix in FI93). From Gardiner (1985) or FI93, the covariance matrix is

$$\begin{aligned}\mathbf{C}^{t}&=\left\langle \underline{\varphi}(t)\cdot\underline{\varphi}^{\mathrm{T}}(t)\right\rangle=\left\langle \int_0^t\int_0^t e^{\mathbf{M}(t-s)}\mathbf{F}\underline{\xi}(s)e^{\mathbf{M}(t-s')}\mathbf{F}\underline{\xi}(s')\,ds'ds\right\rangle\\&=\int_0^t e^{\mathbf{M}(t-s)}\mathbf{F}\mathbf{F}^{\mathrm{T}}e^{\mathbf{M}^{\mathrm{T}}(t-s)}ds\end{aligned} \tag{7.14}$$

The evolution equation for $\mathbf{C}^{t}$ can be derived similarly to the evolution equation for $\mathbf{B}^{t}$. From (7.14) it can be seen that $\mathbf{C}^{0}=0$, and that the limit exists: $\mathbf{C}^{\infty}=\lim_{t\to\infty}\mathbf{C}^{t}$, when $\mathbf{M}$ is asymptotically stable. Differentiation of (7.14) yields

$$\frac{d}{dt}\mathbf{C}^{t}=\mathbf{F}\mathbf{F}^{\mathrm{T}}+\mathbf{M}\mathbf{C}^{t}+\mathbf{C}^{t}\mathbf{M}^{\mathrm{T}} \tag{7.15}$$

with the solution

$$\mathbf{C}^{t}=\mathbf{C}^{\infty}-e^{\mathbf{M}t}\mathbf{C}^{\infty}e^{\mathbf{M}^{\mathrm{T}}t}, \tag{7.16}$$

where the asymptotic covariance matrix is determined from the forward Lyapunov equation:

$$\mathbf{M}\mathbf{C}^{\infty}+\mathbf{C}^{\infty}\mathbf{M}^{\mathrm{T}}=-\mathbf{F}\mathbf{F}^{\mathrm{T}}. \tag{7.17}$$

The ensemble average variance caused by stochastic forcing can be found from $\mathbf{C}^{t}$: it is the trace of $\mathbf{C}^{t}$. The steady state (asymptotic) variance maintained by the forcing is the trace of $\mathbf{C}^{\infty}$.

7.2.4 Eigenanalysis of the B and C matrices

The eigenanalysis of $\mathbf{C}^t$ is known as the Karhunen-Loeve decomposition (hereafter K-L). Since $\mathbf{C}^t$ is positive definite and symmetric (by construction) it has real eigenvalues and mutually orthogonal eigenvectors. The eigenvalues of $\mathbf{C}^t$ give the amount of variance explained by the pattern of the corresponding eigenvector. When the covariance matrix is built approximately from observations (or the output of a model) then these eigenvectors are also known as the empirical orthogonal functions (EOFs). Since our $\mathbf{C}^t$ is not empirical, its eigenvectors will not be called EOFs. Theoretically, if the EOFs of a stochastically forced model are calculated from the output of a simulation run, the EOFs and the percent variance explained by each should correspond to the eigenvectors and eigenvalues of the $\mathbf{C}^\infty$ matrix. This comparison will be made later in this chapter.

Eigenanalysis of the $\mathbf{B}^t$ matrix is similar to K-L decomposition, except that it gives the *forcing* patterns and the amount of variance that each produces (FI93). Like the covariance matrix, $\mathbf{B}^t$ is positive definite symmetric and so has orthogonal eigenvectors and real eigenvalues. For a stochastically forced model in steady state, eigenanalysis of $\mathbf{B}^\infty$ will give the optimal forcing pattern: that eigenvector associated with the largest eigenvalue of $\mathbf{B}^\infty$. If the forcing is spatially uniform, it is reasonable to expect that the pattern that produces the most variance, will be very similar to the pattern responsible for the greatest transient growth (i.e. the τ-optimal). For the asymptotic case, it is reasonable to expect that the principle eigenvector of $\mathbf{B}^\infty$ would correspond to the fastest growing phase of the adjoint. This comparison will be made later in the chapter.

Table 7.1 shows a summary of the general characteristics of the matrices $\mathbf{C}^t$ and $\mathbf{B}^t$ as outlined in this section.

Table 7.1 - Summary of Characteristics of C and B matrices. Details to be found in Section 7.2.		
Matrix symbol	$\mathbf{C}^t$	$\mathbf{B}^t$
Name	Covariance or Correlation	-
Definition	$\int_0^t e^{\mathbf{M}(t-s)}\mathbf{F}\mathbf{F}^{\mathrm{T}}e^{\mathbf{M}^{\mathrm{T}}(t-s)}ds$	$\int_0^t e^{\mathbf{M}^{\mathrm{T}}(t-s)}e^{\mathbf{M}(t-s)}ds$
How asymptotic matrix is computed	Forward Lyapunov: $\mathbf{M}\mathbf{C}^{\infty}+\mathbf{C}^{\infty}\mathbf{M}^{\mathrm{T}}=-\mathbf{F}\mathbf{F}^{\mathrm{T}}$	Backward Lyapunov: $\mathbf{M}^{\mathrm{T}}\mathbf{B}^{\infty}+\mathbf{B}^{\infty}\mathbf{M}=-\mathbf{I}$
How time dependent matrix is computed	$\mathbf{C}^t=\mathbf{C}^{\infty}-e^{\mathbf{M}t}\mathbf{C}^{\infty}e^{\mathbf{M}^{\mathrm{T}}t}$	$\mathbf{B}^t=\mathbf{B}^{\infty}-e^{\mathbf{M}^{\mathrm{T}}t}\mathbf{B}^{\infty}e^{\mathbf{M}t}$
Eigenanalysis yields	Response patterns in order of variance	Forcing patterns in order of variance produced
Asymptotically similar to	EOFs	Adjoint
Time dependent similar to	-	τ-optimals

7.3 Comparison with Simulation

For the sake of comparison with the stochastic analysis outlined in Section 7.2, a time invariant background version of the T.80 model was built. This model will be named C.80, where "C" is for "constant" background. The model was devised so as to be as closely analogous to the T.80 model as possible. The background fields were taken to be the average of the monthly backgrounds of the annual cycle, and all the parameters were then set to the same values as used in the T.80 model. When run in this configuration, the annual growth/decay rate of the model was higher than the desired 0.80 per year, so the ocean-atmospheric coupling efficiency was reduced until the ENSO mode growth rate matched that of T.80. A summary of the parameters and ENSO mode characteristics for T.80 and C.80 are found in Table 7.2. The C.80 model was then run in a 200 year long simulation using the perturbation forcing scheme NND from Chapter 6.

The NND scheme consists of perturbing the (otherwise freely evolving) model twice per month. The perturbations are generated by choosing the amplitude of the $\underline{T}$ components randomly with a normal (Gaussian) distribution.

Table 7.2 - Characteristics of C.80 and T.80 models. Comparison of parameters and ENSO characteristics of T.80 with its constant background equivalent, C.80.

Model	T.80	C.80
Background	Annual cycle	Annually averaged
Western Boundary Reflection (WBR)	0.7	0.7
Ocean Mechanical Damping (1/month)	8.7	8.7
Coupling Efficiency	1.0	0.907
ENSO mode period (years)	3.85	4.02
ENSO mode growth rate (1/year)	0.80	0.80

7.3.1 Comparison with C-inf

The covariance matrix, $\mathbf{C}^{\infty}$, was computed for the C.80 model, and the K-L decomposition was performed on it. In order to conform to the conditions of the simulation, the covariance matrix was computed using random forcing only on the SSTA fields. To do this the forcing matrix was set as $\mathbf{F} = \text{diagonal}[0\cdots0\,1\cdots1]$, where the zero diagonal elements cover the $\underline{r}$ components and the unit diagonal elements cover the $\underline{T}$ components. The covariance matrix will be called $\mathbf{C}_T^r$ to distinguish it from the $\mathbf{F} = \mathbf{I}$ case.

Figure 7.1 shows the first two eigenvectors of $\mathbf{C}_T^{\infty}$, which represent 70.5 and 7.2 percent of the variance of the output of C.80 - if C.80 were run as a stochastic model with Gaussian white noise forcing. The eigenvectors and eigenvalues of $\mathbf{C}_T^{\infty}$ can be compared with the EOFs computed from the output of the C.80 simulation which was run with

Gaussian bimonthly noise perturbations. Table 7.3 shows the percentage of variance explained by each of the top seven EOFs and eigenvectors of $\mathbf{C}_T^{\infty}$, along with the correlation coefficient between the patterns for each. From this table it can be seen that there is very good agreement for the top five EOFs/eigenvectors which account for 70% to 80% of the variance: the correlation is greater than 85% between the EOFs and eigenvectors for each of these five pairs. The correlation breaks down beyond the 6th EOF. The 7th and higher EOFs/eigenvectors each account for less than 1% of the variance and they are not distinguishable from each other according to the criterion of North (1982).

Figure 7.1 shows the SSTA and thermocline fields for the first two eigenvectors of $\mathbf{C}_T^{\infty}$. The first eigenvector, Fig. 7.1a is obviously the pattern of an ENSO mode in its mature phase (compare with Figs. 2.2a and 4.2a). But what about the second eigenvector? Comparing Fig. 7.1b with the imaginary part of a typical ENSO mode (see Fig. 2.2b, which is the ENSO mode for the B88M parameters) suggests that the second eigenvector may be another phase of ENSO mode. Figure 7.2 shows the correlation coefficient between the first and second eigenvectors of $\mathbf{C}_T^{\infty}$ and all phases of C.80's ENSO mode. It is clear from Fig. 7.2 that the first and second eigenvectors of $\mathbf{C}_T^{\infty}$ represent the ENSO mode. This also implies that the first two EOFs represent the ENSO mode, since they are essentially the same as the first two eigenvectors of $\mathbf{C}_T^{\infty}$. This equivalence between the principle eigenmodes of $\mathbf{M}$ and the top two EOFs is *not* a general mathematical rule. However, it is true for this system and is probably a reflection of the degree to which the ENSO mode dominates these models.

How different would this analysis be if the entire covariance matrix $\mathbf{C}^{\infty}$ had been used instead of limiting the stochastic forcing to the SSTA? The results of Chapter 3 suggests that it should not make much difference. Specifically two results from Chapter 3 are relevant: (1) it was noted that the T-optimal, the r-optimal, and the full-

optimal each act quickly to produce the ENSO mode, and (2) in each case (r-forcing, T-forcing and full-forcing) the optimal growth pattern significantly outperformed the second best growth pattern. (Another way of stating this second point is that the first singular value was much greater than the second singular value when doing SV decomposition on either $\mathbf{R}$, $\mathbf{R}_{11}$, or $\mathbf{R}_{22}$). Point (2) implies that the system response to random forcing will be dominated by a single (optimal) pattern, while point (1) implies that the response to that optimal pattern will be the same whether the T-optimal or the full-optimal is operant in the prescription of the noise.

Table 7.3 - Comparison of EOFs with the Eigenvectors of C-inf.

Eigenvector # or EOF #	$\mathbf{C}_T^{\infty}$ Eigenvector Variance Explain (percent)	EOF Variance Explain (percent)	Correlation between EOF and $\mathbf{C}_T^{\infty}$ Eigenvector
1	70.5	64.0	1.00
2	7.2	6.5	0.99
3	1.3	1.6	0.97
4	1.1	1.3	0.96
5	0.7	1.0	0.85
6	0.5	0.7	0.68
7	0.5	0.7	0.49

To check this, the K-L decomposition was performed on the $\mathbf{C}^{\infty}$ matrix. Table 7.4 shows the percent variance explained by the first five eigenvectors of both $\mathbf{C}^{\infty}$ and $\mathbf{C}_T^{\infty}$, along with the correlation coefficient between the corresponding eigenvectors of the two matrices. The correlation between the first four pairs of eigenvectors is very high, greater than 0.96 for each pair. These first four eigenvectors account for greater than 70% of the variance for both forcing regimes, while no other eigenvalue alone accounts for more than 1% of the remaining variance. The percent variance explained by each of the eigenvectors is slightly different for $\mathbf{C}^{\infty}$ and $\mathbf{C}_T^{\infty}$, but overall the system responds similarly to either type of random forcing. This similarity of response points out the

difficulty in trying to distinguish the importance of different forcing patterns by looking only at the system response (i.e. from observations).

Table 7.4 - Comparison the Eigenvectors of C-inf. with Different Forcing Patterns.

Eigenvector #	$\mathbf{C}^{\infty}$ Eigenvector Variance Explain (percent)	$\mathbf{C}_T^{\infty}$ Eigenvector Variance Explain (percent)	Correlation between $\mathbf{C}_T^{\infty}$ and $\mathbf{C}^{\infty}$ Eigenvectors
1	61.6	70.5	1.00
2	6.5	7.2	1.00
3	1.2	1.3	0.96
4	1.0	1.1	0.97
5	0.6	0.7	0.34

7.3.2 Comparison with B-inf Matrix

The $\mathbf{B}^{\infty}$ matrix and its eigenvectors were also computed for C.80 for comparison with the adjoint of $\mathbf{M}$ and the singular vectors of the propagator generated by $\mathbf{M}$. Figure 7.3 shows the SSTA and thermocline fields for the first two eigenvectors of $\mathbf{B}^{\infty}$. The percentage of variance explained by the first two eigenvectors is 61.7% and 6.6%, respectively. No other individual eigenvector explains more than 1.3% of the variance.

The first eigenvector of $\mathbf{B}^{\infty}$, Fig. 7.3a, is obviously an optimal growth pattern: compare with Figs. 3.1b, 3.12a, 3.12c, 3.17a, 3.18a, and 4.5. But what about the second eigenvector, Fig. 7.3b? Comparing Fig. 7.3b with the adjoint of the ENSO mode for the B88M, specifically with Fig 3.1a and (the negative of) Fig. 3.1d, suggests that the second eigenvector of $\mathbf{B}^{\infty}$ corresponds to another phase of the adjoint. To test this, the adjoint of the ENSO mode of $\mathbf{M}$ was calculated, and the correlation coefficient between each phase of the adjoint and the first two eigenvectors of $\mathbf{B}^{\infty}$ was computed. Figure 7.4 shows these correlations as a function of the phase of the adjoint. This figure shows that, just as the first two eigenvectors of the covariance matrix represent the ENSO mode, the first two eigenvectors of $\mathbf{B}^{\infty}$ represent the adjoint of the ENSO mode.

7.3.3 Singular Vectors Revisited

In Chapter 3, it was demonstrated that the first right singular vector (also called τ-optimal) becomes the adjoint for large τ. The conclusion from Section 7.3.2 that the first two eigenvectors of $\mathbf{B}^{\infty}$ are two (orthogonal) phases of the adjoint, and therefore represent the adjoint entirely, suggests that the adjoint might be represented by the first two singular vectors of the propagator, $\mathbf{R}(\tau)$, as $\tau \rightarrow \infty$. Figure 7.5a shows the first two singular values of model C.80 out to 50 months. As was shown in Chapter 3 for the B88M in Fig. 3.7a, the first singular value (SV1) grows as a function of τ to a maximum at about 12 months, and then drops to a local minimum at about 24 months (i.e. at half of the cycle of the ENSO mode). Also shown in Fig 7.5a is the value of SV2 as a function of τ. SV2 is obviously smaller than SV1 everywhere, but it does grow to a maximum where SV1 is at a minimum. Here the first two singular values are nearly the same.

Figure 7.5b shows the correlation coefficient between the first and second singular vectors and the adjoint of the ENSO mode. The singular vectors were compared with all phases of the adjoint, and the correlation shown in Fig 7.5b is the maximum. The phase of the adjoint used for a given τ in Fig. 7.5b is displayed in Fig. 7.5c. From Fig. 7.5b it can be seen that the first singular vector matched the adjoint to within a correlation of 0.9 within 3 months. This result was noted in Chapter 3 - see Fig. 3.2. Also apparent in Fig. 7.5b is that the second singular vector is correlated with the adjoint (at a different phase from the first singular vector) as τ gets larger. The second singular vector takes longer to converge to the adjoint, but does achieve a correlation of 0.7 by $\tau = 9$ months.

By comparing Fig. 7.5a with Fig 7.5c, an explanation for the SV1 minimum/SV2 maximum point (at τ equals about 24 months) can be found. At about 24 months the first and second singular vectors both quickly make a transition to different phases of the adjoint. They seem to "swap" phases, over a period of just one or two months. This is

in agreement with the interpretation of Section 3.1, where the quick transition around day 500 in Fig. 3.3 was linked with the local minimum of SV1 in Fig. 3.7a, but no link with the second singular vector was previously made.

7.3.4 Comparison with the Time Dependent B-matrix

If the eigenvectors of $\mathbf{B}^{\infty}$ are equivalent to the adjoint (i.e. the ∞-optimal), then it seems reasonable to explore the relationship between the τ-optimals (i.e. singular vectors) and the eigenvectors of $\mathbf{B}^{t}$ for $t=\tau$. Accordingly, $\mathbf{B}^{t}$ was computed from $\mathbf{B}^{\infty}$ using (7.13) for time period from one month to 48 months, in one month intervals. The first two eigenvectors of $\mathbf{B}^{t}$ were then computed and compared to the first two singular vectors of the system propagator (for the appropriate time period). Figure 7.6 shows the correlation coefficient as a function of τ between SV1 and the first eigenvector of $\mathbf{B}^{t}$, and the correlation between SV2 and the second eigenvector of $\mathbf{B}^{t}$.

Figure 7.6 shows that there is a connection between the first two eigenvectors of $\mathbf{B}^{t}$ and the first two singular vectors of the system. Over the first 48 months the average correlation coefficient is 0.95 and 0.86 for the first and second (singular vector/eigenvector) pair, respectively. After the 48 months shown, the pattern in Fig. 7.6 between month 24 and month 48 repeats every two years (not shown). Specifically, it repeats with a period of 1/2 the ENSO cycle. This cycle may be partially explained by referring to the cycle of the singular values in Fig. 7.5. The correlation in Fig. 7.6 is highest at around 36 months where SV1 is at a local maximum, and the correlation is at its lowest at month 26 and month 48 where SV1 is at its lowest value. The reason for this correlation profile is not completely clear, but the low correlation is probably due to the inefficiency of the first singular value for those time periods. The first eigenvector of $\mathbf{B}^{t}$ gives the pattern that over the *interval* between 0 and t, contributes the most to the variance at time t, whereas the first singular vector gives the pattern

starting at time 0 that grows to the largest by time t. When the interval is small (i.e. for small t) these two patterns should be close, which explains the high correlation (of the first singular vector) for the first several months in Fig. 7.6. Also, when the interval is of a length where the singular value is effective, the correlation should be high. This explains the good agreement of the first singular vector with the first eigenvector of $\mathbf{B}^t$ in the neighborhood of months 12 and 36. The reason for the poorer correlation in the neighborhood of months 24 and 48 is that the first singular vector, inefficient at these intervals, does not contribute as much to the total variance. The apparent discontinuity in Fig. 7.6 at month 25 occurs right where the first and second singular vectors "swap" phases of the adjoint - see Fig. 7.5. No explanation for this behaviour is proposed. It is also unclear why the second singular vector's correlation with the second eigenvector of $\mathbf{B}^t$ should be low at month 12, but high at month 36.

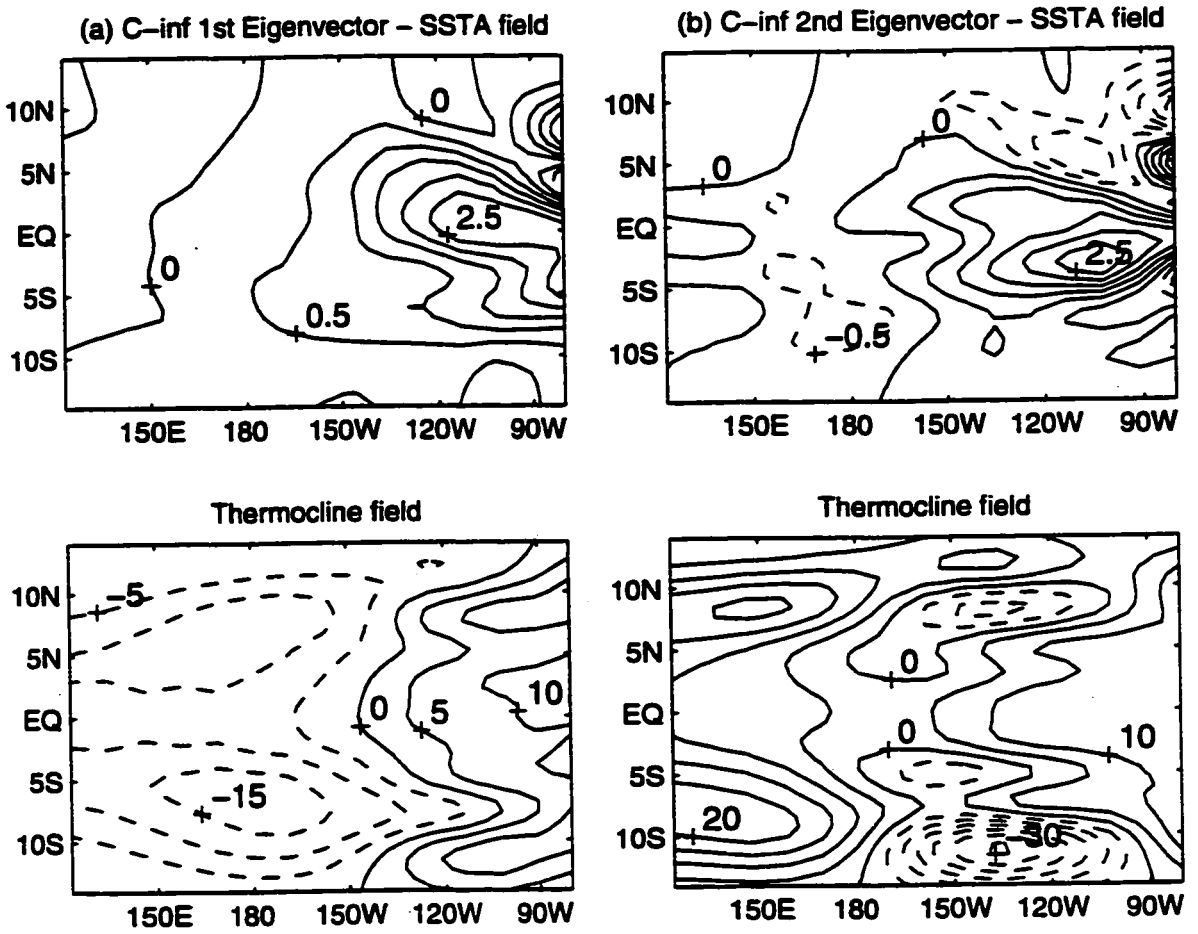

Figure 7.1 - First and Second Eigenvectors of C-inf. Graph (a) shows the SST and thermocline fields of the first eigenvector of $\mathbf{C}^{\infty}$ for model C.80. The contour interval of the SST field is 0.5 degrees C, and the thermocline field contour is 5 meters. (b) Same, for the second eigenvector of $\mathbf{C}^{\infty}$.

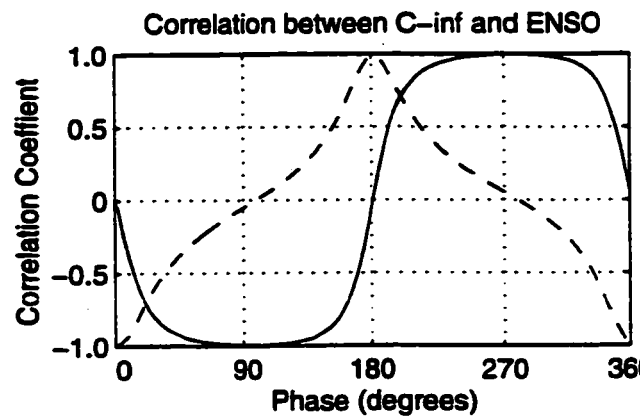

Figure 7.2 - Correlation between Eigenvectors of C-inf and ENSO mode. The correlation coefficient between the first two eigenvectors of C^{∞} and all phases of the ENSO mode for model C.80 are shown.

Key	
Solid line	1st eigenvector
Dashed line	2nd eigenvector

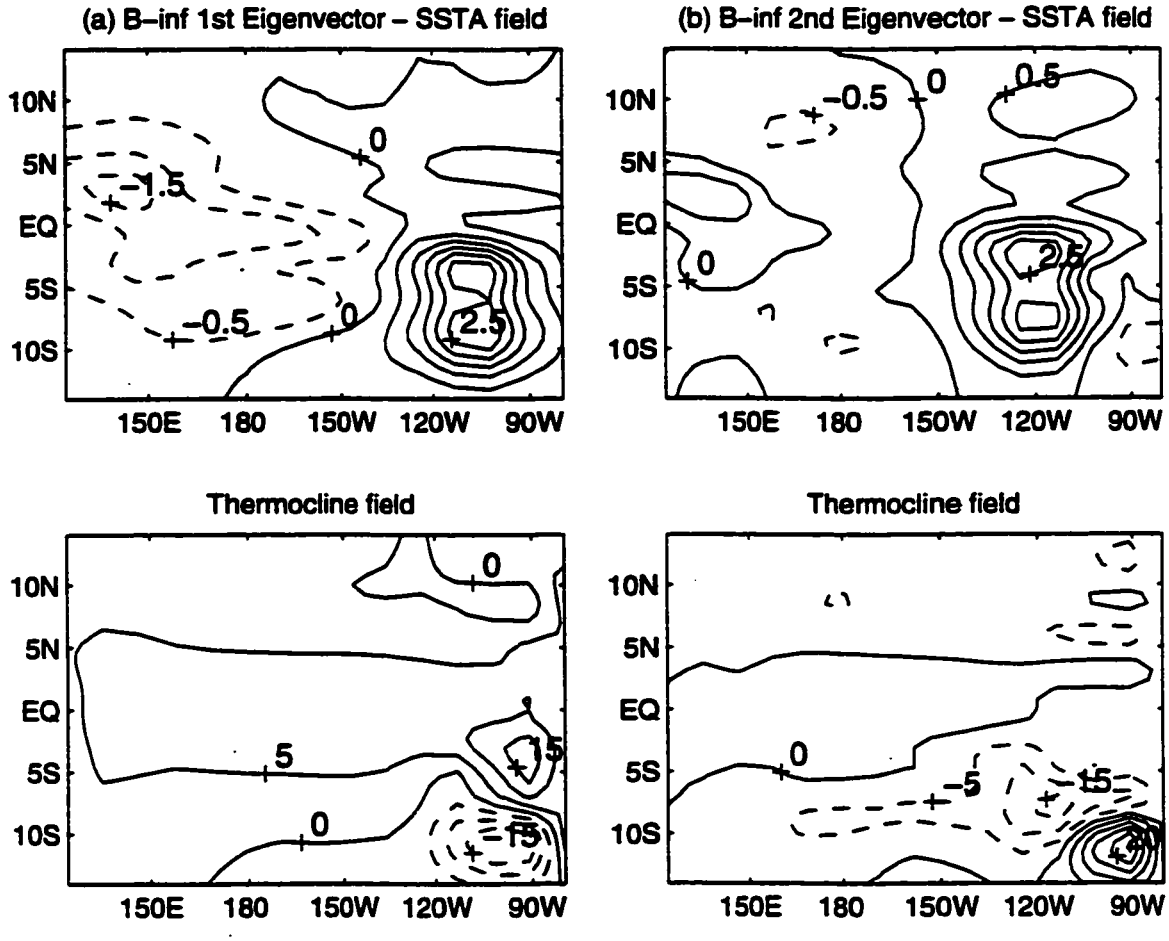

Figure 7.3 - First and Second Eigenvectors of B-inf. Graph (a) shows the SST and thermocline fields of the first eigenvectors of $\mathbf{B}^{\infty}$ for model C.80. The contour interval of the SST field is 0.5 degrees C. and the thermocline field contour is 5 meters. (b) Same but for the second eigenvector of $\mathbf{B}^{\infty}$.

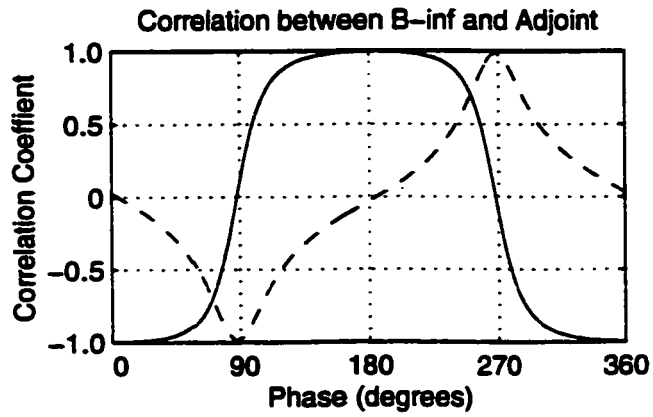

Figure 7.4 - Correlation between Eigenvectors of B-inf and ENSO mode. The correlation coefficient between the first two eigenvectors of $\mathbf{B}^{\infty}$ and all phases of the adjoint of the ENSO mode for model C.80 are shown.

Key	
Solid line	1st eigenvector
Dashed line	2nd eigenvector

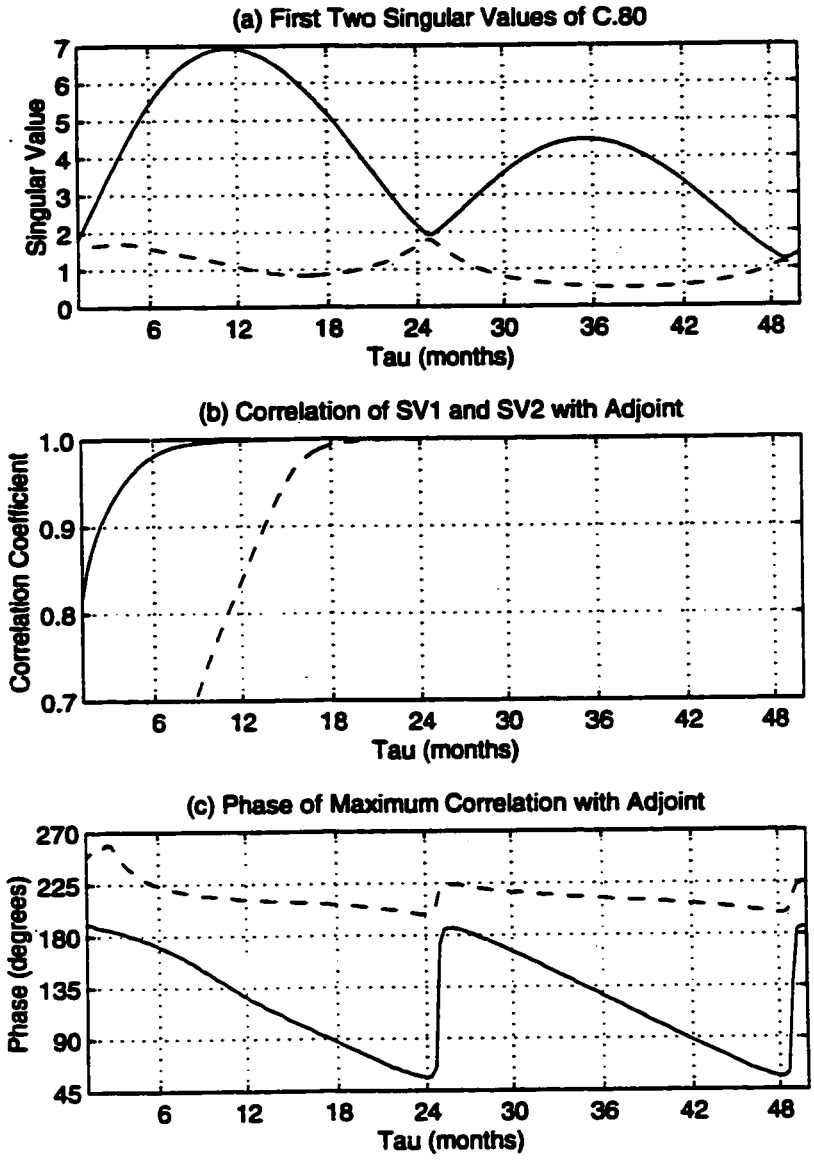

Figure 7.5 - Comparison of the Singular Vectors with the Adjoint of C.80. (a) shows the first two singular values as a function of τ out to 48 months. (b) shows the maximum correlation coefficient as a function of τ between the first and second singular vectors and all phases of the adjoint of the ENSO mode. (c) show the phase of the adjoint for which the singular vector correlation was at a maximum.

Key	
Solid line	1st Sing. Vector
Dashed line	2nd Sing. Vector

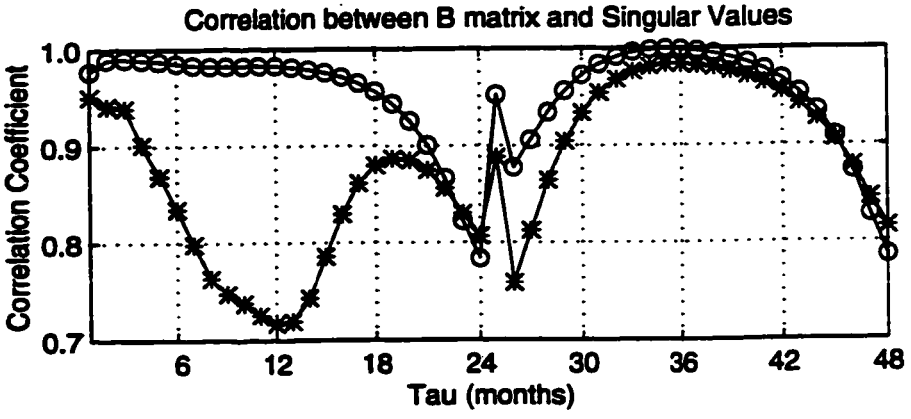

Figure 7.6 - Comparison of the Singular Vectors with Eigenvectors of B-matrix. The correlation coefficient of the first two singular vectors with the first two eigenvectors of $\mathbf{B}^{\tau}$ as a function of τ.

Key	
Circles	1st Sing. Vector
Asterisks	2nd Sing. Vector

Chapter 8: Summary and Discussion

8.1 Summary

In 1987 Zebiak and Cane (1987) coupled a simple two layer ocean model with a simple Gill-type atmosphere model, thus producing the first physically based model of the tropical Pacific that exhibits self-sustaining quasi-periodic fluctuations of the anomalous SST that are qualitatively similar to ENSO. The Zebiak-Cane model (ZCM) has been very successful, both as a "pure" research tool used for understanding the mechanisms of ENSO, and as a forecast model. The nature of the ENSO phenomenon in the ZCM is as follows: (i) ENSO is linearly unstable, (ii) warm and cold event amplitude is limited in size by non-linearities, (iii) event irregularity is caused by chaos. The success of the ZCM has established the unstable chaotic view of ENSO as the dominant view in the field. However, a different hypothesis has been suggested: (i) ENSO is essentially linear, (ii) event size is limited because the system is intrinsically stable, (iii) amplitude is sustained by external forcing, (iv) irregularity is caused by external forcing. In other words, ENSO is best modelled as a linear, stable, stochastically forced phenomenon. The primary objective of this research has been to establish the plausibility of this second hypothesis through the construction of a physical intermediate model similar to the ZCM.

The research starts (Chapter 2) by constructing a linearized version of the Battisti (1988) model, which is very similar to the ZCM. In Chapter 3, this linear ocean atmosphere model (LOAM), in a constant background configuration, is subjected to optimal initial condition analysis. Among a number of secondary results (see Section 3.7), Chapter 3 establishes that LOAM, given the correct initial conditions, can experience transient growth which is much greater than the modal growth of the system (Section 3.1.3). It was also shown that these optimal initial conditions quickly (in 3 to 6

months) develope into the ENSO mode. The model stability was then changed by modifying the background states, and two other cases were tested: a case where the system is neutral and a case where the system is damped. Both of these cases still show large transient growth (see Section 3.4). These results suggest that it might be possible to build a linear model (neutral or damped) that produces ENSO events through stochastic forcing.

In Chapter 4, LOAM was altered to include the annual cycle in the background. Again the optimal conditions for transient growth (singular values) were calculated, but because of the cyclic background, the singular values now have a second dimension. Not only are the singular values a function of optimization period, τ, but they are also a function of the start month. As with the constant background case, the model has large transient growth, but it is also observed that the growth from the optimal conditions tends to peak during the winter months, almost independent of start month and τ (see Fig. 4.9). This suggests that a stochastically forced model, even if the forcing is uniform throughout the year, will tend to have ENSO events peak that during the boreal winter. This is in agreement with observations of the Pacific basin.

LOAM is unstable in its nominal configuration (with B88M parameters), and so must be modified to make it either neutral or damped if it is going to be stochastically forced. There are many ways in which the model could be damped: why not damp it in a way which reduces the modal growth, while preserving the transient growth? In Chapter 5, sensitivity studies are carried out on a number of parameters whose correct values are imprecisely known. These parameter studies show that if the western boundary reflection is reduced, and the mechanical damping of the ocean is increased, LOAM can be stabilized with only small loss in transient growth (see Section 5.2). It should be noted that both of these parameter changes are supported by observational studies. Four candidate models are constructed: two that are slightly damped, one that

is moderately damped, and one that is highly damped (Section 5.3).

In Chapter 6, each of the four candidate models is forced by stochastic perturbations (Section 6.1), and their output is analysed (Section 6.2). The analysis shows that of the four models, the moderately damped model (named T.80) displays behaviour most like the observations. Three perturbation schemes where used, but the models' behaviour under the various schemes was similar. The most generic of the forcing schemes (Section 6.1.1) consisted of twice monthly perturbations in the SSTA field. These perturbations were uniformly distributed in space with a standard deviation of about 0.18 degrees C (for model T.80), which produced ENSO-like variability in the SSTA (see Fig. 6.2 through Fig. 6.4). Analysis of the simulation runs show that the peak ENSO events are the cumulative effect of many perturbations (Figs. 6.13 and 6.14). The analysis also shows that the variability of the Nino3 index can be explained for the most part by the projection of the noise onto the first singular vector (Section 6.2.1). The implication of these models for the limit of predictability of ENSO is explored in Section 6.3. The potential predictability estimate for the most realistic model, T.80, is fairly short: in the range of 12 to 18 months (see Fig. 6.18).

Finally, in Chapter 7 a number of the results of the stochastically perturbed simulations are verified using stochastic differential equations (SDEs). The equations of LOAM are modified to include a Gaussian white noise forcing term, and a time invariant background version of the T.80 model is analysed. The theoretically derived EOFs from the SDE version of LOAM were found to be essentially the same as those from a stochastically perturbed simulation (Section 7.3.1). Also the SST pattern that produced the highest percentage of variance in the SDE model was shown the be essentially the same as the optimal initial conditions previously calculated.

8.2 Discussion

Several other studies have recently been made using singular value decomposition (or optimal initial condition analysis) on intermediate models of ENSO in order to estimate the predictability/error growth of the system. Specifically, Moore and Kleeman (1996, 1997a and 1997b), performed singular vector analysis on the coupled ocean-atmosphere model by Kleeman (1993), while Xue et al. (1996a and 1996b) and Chen et al. (1997) performed similar analysis on the ZCM and Battisti models, respectively. In Chapter 3, an extensive comparison was made between the singular vectors from LOAM, and the singular vectors found in these three studies.

No such direct comparison of results was made between the predictability estimates of LOAM and the predictability estimates of the above three studies. The change in the nature of the model from a chaotic, deterministic model (e.g. ZCM, Battisti and Kleeman models) to a non-chaotic stochastic model, (e.g. LOAM) changes the interpretation of the predictability analysis.

The studies dealing with deterministic chaotic models estimate the limit of predictability as the growth of the (probable) errors in the initial conditions. The brute force method of making this calculation would be to run the initial value problem repeatedly, with a distribution of initial condition that reflect the probable distribution of initial errors (i.e. similar to ensemble forecasting). A more elegant method for approximately solving this problem using singular vector analysis was first suggested by Lorenz (1965), and more recently revived by Farrell (1990) and elaborated by Palmer et al. (1996). This method consists of approximating the short term evolution of the system (from a given state) with the linear tangent propagator. Singular value decomposition is then performed on the linear tangent propagator to find the pattern (or patterns) which produce the most growth.

The difference in the predictability estimates between the two types of models is

simply this: the chaotic deterministic models assume that all error comes from the initial conditions, whereas the linear stochastic model assumes that the initial conditions are less important, and that error growth comes from the intrinsically unpredictable external forcing over the forecast period. Obviously, forecast error comes from both, but the calculations in Chapter 6 show the predictability *limit* (i.e. assuming perfect initial conditions). Because LOAM is linear and stable it is not sensitive to small errors in the initial conditions. The same singular value decomposition that is carried out on the chaotic models can be used on the linear stochastic model (and was in Chapter 3), but it does not have the same implications for predictability.

The linear stochastic model is, in a sense, a step backward in ENSO modeling. The implication of the ZCM is that all the relevant physics of the ENSO phenomenon is contained in the equatorial waveguide, that ENSO's irregularity is internally generated by chaos, and that external forcing has a negligible effect. The implication of LOAM is that the source of irregularity in ENSO is still unknown, and may be external the model.

8.3 Future work

The main point of this research has been to make a plausible, physically based, model of ENSO that is in a different dynamical regime from previous models of ENSO. While the plausibility of the the stable ENSO model has been established by the work done here. Unfortunately, no clear cut test has presented itself that would prove or disprove the validity of this dynamical regime. Nevertheless, there is much work that can be done to increase or decrease the weight of the evidence for the model. In addition, there is much work to be done to determine the implications of this model (assuming that the model is valid). This section has been divided into three categories of possible future work: (1) model verification, (2) model improvement, and (3) model implications.

8.3.1 Model verification

A number of statistical tests were run in Chapter 6 to compare the behaviour of LOAM with the observations of the Equatorial Pacific. Additionally, some simple hindcasting was done in Chapter 5. Other work that could be done for model verification are:

1) *Improved Hindcasting.* To improve hindcasting, the assimilation technique for LOAM should be improved. The method used in Chapter 5, which is outlined in Appendix E, uses only the history of the SST to initialize the models. This was done because the LOAM, as it is currently written, can only solve the initial value problem. For most forecasting models, the thermocline and currents are initialized by running the ocean portion of the model being forced by observational winds (i.e. as a boundary value problem). But since LOAM is not set up to run the boundary value problem, and since observational data of the thermocline exists for only the last ten years or so, the SST-only assimilation of Appendix E was used. An obvious improvement would be to make an integrable version of LOAM so that wind data can be assimilated into the thermocline initial state.

2) *Comparison to Zebiak-Cane Model.* Even though LOAM is supposed to be an incremental improvement to the ZCM, no direct comparison was made between the two models in this research. This was avoided because it was felt that the most important comparison point between the two models would be the hindcast accuracy. As dramatic as the differences in these two models may appear (in terms of their mathematical properties) they will probably produce similar forecasts if initialized equivalently. The main parameter differences: the western boundary reflection and ocean damping, effect the longer time scale behaviour of the models, and will not have as strong effect on the 6 to 12 month forecasts. To make an accurate comparison both models will have to be initialized similarly, and presumably using the best available assimilation technique.

8.3.2 Model improvement

LOAM, like the ZCM and B88M from which it was derived, has a number of known defects that probably can be eliminated. These defects include: (i) the mature ENSO event (i.e. first EOF) in LOAM is too equatorially confined, and compared to observations does not extend far enough westward into the central Pacific; (ii) the EOFs of the observations indicate that nature has additional degrees of freedom compared to LOAM which has only the ENSO mode; (iii) the Nino3 standard deviation (by month) of LOAM is noticeably different form observations (see Fig. 6.4 for example); and (iv) observations show that the warm and cold events are not symmetric in their development (warm events tend to be stronger than cold), but LOAM, due to its linearity and the uniformity of the forcing applied to it, produces warm and cold events which are equivalent. These problems with the model might be solved by the following model improvements.

1) *Improve Background Fields (Upwelling).* Two of the background fields are produced directly from observations: the SST and winds. However, the background surface currents and upwelling fields are both produced by running the observed winds over the model itself. This was done because of lack of observation of these fields, although there is no particular reason to believe that these models produce an accurate annual cycle. The upwelling field is particularly important, and probably the least well known of the background fields. There are two approaches that might be used to improve the background fields. (i) Using an existing model that is designed to reproduce the annual cycle, generate the currents and upwelling from the observed winds. (ii) From the best available observations, establish a range within which the true upwelling probably exists, and then explore the model response to the range of plausible background fields in order to eliminate some of the known deficiencies listed above. In

particular, the disparity between LOAM and nature that is evident in the higher order EOFs and in the annual cycle of SST variance may well be the fault of incorrect background fields.

2) *Improved Background Fields (Thermocline).* The background thermocline field in this model is quite simple: it has no annual cycle and varies only in the zonal direction. Owing to the improvements in the observing system in the last 10 years (since the ZCM was built), an annual cycle and meridional variation is known well enough to be added to the model. As with altering other background fields, this may improve the EOF structure, and/or the annual cycle of variance of the model.

3) *Change Forcing.* A few different forcing regimes were used in this research, but much more could be done in this area. The problem can be attacked on two fronts. (i) Determine from observations the possible forcing structures and amplitudes (i.e. the noise). Of specific interest is how well the forcing projects onto the optimals, and whether the forcing is constant over the year or has an annual cycle. (ii) Within the constraints of observational data, the reaction of the model to various forcing regimes should be explored. Specifically, the possible effects of an annual cycle in the forcing should be explored. More realistic forcing schemes have the potential to explain the deficiency in the annual cycle of variance, that is, deficiency (iii) above. It is even possible that if the forcing where not symmetric with respect to warm and cold events, it could address deficiency (iv) above.

4) *Include Nonlinearity.* The introduction of nonlinearity to LOAM would make it impossible to write the equations in matrix-operator form, the simplicity of which provides much of the power of LOAM as a research tool. Nevertheless, a nonlinear response by the atmosphere to SST may well be the explanation for the differences in the amplitude of warm and cold events found in the observations.

5)*Miscellaneous Improvements.* The two following improvements do not

specifically address any of the model deficiencies listed above, but may improve the model overall performance. (a) The Gill-type atmosphere is probably the weakest part of the coupled model. A multi-layer atmosphere, or even an empirical model of the atmosphere may improve performance. (b) One of the ocean characteristics which the mechanical damping parameter in the ocean is meant to parameterize dissipation of energy, including an ad hoc treatment of the loss of energy at the surface via vertical propagation. This vertical propagation is important in nature, but disallowed by the 1.5 layer dynamics in LOAM. With the increased importance of the drag in T.80, it may make sense to add a second layer to the ocean model to more accurately characterize mechanical dissipation.

8.3.3 Model implications

Assuming that this model reflects some of the characteristics of the real ENSO system, a number of important questions about ENSO can be addressed.

1) *What is the potential predictability limit of ENSO?*

This a question of fundamental importance, and is addressed somewhat in Chapter 6, but more must be done to better answer this question. The next step is to use LOAM, preferably a version which includes some of the improvements listed above, to establish a "best guess" model. Currently, T.80 is the best guess, but reflects only a rather coarse search of parameter space. The sensitivity of the predictability then needs to be tested. The results of Chapter 6 indicate that the predictability limit may be sensitive to the stability of the ENSO mode.

2a) *What is the best assimilation scheme for forecasting?*

2b) *What is the best sensor array for forecasting?*

These are related questions. The underlying question is: what is the importance of resolving the optimal structure for the prediction of ENSO? The SST field for 6

months in the future (for example) could be thought of, crudely, as the sum of the noise forcing integrated over three stages of development:

(1) the period from $t = -\infty$ to $t = -3$ *months*; by $t = 0$ the signal from this forcing will look like the ENSO mode,

(2) the period from $t = -3$ *months* to $t = 0$; the signal from this forcing period will not have developed fully into the ENSO mode, and so may not be easy to resolve,

(3) the period from $t = 0$ to $t = 6$ *months*; since this forcing is in the future it will probably be unknowable (except possibly in a statistical manner).

Resolving the current phase and amplitude of the ENSO mode from stage (1) is obviously an important part of job of the assimilation scheme and optimals can obviously help. However, can our knowledge of the optimals help to resolve the contribution from stage (2)? Unless the forcing from stage (3) can be predicted to some degree, noise forcing during stage (3) will determine the (minimum) error bound on the forecast.

3) *Is the thermocline either unimportant or in steady state with the SST, as implied by Penland and Sardeshmukh (1995), and thus redundant information for the ENSO forecast?*

Penland and Sardeshmukh (1995), hereafter PS95, also built a linear, stochastically driven model for ENSO. PS95's model is a statistical Markov model, based only on the observations of the SST. The ability to model ENSO using only SST as a variable, implies that the thermocline is either unimportant to ENSO, or else approximately in steady state with the SST. LOAM can be modified to put the thermocline in steady state with the atmosphere, and the plausibility of this model of ENSO can be explored.

4) *Is the annual cycle in the variance caused by: (a) the annual cycle in the background states, (b) the annual cycle in the stochastic forcing, or (c) both?*

Unlike LOAM, the Markov model of PS95 has no annual cycle in the background

states (i.e. PS95 forms a single propagator matrix that is independent of time). PS95 reproduces the statistics of ENSO (in particular the annual cycle of variance) by using a forcing function that has an annual cycle. The response of LOAM to cyclic forcing can be explored.

5) *What is the cause of the asymmetry between warm and cold events: non-linearities or asymmetric forcing?*

LOAM does not reproduce the asymmetry between warm and cold events in its current incarnation. Can this asymmetry be explained with asymmetric forcing, or will non-linearities be required?

REFERENCES

Battisti, D.S., 1988: The dynamics and thermodynamics of a warming event in a coupled tropical atmosphere-ocean model. *J.Atmos.Sci.*, **45**, 2889-2919.

Battisti, D.S., and A.C. Hirst, 1989: Interannual variability in the tropical atmosphere-ocean system: influence of the basic state, ocean geometry and nonlinearity. *J.Atmos.Sci.*, **46**, 1687-1712.

Blumenthal, M.B., 1991: Predictability of a coupled ocean-atmosphere model. *J. Climate*, **4**, 766-784.

Borges, M.D., and P.D. Sardeshmukh, 1995: Barotropic Rossby wave dynamics of zonally varying upper-level flows during northern winter. *J. Atmos. Sci.*, **52**, 3779-3796.

Buizza, R., and T.N. Palmer, 1995: The singular-vector structure of the atmospheric general circulation. *J. Atmos. Sci.*, **52**, 1434-1456.

Cane, M.A., and E.S. Sarachik, 1976: Forced baroclinic ocean motions, I: the linear equatorial unbounded case. *J. Mar. Res.*, **34**, 629-665.

Cane, M.A., and E.S. Sarachik, 1977: Forced baroclinic ocean motions, II: the linear equatorial bounded case. *J. Mar. Res.*, **35**, 395-432.

Cane, M.A., and E.S. Sarachik, 1979: Forced baroclinic ocean motions, III: the linear equatorial basin case. *J. Mar. Res.*, **37**, 355-398.

Cane, M.A., S.E. Zebiak, and S.C. Dolan, 1986: Experimental forecasts of El Nino. *Nature*, **321**, 827-832.

Chang, P., Ji, L., Li, H., and M. Flugel, 1997: Chaotic dynamics versus stochastic processes in El Nino-Southern Oscillation in coupled ocean-atmosphere models. *Physica D.*, in press.

Chen, D., S.E. Zebiak, A.J. Busalacchi, and M.A. Cane, 1995: An improved procedure for El Nino forecasting: implications for predictability. *Science*, **269**, 1699-1702.

Chen, Y.-Q., D.S. Battisti, T.N. Palmer, J. Barsugli, and E.S. Sarachik, 1997: A study of the predictability of tropical Pacific SST in a coupled atmosphere-ocean model using singular vector analysis: the role of the annual cycle and the ENSO cycle. *Mon. Weather Rev.*, in press.

Clarke, A. J., 1983: The reflection of equatorial waves from oceanic boundaries. *J. Phys. Oceanogr.*, **13**, 1193-1207.

Clarke, A. J., 1991: On the reflection and transmission of low-frequency energy at the irregular western Pacific Ocean boundary. *J. Geophys. Res.*, **96**, 3289-3305.

du Penhoat, Y., and M.A. Cane 1991: Effects of low-latitude western boundary gaps on the reflection of equatorial motions. *J. Geophys. Res.*, **96**, 3307-3322.

Farrell, B., 1988a: Optimal excitation of perturbations in viscous shear flow. *Phys. Fluids*, **31**, 2093-2102.

Farrell, B., 1988b: Optimal excitation of neutral Rossby waves. *J. Atmos. Sci.*, **45**, 163-172.

Farrell, B., 1989: Optimal excitation of baroclinic waves. J. Atmos. Sci., 46, 1193-1206.

Farrell, B., 1990: Small error dynamics and the predictability of atmospheric flows. *J. Atmos. Sci.*, **47**, 2409-2416.

Farrell, B., and P. Ioannou, 1993: Stochastic forcing of the linearized Navier-Stokes equations. *Phys. Fluids A*, **5**, 2600-2609.

Gardiner, G. 1985: *Handbook of Stochastic Methods*, 2nd Ed. Springer, 80-115.

Gill, A.E., 1980: Some simple solutions for heat-induced tropical circulation. *Quart. J. R. Metr. Soc.*, **106**, 447-462.

Hayes, S.P., L.J. Mangum, J. Picaut, A. Sumi, and K. Takeuchi, 1991: TOGA-TAO: A moored array for real-time measurements in the tropical Pacific Ocean. *Bull. Amer. Meteor. Soc.*, **72**, 339-347.

Hirst, A.C., 1988: Slow instabilities in tropical ocean basin-global atmosphere models. *J. Atmos. Sci.*, **45**, 830-852.

Iooss, G., and D.D. Joseph, 1980: *Elementary Stability and Bifurcation Theory*, Springer-Verlag, 126-133.

Jin, F., D. Neelin, and M. Ghil, 1994: El Nino on the Devil's Staircase: Annual subharmonic steps to chaos. *Science*, **264**, 70-72.

Kirtman, B., and P. Schopf, 1997: Decadal Variability in ENSO Predictability and Prediction. *J. Atmos. Sci.*, submitted.

Kleeman, R., 1993: On the dependence of hindcast skill on ocean thermodynamics is a coupled ocean-atmosphere model. *J. Climate*, **6**, 2012-2033.

Lacarra, J.-F., and O. Talagrand, 1988: Short-ranged evolution of small perturbations in a barotropic model. *Tellus*, **40A**, 81-95.

Latif, M., T.P. Barnett, M.A. Cane, M.Fluegel, N.E. Graham, H. von Storch, J.-S. Xu, and S.E. Zebiak, 1994: A review of ENSO prediction studies. *Climate Dynamics*, **9**, 167-179.

Linzen, R., and S. Nigam, 1987: On the role of sea surface temperature gradients in forcing low-level winds and convergence in the tropics. *J. Atmos. Sci.*, **44**, 2440-2458.

Lorenz, E.N., 1965: A study of the predictability of a 28-variable atmospheric model. *Tellus*, **17**, 321-333.

Luenberger, D.G., 1969: *Optimization by Vector Space Methods*. John Wiley and Sons, 22-24.

Madden, R.A., and P.R. Julian, 1971: Detection of a 40-50 day oscillation in the zonal wind in the tropical Pacific. *J. Atmos. Sci.*, **28**, 702-708.

Mantua, N.J., and D.S. Battisti, 1995: Aperiodic variability in the Zebiak-Cane coupled ocean-atmosphere model: air-sea interactions in the western equatorial Pacific. *J.Climate*, **8**, 2897-2927.

Moore, A.M., and R. Kleeman, 1996: The dynamics of error growth and predictability in a coupled model of ENSO. *Q. J. R. Meteorol. Soc.*, **122**, 1405-1446.

Moore, A.M., and R. Kleeman, 1997a: The singular vectors of a coupled ocean-atmosphere model of ENSO. I: Thermodynamics, energetics and error growth. *Q. J. R. Meteorol. Soc.*, **123**, 953-982.

Moore, A.M., and R. Kleeman, 1997b: The singular vectors of a coupled ocean-atmosphere model of ENSO. II: Sensitivity studies and dynamical interpretation. *Q. J. R. Meteorol. Soc.*, **123**, 983-1006.

Moura, A.D., 1994: Prospects for seasonal-to-interannual climate prediction and applications for sustainable development. *World Meterological Society Bulletin*, **43**, 207-215.

Noble, B., and J.W. Daniel, 1988: *Applied linear algebra*. 3rd Ed. Prentice-Hall, 338-345.

North, G.R., 1982: Sampling errors in the estimation of empirical orthogonal functions. *Mon. Wea. Rev.*, **110**, 699-706.

Palmer, T.N., R. Gelaro, J. Barkmeijer, and R. Buizza, 1996: Singular vectors, metrics, and adaptive observations. *J. Atmos. Sci.*, submitted.

Penland, C., and P.D. Sardeshmukh, 1995: The optimal growth of tropical sea surface temperature anomalies. *J. Climate*, **8**, 1999-2024.

Philander, S.G.H., R.C. Pacanowski, N.-C. Lau, and M.J. Nath, 1992: Simulation of ENSO with a global atmospheric GCM coupled to a high-resolution tropical Pacific Ocean GCM. *J. Climate*, **5**, 308-329.

Picaut, J., C. Menkes, J-P. Boulanger, and Y. du Penhout, 1993: Dissipation in a Pacific equatorial long wave model. *TOGA Notes*, January 1993, 11-15

Rasmusson, E.M., and T.H. Carpenter, 1982: Variations in tropical sea surface temperatures and surface wind fields associated with the Southern Oscillation and El Nino. *Mon. Wea. Rev.*, **110**, 354-384.

Salby, M.L., and H.H. Hendon, 1994: Interseasonal behavior of clouds, temperature, and motion in the tropics. *J. Atmos. Sci.*, **51**, 2207-2224.

Suarez, M.J., and P.S. Schopf, 1988: A delayed action oscillator for ENSO. *J. Atmos. Sci.*, **45**, 3283-3287.

Thompson, C.J., 1997: Initial conditions for optimal growth in a coupled ocean-atmosphere model of ENSO. *J. Atmos. Sci.*, in press.

Tziperman, E., L. Stone, M. Cane, H. Jarosh, 1994: El Nino chaos: Overlapping of resonances between the seasonal cycle and the Pacific ocean-atmosphere oscillator. *Science*, **264**, 72-74.

Wakata, Y., and E.S. Sarachik, 1991: Unstable coupled atmosphere-ocean basin modes in the presence of a spatially varying basic state. *J. Atmos. Sci.*, **48**, 2060-2077.

Woodruff, S.D., S.J. Lubker, K. Wolter, S.J. Worley, and J.D. Elms, 1993: Comprehensive Ocean-Atmosphere Data Set (COADS) Release 1a: 1980-1992. *Earth System Monitor*, **4**, 1-8.

Xue, Y., M.A. Cane, and S.E. Zebiak, 1996a: Predictability of a coupled model of ENSO using singular vector analysis. Part I: Optimal growth in seasonal background and ENSO cycles. *Mon. Weather Rev.*, submitted.

Xue, Y., M.A. Cane, S.E. Zebiak, and T.N. Palmer, 1996b: Predictability of a coupled model of ENSO using singular vector analysis. Part II: Optimal growth and forecast skill. *Mon. Weather Rev.*, submitted.

Zebiak, S.E., 1986: Atmospheric convergence feedback in a simple model for El Nino. *J. Atmos. Sci.*, **114**, 1263-1271.

Zebiak, S.E., and M.A. Cane, 1987: A model ENSO. *Mon. Weather Rev.*, **115**, 2262-2278.

Appendix A: Non-Dimensionalization of Equations

A.1 Scaling

The basic linear equations (2.1) through (2.37) will be non-dimensionalized using different scales for the ocean and the atmosphere. The atmosphere will use a length scale of

$$\lambda_a = (c_a/\beta)^{1/2}, \tag{A.1}$$

and a time scale

$$\mu_a = (c_a\beta)^{-1/2}. \tag{A.2}$$

Similarly, for the ocean

$$\lambda_o = (c_o/\beta)^{1/2}, \text{ and} \tag{A.3}$$

$$\mu_o = (c_o\beta)^{-1/2}. \tag{A.4}$$

The values of $c_a = 60\, ms^{-1}$, and $c_o = 2.9\, ms^{-1}$ are used here for the atmospheric and oceanic characteristic wave speeds, respectively, and $\beta = 2.2915 \cdot 10^{-11}\, m^{-1}s^{-1}$.

A.2 Atmosphere Non-dimensionalization

From above the (non-dimensional) independent variables are set

$$x^* = x/\lambda_a, \text{ and } t^* = t/\mu_a.$$

The dependent variables are then set

$$U^* = U/c_a,\ V^* = V/c_a,\ \varphi^* = \varphi/c_a^2, \text{ and } T^* = T/\overline{\Delta T},$$

where the temperature non-dimensionalization is $\overline{\Delta T} = 14C$. The non-dimensional atmospheric equations become:

$$A^*U^* - y^*V^* + \frac{\partial \varphi^*}{\partial x^*} = 0, \tag{A.5}$$

$$y^*U^* + A^*V^* + \frac{\partial \varphi^*}{\partial y^*} = 0, \tag{A.6}$$

$$\frac{\partial U^*}{\partial x^*} + \frac{\partial V^*}{\partial y^*} + A^*\varphi^* = -K_Q^*T^* + K_C^*\left(\frac{\partial U^*}{\partial x^*} + \frac{\partial V^*}{\partial y^*}\right), \tag{A.7}$$

where

$$A^* = A\mu_a,\ K_Q^* = K_Q\left(\overline{\Delta T}\mu_a / c_a^2\right),\ \text{and}\ K_C^* = K_C / c_a^2. \tag{A.8}$$

Combining (2.9) with (A.8) the following is obtained,

$$K_Q^* = \gamma^*\left[\frac{T_{ref}}{\overline{T}}\right]^2 \exp\left(b\left(\frac{1}{T_{ref}} - \frac{1}{\overline{T}}\right)\right),\ \text{where}\ \gamma^* = \sqrt{2}\gamma\overline{\Delta T}/c_a. \tag{A.9}$$

A.3 Ocean Non-dimensionalization

From above the (non-dimensional) independent variables are set

$$x^* = x/\lambda_o,\ \text{and}\ t^* = t/\mu_o.$$

The dependent variables are then set

$$u^* = u/c_o,\ v^* = v/c_o,\ h^* = h/H_0, U_o^* = U/c_o,\ \text{and}\ V_o^* = V/c_o.$$

The non-dimensional equations for the ocean dynamics then become:

$$a^*u^* - y^*v^* + \frac{\partial h^*}{\partial x^*} = -\frac{\partial u^*}{\partial t^*} + (K_S^x)^* U_o^* + (K_S^c)^* V_o^*, \tag{A.10}$$

$$y^*u^* + a^*v^* + \frac{\partial h^*}{\partial y^*} = (K_S^c)^* U_o^* + (K_S^y)^* V_o^*, \tag{A.11}$$

$$\frac{\partial u^*}{\partial x^*} + \frac{\partial v^*}{\partial y^*} + a^*h^* = -\frac{\partial h^*}{\partial t^*}, \tag{A.12}$$

where

$$a^* = a\mu_o,\ (K_S^x)^* = \mu_o K_S^x,\ (K_S^y)^* = \mu_o K_S^y,\ \text{and}\ (K_S^c)^* = \mu_o K_S^c. \tag{A.13}$$

Note that the non-dimensional wind variables still use atmospheric scaling.

A.4 Ekman Layer Non-dimensionalization

The Ekman layer used the same scaling as the ocean dynamics with

$$u_s^* = u_s/c_o,\ \text{and}\ v_s^* = v_s/c_o.$$

The non-dimensionalization of (2.23) and (2.24) becomes:

$$r_s^*u_s^* - y^*v_s^* = \frac{H_0}{H_1}\left[(K_S^x)^* U_o^* + (K_S^c)^* V_o^*\right] \equiv \sigma_x^*,\ \text{and} \tag{A.14}$$

$$y^*u_s^* + r_s^*v_s^* = \frac{H_0}{H_1}\left[(K_S^c)^* U_o^* + (K_S^y)^* V_o^*\right] \equiv \sigma_y^*, \tag{A.15}$$

where $r_s^* = r_s \mu_o$, and the other coefficients are as above. Some algebraic manipulation yields:

$$u_s^* = \frac{y^* \sigma_y^* + r_s^* \sigma_x^*}{(r_s^*)^2 + (y^*)^2}, \text{ and} \tag{A.16}$$

$$v_s^* = \frac{r_s^* \sigma_y^* - y^* \sigma_x^*}{(r_s^*)^2 + (y^*)^2}. \tag{A.17}$$

Also for use in the thermal equation (2.20) to (2.26) can be combined to obtain

$$v_1^* = v^* + \frac{H_2}{H_0} v_s^*, \text{ and} \tag{A.18}$$

$$u_1^* = u^* + \frac{H_2}{H_0} u_s^*. \tag{A.19}$$

A.5 Thermal Equation Non-dimensionalization

The independent variables are set as in the ocean and the dependent variables,

$$u_1^* = u_1 / c_o,\ v_1^* = v_1 / c_o,\ h^* = h / H_0, \text{ and } T^* = T / \overline{\Delta T}.$$

This yields

$$\left[K_w^* \frac{\partial}{\partial x^*} + \overline{T}_x^*\right] u_1^* + \left[K_w^* \frac{\partial}{\partial y^*} + \overline{T}_y^*\right] v_1^* - K_T^* h^* + \left[\overline{u}_1^* \frac{\partial}{\partial x^*} + \overline{v}_1^* \frac{\partial}{\partial y^*} + d^*\right] T^* = -\frac{\partial T^*}{\partial t^*}, \tag{A.20}$$

where

$$K_w^* = \left(\frac{1}{\overline{\Delta T}}\right) K_w,\ \overline{T}_x^* = \left(\frac{\lambda_o}{\overline{\Delta T}}\right) \overline{T}_x,\ \overline{T}_y^* = \left(\frac{\lambda_o}{\overline{\Delta T}}\right) \overline{T}_y,\ K_T^* = \left(\frac{H_0 \mu_o}{\overline{\Delta T}}\right) K_T, \text{ and} \tag{A.21}$$

$$\overline{u}_1^* = \overline{u}_1 / c_o,\ \overline{v}_1^* = \overline{v}_1 / c_o, \text{ and } d^* = \mu_o d. \tag{A.22}$$

A.6 Combining Ekman Layer with Thermal Equation

At this point all variables are non-dimensional and asterisks are dropped. The thermal equation (A.20) can be written in terms of the dependent variables only if the Ekman layer equations, (A.14) through (A.19), are substituted. After some algebra the thermal equation becomes:

$$\left[K_U^x\frac{\partial}{\partial x}+K_U^y\frac{\partial}{\partial y}+K_U\right]U_o+\left[K_V^x\frac{\partial}{\partial x}+K_V^y\frac{\partial}{\partial y}+K_V\right]V_o+$$
$$\left[K_w\frac{\partial}{\partial x}+\bar{T}_x\right]u+\left[K_w\frac{\partial}{\partial y}+\bar{T}_y\right]v-K_T h+\left[\bar{u}_1\frac{\partial}{\partial x}+\bar{v}_1\frac{\partial}{\partial y}+d\right]T=-\frac{\partial T}{\partial t} \tag{A.23}$$

where

$$K_U^x(x,y)=\frac{H_2}{H_1}\cdot\frac{1}{r_s^2+y^2}\left[yK_wK_S^c+r_sK_wK_S^x\right], \tag{A.24}$$

$$K_U^y(x,y)=\frac{H_2}{H_1}\cdot\frac{1}{r_s^2+y^2}\left[r_sK_wK_S^c-yK_wK_S^x\right], \tag{A.25}$$

$$\begin{aligned}K_U(x,y)=\frac{H_2}{H_1}\cdot\frac{1}{r_s^2+y^2}\Big[\;& yK_w\left(K_S^c\right)_x+y\bar{T}_xK_S^c+r_sK_w\left(K_S^x\right)_x+r_s\bar{T}_xK_S^x\\&+r_sK_w\left(K_S^c\right)_y+r_s\bar{T}_yK_S^c-K_wK_S^x-yK_w\left(K_S^x\right)_y-y\bar{T}_yK_S^x\\&+\frac{2y^2}{r_s^2+y^2}K_wK_S^x-\frac{2yr_s}{r_s^2+y^2}K_wK_S^c\Big]\end{aligned} \tag{A.26}$$

and

$$K_V^x(x,y)=\frac{H_2}{H_1}\cdot\frac{1}{r_s^2+y^2}\left[yK_wK_S^y+r_sK_wK_S^c\right], \tag{A.27}$$

$$K_V^y(x,y)=\frac{H_2}{H_1}\cdot\frac{1}{r_s^2+y^2}\left[r_sK_wK_S^y-yK_wK_S^c\right], \tag{A.28}$$

$$\begin{aligned}K_V(x,y)=\frac{H_2}{H_1}\cdot\frac{1}{r_s^2+y^2}\Big[\;& yK_w\left(K_S^y\right)_x+y\bar{T}_xK_S^y+r_sK_w\left(K_S^c\right)_x+r_s\bar{T}_xK_S^c\\&+r_sK_w\left(K_S^y\right)_y+r_s\bar{T}_yK_S^y-K_wK_S^c-yK_w\left(K_S^c\right)_y-y\bar{T}_yK_S^c\\&+\frac{2y^2}{r_s^2+y^2}K_wK_S^c-\frac{2yr_s}{r_s^2+y^2}K_wK_S^y\Big].\end{aligned} \tag{A.29}$$

A.7 Some Diagnostic Recombinations

For diagnostic purposes it may be convenient to rearrange the above equations. For instance, the surface currents are never solved for explicitly. Taking the appropriate terms from equations (A.23) through (A.29) they can be found as,

$$u_1=u+M_U^{u_1}U_o+M_V^{u_1}V_o, \text{ and} \tag{A.30}$$

$$v_1=M_U^{v_1}U_o+M_V^{v_1}V_o, \tag{A.31}$$

where

$$M_U^{u_s} = \frac{H_2}{H_1}\cdot\frac{1}{r_s^2+y^2}\left[yK_S^c + r_sK_S^x\right],\ M_V^{u_s} = \frac{H_2}{H_1}\cdot\frac{1}{r_s^2+y^2}\left[yK_S^y + r_sK_S^c\right], \tag{A.32}$$

$$M_U^{v_s} = \frac{H_2}{H_1}\cdot\frac{1}{r_s^2+y^2}\left[r_sK_S^c - yK_S^x\right], \text{and } M_V^{v_s} = \frac{H_2}{H_1}\cdot\frac{1}{r_s^2+y^2}\left[r_sK_S^y - yK_S^c\right]. \tag{A.33}$$

Turning to the thermal equation (2.34), the advective terms can be written in slightly expanded form as

$$-\frac{\partial T}{\partial t} = K_w\frac{\partial}{\partial x}\left(u+\frac{H_2}{H_0}u_s\right)+\overline{T}_x\left(u+\frac{H_2}{H_0}u_s\right)+K_w\frac{\partial}{\partial y}\left(\frac{H_2}{H_0}v_s\right)+\overline{T}_y\left(\frac{H_2}{H_0}v_s\right)+\ldots \tag{A.34}$$

The four shear terms are a function only of the surface winds and can be written

$$K_w\frac{\partial}{\partial x}\left(\frac{H_2}{H_0}u_s\right) = \left[K_U^x\frac{\partial}{\partial x}+W_U^{u_s}\right]U_o+\left[K_V^x\frac{\partial}{\partial x}+W_V^{u_s}\right]V_o, \tag{A.35}$$

where

$$W_U^{u_s} = \frac{H_2}{H_1}\cdot\frac{1}{r_s^2+y^2}\left[yK_w\left(K_s^c\right)_x + r_sK_w\left(K_s^x\right)_x\right], \text{and} \tag{A.36}$$

$$W_V^{u_s} = \frac{H_2}{H_1}\cdot\frac{1}{r_s^2+y^2}\left[yK_w\left(K_s^y\right)_x + r_sK_w\left(K_s^c\right)_x\right], \tag{A.37}$$

and

$$\overline{T}_x\left(\frac{H_2}{H_0}u_s\right) = A_U^{u_s}U_o + A_V^{u_s}V_o, \tag{A.38}$$

where

$$A_U^{u_s} = \frac{H_2}{H_1}\cdot\frac{1}{r_s^2+y^2}\left[y\overline{T}_xK_s^c + r_s\overline{T}_xK_s^x\right], \text{and} \tag{A.39}$$

$$A_V^{u_s} = \frac{H_2}{H_1}\cdot\frac{1}{r_s^2+y^2}\left[y\overline{T}_xK_s^y + r_s\overline{T}_xK_s^c\right], \tag{A.40}$$

and

$$K_w\frac{\partial}{\partial y}\left(\frac{H_2}{H_0}v_s\right) = \left[K_U^y\frac{\partial}{\partial y}+W_U^{v_s}\right]U_o+\left[K_V^y\frac{\partial}{\partial y}+W_V^{v_s}\right]V_o, \tag{A.41}$$

where

$$W_U^{v_s} = \frac{H_2}{H_1}\cdot\frac{1}{r_s^2+y^2}\left[r_sK_w\left(K_s^c\right)_y - K_wK_s^x - yK_w\left(K_s^x\right)_y + \frac{2y^2}{r_s^2+y^2}K_wK_s^x - \frac{2yr_s}{r_s^2+y^2}K_wK_s^c\right]. \tag{A.42}$$

and

$$W_V^{v_s} = \frac{H_2}{H_1} \cdot \frac{1}{r_s^2 + y^2} \left[r_s K_w \left(K_s^y \right)_y - K_w K_s^c - y K_w \left(K_s^c \right)_y + \frac{2y^2}{r_s^2 + y^2} K_w K_s^c - \frac{2 y r_s}{r_s^2 + y^2} K_w K_s^y \right], \tag{A.43}$$

and

$$\bar{T}_y \left(\frac{H_2}{H_0} v_s \right) = A_U^{v_s} U_o + A_V^{v_s} V_o, \tag{A.44}$$

where

$$A_U^{v_s} = \frac{H_2}{H_1} \cdot \frac{1}{r_s^2 + y^2} \left[r_s \bar{T}_y K_s^c - y \bar{T}_y K_s^x \right], \text{ and} \tag{A.45}$$

$$A_V^{v_s} = \frac{H_2}{H_1} \cdot \frac{1}{r_s^2 + y^2} \left[r_s \bar{T}_y K_s^y - y \bar{T}_y K_s^c \right]. \tag{A.46}$$

Appendix B: Spectral Decomposition of Equations

B.1 Projecting the Atmosphere onto Hermite Space

The equations, now linearized and non-dimensionalized, are projected onto Hermite functions in the meridional (y) direction. For the ocean dynamics, the three equations are projected onto the long-wavelength Rossby solutions. The Hermite functions onto which the atmosphere and temperature variables will be projected are defined as

$$\psi_n(y) = \pi^{-1/4}\left(2^n n!\right)^{-1/2} \cdot H_n(y) \cdot \exp\left(-y^2/2\right) \quad for \quad n = 0,1,2,\ldots \tag{B.1}$$

where $H_n(y)$ are Hermite polynomials. These functions form a complete set that spans the space of continuous functions on the interval $-\infty < y < \infty$. They are orthogonal on this interval and therefore

$$\int_{-\infty}^{\infty} \psi_n \cdot \psi_m \, dy = \begin{cases} 0 & when \quad n \neq m \\ 1 & when \quad n = m \end{cases}. \tag{B.2}$$

They also have the useful recursive propertys

$$\frac{\partial \psi_n}{\partial y} = \left(\frac{n}{2}\right)^{1/2} \psi_{n-1} - \left(\frac{n+1}{2}\right)^{1/2} \psi_{n+1}, \text{ and} \tag{B.3}$$

$$y\psi_n = \left(\frac{n}{2}\right)^{1/2} \psi_{n-1} + \left(\frac{n+1}{2}\right)^{1/2} \psi_{n+1}. \tag{B.4}$$

The atmospheric variables are expressed as the sum of a finite number of Hermite functions . So

$$U(x,y) = \sum_{n=0,1,\ldots}^{N_a} U_n(x)\psi_n^a(y), \tag{B.5}$$

$$V(x,y) = \sum_{n=0,1,\ldots}^{N_a} V_n(x)\psi_n^a(y), \tag{B.6}$$

$$\varphi(x,y) = \sum_{n=0,1,\ldots}^{N_a} \varphi_n(x)\psi_n^a(y), \text{ and} \tag{B.7}$$

$$T^a(x,y) = \sum_{n=0,1,\ldots}^{N_a} T_n^a(x)\psi_n^a(y). \tag{B.8}$$

The "a" subscript on the Hermite functions indicates that they are in the atmospheric

scaling. Note that the temperature variable is expressed in atmospheric scaling. In the thermal equation, ocean scaling will be used, and so an appropriate translation will be required. With the asterisks dropped, the first non-dimensional atmospheric equation (A.5) can be written

$$A\sum_n U_n\psi_n^a - \sum_n V_n\left(y\psi_n^a\right) + \sum_n \frac{\partial\varphi_n}{\partial x}\psi_n^a = 0. \tag{B.9}$$

Substituting in (B.4)

$$A\sum_n U_n\psi_n^a - 2^{-1/2}\sum_n V_n\left(n^{1/2}\psi_{n-1}^a + (n+1)^{1/2}\psi_{n+1}^a\right) + \sum_n \frac{\partial\varphi_n}{\partial x}\psi_n^a = 0, \tag{B.10}$$

and taking

$$\int_{-\infty}^{\infty} (\text{B.10})\cdot\psi_m^a\, dy \quad for \quad m = 0,1,\ldots,N_a, \tag{B.11}$$

yields a set of equations

$$AU_m + \frac{\partial\varphi_m}{\partial x} - 2^{-1/2}\left((m+1)^{1/2}V_{m+1} + m^{1/2}V_{m-1}\right) = 0 \quad for \quad m = 0,1,\ldots,N_a. \tag{B.12}$$

Notice that a single equation in x and y has been turned into a series of equations in x only. Similar manipulations with (A.6) yields

$$\begin{aligned} &2^{-1/2}\left((m+1)^{1/2}U_{m+1} + m^{1/2}U_{m-1}\right) + AV_m \\ &\quad + 2^{-1/2}\left((m+1)^{1/2}\varphi_{m+1} - m^{1/2}\varphi_{m-1}\right) = 0 \quad for \quad m = 0,1,\ldots,N_a. \end{aligned} \tag{B.13}$$

Things are somewhat more complicated for (A.7), but the same manipulations yield

$$\begin{aligned} &\frac{\partial U_m}{\partial x} + 2^{-1/2}\left((m+1)^{1/2}V_{m+1} - m^{1/2}V_{m-1}\right) + A\varphi_m + \sum_{n=0,1,\ldots}^{N_a} T_n^a\left(K_Q\right)_{nm}^{\psi\psi} \\ &\quad - \sum_{n=0,1,\ldots}^{N_a} \frac{\partial U_n}{\partial x}\left(K_C\right)_{nm}^{\psi\psi} - \sum_{n=0,1,\ldots}^{N_a} V_n\left(K_C\right)_{nm}^{\partial y\psi} = 0 \quad for \quad m = 0,1,\ldots,N_a \end{aligned} \tag{B.14}$$

where

$$\left(F(y)\right)_{nm}^{\psi\psi} \equiv \int_{-\infty}^{\infty} F(y)\cdot\psi_n\cdot\psi_m dy, \text{ and} \tag{B.15}$$

$$\left(F(y)\right)_{nm}^{\partial y\psi} \equiv \int_{-\infty}^{\infty} F(y)\cdot 2^{-1/2}\left(n^{1/2}\psi_{n-1} - (n+1)^{1/2}\psi_{n+1}\right)\cdot\psi_m dy. \tag{B.16}$$

It may seem that there is difficulty for the $m = 0$ cases since there is no negatively indexed Hermite function, but the coefficient for this undefined function is always zero.

B.2 Projecting the SST Equation onto Hermite Space

Next the SST equation (A.23) will be reduced in a similar manner. Here

$$U^o(x,y) = \sum_{n=0,1,\ldots}^{N_o} U_n^o(x)\psi_n^o(y), \tag{B.17}$$

$$u(x,y) = \sum_{n=0,1,\ldots}^{N_o} u_n(x)\psi_n^o(y), \tag{B.18}$$

$$T(x,y) = \sum_{n=0,1,\ldots}^{N_o-2} T_n(x)\psi_n^o(y), \tag{B.19}$$

and similarly for other dependent variables. Notice that the temperature variable will be expanded in two less Hermite functions than the ocean variables - this is done for numerical reasons and is explained elsewhere. In this case all Hermite functions are scaled using the ocean meridional scaling. Substituting and integrating as was done to the atmosphere in the previous section yields a series of equations in x only:

$$\begin{aligned}
\sum_{n=0,1,\ldots}^{N_o} \Big\{ & \left(K_U^x\right)_{nm}^{\psi\psi} \frac{\partial U_n^o}{\partial x} + \left(K_U^y\right)_{nm}^{\partial\psi} U_n^o + \left(K_U\right)_{nm}^{\psi\psi} U_n^o \\
& + \left(K_V^x\right)_{nm}^{\psi\psi} \frac{\partial V_n^o}{\partial x} + \left(K_V^y\right)_{nm}^{\partial\psi} V_n^o + \left(K_V\right)_{nm}^{\psi\psi} V_n^o \\
& + \left(K_w\right)_{nm}^{\psi\psi} \frac{\partial u_n}{\partial x} + \left(\overline{T}_x\right)_{nm}^{\psi\psi} u_n + \left(K_w\right)_{nm}^{\partial\psi} v_n + \left(\overline{T}_y\right)_{nm}^{\psi\psi} v_n - \left(K_T\right)_{nm}^{\psi\psi} h_n \Big\} \\
& + \sum_{n=0,1,\ldots}^{N_o-2} \left\{ \left(\overline{u}_1\right)_{nm}^{\psi\psi} \frac{\partial T_n}{\partial x} + \left(\overline{v}_1\right)_{nm}^{\partial\psi} T_n + \left(d\right)_{nm}^{\psi\psi} T_n \right\} = -\frac{\partial T_m}{\partial t} \quad for \quad m = 0,1,\ldots,N_o-2
\end{aligned} \tag{B.20}$$

B.3 Projecting Ocean Dynamics onto Rossby Space

The three ocean equations (A.10)-(A.12) when unforced have a set of vector solutions that form a complete set. (See Cane and Sarachik, 1976 and others.) Cane and Sarachik give the long-wavelength version of these vectors as

$$\begin{bmatrix} u \\ v \\ h \end{bmatrix}_n = \vec{\xi}_n \equiv \begin{bmatrix} \xi_n^- \\ 0 \\ \xi_n^+ \end{bmatrix} = \begin{bmatrix} \left(\frac{n}{4n+2}\right)^{1/2} \psi_{n+1}^o - \left(\frac{n+1}{4n+2}\right)^{1/2} \psi_{n-1}^o \\ 0 \\ \left(\frac{n}{4n+2}\right)^{1/2} \psi_{n+1}^o + \left(\frac{n+1}{4n+2}\right)^{1/2} \psi_{n-1}^o \end{bmatrix} \quad for \quad n = -1,0,1,\ldots,\infty \qquad \text{(B.21)}$$

where the Hermite functions are defined above (B.1), with the additional definition that

$$\psi_{-2}^o \equiv 0, \text{and } \psi_{-1}^o \equiv 0. \qquad \text{(B.22)}$$

Here the subscript n=-1 indicates the Kelvin wave, n=0 the gravest antisymmetric Rossby wave, n=1 the gravest symmetric Rossby wave, and so on. The ocean dynamics can be expressed as

$$\vec{\mathbf{r}} = \begin{bmatrix} u \\ v \\ h \end{bmatrix} = \sum_{n=-1,0,1}^{N_o-1} r_n(x) \cdot \vec{\xi}_n . \qquad \text{(B.23)}$$

The ocean equation becomes in vector form

$$\mathbf{L}\vec{\mathbf{r}} = \vec{\mathbf{f}}_o , \qquad \text{(B.24)}$$

where

$$\mathbf{L} = \begin{bmatrix} a + \frac{\partial}{\partial t} & -y & \frac{\partial}{\partial x} \\ y & a & \frac{\partial}{\partial y} \\ \frac{\partial}{\partial x} & \frac{\partial}{\partial y} & a + \frac{\partial}{\partial t} \end{bmatrix}, \text{and } \vec{\mathbf{f}}_o = \begin{bmatrix} K_S^x U^o + K_S^c V^o \\ K_S^c U^o + K_S^y V^o \\ 0 \end{bmatrix}. \qquad \text{(B.25)}$$

Then defining an inner product:

$$\left\langle \begin{bmatrix} f_1 \\ f_2 \\ f_3 \end{bmatrix} \middle\| \begin{bmatrix} g_1 \\ g_2 \\ g_3 \end{bmatrix} \right\rangle \equiv \int_{-\infty}^{\infty} (f_1 \cdot g_1 + f_2 \cdot g_2 + f_3 \cdot g_3)\, dy, \qquad \text{(B.26)}$$

a series of equations in Rossby space can be found from

$$\left\langle \mathbf{L}\vec{\mathbf{r}} \middle| \vec{\xi}_m \right\rangle = \left\langle \vec{\mathbf{f}}_o \middle| \vec{\xi}_m \right\rangle \quad for \quad m = -1,0,1,\ldots,N_o - 1. \qquad \text{(B.27)}$$

This yields the single set of equations

$$\frac{\partial r_m}{\partial t} + a r_m - \frac{1}{2m+1}\frac{\partial r_m}{\partial x} = \sum_{n=0,1,\ldots}^{N_o} U_n^o \left(K_S^x\right)_{nm}^{\psi\xi} + \sum_{n=0,1,\ldots}^{N_o} V_n^o \left(K_S^c\right)_{nm}^{\psi\xi} \quad for \quad m = -1,0,1,\ldots,N_o - 1,$$

(B.28)

where

$$(F(y))_{nm}^{\psi\xi} \equiv \int_{-\infty}^{\infty} F \cdot \psi_n^o \cdot \xi_m^- \, dy. \tag{B.29}$$

Note that the atmospheric components have been expressed in the same manner as was used in section B.2

B.4 Conversions

Two scale conversions are required to couple the above equations: converting atmospheric scales to ocean scales and visa versa. In sections B.1 and B.2 , two different sets of the Hermite functions are used, ψ_n^a, and ψ_n^o. The difference between these is that they use different non-dimensional y, so

$$\psi_n^a(\lambda_a y) = \psi_n^o(\lambda_o y) = \psi_n(y). \tag{B.30}$$

Thus the relationship between the coefficients of the expansions of the zonal wind can be written as

$$\sum_{n=0,1,\ldots}^{N_o} U_n^o \cdot \psi_n(y) = \frac{c_a}{c_o} \sum_{n=0,1,\ldots}^{N_a} U_n \cdot \psi_n\left(\frac{\lambda_a}{\lambda_o} y\right). \tag{B.31}$$

Taking

$$\int_{-\infty}^{\infty} (\text{B.31}) \cdot \psi_m(y) dy \quad for \quad m = 0,1,\ldots,N_o, \tag{B.32}$$

yields

$$U_m^o = \frac{c_a}{c_o} \sum_{n=0,1,\ldots}^{N_a} U_n P_{nm}^{ao} \quad for \quad m = 0,1,\ldots,N_o, \tag{B.33}$$

where

$$P_{nm}^{ao} \equiv \int_{-\infty}^{\infty} \psi_n\left(\frac{\lambda_a}{\lambda_o} y\right) \cdot \psi_m(y) dy. \tag{B.34}$$

Converting temperature in the opposite direction is performed in a similar manner, with

$$T_m^a = \sum_{n=0,1,\ldots}^{N_o-2} T_n P_{nm}^{oa} \quad for \quad m = 0,1,\ldots,N_a, \tag{B.35}$$

where

$$P_{nm}^{oa} \equiv \int_{-\infty}^{\infty} \psi_n\left(\frac{\lambda_o}{\lambda_a} y\right) \cdot \psi_m(y) dy. \tag{B.36}$$

The conversion for the meridional winds, V_n^o, is the same as (B.33). The only other conversions that are required are to get the ocean currents , (u_n, v_n), and thermocline depth, h_n, from the Rossby wave components. These relationships can be found from (B.21) and (B.23). For the meridional current

$$u(x,y) = \sum_{n=0,1,\ldots}^{N_o} u_n \psi_n = \sum_{n=-1,0,1,\ldots}^{No-1} r_n \left[\left(\frac{n}{4n+2}\right)^{1/2} \psi_{n+1} - \left(\frac{n+1}{4n+2}\right)^{1/2} \psi_{n-1} \right]. \tag{B.37}$$

Integrating as before

$$\int_{-\infty}^{\infty} (B.37) \cdot \psi_m(y) dy \quad for \quad m = 0,1,\ldots,N_o, \tag{B.38}$$

and taking into account the orthogonality relationship (B.2) yields

$$u_m = \left(\frac{m-1}{4m-2}\right)^{1/2} r_{m-1} - \left(\frac{m+2}{4m+6}\right)^{1/2} r_{m+1} \quad for \quad m = 0,1,\ldots,N_o, \tag{B.39}$$

where

$$r_{N_o+1} = r_{N_o} = 0. \tag{B.40}$$

The thermocline relationship can be found through similar calculations as

$$h_m = \left(\frac{m-1}{4m-2}\right)^{1/2} r_{m-1} + \left(\frac{m+2}{4m+6}\right)^{1/2} r_{m+1} \quad for \quad m = 0,1,\ldots,N_o. \tag{B.41}$$

Since the long Rossby wave has minute meridional currents, see (B.21), these are simply set to zero:

$$v_m = 0 \quad for \quad m = 0,1,\ldots,N_o. \tag{B.42}$$

Appendix C: Discretization of Equations

C.1 Discretization Scheme

In Appendix B, the ocean and atmospheric equations were projected onto the Hermite functions in y, thus turning them from PDEs in x, y, and t, into equations in x and t only. Because we are looking for the eigenvector solution to the equation, we can eliminate the independent variable t by looking for solutions of the form

$$r_n(x,t) = r_n(x)\cdot\exp(-i\omega t), \text{ and} \tag{C.1}$$

$$T_n(x,t) = T_n(x)\cdot\exp(-i\omega t), \tag{C.2}$$

where $i=\sqrt{-1}$. Thus making the time derivative terms:

$$\frac{\partial r_n}{\partial t} = -i\omega r_n, \text{ and } \frac{\partial T_n}{\partial t} = -i\omega T_n. \tag{C.3}$$

Then if the equations are discretized in the x-direction, the eigenvalue problem in reduced to a linear algebra problem. Ignoring boundary conditions on the ocean for the moment, and noting that the atmosphere has no time dependence, the ocean and thermal equations, (B28) and (B20) respectively, can be expressed as

$$\begin{bmatrix} M_{11} & M_{12} \\ M_{21} & M_{22} \end{bmatrix} \begin{bmatrix} \underline{r} \\ \underline{T} \end{bmatrix} = i\omega \begin{bmatrix} \underline{r} \\ \underline{T} \end{bmatrix}, \tag{C.4}$$

where

$$\underline{r} = \begin{bmatrix} r_{-1}(x_1) & r_{-1}(x_2) & \cdots & r_{-1}(x_{M_o}) & r_0(x_1) & r_0(x_2) & \cdots & r_{N_o-1}(x_{M_o}) \end{bmatrix}^T, \text{and} \tag{C.5}$$

$$\underline{T} = \begin{bmatrix} T_0(x_1) & T_0(x_2) & \cdots & T_0(x_{M_o}) & T_1(x_1) & T_1(x_2) & \cdots & T_{N_o-2}(x_{M_o}) \end{bmatrix}^T. \tag{C.6}$$

The $M_{\#\#}$ are matrix operators which will be determined in this appendix, and where x_0, and x_{M_o} are the furthest west and furthest east coordinates of the ocean basin.

C.2 Atmospheric Equations

Equations (B.12), (B.13), and (B.14) determine the state of the atmosphere from the current state of the SST. After discretizing in x, they can be written as a single

matrix equation:

$$\mathbf{A}\begin{bmatrix}\underline{U}\\ \underline{V}\\ \underline{\varphi}\end{bmatrix}=\begin{bmatrix}A_{11} & A_{12} & A_{13}\\ A_{21} & A_{22} & A_{23}\\ A_{31} & A_{32} & A_{33}\end{bmatrix}\begin{bmatrix}\underline{U}\\ \underline{V}\\ \underline{\varphi}\end{bmatrix}=\begin{bmatrix}\underline{0}\\ \underline{0}\\ A_{44}\underline{T}^{a}\end{bmatrix}. \tag{C.7}$$

where

$$\underline{U}=\left[U_0(x_1)\;\; U_0(x_2)\;\; \ldots\;\; U_0(x_{M_a})\;\; U_1(x_1)\;\; U_1(x_2)\;\; \ldots\;\; U_{N_a}(x_{M_a})\right]^T, \tag{C.8}$$

$$\underline{T}^{a}=\left[T_0^a(x_1)\;\; T_0^a(x_2)\;\; \ldots\;\; T_0^a(x_{M_a})\;\; T_1^a(x_1)\;\; T_1^a(x_2)\;\; \ldots\;\; T_{N_a}^a(x_{M_a})\right]^T, \tag{C.9}$$

and similarly for the other variables, the $A_{\#\#}$ are operator matrices which will be determined. There also exist two conversion matrices which move dependent variables from the ocean to the atmospheric coordinates and back:

$$\underline{T}^{a}=P_{OA}\underline{T}, \text{ and } \underline{U}^{o}=\left(\frac{c_a}{c_o}\right)P_{AO}\underline{U}. \tag{C.10}$$

These matrices can be determined from equations (B.31) through (B.36). An added complication to the conversion matrices is that in general the x-resolution of the atmosphere will be greater than the resolution of the ocean. For use in the ocean and SST equations the atmospheric variables can be expressed direct as linear functions of the temperature by inverting (C.7),

$$\begin{bmatrix}\underline{U}\\ \underline{V}\\ \underline{\varphi}\end{bmatrix}=\mathbf{A}^{-1}\begin{bmatrix}\underline{0}\\ \underline{0}\\ A_{44}\underline{T}^{a}\end{bmatrix}. \tag{C.11}$$

Including the scaling conversions

$$\underline{U}^{o}=M_{TU}\underline{T}, \text{ and } \underline{V}^{o}=M_{TV}\underline{T}, \tag{C.12}$$

where

$$M_{TU}=\left(\frac{c_a}{c_o}\right)P_{AO}\left[\mathbf{A}^{-1}\right]_{13}A_{44}P_{OA}, \text{ and} \tag{C.13}$$

$$M_{TV}=\left(\frac{c_a}{c_o}\right)P_{AO}\left[\mathbf{A}^{-1}\right]_{23}A_{44}P_{OA}. \tag{C.14}$$

Here $\left[\mathbf{A}^{-1}\right]_{13}$ and $\left[\mathbf{A}^{-1}\right]_{23}$ are the appropriate sub-matrices of the inversion. These two matrices can be approximated in the long wavelength with the simple assumption that

$A_{22} = \underline{0}$, which converts the matrix equation (C.7) into three separate equations,

$$\varphi = -A_{23}^{-1} A_{21} \underline{U},$$

$$\underline{V} = -A_{12}^{-1}\left(A_{11} - A_{13}A_{23}^{-1}A_{21}\right)\underline{U}, \text{ and}$$

$$\left[A_{31} - A_{32}A_{12}^{-1}\left(A_{11} - A_{13}A_{23}^{-1}A_{21}\right) - A_{33}A_{23}^{-1}A_{21}\right]\underline{U} = A_{44}\underline{T}^{a}.$$

From which the two approximations can be found,

$$\left[\mathbf{A}^{-1}\right]_{13} \equiv \left[A_{31} - A_{32}A_{12}^{-1}\left(A_{11} - A_{13}A_{23}^{-1}A_{21}\right) - A_{33}A_{23}^{-1}A_{21}\right]^{-1}, \text{ and}$$

$$\left[\mathbf{A}^{-1}\right]_{23} \equiv -A_{12}^{-1}\left(A_{11} - A_{13}A_{23}^{-1}A_{21}\right)\left[\mathbf{A}^{-1}\right]_{13}.$$

This cuts the size of the matrix which needs inversion by a factor of three.

C.3 Ocean and SST Equations

Similarly discretizing the winds in the oceanic scale and coordinates,

$$\underline{U}^{o} = \left[U_0^{o}(x_1) \;\; U_0^{o}(x_2) \;\; \ldots \;\; U_0^{o}(x_{M_o}) \;\; U_1^{o}(x_1) \;\; U_1^{o}(x_2) \;\; \ldots \;\; U_{N_o}^{o}(x_{M_o})\right]^{T}, \qquad \text{(C.15)}$$

and using the Rossby component discretization (C.5), the ocean dynamic equation (B.28) can be expressed in matrix form as

$$O_1 \underline{r} + O_2 \underline{U}^{o} + O_3 \underline{V}^{o} = i\omega \underline{r}. \qquad \text{(C.16)}$$

Similarly for the SST equation (B.20),

$$S_1 \underline{U}^{o} + S_2 \underline{V}^{o} + S_3 \underline{u} + S_4 \underline{h} + S_5 \underline{T} = i\omega \underline{T}. \qquad \text{(C.17)}$$

Recalling now (C.4)

$$\begin{bmatrix} M_{11} & M_{12} \\ M_{21} & M_{22} \end{bmatrix} \begin{bmatrix} \underline{r} \\ \underline{T} \end{bmatrix} = i\omega \begin{bmatrix} \underline{r} \\ \underline{T} \end{bmatrix},$$

it is seen that

$$M_{11} = O_1, \qquad \text{(C.18)}$$

$$M_{12} = O_2 M_{TU} + O_3 M_{TV}, \qquad \text{(C.19)}$$

$$M_{21} = S_3 M_{ur} + S_4 M_{hr}, \qquad \text{(C.20)}$$

$$M_{22} = S_1 M_{TU} + S_2 M_{TV} + S_5, \qquad \text{(C.21)}$$

where the conversions

$$\underline{u} = M_{ur}\underline{r}, \text{ and } \underline{h} = M_{hr}\underline{r}, \tag{C.22}$$

can be found from (B.39) and (B.41), respectively.

C.4 Boundary Conditions

Equation (C.4) is still not the final formulation since the oceanic boundary conditions still need to be included. In Cane and Sarachik (1976), it is shown that the appropriate conditions on the Rossby components are, for the western boundary

$$r_{-1}(x_0) = \sum_{n=0,1,2,\ldots}^{N_o-1} \alpha_n r_n(x_0), \tag{C.23}$$

where

$$\alpha_n = \left[\frac{n}{n+1}\cdot\frac{n-2}{n-1}\cdot\ldots\cdot\frac{1}{2}\right]^{1/2}\left(2n^2+n\right)^{-1/2}, \tag{C.24}$$

or recursively

$$\alpha_n = \alpha_{n-2}\cdot\left[\frac{(n-2)(2n-3)}{(n+1)(2n+1)}\right]^{1/2}, \tag{C.26}$$

with

$$\alpha_0 = 0, \text{ and } \alpha_1 = (6)^{-1/2}. \tag{C.27}$$

For the eastern boundary:

$$r_n\left(x_{M_o}\right) = \beta_n \cdot r_{-1}\left(x_{M_o}\right), \tag{C.28}$$

where

$$\beta_n = \left[\frac{n}{n+1}\cdot\frac{n-2}{n-1}\cdot\ldots\cdot\frac{1}{2}\right]^{1/2}\left(\frac{2n+1}{n}\right)^{1/2}, \tag{C.29}$$

or recursively

$$\beta_n = \beta_{n-2}\cdot\left[\frac{(n-2)(2n+1)}{(n+1)(2n-3)}\right]^{1/2}, \tag{C.30}$$

with

$$\beta_0 = 0, \text{ and } \beta_1 = (3/2)^{1/2}. \tag{C.31}$$

So if a shortened version of the ocean vector is defined

$$\underline{r'} = \left[r_{-1}(x_2) \quad r_{-1}(x_3) \quad \ldots \quad r_{-1}(x_{M_o}) \quad r_0(x_1) \quad r_0(x_2) \right.$$
$$\left. \ldots \quad r_0(x_{M_o-1}) \quad r_1(x_1) \quad \ldots \quad r_{N_o-1}(x_{M_o-1}) \right]^T, \tag{C.32}$$

where those components defined by the boundary conditions are dropped, then a matrix

$$\underline{r} = B_1 \underline{r'}, \tag{C.33}$$

can be defined from (C.23) through (C.31). Also a matrix B_2, is used to eliminate the now unnecessary rows of the the ocean equations, making the final version of the eigenvector problem:

$$\begin{bmatrix} B_2 M_{11} B_1 & B_2 M_{12} \\ M_{21} B_1 & M_{22} \end{bmatrix} \begin{bmatrix} \underline{r'} \\ \underline{T} \end{bmatrix} = i\omega \begin{bmatrix} \underline{r'} \\ \underline{T} \end{bmatrix}. \tag{C.34}$$

Appendix D: Matrix Form of Equations

D.1 Ordering of Matrices

Appendix C outlines how the eigenvalue matrix is formed from all its submatrices. This appendix shows how all the submatrices are formed. For convience the following notation will be used:

$$\hat{N}_a \equiv N_a + 1, \text{ and } \hat{N}_o \equiv N_o + 1,$$

which are the number of Hermite functions used in the atmospheric and oceanic expansions, respectively. Some of the submatrices are more easily formed for an alternate ordering of the components of the vector variables. For example

$$\underline{U} = \left[U_0(x_1) \;\; U_0(x_2) \;\; \cdots \;\; U_0(x_{M_a}) \;\; U_1(x_1) \;\; U_1(x_2) \;\; \cdots \;\; U_{N_a}(x_{M_a})\right]^T, \tag{D.1}$$

whereas the ordering

$$\hat{\underline{U}} = \left[U_0(x_1) \;\; U_1(x_1) \;\; \cdots \;\; U_{N_a}(x_1) \;\; U_0(x_2) \;\; U_1(x_2) \;\; \cdots \;\; U_{N_a}(x_{M_a})\right]^T, \tag{D.2}$$

is more convenient in many cases. In the first case each Hermite function is traced over the basin before the next is started, in the second case all Hermites are visited at each zonal location in turn. A reordering matrix is defined

$$\hat{\underline{U}} = \underline{\underline{R}}_a \underline{U}, \tag{D.3}$$

such that if a matrix operator in the alternate ordering can be found , $\hat{\underline{\underline{M}}}\hat{\underline{U}}$, the equivalent operator in the original order is $\underline{\underline{R}}_a^{-1}\hat{\underline{\underline{M}}}\underline{\underline{R}}_a\underline{U} = \underline{\underline{M}}\underline{U}$. It is built as

$$\underbrace{\underline{\underline{R}}_a}_{\hat{N}_a M_a \times \hat{N}_a M_a} = \begin{bmatrix} \underline{\underline{r}}_a & \cdots & \cdots & \cdots & \underline{\underline{0}} \\ \underline{\underline{z}}_{(1,\hat{N}_a)} & \underline{\underline{r}}_a & \cdots & \cdots & \underline{\underline{0}} \\ \underline{\underline{z}}_{(1,\hat{N}_a)} & \underline{\underline{z}}_{(1,\hat{N}_a)} & \underline{\underline{r}}_a & \cdots & \underline{\underline{0}} \\ \vdots & \vdots & \vdots & \ddots & \vdots \\ 0 & 0 & \underline{\underline{0}} & \cdots & \underline{\underline{r}}_a \end{bmatrix}, \tag{D.4}$$

where

$$\underset{\hat{N}_a \times M_a(\hat{N}_a-1)+1}{\underbrace{\underline{\underline{r}}_{\underline{\underline{a}}}}} = \begin{bmatrix} \overbrace{1\ 0\ \cdots\ 0}^{M_a} & \overbrace{0\ 0\ \cdots\ 0}^{M_a} & \overbrace{\cdots}^{M_a(\hat{N}_a-3)} & \overbrace{0}^{1} \\ 0\ 0\ \cdots\ 0 & 1\ 0\ \cdots\ 0 & \cdots & 0 \\ \vdots & \vdots & \ddots & \vdots \\ 0\ 0\ \cdots\ 0 & 0\ 0\ \cdots\ 0 & \cdots & 1 \end{bmatrix} \Big\} \hat{N}_a, \tag{D.5}$$

and

$$\underset{\underline{\underline{z}}_{(a;b)}}{} \equiv a \times b \quad \textit{zero matrix}. \tag{D.6}$$

The notation $\underline{\underline{0}}$ indicates a matrix of all zeros which is of the appropriate size for its location.

D.2 Atmospheric Matrices

The subdivision of the atmosphere matrix are given in (C.7) and the governing equations are (B.12) through (B.14). From (B.12) it can be seen that

$$\underset{\left(\hat{N}_a M_a\right)^2}{\underbrace{A_{11}}} = A \cdot \underline{\underline{I}}_{(\hat{N}_a M_a)^2}. \tag{D.7}$$

Also

$$\underset{\left(\hat{N}_a M_a\right)^2}{\underbrace{A_{12}}} = \underline{\underline{R}}_a^{-1} \cdot \begin{bmatrix} \underline{\underline{a}}_{12} & \underline{\underline{0}} & \cdots & \underline{\underline{0}} \\ \underline{\underline{0}} & \underline{\underline{a}}_{12} & \cdots & \underline{\underline{0}} \\ \vdots & \vdots & \ddots & \vdots \\ \underline{\underline{0}} & \underline{\underline{0}} & \cdots & \underline{\underline{a}}_{12} \end{bmatrix} \cdot \underline{\underline{R}}_a, \tag{D.8}$$

where

$$\underset{\hat{N}_a \times \hat{N}_a}{\underbrace{\underline{\underline{a}}_{12}}} = -2^{-1/2} \begin{bmatrix} 0 & 1^{1/2} & 0 & 0 & \cdots & 0 \\ 1^{1/2} & 0 & 2^{1/2} & 0 & \cdots & 0 \\ 0 & 2^{1/2} & 0 & 3^{1/2} & \cdots & 0 \\ 0 & 0 & \ddots & \ddots & \ddots & \vdots \\ \vdots & \vdots & \cdots & (N_a-1)^{1/2} & 0 & N_a^{1/2} \\ 0 & 0 & \cdots & 0 & N_a^{1/2} & 0 \end{bmatrix}. \tag{D.9}$$

And finally for (B.12)

$$\underbrace{A_{13}}_{(\hat{N}_a M_a)^2} = \underline{\underline{D}}_a = \begin{bmatrix} \underline{\underline{d}}_a & \underline{\underline{0}} & \cdots & \underline{\underline{0}} \\ \underline{\underline{0}} & \underline{\underline{d}}_a & \cdots & \underline{\underline{0}} \\ \vdots & \vdots & \ddots & \vdots \\ \underline{\underline{0}} & \underline{\underline{0}} & \cdots & \underline{\underline{d}}_a \end{bmatrix}, \tag{D.10}$$

where

$$\underbrace{\underline{\underline{d}}}_{M_a \times M_a} \equiv \frac{1}{2\Delta x_a} \begin{bmatrix} 0 & 1 & 0 & 0 & \cdots & -1 \\ -1 & 0 & 1 & 0 & \cdots & 0 \\ 0 & -1 & 0 & 1 & \cdots & 0 \\ \vdots & \vdots & \ddots & \ddots & \ddots & \vdots \\ 0 & 0 & \cdots & -1 & 0 & 1 \\ 1 & 0 & \cdots & 0 & -1 & 0 \end{bmatrix}. \tag{D.11}$$

The matrix $\underline{\underline{d}}$ represents a second order finite differencing scheme in x, to model the partial derivative in x. The constant Δx_a is the step size in x. From (B.13) it can be seen that

$$A_{21} = -A_{12}, \text{ and } A_{22} = A_{11}. \tag{D.12}$$

Also from (B.13)

$$\underbrace{A_{23}}_{(\hat{N}_a M_a)^2} = \underline{\underline{R}}_a^{-1} \cdot \begin{bmatrix} \underline{\underline{a}}_{23} & \underline{\underline{0}} & \cdots & \underline{\underline{0}} \\ \underline{\underline{0}} & \underline{\underline{a}}_{23} & \cdots & \underline{\underline{0}} \\ \vdots & \vdots & \ddots & \vdots \\ \underline{\underline{0}} & \underline{\underline{0}} & \cdots & \underline{\underline{a}}_{23} \end{bmatrix} \cdot \underline{\underline{R}}_a, \tag{D.13}$$

where

$$\underbrace{\underline{\underline{a}}_{23}}_{\hat{N}_a \times \hat{N}_a} = 2^{-1/2} \begin{bmatrix} 0 & 1^{1/2} & 0 & 0 & \cdots & 0 \\ -1^{1/2} & 0 & 2^{1/2} & 0 & \cdots & 0 \\ 0 & -2^{1/2} & 0 & 3^{1/2} & \cdots & 0 \\ 0 & 0 & \ddots & \ddots & \ddots & \vdots \\ \vdots & \vdots & \cdots & -(N_a-1)^{1/2} & 0 & N_a^{1/2} \\ 0 & 0 & \cdots & 0 & -N_a^{1/2} & 0 \end{bmatrix}. \tag{D.14}$$

The final atmospheric equation (B.14) yields

$$\underbrace{A_{31}}_{(\hat{N}_a M_a)^2} = \underline{\underline{D}}_a - \underline{\underline{\underline{\underline{K_C^{VV}}}}} \cdot \underline{\underline{D}}_a, \tag{D.15}$$

where

$$\underbrace{\underline{\underline{K_C^{\psi\psi}}}}_{(\hat{N}_a M_a)^2} = \begin{bmatrix} \underline{\underline{[K_C]_{00}^{\psi\psi}}} & \underline{\underline{[K_C]_{10}^{\psi\psi}}} & \cdots & \underline{\underline{[K_C]_{N_a 0}^{\psi\psi}}} \\ \underline{\underline{[K_C]_{01}^{\psi\psi}}} & \underline{\underline{[K_C]_{11}^{\psi\psi}}} & \cdots & \vdots \\ \vdots & \vdots & \ddots & \vdots \\ \underline{\underline{[K_C]_{0N_a}^{\psi\psi}}} & \cdots & \cdots & \underline{\underline{[K_C]_{N_a N_a}^{\psi\psi}}} \end{bmatrix}, \tag{D.16}$$

with

$$\underbrace{\underline{\underline{[K_C]_{nm}^{\psi\psi}}}}_{M_a \times M_a} = \begin{bmatrix} (K_C(x_1))_{nm}^{\psi\psi} & 0 & \cdots & 0 \\ 0 & (K_C(x_2))_{nm}^{\psi\psi} & \cdots & 0 \\ \vdots & \vdots & \ddots & \vdots \\ 0 & 0 & \cdots & (K_C(x_{M_a}))_{nm}^{\psi\psi} \end{bmatrix}. \tag{D.17}$$

The definition of the constants $(K_C(x))_{nm}^{\psi\psi}$ is given by (B.15). Also from (B.14)

$$\underbrace{\underline{A_{32}}}_{(\hat{N}_a M_a)^2} = A_{23} - \underline{\underline{K_C^{\partial\psi}}}, \tag{D.18}$$

where $\underline{\underline{K_C^{\partial\psi}}}$ is defined as in (D.16) and (D.17), but of course using (B.16) to define the constants. Next from (B.14) is

$$\underbrace{\underline{A_{33}}}_{(\hat{N}_a M_a)^2} = A \cdot \underline{\underline{I}}_{(\hat{N}_a M_a)^2}. \tag{D.19}$$

And finally from (B.14) comes the SST forcing term

$$\underbrace{\underline{A_{44}}}_{(\hat{N}_a M_a)^2} = -\underline{\underline{K_Q^{\psi\psi}}}. \tag{D.20}$$

D.3 Matrices for Ocean Dynamics

The ocean dynamics are described (B.28). The first matrix from (C.16) is

$$\underbrace{\underline{O_1}}_{(\hat{N}_o M_o)^2} = a \cdot \underline{\underline{I}}_{(\hat{N}_o M_o)^2} + \begin{bmatrix} \underline{\underline{d}}_{o} & \underline{\underline{0}} & \underline{\underline{0}} & \underline{\underline{0}} & \cdots & \underline{\underline{0}} \\ \underline{\underline{0}} & \underline{\underline{-(1)d}}_{o} & \underline{\underline{0}} & \underline{\underline{0}} & \cdots & \underline{\underline{0}} \\ \underline{\underline{0}} & \underline{\underline{0}} & \underline{\underline{-(1/3)d}}_{o} & \underline{\underline{0}} & \cdots & \underline{\underline{0}} \\ \underline{\underline{0}} & \underline{\underline{0}} & \underline{\underline{0}} & \underline{\underline{-(1/5)d}}_{o} & \cdots & \underline{\underline{0}} \\ \vdots & \vdots & \vdots & \vdots & \ddots & \vdots \\ \underline{\underline{0}} & \underline{\underline{0}} & \underline{\underline{0}} & \underline{\underline{0}} & \cdots & \underline{\underline{-(2N_o-1)^{-1}d}}_{o} \end{bmatrix}, \tag{D.21}$$

where

$$\underbrace{\underline{\underline{d}}_o}_{M_o \times M_o} \equiv \frac{1}{2\Delta x_o}\begin{bmatrix} -2 & 2 & 0 & 0 & \cdots & 0 \\ -1 & 0 & 1 & 0 & \cdots & 0 \\ 0 & -1 & 0 & 1 & \cdots & 0 \\ \vdots & \vdots & \ddots & \ddots & \ddots & \vdots \\ 0 & 0 & \cdots & -1 & 0 & 1 \\ 0 & 0 & \cdots & 0 & -2 & 2 \end{bmatrix}. \tag{D.22}$$

Also (B.28) gives

$$\underbrace{O_2}_{(\tilde{N}_o M_o)^2} = -\underline{\underline{\left(K_S^x\right)^{\psi\xi}}} = -\begin{bmatrix} \underline{\underline{\left[K_S^x\right]_{0,-1}^{\psi\xi}}} & \underline{\underline{\left[K_S^x\right]_{1,-1}^{\psi\xi}}} & \cdots & \underline{\underline{\left[K_S^x\right]_{N_o,-1}^{\psi\xi}}} \\ \underline{\underline{\left[K_S^x\right]_{0,0}^{\psi\xi}}} & \underline{\underline{\left[K_S^x\right]_{1,0}^{\psi\xi}}} & \cdots & \vdots \\ \vdots & \vdots & \ddots & \vdots \\ \underline{\underline{\left[K_S^x\right]_{0,N_o-1}^{\psi\xi}}} & \cdots & \cdots & \underline{\underline{\left[K_S^x\right]_{N_o,N_o-1}^{\psi\xi}}} \end{bmatrix}. \tag{D.23}$$

where $\underline{\underline{\left[K_S^x\right]_{n,m}^{\psi\xi}}}$ is defined as in (D.17). Finally

$$\underbrace{O_3}_{(\tilde{N}_o M_o)^2} = -\underline{\underline{\left(K_S^c\right)^{\psi\xi}}}. \tag{D.24}$$

D.4 SST Matrices

The SST matrices are determined from (B.20) and are

$$\begin{aligned} \underbrace{S_1}_{(\tilde{N}_o-2)M_o \times \tilde{N}_o M_o} = & \begin{bmatrix} \underline{\underline{\left[K_U^x\right]_{0,0}^{\psi\psi}}} & \cdots & \underline{\underline{\left[K_U^x\right]_{N_o,0}^{\psi\psi}}} \\ \vdots & \ddots & \vdots \\ \underline{\underline{\left[K_U^x\right]_{0,N_o-2}^{\psi\psi}}} & \cdots & \underline{\underline{\left[K_U^x\right]_{N_o,N_o-2}^{\psi\psi}}} \end{bmatrix} \cdot \underline{\underline{D}}_o \\ & + \begin{bmatrix} \underline{\underline{\left[K_U^y\right]_{0,0}^{\partial y\psi}}} & \cdots & \underline{\underline{\left[K_U^y\right]_{N_o,0}^{\partial y\psi}}} \\ \vdots & \ddots & \vdots \\ \underline{\underline{\left[K_U^y\right]_{0,N_o-2}^{\partial y\psi}}} & \cdots & \underline{\underline{\left[K_U^y\right]_{N_o,N_o-2}^{\partial y\psi}}} \end{bmatrix} + \begin{bmatrix} \underline{\underline{\left[K_U\right]_{0,0}^{\psi\psi}}} & \cdots & \underline{\underline{\left[K_U\right]_{N_o,0}^{\psi\psi}}} \\ \vdots & \ddots & \vdots \\ \underline{\underline{\left[K_U\right]_{0,N_o-2}^{\psi\psi}}} & \cdots & \underline{\underline{\left[K_U\right]_{N_o,N_o-2}^{\psi\psi}}} \end{bmatrix}, \end{aligned} \tag{D.25}$$

and similarly

$$\underbrace{S_2}_{(\hat{N}_o-2)M_o\times\hat{N}_oM_o}=\begin{bmatrix}\underline{[K_V^x]_{0,0}^{\psi\psi}} & \cdots & \underline{[K_V^x]_{N_o,0}^{\psi\psi}}\\ \vdots & \ddots & \vdots\\ \underline{[K_V^x]_{0,N_o-2}^{\psi\psi}} & \cdots & \underline{[K_V^x]_{N_o,N_o-2}^{\psi\psi}}\end{bmatrix}\cdot\underline{\underline{D}}_o$$
$$+\begin{bmatrix}\underline{[K_V^y]_{0,0}^{\partial y\psi}} & \cdots & \underline{[K_V^y]_{N_o,0}^{\partial y\psi}}\\ \vdots & \ddots & \vdots\\ \underline{[K_V^y]_{0,N_o-2}^{\partial y\psi}} & \cdots & \underline{[K_V^y]_{N_o,N_o-2}^{\partial y\psi}}\end{bmatrix}+\begin{bmatrix}\underline{[K_V]_{0,0}^{\psi\psi}} & \cdots & \underline{[K_V]_{N_o,0}^{\psi\psi}}\\ \vdots & \ddots & \vdots\\ \underline{[K_V]_{0,N_o-2}^{\psi\psi}} & \cdots & \underline{[K_V]_{N_o,N_o-2}^{\psi\psi}}\end{bmatrix}, \tag{D.26}$$

where

$$\underbrace{\underline{\underline{D}}_o}_{(\hat{N}_oM_o)^2}\equiv\begin{bmatrix}\underline{\underline{d}}_o & \underline{\underline{0}} & \cdots & \underline{\underline{0}}\\ \underline{\underline{0}} & \underline{\underline{d}}_o & \cdots & \underline{\underline{0}}\\ \vdots & \vdots & \ddots & \vdots\\ \underline{\underline{0}} & \underline{\underline{0}} & \cdots & \underline{\underline{d}}_o\end{bmatrix}. \tag{D.27}$$

Equation (B.20) also gives

$$\underbrace{S_3}_{(\hat{N}_o-2)M_o\times\hat{N}_oM_o}=\begin{bmatrix}\underline{[K_w]_{0,0}^{\psi\psi}} & \cdots & \underline{[K_w]_{N_o,0}^{\psi\psi}}\\ \vdots & \ddots & \vdots\\ \underline{[K_w]_{0,N_o-2}^{\psi\psi}} & \cdots & \underline{[K_w]_{N_o,N_o-2}^{\psi\psi}}\end{bmatrix}\cdot\underline{\underline{D}}_o+\begin{bmatrix}\underline{[\overline{T}_x]_{0,0}^{\psi\psi}} & \cdots & \underline{[\overline{T}_x]_{N_o,0}^{\psi\psi}}\\ \vdots & \ddots & \vdots\\ \underline{[\overline{T}_x]_{0,N_o-2}^{\psi\psi}} & \cdots & \underline{[\overline{T}_x]_{N_o,N_o-2}^{\psi\psi}}\end{bmatrix}, \tag{D.28}$$

and

$$\underbrace{S_4}_{(\hat{N}_o-2)M_o\times\hat{N}_oM_o}=-\begin{bmatrix}\underline{[K_T]_{0,0}^{\psi\psi}} & \cdots & \underline{[K_T]_{N_o,0}^{\psi\psi}}\\ \vdots & \ddots & \vdots\\ \underline{[K_T]_{0,N_o-2}^{\psi\psi}} & \cdots & \underline{[K_T]_{N_o,N_o-2}^{\psi\psi}}\end{bmatrix}. \tag{D.29}$$

And finally from (B.20)

$$\underbrace{S_S}_{[(\hat{N}_o-2)M_o]^2} = \begin{bmatrix} \underline{\underline{[\overline{u}_1]^{\psi\psi}_{0,0}}} & \cdots & \underline{\underline{[\overline{u}_1]^{\psi\psi}_{N_o-2,0}}} \\ \vdots & \ddots & \vdots \\ \underline{\underline{[\overline{u}_1]^{\psi\psi}_{0,N_o-2}}} & \cdots & \underline{\underline{[\overline{u}_1]^{\psi\psi}_{N_o-2,N_o-2}}} \end{bmatrix} \cdot \underbrace{\underline{\underline{D}}_o}_{[(N_o-2)M_o]^2}$$
$$+ \begin{bmatrix} \underline{\underline{[\overline{v}_1]^{\partial y\psi}_{0,0}}} & \cdots & \underline{\underline{[\overline{v}_1]^{\partial y\psi}_{N_o-2,0}}} \\ \vdots & \ddots & \vdots \\ \underline{\underline{[\overline{v}_1]^{\partial y\psi}_{0,N_o-2}}} & \cdots & \underline{\underline{[\overline{v}_1]^{\partial y\psi}_{N_o-2,N_o-2}}} \end{bmatrix} + \begin{bmatrix} \underline{\underline{[d]^{\psi\psi}_{0,0}}} & \cdots & \underline{\underline{[d]^{\psi\psi}_{N_o-2,0}}} \\ \vdots & \ddots & \vdots \\ \underline{\underline{[d]^{\psi\psi}_{0,N_o-2}}} & \cdots & \underline{\underline{[d]^{\psi\psi}_{N_o-2,N_o-2}}} \end{bmatrix}, \tag{D.30}$$

where an appropriately truncated version of $\underline{\underline{D}}_o$ is used.

D.5 Conversion Matrices

The previous sections cover all the basic equations. Here the conversion matrices will be built. To find the conversion between the Rossby wave components and the ocean currents use (B.39) to get

$$\underbrace{\underline{\underline{M}}_{ur}}_{(\hat{N}_o M_o)^2} = \underline{\underline{R}}_o^{-1} \cdot \begin{bmatrix} \underline{\underline{m}}_{ur} & \underline{\underline{0}} & \cdots & \underline{\underline{0}} \\ \underline{\underline{0}} & \underline{\underline{m}}_{ur} & \cdots & \underline{\underline{0}} \\ \vdots & \vdots & \ddots & \vdots \\ \underline{\underline{0}} & \underline{\underline{0}} & \cdots & \underline{\underline{m}}_{ur} \end{bmatrix} \cdot \underline{\underline{R}}_o, \tag{D.31}$$

where

$$\underbrace{\underline{\underline{m}}_{ur}}_{\hat{N}_o \times \hat{N}_o} = \begin{bmatrix} (1/2)^{1/2} & 0 & -(1/3)^{1/2} & 0 & \cdots & 0 \\ 0 & (0/2)^{1/2} & 0 & -(3/10)^{1/2} & \cdots & 0 \\ \vdots & \ddots & \ddots & \ddots & \cdots & \vdots \\ 0 & \cdots & \left(\frac{m-1}{4m-2}\right)^{1/2} & 0 & -\left(\frac{m+2}{4m+6}\right)^{1/2} & \cdots \\ \vdots & \vdots & \ddots & \ddots & \ddots & \vdots \\ 0 & 0 & \ddots & \ddots & 0 & -\left(\frac{N_o}{4N_o-2}\right)^{1/2} \\ 0 & 0 & \cdots & 0 & \left(\frac{N_o-2}{4N_o-6}\right)^{1/2} & 0 \\ 0 & 0 & \cdots & \cdots & 0 & \left(\frac{N_o-1}{4N_o-2}\right)^{1/2} \end{bmatrix}. \tag{D.32}$$

And where $\underline{\underline{R}}_o$ is similar to $\underline{\underline{R}}_a$, but with oceanic dimensions. For the thermocline depth

$$\underbrace{\underline{\underline{M}}_{hr}}_{(\hat{N}_o M_o)^2} = \underline{\underline{R}}_o^{-1} \cdot \begin{bmatrix} \underline{\underline{m}}_{hr} & \underline{\underline{0}} & \cdots & \underline{\underline{0}} \\ \underline{\underline{0}} & \underline{\underline{m}}_{hr} & \cdots & \underline{\underline{0}} \\ \vdots & \vdots & \ddots & \vdots \\ \underline{\underline{0}} & \underline{\underline{0}} & \cdots & \underline{\underline{m}}_{hr} \end{bmatrix} \cdot \underline{\underline{R}}_o, \tag{D.33}$$

where

$$\underbrace{\underline{\underline{m}}_{uh}}_{\hat{N}_o \times \hat{N}_o} = \begin{bmatrix} (1/2)^{1/2} & 0 & (1/3)^{1/2} & 0 & \cdots & 0 \\ 0 & (0/2)^{1/2} & 0 & (3/10)^{1/2} & \cdots & 0 \\ \vdots & \ddots & \ddots & \ddots & \cdots & \vdots \\ 0 & \cdots & \left(\frac{m-1}{4m-2}\right)^{1/2} & 0 & \left(\frac{m+2}{4m+6}\right)^{1/2} & \cdots \\ \vdots & \vdots & \ddots & \ddots & \ddots & \vdots \\ 0 & 0 & \ddots & \ddots & 0 & \left(\frac{N_o}{4N_o-2}\right)^{1/2} \\ 0 & 0 & \cdots & 0 & \left(\frac{N_o-2}{4N_o-6}\right)^{1/2} & 0 \\ 0 & 0 & \cdots & \cdots & 0 & \left(\frac{N_o-1}{4N_o-2}\right)^{1/2} \end{bmatrix}. \tag{D.34}$$

Converting from ocean coordinates to atmospheric coordinate involves both interpolation, since the grid for the atmosphere is finer, and the scale transformation. The ocean to atmosphere transformation is performed on the temperature field only, recalling (C.10), $\underline{T}^a = P_{OA}\underline{T}$. Assume that the mesh is four times finer in the atmosphere, and use linear interpolation, then

$$\underbrace{P_{OA}}_{\hat{N}_a M_a \times (\hat{N}_o - 2) M_o} = \underbrace{\underline{\underline{P}}^{oa}}_{(\hat{N}_a M_a)^2} \cdot \underbrace{\underline{\underline{\underline{Q}}}^{41}}_{\hat{N}_a M_a \times (\hat{N}_o - 2) M_o}, \tag{D.35}$$

where

$$\underbrace{\underline{\underline{P}}^{oa}}_{(\hat{N}_a M_a)^2} = \begin{bmatrix} P^{oa}_{00}\underline{\underline{I}}_{M_a^2} & P^{oa}_{10}\underline{\underline{I}}_{M_a^2} & \cdots & P^{oa}_{N_a 0}\underline{\underline{I}}_{M_a^2} \\ P^{oa}_{01}\underline{\underline{I}}_{M_a^2} & P^{oa}_{11}\underline{\underline{I}}_{M_a^2} & \cdots & \vdots \\ \vdots & \vdots & \ddots & \vdots \\ P^{oa}_{0N_a}\underline{\underline{I}}_{M_a^2} & \cdots & \cdots & P^{oa}_{N_a N_a}\underline{\underline{I}}_{M_a^2} \end{bmatrix}, \tag{D.36}$$

with the constants P^{oa}_{nm} defined by (B.36) and where

$$\underbrace{\underline{\underline{\underline{Q}}}^{41}}_{\hat{N}_a M_a \times (\hat{N}_o - 2) M_o} = \begin{bmatrix} \underline{\underline{q}}^{41} & \underline{\underline{0}} & \cdots & \underline{\underline{0}} \\ \underline{\underline{0}} & \underline{\underline{q}}^{41} & \cdots & \underline{\underline{0}} \\ \vdots & \vdots & \ddots & \vdots \\ \underline{\underline{0}} & \underline{\underline{0}} & \cdots & \underline{\underline{q}}^{41} \\ \underline{\underline{0}} & \cdots & \cdots & \underline{\underline{0}} \\ \underline{\underline{0}} & \cdots & \cdots & \underline{\underline{0}} \end{bmatrix} \begin{matrix} \\ \\ \\ \}(\hat{N}_a - 2)M_a \\ \\ \}2M_a \end{matrix}, \tag{D.37}$$

with

$$\underbrace{\underline{\underline{q}}^{41}}_{M_a \times M_o} = \overbrace{\begin{bmatrix} \underline{\nu}_1 & \underline{\nu}_2 & \underline{0} & \cdots & \underline{0} \\ \underline{0} & \underline{\nu}_1 & \underline{\nu}_2 & \cdots & \underline{0} \\ \vdots & \vdots & \ddots & \ddots & \vdots \\ \underline{0} & \underline{0} & \cdots & \underline{\nu}_1 & \underline{\nu}_2 \\ \underline{0} & \underline{0} & \cdots & \underline{0} & \underline{\nu}_1 \\ 0 & \cdots & \cdots & \cdots & 0 \\ \vdots & \cdots & 0 & \cdots & \vdots \\ 0 & \cdots & \cdots & \cdots & 0 \end{bmatrix}}^{M_o} \begin{matrix} \\ \\ \\ \\ \}4M_o \\ \}M_a - 4M_o \\ \\ \\ \end{matrix}, \text{ where } \underline{\nu}_1 = \begin{bmatrix} 1 \\ 3/4 \\ 1/2 \\ 1/4 \end{bmatrix}, \text{ and } \underline{\nu}_2 = \begin{bmatrix} 0 \\ 1/4 \\ 1/2 \\ 3/4 \end{bmatrix}. \tag{D.38}$$

The atmosphere to ocean transformation is performed on the wind fields only, recalling equation (C.10), $\underline{U}^o = (c_a / c_o) P_{AO}\underline{U}$. Once again assuming that the atmosphere

is on a mesh which is 4 time finer gives

$$\underbrace{P_{AO}}_{\hat{N}_o M_o \times \hat{N}_a M_a} = \underbrace{\underline{\underline{Q}}^{14}}_{\hat{N}_o M_o \times \hat{N}_a M_a} \cdot \underbrace{\underline{\underline{P}}^{ao}}_{(\hat{N}_a M_a)^2}, \tag{D.39}$$

where

$$\underbrace{\underline{\underline{P}}^{ao}}_{(\hat{N}_a M_a)^2} = \begin{bmatrix} P_{00}^{ao}\underline{\underline{I}}_{M_a^2} & P_{10}^{ao}\underline{\underline{I}}_{M_a^2} & \cdots & P_{N_a 0}^{ao}\underline{\underline{I}}_{M_a^2} \\ P_{01}^{ao}\underline{\underline{I}}_{M_a^2} & P_{11}^{ao}\underline{\underline{I}}_{M_a^2} & \cdots & \vdots \\ \vdots & \vdots & \ddots & \vdots \\ P_{0N_a}^{ao}\underline{\underline{I}}_{M_a^2} & \cdots & \cdots & P_{N_a N_a}^{ao}\underline{\underline{I}}_{M_a^2} \end{bmatrix}, \tag{D.40}$$

and

$$\underbrace{\underline{\underline{Q}}^{14}}_{\hat{N}_o M_o \times \hat{N}_a M_a} = \begin{bmatrix} \underline{\underline{q}}^{14} & \underline{\underline{0}} & \cdots & \underline{\underline{0}} & 0 & \cdots & 0 \\ \underline{\underline{0}} & \underline{\underline{q}}^{14} & \cdots & \underline{\underline{0}} & \vdots & \cdots & \vdots \\ \vdots & \vdots & \ddots & \vdots & \vdots & \cdots & \vdots \\ \underbrace{\underline{\underline{0}}}_{\hat{N}_o M_a} & \underline{\underline{0}} & \cdots & \underbrace{\underline{\underline{q}}^{14}}_{\hat{N}_o M_a} & \underbrace{0}_{(\hat{N}_a - \hat{N}_o)M_a} & \cdots & 0 \end{bmatrix}, \tag{D.41}$$

with

$$\underbrace{\underline{\underline{q}}^{14}}_{M_o \times M_a} = \overbrace{\begin{bmatrix} \underline{\nu}_3 & \underline{0} & \cdots & \underline{0} & 0 & \cdots & 0 \\ \underline{0} & \underline{\nu}_3 & \cdots & \underline{0} & 0 & \cdots & 0 \\ \vdots & \vdots & \ddots & \vdots & \vdots & \ddots & \vdots \\ \underbrace{\underline{0}}_{4M_o} & \underline{0} & \cdots & \underbrace{\underline{\nu}_3}_{4M_o} & \underbrace{0}_{M_a - 4M_o} & \cdots & 0 \end{bmatrix}}^{M_a}, \text{ where } \underline{\nu}_3 = [1 \quad 0 \quad 0 \quad 0]. \tag{D.42}$$

D.6 Boundary Condition Matrices

The boundary condition are given in section C.3, and consist of two matrices one which determines the values of the boundary variables, B_1, and the other which eliminate unneeded rows of the ocean dynamics equation. B_2. From (C.23) it can be can be determined that

$$\underbrace{B_1}_{\substack{\tilde{N}_o M_o \\ \times \\ \hat{N}_o(M_o-1)}} = \begin{bmatrix} \overbrace{0 \cdots 0\ 0}^{M_o-1} & \overbrace{\alpha_1\ 0 \cdots 0}^{M_o-1} & \overbrace{\alpha_2\ 0 \cdots 0}^{M_o-1} & \cdots & \overbrace{\alpha_{N_0-1}\ 0 \cdots 0}^{M_o-1} \\ \underset{=(M_o-1)^2}{I} & \underset{=(M_o-1)^2}{Z} & \underset{=(M_o-1)^2}{Z} & & \underset{=(M_o-1)^2}{Z} \\ \left.\begin{matrix} \underset{=(M_o-1)^2}{Z} \\ 0 \cdots 0\ \beta_1 \end{matrix}\right\} M_o & \begin{matrix} \underset{=(M_o-1)^2}{I} \\ 0\ 0 \cdots 0 \end{matrix} & \underset{=}{0} & \cdots & \underset{=}{0} \\ \left.\begin{matrix} \underset{=(M_o-1)^2}{Z} \\ 0 \cdots 0\ \beta_2 \end{matrix}\right\} M_o & \underset{=}{0} & \begin{matrix} \underset{=(M_o-1)^2}{I} \\ 0\ 0 \cdots 0 \end{matrix} & \cdots & \underset{=}{0} \\ \vdots & \vdots & \vdots & \ddots & \vdots \\ \left.\begin{matrix} \underset{=(M_o-1)^2}{Z} \\ 0 \cdots 0\ \beta_{N_0-1} \end{matrix}\right\} M_o & \underset{=}{0} & \underset{=}{0} & \cdots & \underset{=(M_o-1)^2}{I}\ 0\ 0 \cdots 0 \end{bmatrix} \tag{D.43}$$

where the constants are given by equations (C.24) to (C.31). The second matrix then is

$$\underbrace{B_2}_{\hat{N}_o(M_o-1)\times\hat{N}_o M_o} = \begin{bmatrix} \left.\begin{matrix} 0 \\ \vdots \\ 0 \end{matrix}\right\} M_o & & & & \\ \underset{=(M_o-1)^2}{I} & \underset{=}{0} & \underset{=}{0} & \cdots & \underset{=}{0} \\ \underset{=}{0} & \left.\begin{matrix} \underset{=(M_o-1)^2}{I} \\ 0 \cdots 0 \end{matrix}\right\} M_o & \underset{=}{0} & \cdots & \underset{=}{0} \\ \underset{=}{0} & \underset{=}{0} & \left.\begin{matrix} \underset{=(M_o-1)^2}{I} \\ 0 \cdots 0 \end{matrix}\right\} M_o & \cdots & \underset{=}{0} \\ \vdots & \vdots & \vdots & \ddots & \vdots \\ \underset{=}{0} & \underset{=}{0} & \underset{=}{0} & \cdots & \left.\begin{matrix} \underset{=(M_o-1)^2}{I} \\ 0 \cdots 0 \end{matrix}\right\} M_o \end{bmatrix}. \tag{D.44}$$

Appendix E: Assimilation of Temperature data

In matrix form the differential equation for the ocean-atmosphere system can written as:

$$\begin{bmatrix} M_{11} & M_{12} \\ M_{21} & M_{22} \end{bmatrix} \begin{bmatrix} \underline{r} \\ \underline{T} \end{bmatrix} = -\frac{d}{dt} \begin{bmatrix} \underline{r} \\ \underline{T} \end{bmatrix}, \tag{E.1}$$

where $\underline{T}$ is a column vector of the SST discretization and $\underline{r}$ is a vector of the Rossby wave discretization of the ocean dynamics. The matrices $M_{\#\#}$ are discretized linear operators determined by the original differential equations. See Chapter 2 and Appendices A through D.

Since (E.1) is a set of linear ODEs, its solution is determined exactly for all time, given a set of initial conditions. This solution can be written:

$$\begin{bmatrix} \underline{r}(t) \\ \underline{T}(t) \end{bmatrix} = \exp(-\begin{bmatrix} M_{11} & M_{12} \\ M_{21} & M_{22} \end{bmatrix} t) \cdot \begin{bmatrix} \underline{r}(0) \\ \underline{T}(0) \end{bmatrix}, \tag{E.2}$$

or

$$\begin{bmatrix} \underline{r}(t) \\ \underline{T}(t) \end{bmatrix} = \begin{bmatrix} R_{11}(t) & R_{12}(t) \\ R_{21}(t) & R_{22}(t) \end{bmatrix} \cdot \begin{bmatrix} \underline{r}(0) \\ \underline{T}(0) \end{bmatrix}, \tag{E.3}$$

where exp(•) is the matrix exponential. The matrices $R_{\#\#}$ are called the linear propagators. Keep in mind here that since this is a coupled model,

$$R_{11}(t) \neq \exp(-M_{11}t), \tag{E.4}$$

but rather determined by all the matrices $M_{\#\#}$.

Since, historically, actual data for the state of the ocean currents and thermocline perturbation are not available, a method to initialize both the ocean and SST from only the SST data is needed. There are several data sets available which give the SST over time at fixed intervals, i.e. they give $\underline{T}(t_0), \underline{T}(t_1), \ldots, \underline{T}(t_n)$. If both the data and the model where perfect, this data could be determined exactly by:

$$\begin{bmatrix} \underline{T}(t_0) \\ \underline{T}(t_1) \\ \vdots \\ \underline{T}(t_n) \end{bmatrix} = \begin{bmatrix} R_{21}(t_0) & R_{22}(t_0) \\ R_{21}(t_1) & R_{22}(t_1) \\ \vdots & \vdots \\ R_{21}(t_n) & R_{22}(t_n) \end{bmatrix} \cdot \begin{bmatrix} \underline{r}_0 \\ \underline{T}_0 \end{bmatrix}, \tag{E.5}$$

which is the classic linear algebra problem

$$\underline{b} = A\underline{x}, \tag{E.6}$$

where A is in general not a square matrix and therefore not invertible. Our objective is therefore to find a set of initial conditions, $\underline{x}$, which fits the data, $\underline{b}$, in some optimal way. The easiest way to do this is to minimize $\|\underline{b} - A\underline{x}\|_2$, which has the solution

$$\underline{x} = A^+\underline{b}, \tag{E.7}$$

where A^+ is the pseudoinverse of A. This gives the initial state of the ocean and SST, which when propagated forward by the model, gives SST output, that optimally matches the SST data in a least squared sense.

The COADS data consists of fields of monthly SSTA. Because of the difficulty of the matrix inversion in (E.5), only a limited set of the available data was used. Specifically, for all the hindcasts presented in Chapter 5, two years of data were used, but only every third month. For example, for a forecast starting in January of 1970, the full SSTA fields for January 1968, April 1968, July 1968, and so on to January 1970 were used.

Appendix F: Derivation of the Norm

There are an infinity of norms that could be used to perform the optimization in this research. In this appendix, the norm which was chosen will be formally derived, and its use justified.

In Section 3.1.1 the norm that is used throughout this research is defined by equation (3.1.1) as

$$\left\|\underline{\varphi}\right\|_{2w} = \left(\begin{bmatrix} w_1 \underline{r} \\ w_2 \underline{T} \end{bmatrix}^{\mathrm{H}} \begin{bmatrix} w_1 \underline{r} \\ w_2 \underline{T} \end{bmatrix} \right)^{1/2}. \tag{F.1}$$

where w_1 and w_2 are variable weights that scale the temperature portion of the norm, $\underline{T}^{\mathrm{H}}\underline{T}$, relative to the ocean dynamics portion of the norm, $\underline{r}^{\mathrm{H}}\underline{r}$. In Sec. 3.5 it is shown that the shape of the T-field part, and r-field part of the optimals are insensitive to the weighting, but why measure these two sub-fields in this way?

The norm should be picked in an appropriate manner to measure the quantities of interest for the application at hand. In Chapter 3 the primary goal is to quantify those measurement errors in the SST and in the ocean dynamics (thermocline and surface currents) that give the largest growth in the error of SST prediction. In Sections F.1 and F.2, L_2 norms for the SST and ocean dynamics will be derived separately. Section F.3 will discuss why these two sub-norms were then combined with a variable weighting, rather than deriving a fixed weighting based on an energy norm, or some other physical property.

In Chapters 4 through 6, the primary reason for finding the optimal structures is to uncover ways to enhance the model's transient growth in order to make LOAM a reasonable stochastic model. Section F.4 discusses the use of the L_2 norm for the parameter studies of Chapter 4 and 5, and justifies this choice of norm using the results of Chapter 6. In section F.5, a possible weighting scheme to account for non-uniform

forcing is developed. Section F.6 is a survey of the norms used in several recent studies that look at optimal growth in intermediate ENSO models.

F.1 Derivation of SST measure.

SST data from the equatorial Pacific comes in two forms: data on a regular grid from the TOGA/TAO array, and irregularly spaced ship track data. If the data came only on the regular grid it might be tempting to calculate the SST error as the RMS error of the T field projected onto the array locations. That is

$$\|\mathrm{SST}\| = RMS\ error = \left(\frac{1}{N}\sum_{n=1}^{N} T_n^2\right)^{1/2}, \qquad \text{(F.2)}$$

where N is the number of array locations and T_n is anomalous SST at each location. However, in order to account for the irregular data (and to make the analysis more general) it makes sense to define the error as the equivalent continuous L_2 norm, and then discretize this norm to match the discretization of the numerical scheme being employed. So the error (L_2 norm) is defined by

$$\|\mathrm{SST}\|_2 = \left(\int_{x=x_W}^{x_E}\left(\int_{y=-\infty}^{\infty} T^*(x,y)\cdot T(x,y)\,dy\right)dx\right)^{1/2}, \qquad \text{(F.3)}$$

where x_E and x_W are the eastern and western boundaries of the basin, respectively. Substituting the spectral decomposition of the SST from (B.19) this becomes

$$\|\mathrm{SST}\|_2 = \left(\int_{x=x_W}^{x_E}\int_{y=-\infty}^{\infty}\left\{\left(\sum_{n=0}^{N_o-2} T_n^*(x)\psi_n(y)\right)\left(\sum_{n=0}^{N_o-2} T_n(x)\psi_n(y)\right)\right\}dy\,dx\right)^{1/2}. \qquad \text{(F.4)}$$

Since the Hermite functions are orthornormal (see equation B.2), only the $T_n^*(x)\cdot T_n(x)$ terms of the multinomial expansion of the bracketed term survive the integration in y, and so (F.4) becomes

$$\|\mathrm{SST}\|_2 = \left(\int_{x=x_W}^{x_E}\left(\sum_{n=0.}^{N_o-2} T_n^*(x)\cdot T_n(x)\right)dx\right)^{1/2}. \qquad \text{(F.5)}$$

The SST is then discretized into M_o points in x, and the final integral can be

approximated using the rectangle rule. Equation (F.5) becomes

$$\|\mathrm{SST}\|_2 = \left(\sum_{m=1}^{M_o} \sum_{n=0.}^{N_o-2} T_n^*(x_m) \cdot T_n(x_m) \Delta x \right)^{1/2}, \qquad \text{(F.6)}$$

where Δx is the (constant) spacing between points. Writing SST as a column vector (equation C.6), this becomes

$$\|\mathrm{SST}\|_2 = \Delta x^{1/2} \left(\underline{T}^{\mathrm{H}} \underline{T} \right)^{1/2}, \qquad \text{(F.6)}$$

which is the same form as used for the SST part of the L_{2w} norm from Chapter 3. Since the coefficient $\Delta x^{1/2}$ is constant for a given discretization (and will also appear on the ocean dynamics part of the norm), it is simply absorbed into the weighting coefficients. Note that the absolute value of the norm is never used, only the growth of the fields over a fixed period of time. Because of this, even without the $\Delta x^{1/2}$ coefficient to scale the norm for changes in discretization, the growth rates from runs using different resolutions are comparable (as was done in Section 3.5).

F.2 Derivation of ocean dynamics measure

The derivation of the ocean dynamics part of the L_{2w} norm follows the exact same steps as the derivation of the SST portion of the norm. This can be done since the equatorial ocean modes are also orthonormal, and yields:

$$\|ocean\|_2 = \Delta x^{1/2} \left(\underline{r}^{\mathrm{H}} \underline{r} \right)^{1/2}. \qquad \text{(F.7)}$$

While a forecaster may well initialize his/her model with equatorial ocean waves (i.e. with the thermocline and currents "dynamically consistent"), these Rossby waves are not measured directly. Perhaps a norm built out of the measured quantities would be more desirable. For instance, the local perturbation energy of the ocean (see equations 2.2.12, 2.2.13, and 2.2.14) is given by (see Hirst 1986a) :

$$E \propto \left[u^2 + v^2 + \frac{g'}{H_0} h^2 \right]. \qquad \text{(F.8)}$$

Setting the meridional velocity to zero, as in the long-wavelength approximation used

here (equation B.21), and converting to the non-dimensional variables (see Sec. A.3) yields:

$$E \propto \left[\left(u^*\right)^2 + \left(h^*\right)^2 \right], \tag{F.9}$$

where the star indicates the non-dimensional variable. Transforming this into a norm on the discrete components of h and u, yields

$$\|ocean\|_E = \Delta x \left[\underline{u}^{\mathrm{H}} \underline{u} + \underline{h}^{\mathrm{H}} \underline{h} \right]. \tag{F.10}$$

[Interestingly, this happens also to be the sum of the squares of the RMS errors of the thermocline and zonal currents.] But how does it compare to the L_2 norm on the equatorial wave components (F.7)?

Using the relationship between the r, h and u components (at a fixed x) given by (B.39, B.40 and B.41) yields

$$u_m^* u_m + h_m^* h_m = \left(\frac{m-1}{2m-1} \right) r_{m-1}^* r_{m-1} + \left(\frac{m+2}{2m+3} \right) r_{m+1}^* r_{m+1} \quad for \quad m = 0,1,...,N_o. \tag{F.11}$$

Some algebra shows that for fixed x,

$$\left[\underline{u}^{\mathrm{H}} \underline{u} + \underline{h}^{\mathrm{H}} \underline{h} \right]_{fixed\, x} = \sum_{m=0}^{N_o} \left(u_m^* u_m + h_m^* h_m \right) = r_{-1}^* r_{-1} + 0 \cdot r_0^* r_0 + r_1^* r_1 + r_2^* r_2 + ... + r_{N_o-1}^* r_{N_o-1}. \tag{F.12}$$

Since the Yanni wave, r_0, is defined as zero in this model, summing over the x-values gives:

$$\underline{u}^{\mathrm{H}} \underline{u} + \underline{h}^{\mathrm{H}} \underline{h} = \underline{r}^{\mathrm{H}} \underline{r}, \text{ or } \|ocean\|_2^2 = \|ocean\|_E. \tag{F.13}$$

Therefore, optimals computed using the perturbation energy norm (F.10) would be equivalent to the optimals computed using the L_2 norm of the equatorial wave components (F.7). The equatorial wave component norm was used.

F.3 Why not an Energy norm?

If the L_2 norm of the ocean variables are so closely related to their perturbation energy norm, then why not build an energy norm for the SST? Could not the two energy norms then be combined to form a full norm without the variable weighting terms of

(F.1)?

There are several difficulties with this scheme. First of all, it is unclear how an energy norm for the SST could be formed. The latent heat energy of a fixed volume of water is proportional to its temperature. Since LOAM has a upper layer of fixed depth, the energy (per unit area) would be proportional to the temperature, that is

$$\text{SST pertubation energy} \propto \int_{x=x_E}^{x_W} \left(\int_{y=-\infty}^{\infty} T(x,y)dy \right) dx. \qquad \text{(F.14)}$$

But this quantity violates the first requirement for a norm (see Luenberger, 1969): it can take on negative values. Remember, $T(x,y)$ is the anomalous temperature, and can be negative. Even if this problem is solved by using the total energy (by adding the background SST fields to the anomalous field), the quantity violates the second requirement of a norm: it is not zero for $T(x,y)=0$. The perturbation energy norm used above for the ocean dynamics suffers from a similar difficulty. The total energy is

$$\text{Total Ocean energy} \propto \left[(u+\overline{u})^2+(h+\overline{h})^2\right], \qquad \text{(F.15)}$$

where $\overline{u}$ and $\overline{h}$ are the background states. But this violates the second requirement for a norm. The anomalous energy is given by

$$\text{Anomalous Ocean energy} \propto \left[(u+\overline{u})^2+(h+\overline{h})^2\right]-\left[\overline{u}^2+\overline{h}^2\right]. \qquad \text{(F.16)}$$

But this quantity can take on negative values, and therefore is not a norm. The "energy" norm that is used in Sec. F.2 is generally called the perturbation energy norm, but while it is norm, it is not actually the perturbation energy. The perturbation energy would more accurately be described by (F.16).

Absent a real energy norm for either sub-field, it is not clear that whatever "pseudo-energy" norm which might be devised for the SST and the ocean will describe any physically significant weighting between the two fields. By solving the error growth problem with the weighting between the sub-fields as a variable, the reader can make his/her own judgement about the proper weighting. In particular, a forecaster who is interested in the future error in SST predictions, would use a weighting which reflected

his/her ability to resolve each of the two sub-optimals. This weighting would be determined by the quality of the data available, not any physical characteristic of the system.

F.4 Modeling studies (Transient Growth Enhancement)

In Chapter 3, the appropriate norm can be defined by the application, but for the rest of the study, the research is no longer tied so closely to an application. Instead, the norm is used (or at least the optimals it produces) to analyse how the model could be modified to increase the transient growth relative to the modal growth. While it would have been difficult to prove beforehand that a specific norm would be effective, an examination of the results shows that the norm used here worked well.

Specifically, in Section 6.2.1, the Nino3 timeseries for a set of stochastically forced runs was compared to the Nino3 timeseries for the same models, driven with the same noise, but with the noise projected onto the (9,5)-optimal pattern. The results (Table 6.7 and Fig. 6.15) showed that the vast majority of the Nino3 variability can be explained by the optimals produced by the L_2 norm of (F.1). Therefore, one of the following must be the case: (i) using a different norm would produce optimals that look very much like the optimals of the L_2 norm; (ii) using a different norm would produce a different optimal, but this optimal would not explain very much of the ENSO variability (in a system forced by spacially uniform noise.) Neither of these eventualities make exploring other norms seem likely to be a productive line of research.

One should consider alternate norms if it turns out that the empirically determined forcing patterns so not project strongly onto the current optimals, found using the norm in (F.1). Since the emphasis in ENSO research has been on chaotic models, little is known about the structure of the external forcing. In the absence of such

information, the most generic external forcing should be assumed: spacially uniform white noise. Two non-uniform forcing regimes were explored in Chapter 6, but both regimes projected more strongly onto the optimals than the uniform noise case. Should further research into the nature of the external forcing indicate some coherent forcing patterns that do not project strongly enough onto the optimal structure to explain the ENSO variability, then other norms, or even other parameter regimes should be explored.

F.5 Spacially Non-Uniform Forcing

As stated in Section F.4, the L_2 norm (over the variables' discretized components) is the correct norm under the assumption of noise that is spacially uniform (over the variables' discretized components). What if the noise is not spacially uniform? In this case a weighting function on the initial state can be used to calculate the appropriate optimal initial conditions. This optimization can be calculated by rendering stationary the following functional:

$$F = \underline{\varphi}_0^{\mathrm{H}} \mathbf{R}_t^{\mathrm{H}} \mathbf{R}_t \underline{\varphi}_0 + \lambda\left(\underline{\varphi}_0^{\mathrm{H}} \mathbf{W} \underline{\varphi}_0 - 1\right), \tag{F.17}$$

where $\underline{\varphi}_0 = \left[\begin{matrix} \underline{r} \\ \underline{T} \end{matrix}\right]_{t=0}$ is the initial condition, $\mathbf{R}_t$ is the propagator from the initial time to the time of interest, $\mathbf{W}$ is the weighting function (or any positive definite matrix), and λ is a Lagrange multiplier.

The requirement for stationarity is the eigenvalue problem

$$\mathbf{R}_t^{\mathrm{H}} \mathbf{R}_t \underline{\varphi}_0 + \lambda \mathbf{W} \underline{\varphi}_0 = 0 \text{ or } \left(\mathbf{W}^{-1} \mathbf{R}_t^{\mathrm{H}} \mathbf{R}_t + \lambda \mathbf{I}\right) \underline{\varphi}_0 = 0. \tag{F.18}$$

Notice that in this formulation, the weighting function is applied only to the initial conditions, and so acts as a cost function. If desired, the weighting function could also be applied to the size of the vector in its final state. This was not done here because for this application (stochastic ENSO modeling) the shape of the final state is known. That is, we are looking for initial conditions that lead to the maximum growth of the ENSO

mode. Perhaps, rather than leaving the final state neutrally weighted, as was done throughout most of this study, a weighting biased toward ENSO events could be devised. For instance, heavy weighting could be given to the SST in the Nino3 region. However, as is shown in Chapters 3 through 6, no such bias was necessary for the optimals to produce ENSO events.

Ideally the cost function will be chosen to strongly weight those areas that are either (i) more susceptible to perturbation due to external forcing, or (ii) receive more external forcing. The physical mechanisms of the external forcing are, by definition, not contained in the model, and are beyond the scope of this study. However, for demonstration purposes, a cost function of type (i) will be devised. It has been observed that in the equatorial Pacific that SST tends to saturate above a certain temperature. A cost function is suggested by Wallace (1997, personal communication) that maps the background SST to values between 1.0 and 0.3. Areas where the background SST are greater than 28 C are set to 1.0 while areas with SST less than 25 C are set to 0.3. The cost function for SST values between 25 C and 28 C are mapped linearly to values from 0.3 to 1.0. Figure F.1 shows the cost function for this scheme. Figure F.2 shows the effect of this weighting scheme on the optimal initial conditions of model C.80. Figure F.2a displays the 360 day T-optimal with no cost function, and Figure F.2b show the 360 day T-optimal using the cost function from Figure F.1. As might be anticipated, the T-optimal's warm pool in the south-east Pacific is intensified since this is an area where the background SST is relatively cold. In the west central pacific, the broad cold pool of the T-optimal is reduced in magnitude since this is a relatively expensive area according to the cost function.

An alternative method to account for spacially non-uniform forcing might be derived from the covariance metric outlined in Palmer et al. (1996) in the context of the analysis of forecast error growth. Palmer et al. (1996) argues that for an initial value

problem where the probability distribution of the initial errors is known, there is a preferred metric: the covariance metric (sometimes called the Mahalanobis metric). The norm for this metric is derived so that the initial error ball is round. That is, for the specified probability distribution of errors, the magnitude of the error is the same in any direction. For the assumption of spacially white error, the covariance norm is simply the L_2 norm. In the context of the initial value problem, then the use of the L_2 norm in Chapter 3 of this study is a tacit assumption of a uniform distribution of error.

F.5 Norms Used in Comparable Studies

Three other studies of the singular vectors of intermediate models of the equatorial Pacific have recently been completed. In this section the norms used in each study will be briefly reviewed. The singular vectors of these three studies are compared with LOAM's singular vectors in Section 3.6.

F.5.1 Chen et al.

Chen et al (1997), hereafter C97, computes the singular vectors of the Battisti model (1988) in order to study the predictability of ENSO. C97 computes the tangent linear propagator from the full non-linear model by sucessively perturbing each of the grid points of the SSTA, and recording the model's response to each perturbation over a fixed period of time. The propagator for that time period can then be estimated. C97 perturbs only the SSTA, and thus calculates the SSTA to SSTA propagator. In other words, the ocean dynamics variables are assumed to be zero at the initial time. C97 uses the L_2 norm on the grid of SSTA, and so effectively assumes a spacially uniform distribution of initialization errors for the predictability problem.

Not surprisingly, since C97 uses essentially the same model and exactly the same norm as in this study, the SSTA patterns of C97's principle singular vectors look

very similar to the T-optimals calculated here. See section 3.6.1 for a detailed comparison.

F.5.2 Xue et al.

Xue et al. (1996a) and Xue et al. (1996b), hereafter X96a and X96b, respectively, also use singular vectors to study the predictably of the ENSO phenomenon. X96a uses a Markov model built from the output of the ZCM in order to calculate the linear tangent propagator. Before building the Markov model, however, X96a reduces the dimension of the problem by projecting the model data into a reduced EOF space. The reduced EOF space includes the oceanic currents, thermocline depth, SSTA, and winds. The EOF space also includes the wind divergence and heating anomaly fields, but the effects of these two fields are made negligible through a weighting factor.

The norm used by X96a is the L_2 norm of the amplitude of the EOF components. This norm, with the exception of the addition of the wind components, is the EOF space equivalent of the L_2 norm used on LOAM. It should be noted, that unlike LOAM, the ZCM winds are prognostic variables. The winds do not appear as prognostic variables in the ZCM equations, but are made prognostic by the numerics of the ZCM. Specifically, in the convergence feedback for the winds, the final term in (A.7), the iterative scheme for resolving U and V is not allowed to converge.

The principle singular vectors produced in X96a are similar to those produced in this study, though there are some differences. For details see Section 3.6.1. In general, the optimal thermocline fields from LOAM and X96a are the same, but the SSTA optimal field of X96a lacks the N-S dipole in the eastern Pacific which is found in the LOAM T-optimal. How much of this difference is due to the model differences, due to the inclusion of the winds in the norm, or due to the of EOFs in the norm is unclear. It is interesting to note that in X96a, the SSTA-only optimal is also computed, and this

looks very similar to the T-optimals of LOAM and C97.

In X96b, the same Markov model is used to address the predictability problem. Instead of the L_2 norm, however, the covariance norm from Palmer et al. (1996) is used. As an estimate of the error distribution, X96b uses the difference between the initial fields produced by the assimilation scheme of Zebiak and Cane (1987) and the improved scheme of Chen et al. (1995). The X96b singular vectors look different from the those produced by the L_2 norm in X96a. The one singular vector shown in X96b (Fig. 17) looks similar to the ENSO mode. Since analysing the predictability problem from the initial value point of view was not attempted in this study, there are no LOAM singular vectors to compare with the results of X96b.

F.5.3 Moore and Kleeman

Moore and Kleeman (1996), hereafter MK96, also uses singular vector decomposition to analyse the predictability limits of an intermediate coupled model of ENSO. MK96 uses the model of Kleeman (1993), which while having ocean dynamics and atmospheric dynamics equations similar to LOAM, has a much different thermodynamic equation. See Section 3.6.3 for details.

MK96 bases its norm on a perturbation "energy" equation like those discussed in Section F.3 of this appendix. MK96's norm is defined as the discretization of

$$E(t) = \iint \tfrac{1}{2} m_a \left(U^2 + V^2 + \varphi^2 / c^2\right) dxdy + \iint \tfrac{1}{2} m_o \left(u^2 + h^2\right) dxdy, \qquad \text{(F.19)}$$

where the variable symbols are the same as those in this study. MK96 avoids the difficulty of defining a meaningful perturbation energy to the ocean thermal layer by simply not including it in the norm. As discussed in Section 3.6.3, the thermocline part of the principle singular vector looks qualitatively similar to the thermocline optimals produced by LOAM, but the SSTA potion of MK96's singular vector looks quite different. Specifically, the SSTA fields have a high wavenumber component in the zonal direction. Whether the difference in the optimals from MK96 and the optimals from

this study is due to the different model physics, or the different norm is not clear. It should be noted, however, that experiments were performed on LOAM using the norm from equation (F.19). The r-optimals produced by LOAM were relatively unchanged by the use of (F.19), but the T-optimals displayed a high wavenumber structure in both the zonal and meridional direction (not shown).

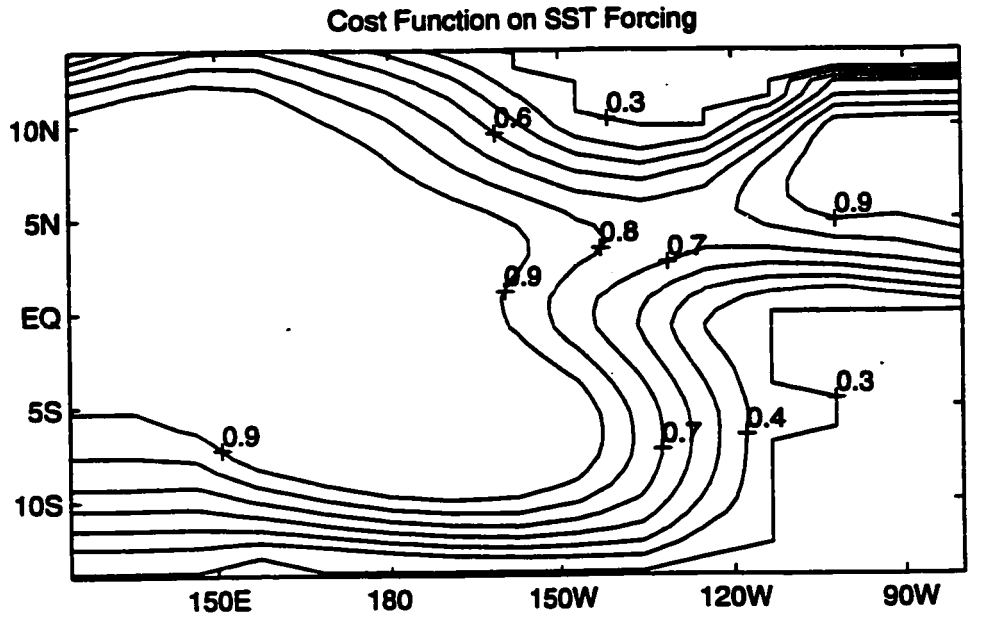

Figure F.1 - Cost Function on SST. This graph shows the cost function as derived from the SST background state by the scheme described in Sec. F.5.

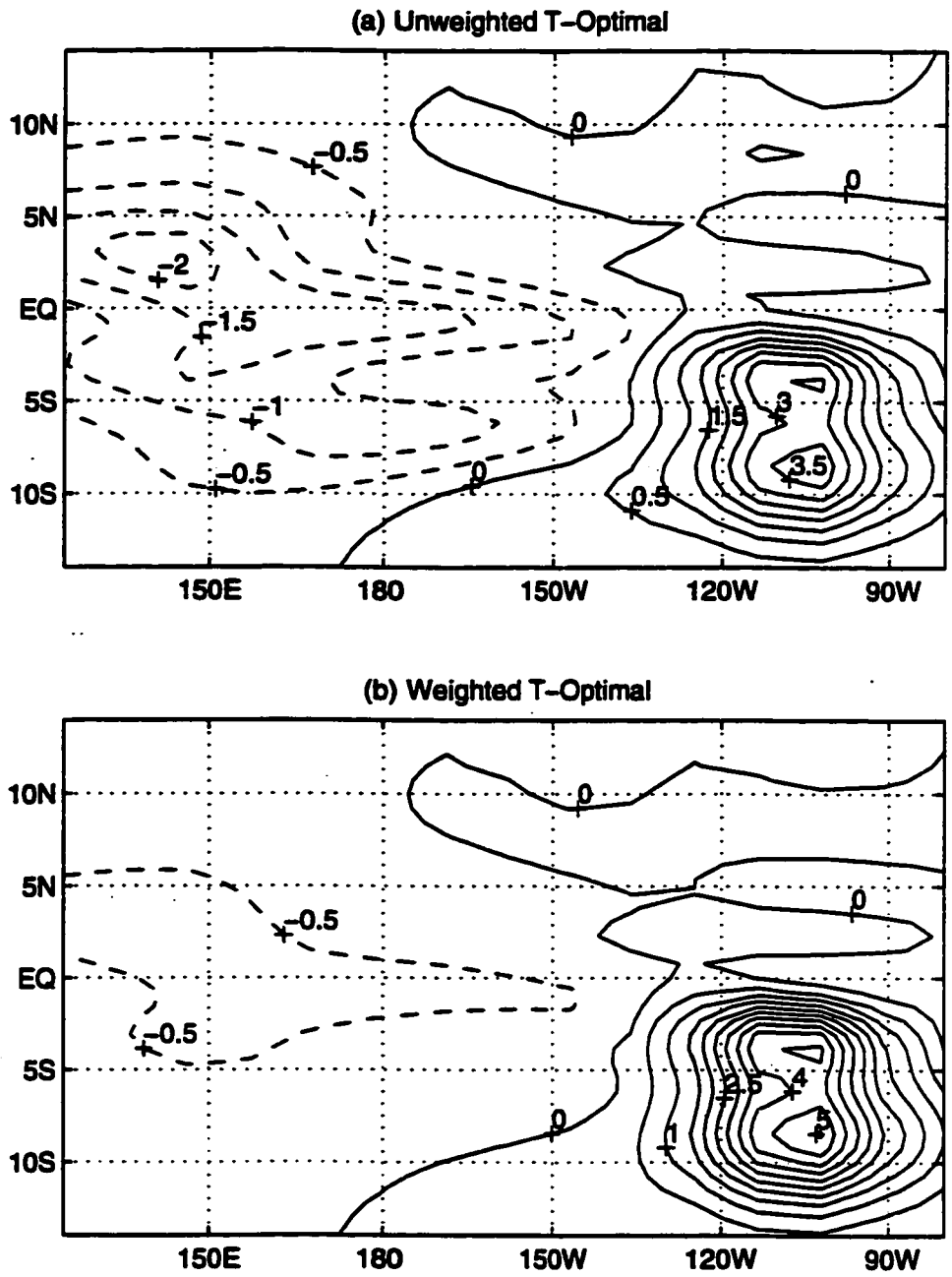

Figure F.2 - 360 Day T-Optimals, Weighted and Unweighted. Graph (a) shows the T-optimal for the C.80 model without a cost function applied. Graph (b) shows the same T-optimal, but with the cost function (Fig. F.1) applied.

Appendix G: Perturbation Energy Analysis

G.1 Definition of Norm

In an attempt to derive an "energy-like" norm of the type found in Hanifi et al. (1995), the energy evolution equation is developed for a norm of the form

$$\langle E \rangle = \int_{x=x_E}^{x_W} \int_{y=-\infty}^{\infty} \left[(ST)^2 + (R_1 u)^2 + (R_2 h)^2 \right] dy\, dx, \tag{G.1}$$

where S, R_1, and R_2 are operators. The energy evolution equations will be derived separately for $\langle E_T \rangle = \left\langle (ST)^2 \right\rangle$, and $\langle E_O \rangle = \left\langle (R_1 u)^2 + (R_2 h)^2 \right\rangle$, the thermal layer and ocean dynamics part of the the full norm, respectively, where $\langle \bullet \rangle$ symbolizes the area integration over the appropriate limits.

Starting with the thermal equation,

$$\frac{\partial}{\partial t}\langle E_T \rangle = \left\langle 2(ST)\frac{\partial}{\partial t}(ST) \right\rangle = 2\left\langle (ST)(ST_t) \right\rangle, \tag{G.2}$$

and substituting in the SST evolution equation from (A.23) yields

$$\tfrac{1}{2}\langle E_T \rangle_t = -\left\langle ST(SL_T T) \right\rangle - \left\langle ST\left(S\left[K_w \tfrac{\partial}{\partial z} - \overline{T}_x\right]u\right) \right\rangle + \left\langle ST(SK_T h) \right\rangle, \tag{G.3}$$

where L_T includes all terms which operate on T. The first term in (G.3) can be expanded as

$$\begin{aligned} \left\langle ST(SL_T T) \right\rangle = {} & \left\langle ST\left(S\overline{u}_x \tfrac{\partial}{\partial x} T\right) \right\rangle + \left\langle ST\left(S\overline{v}_x \tfrac{\partial}{\partial y} T\right) \right\rangle + \left\langle ST(SdT) \right\rangle + \\ & \left\langle STS\left[K_U^x \tfrac{\partial}{\partial x} + K_U^y \tfrac{\partial}{\partial y} + K_U\right] U_{(T)} \right\rangle + \left\langle STS\left[K_V^x \tfrac{\partial}{\partial x} + K_V^y \tfrac{\partial}{\partial y} + K_V\right] V_{(T)} \right\rangle \end{aligned} \tag{G.4}$$

where $U_{(T)}$, and $V_{(T)}$ are the zonal and meridional wind velocities, determined at any time by the SST from equations (A.5)-(A.9).

The ocean dynamics energy evolution is given by,

$$\tfrac{1}{2}\langle E_O \rangle_t = \left\langle (R_1 u)(R_1 u_t) + (R_2 h)(R_2 h_t) \right\rangle. \tag{G.5}$$

Substituting the time derivative terms for the zonal current (A.10) and the thermocline perturbation (A.12) yields,

$$\tfrac{1}{2}\langle E_O\rangle_t = -\left\langle a(R_1u)^2\right\rangle - \left\langle a(R_2h)^2\right\rangle + \left\langle R_1uR_1\left(K_S^xU_{(T)} + K_S^cV_{(T)}\right)\right\rangle - \left\langle R_2hR_2\,\tfrac{\partial}{\partial x}u\right\rangle - \left\langle R_1uR_1\,\tfrac{\partial}{\partial x}h\right\rangle \qquad \text{(G.6)}$$

Equation (G.6) can be simplified to

$$\tfrac{1}{2}\langle E_O\rangle_t = -a\langle E_O\rangle + \langle R_1uR_1L_WT\rangle - \langle R_2hR_2\,\tfrac{\partial}{\partial x}u\rangle - \langle R_1uR_1\,\tfrac{\partial}{\partial x}h\rangle, \qquad \text{(G.7)}$$

where L_W operates on T to give the windstress forcing. All the terms, along with their physical interpretations, are summarized in Table G.1.

Table G.1 - Terms of the Energy Evolution Equation.

Term #	$\tfrac{1}{2}\langle E\rangle_t =$	Description
1	$-\left\langle ST\left(SK_w\,\tfrac{\partial}{\partial x}u\right)\right\rangle$	Anom. upwelling on BG vert. SST
2	$+\left\langle ST\left(S\overline{T}_x u\right)\right\rangle$	Anom. advection on BG SST
3	$+\left\langle ST\left(SK_T h\right)\right\rangle$	BG upwelling on Anom. Tcline
4	$-\left\langle ST\left(S\overline{u}_x\,\tfrac{\partial}{\partial x}T\right)\right\rangle$	SSTA on BG zonal advection
5	$-\left\langle ST\left(S\overline{v}_x\,\tfrac{\partial}{\partial y}T\right)\right\rangle$	SSTA on BG merid. advection
6	$-\langle ST(SdT)\rangle$	Thermal damping
7	$-\left\langle STS\left[K_U^x\,\tfrac{\partial}{\partial x} + K_U^y\,\tfrac{\partial}{\partial y} + K_U\right]U_{(T)}\right\rangle$ $-\left\langle STS\left[K_V^x\,\tfrac{\partial}{\partial x} + K_V^y\,\tfrac{\partial}{\partial y} + K_V\right]V_{(T)}\right\rangle$	Anom. Ekman upwelling and advection
8	$-\left\langle a(R_1u)^2\right\rangle - \left\langle a(R_2h)^2\right\rangle$	Ocean mechanical damping
9	$-\left\langle R_2hR_2\,\tfrac{\partial}{\partial x}u\right\rangle$	Zonal current gradient
10	$-\left\langle R_1uR_1\,\tfrac{\partial}{\partial x}h\right\rangle$	Thermocline gradient
11	$+\left\langle R_1uR_1L_WT\right\rangle$	Windstress forcing

In Hanifi et al. (1995) the operators (or in their case, constants) are determined from the energy evolution equation by setting equal to zero the sum of certain components which physical reasoning indicates should be zero in an energy-like norm.

In particular, Hanifi et al. (1995), set the pressure related transfer terms to zero - reasoning that an energy-like norm should not create or destroy energy (averaged over the entire system), through compression work. One equivalent idea for this system might be that no energy-like-amplitude should be gained or lost through advection of SST. Unfortunately it is not clear that this particular set of terms can be zeroed using a norm of the form of (G.1).

However, the terms of Table G.1 can still be examined to try to find the relationships between the operators R_1, R_2, and S that generate a reasonable norm.

G.2 The relationship between R_1 and R_2

First, the four terms of the ocean energy evolution (terms 8, 9, 10, and 11 in Table G.1) are examined. Term 8 represents the energy lost due to the mechanical damping in the ocean. This term represent intrinsic energy loss and should not be zeroed out (in other words, the relationship between R_1 and R_2 should not be determined using this term). Term 11 represents the mechanical energy input to ocean by the SST (through the winds). Since the operator R_2 does not appear in term 11, it obviously cannot be used to generate a relationship between R_1 and R_2.

This leaves terms 9 and 10, which represent the transfer of energy between the thermocline perturbation and the zonal velocity. There is no obvious reason to believe that energy is created or destroyed in this process, and since R_1 and R_2 appear in these two terms, it seems reasonable to determine the relationship between R_1 and R_2 using these two terms. The goal is to determine R_1 and R_2 such that

$$\int_{x=x_E}^{x_W}\int_{y=-\infty}^{\infty}\left[R_2 h R_2 \tfrac{\partial}{\partial x}u + R_1 u R_1 \tfrac{\partial}{\partial x}h\right]dy\,dx = 0. \qquad \text{(G.8)}$$

If it is assumed that $\frac{\partial}{\partial x}R_2 = 0$, then the first term can be integrated by parts, yielding

$$\int_{y=-\infty}^{\infty}\left[R_2 h R_2 u\big|_{x_W} - R_2 h R_2 u\big|_{x_E} - \int_{x_E}^{x_W} R_2 u R_2 \tfrac{\partial}{\partial x}h\,dx + \int_{x_E}^{x_W} R_1 u R_1 \tfrac{\partial}{\partial x}h\,dx\right]dy = 0. \qquad \text{(G.9)}$$

If it is further assumed that $R_1 = R_2$, and taking into account that the boundary condition on the eastern boundary is $u(x_E, y) = 0$ (see Hirst, 1988), then (G.9) reduces to a constraint on the western boundary:

$$\int_{y=-\infty}^{\infty} [R_1 h R_1 u]_{x_W} \, dy = 0. \qquad \text{(G.10)}$$

The western boundary conditions are (from Hirst 1988) that $\int_{y=-\infty}^{\infty} u(x_W, y) dy = 0$ and h is unconstrained. This boundary condition does not imply that (G.10) is correct. Nor is it obvious what (non-trivial) R_1 would make (G.10) true.

In fact, (G.10) is probably not a reasonable constraint for an energy-like norm, since in the long wavelength approximation the western boundary is not a perfect reflector. That is, even assuming a western boundary reflection coefficient of one, energy is lost on this boundary through boundary Kelvin waves which carry energy along the coast on a scale below the resolution of this model (see Clark, 1983).

Still, this may be acceptable: With the above constraints (that $R_1 = R_2$,and $\frac{\partial}{\partial x} R_2 = 0$), terms 9 and 10 are conserved everywhere except on the western boundary - a location where it is reasonable that they not be conserved.

G.3 The Relationship between R_1 (or R_2) and S

Examination of the terms in Table G.1 shows that there are only a few terms that might be used to set a relationship between S and R_1. Term 11 contains both u and T, as do terms 1 and 2. This gives exactly three relationships which might potentially be used to determine S from R_1:

$$\langle R_1 u R_1 L_W T \rangle + \langle ST(S\bar{T}_x u) \rangle \stackrel{?}{=} 0, \text{ or} \qquad \text{(G.11)}$$

$$\langle R_1 u R_1 L_W T \rangle - \langle ST(SK_w \tfrac{\partial}{\partial x} u) \rangle \stackrel{?}{=} 0, \text{ or} \qquad \text{(G.12)}$$

$$\langle R_1 u R_1 L_W T \rangle - \langle ST(S[K_w \tfrac{\partial}{\partial x} - \bar{T}_x]u) \rangle \stackrel{?}{=} 0. \qquad \text{(G.13)}$$

Equation (G.11) implies that the kinetic energy change due to the winds acting on the

(meridional) current is in balance with the energy change due to the advection of background SST by the (meridional) current. There is no obvious physical reason why this should be true. Also, there is no obvious motivation for this condition to be enforced through the choice of the norm. Equation (G.12) implies that the kinetic energy change due to the winds acting on the currents is in balance with the energy change due to the anomalous upwelling acting on the background vertical temperature gradient. Once again, there is no obvious reason why this should be true. The third equation, (G.13), simply includes both thermal equations' terms, and once again has no physical motivation.

Nevertheless, what if one of the relationships in equations (G.11) through (G.13) were assumed to be true. For (G.11) to be true for any u and T fields would seem to imply that $R_1 = \pm S\overline{T}_x$ and $S = \mp R_1 L_W$, or that $S = -S\overline{T}_x L_W$, for which there would seem to be no non-trivial solution. There are similar problems in trying to find the solutions of equations (G.12) and (G.13).

If S cannot be determined in relationship to R_1, maybe it can be determined independently of R_1. Perhaps all or some of the advection terms in the energy evolution equation can be set to zero. This makes physical sense, since it is reasonable that advection would not create or destroy an "energy-like" quantity. The advection terms are numbers 2, 4, 5, and parts of 7, and so the relation might be:

$$\left\langle ST\left(S\overline{T}_x u\right) - ST\left(S\overline{u}_x \tfrac{\partial}{\partial x} T\right) - ST\left(S\overline{v}_x \tfrac{\partial}{\partial y} T\right) + ST(SL_E T)\right\rangle \stackrel{?}{=} 0, \qquad \text{(G.14)}$$

where L_E is the operator through which the SST acts to advect on itself through the Ekman layer. (See equations (A.5), (A.6), (A.7), (A.9), and (A.23) through (A.29)). Since u and T are independent of each other, the first would have to be dropped from the (potential) constraint. This is because if $u(x,y) = 0$, and $T(x,y) = T_1 \neq 0$, and if (G.14) were true, this would imply that $\left\langle -ST_1\left(S\overline{u}_x \tfrac{\partial}{\partial x} T_1\right) - ST_1\left(S\overline{v}_x \tfrac{\partial}{\partial y} T_1\right) + ST_1(SL_E T_1)\right\rangle = 0$ for any T_1, and therefore that $\left\langle ST\left(S\overline{T}_x u\right)\right\rangle = 0$ for any u and T. Since $\overline{T}_x \neq 0$, this would imply that $S = 0$, the trivial result.

Therefore, there are only three potential relationships:

$$\left\langle ST\left(S\overline{u}_x \tfrac{\partial}{\partial x}T\right) - ST\left(S\overline{v}_x \tfrac{\partial}{\partial y}T\right) + ST(SL_E T)\right\rangle \stackrel{?}{=} 0 \qquad \text{(G.15)}$$

$$\left\langle -ST\left(S\overline{u}_x \tfrac{\partial}{\partial x}T\right) - ST\left(S\overline{v}_x \tfrac{\partial}{\partial y}T\right)\right\rangle \stackrel{?}{=} 0, \text{ or} \qquad \text{(G.16)}$$

$$\langle ST(SL_E T)\rangle \stackrel{?}{=} 0 \qquad \text{(G.17)}$$

No non-trivial solution to any of these equations is evident, and so the method of Hanifi et al. is apparently not tractable on this system.

VITA

Christopher John Thompson was born on February 3, 1962 in Pasadena, California. He received his B.S. in Engineering Science from University of California at San Diego in 1985, and a M.A. in Applied Mathematics from California State University at Fullerton in 1988. From 1985 to 1990 he worked as a project engineer for L'Garde Inc. in Tustin California.

IMAGE EVALUATION TEST TARGET (QA-3)

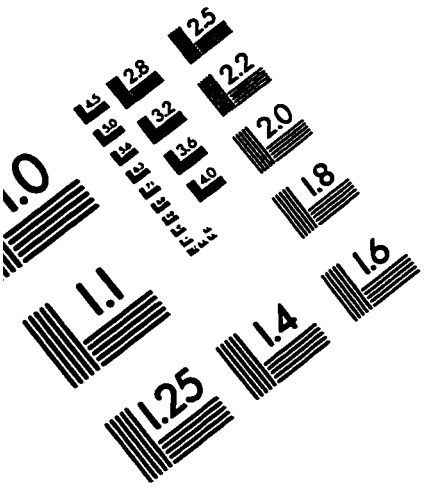

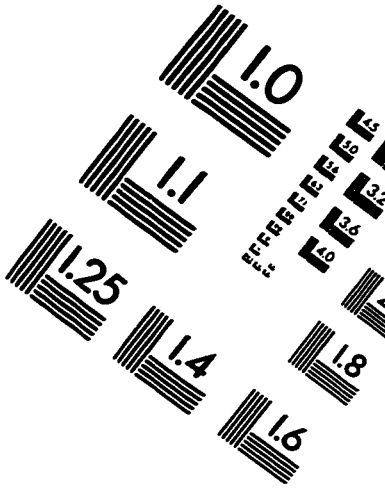

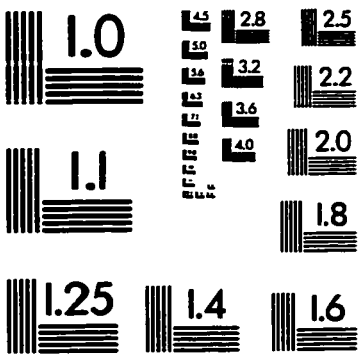

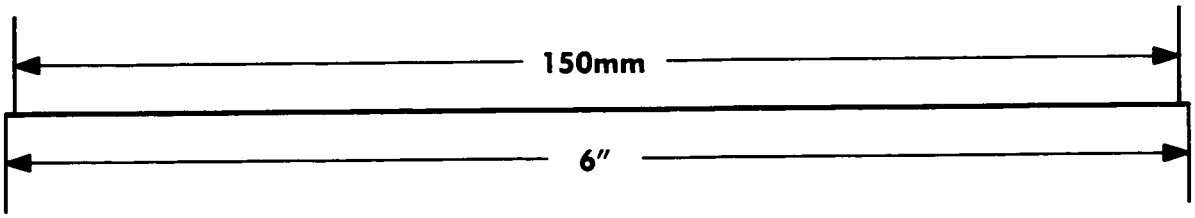

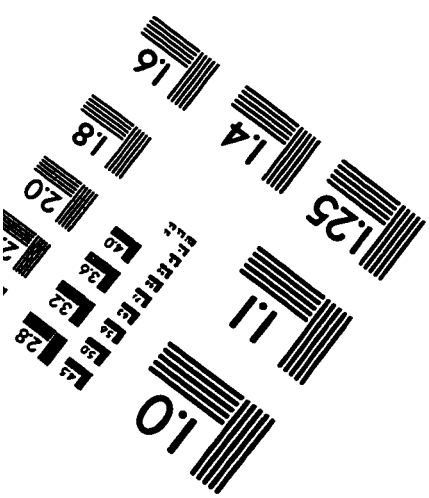

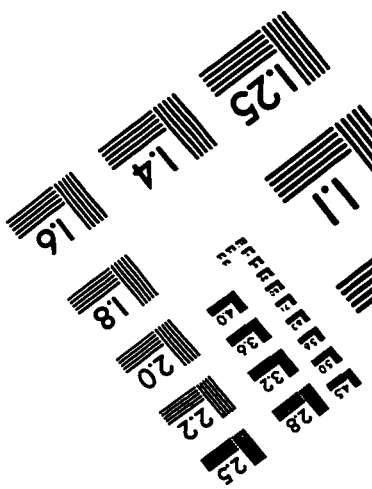

APPLIED IMAGE, Inc
1653 East Main Street
Rochester, NY 14609 USA
Phone: 716/482-0300
Fax: 716/288-5989